Imperial College London

Single Pixel Polarimetric Imaging through Scattering Media

Seow Kai Ling Cheryl

Imperial College London
Department of Physics

Thesis submitted in partial fulfilment of the requirements
for the degree of Doctor of Philosophy
and the Diploma of Imperial College

May 28, 2020

Abstract

Compared to pure intensity-based imaging techniques, polarimetric imaging can provide additional information, particularly about an imaged object's compositional, morphological and microstructural properties. The value of polarimetric imaging has already been demonstrated in various applications, such as early glaucoma detection and cancer discrimination. Its applicability, however, to practical *in-vivo* imaging situations is limited as the object of interest is often located behind a scattering layer, such as biological tissue, which scrambles both the spatial and polarimetric information about the object that is contained in the propagating light. As such, this work set out to find a means of conducting polarimetric imaging through scattering media.

Under the assumption that it is possible to illuminate the object plane with the required spatial patterns, single pixel cameras can enable imaging in scattering environments and were hence thoroughly investigated in this thesis as a route to polarimetric imaging through scattering media. A theoretical model for single pixel polarimetric imaging was first developed, and conditions under which the proposed method was feasible were identified and verified using 2D coupled line dipole simulations. The proposed method was further tested through experiments conducted using an in-house custom-built setup, composed of off-the-shelf components. To mitigate noise and to ensure that the obtained polarimetric image was physical, a constrained least squares algorithm was proposed and implemented. Experiments with various test objects hidden behind scattering phantoms showed that single pixel polarimetric imaging was able to successfully reconstruct the polarimetric images of the hidden object, whereas a spatially resolved detector in the same configuration resulted in an image that bore no resemblance to the test object. Further experiments that were conducted with the same test objects hidden behind chicken breast slices were, unfortunately, unable to recover an accurate polarimetric image of the hidden object. Additional investigations identified two factors that had likely affected the image reconstruction - spatial inhomogeneity and temporally varying transmittance of the chicken breast, both of which were unaccounted for in the data processing. On the basis of the experiments and simulations conducted in this work, single pixel polarimetric imaging was found to be a feasible approach for polarimetric imaging through scattering media. Finally, further improvements to establish single pixel polarimetric imaging as a practical technique are discussed.

Declaration of Originality

I hereby declare that the contents of this thesis are my own work, unless otherwise referenced.

Copyright Declaration

For my family.

Acknowledgements

Getting to this point in my journey has not been easy, and I could not have done it alone. I would like to take this opportunity to sincerely thank all those who have contributed to this work.

First and foremost, I would like to express my heartfelt thanks to Prof. Peter Török, Dr. Kenny Weir and Dr. Matthew Foreman for their continued guidance and supervision during my PhD. I am especially indebted to Matt for his persistent support and patience throughout this PhD. Thank you Matt for entertaining all of my questions and for everything that you've taught me. Thank you also for your thorough and useful feedback on so many aspects of my work, including each and every chapter of this thesis.

Special thanks also to Prof. Carl Paterson, whose timely advice I have benefited from at various milestones during my PhD. I am also much obliged for his generosity in loaning me lab equipment for this work.

My heartfelt gratitude goes to Martin, Simon and John from the Optics workshop for all of their invaluable help and support. Thank you for going above and beyond to help me in so many ways in this PhD, especially during the time when I was trying to figure out the fabrication of the scattering phantoms. Thank you for your help with the epoxy moulds, and for helping me with the vacuum chamber. My sincere thanks also goes to Dr. Khadija B. Tahir, who kindly shared with me her experience in making scattering phantoms.

Needless to say, this thesis would not have been possible without the generous financial support from my employer, DSO National Laboratories. Thank you for giving me this opportunity to further my studies. I would also like to acknowledge my fellow colleagues, whose continual support and friendship I am always grateful for.

A big thank you also to my teachers and colleagues in Photonics. In a special way, I'd like to thank my group members/office mates, Yuchen, Chengze, Joel and Niall, for putting up with so many of my questions, and more importantly, for their friendship. In addition, I would like to express my appreciation to Kathy for helping me with all biology-related questions. I've also been lucky enough to meet some great and supportive friends here in London, because of whom London has now become for me a home away from home. This supportive network of friends has been truly kept me sane and I am grateful for each and every one of them.

The greatest thanks of all goes to my family, whose love and support have sustained me through the toughest of times. Mum, Dad and Joseph, thank you for always believing in me and supporting me in my decision to pursue this PhD.

Last, but definitely not the least, I would like to thank God for putting each and every one of these people in my life, and for His providence in all things.

Abbreviations and acronyms

CCD	Charge coupled device
CMOS	Complementary metal oxide semiconductor
CLSQR	Constrained least squares (algorithm)
CV	Coefficient of variation
DMD	Digital micro-mirror device
DOP	Degree of polarisation
DOCP	Degree of circular polarisation
DOLP	Degree of linear polarisation
ECM	Eigenvalue calibration method
LCSLM	Liquid crystal spatial light modulator
LCVWP	Liquid crystal variable waveplate
MFP	Mean free path
NA	Numerical aperture
ND	Neutral density (filter)
OCT	Optical coherence tomography
PSA	Polarisation state analyser
PSG	Polarisation state generator
RMSE	Root-mean-square error
SLM	Spatial light modulator
SNR	Signal to noise ratio
TMFP	Transport mean free path
VTM	Vector amplitude transmission matrix
VWP	Variable waveplate

Contents

List of Figures

List of Tables

Chapter 1

Introduction

1.1 Motivation and Aims

Optical imaging is a powerful and indispensable tool for applications in biomedicine. For instance, it enables the quantitative measurement and monitoring of biological tissues, hence making it critical to the advancement of relevant technology, such as improved medical diagnostics and treatment. Most commonly, it is light intensity that is measured in imaging, with some methods including a discrimination of the light frequency. Yet, knowledge of the polarisation of light, which is often ignored, can empower additional imaging functionalities, as it contains useful information about the object's compositional, morphological and microstructural properties. These properties are related to the polarimetric features of the imaged object, such as its depolarisation, birefringence and diattenuation, which affect the measured polarisation state. For example, collagen has a fibrous structure that exhibits retardance and linear diattenuation. Using imaging polarimetry, these polarimetric properties have been measured and utilised for the determination of the density and orientation of collagen samples [1, 2], which are vital information for investigations of cartilage diseases, such as osteoarthritis. In addition, being sensitive to structure, imaging polarimetry has also found use in cancer discrimination [3, 4], as the structure of the cancerous tissue is altered due to factors such as increased

vascularisation and cell density. Further examples of biomedical applications of polarisation imaging include early glaucoma detection [5, 6] and bacterial studies [7].

Unfortunately, the applicability of polarimetric imaging is often limited in practical *in-vivo* imaging geometries, where the object of interest (e.g. a tumour) is often located behind a scattering medium, such as biological tissue. Scattering scrambles both the spatial and polarisation information of light propagating through these scattering media, such that in many cases, the obtained image bears little resemblance to the obscured object, but instead shows a random distribution of intensity and polarisation states. To date, by utilising techniques that isolate unscattered light (as discussed later in this chapter), *in-vivo* polarimetric imaging can be performed up to depths on the order of one transport mean free path (TMFP) [8]. The ability to image deeper, however, is required for many applications, such as for the *in-vivo* imaging of cancerous regions in deeper layers of skin without the use of invasive biopsies [9]. In view of this need, this work aims to find a means that would enable polarimetric imaging at greater depths (up to multiple times of the TMFP), with a focus on techniques for biomedical applications.

In this section, state-of-the-art techniques for imaging through scattering media are first reviewed. Then, based on this understanding, the research direction for this thesis is presented.

1.1.1 Imaging with Ballistic Light

One way to form an image of an obscured object is to reject scattered light and collect only the unscattered (or otherwise known as ballistic) component of light, by distinguishing based on the properties preserved mainly by unscattered light. For example, confocal microscopy [10] discriminates ballistic photons spatially by rejecting scattered light via a spatial pinhole located in a plane that is the imaging conjugate of the object plane. This is otherwise known as spatial-gating. On the other hand, optical coherence tomography (OCT) [11] uses coherence-gating to isolate the ballistic component of light by using an interferometric setup that is illuminated by a broadband light source with low temporal coherence (i.e. a short

coherence length). Temporal filtering of the ballistic signal has also been used in time-gated ballistic imaging [12, 13], where a pulsed light source and time-resolved detection discriminates ballistic photons based on their time-of-flight. It should be noted that though distinct in their experimental implementation, OCT and temporal filtering with a pulsed source are fundamentally similar as both techniques aim to reject photons that, due to scattering, have taken longer paths in the scattering medium. Alternatively, instead of using a pulsed beam, the intensity or polarisation state of a continuous wave source can be temporally modulated [14, 15]. The ballistic component can then be extracted via a band-pass filter of the collected signal in Fourier space about the known modulation frequency. Finally, ballistic light can also be segregated via its polarisation state, that is, polarisation-gating [16]. In polarisation-gating, polarisation optics is used to collect only the co-polarised component of the light returning from the test specimen, that is, the light that maintains the polarisation state of the incident light. Since scattering scrambles both the propagation direction and polarisation state of light, collecting only the co-polarised component of light reduces the amount of scattered light in the measured signal.

The four above-mentioned ways of discriminating ballistic photons - spatial filtering, temporal filtering, coherence gating and polarisation gating, have been used separately or in combination with each other, and have been shown to be widely successful. The intensity of ballistic light, however, decreases exponentially with depth in the scattering medium, as described by the Beer-Lambert law (discussed in Chapter 2). This phenomenon fundamentally limits the imaging depth of these techniques. This limitation is alleviated slightly by the fact that biological tissues scatter mostly in the forward direction, so that the spatial and polarimetric information of the imaged object can persist even after a few scattering events. Nevertheless, at best, these techniques operate at a maximum penetration depth of about one TMFP, which is the average distance after which the propagation direction of the scattered photons become uncorrelated with their initial propagation direction, and can be taken to be fully random. For biological tissue, the TMFP is on the order of 1mm [8, 17, 18].

Rather than rejecting scattered light, some techniques have opted, instead, to reduce the amount of scattered light produced in the first place. This can be done, for example, through optical clearing [19], where chemical treatment is applied to the sample to make it more transparent. Such methods, however, are toxic and cannot be applied to living samples. The amount of scattered light produced can also be reduced by turning to longer wavelengths. The scattering cross section, which describes the proportion of incident light that is scattered, has an inverse relationship with wavelength, so less scattering occurs at longer wavelengths. This phenomenon is used in techniques such as photoacoustic imaging [20, 21] and multi-photon microscopy [22, 23]. Nevertheless, equipment suited for wavelengths outside of the visible range tend to be more expensive and these techniques suffer fundamentally from poorer imaging resolution due to the larger diffraction limit at longer wavelengths.

1.1.2 Imaging with Scattered Light

Given the drawbacks of the above-mentioned techniques, there is a growing interest to make use of scattering rather than get rid of it. In the weakly scattering regime, rather than rejecting scattered light entirely, the distortion to the incident wavefront caused by scattering can be corrected by using adaptive optics [24]. In this method, the wavefront originating from a guide star located near to the imaging area of interest is analysed using a wavefront sensor, such as a Shack-Hartmann lenslet array, and the wavefront distortions are then corrected for using a spatial light modulator (SLM), like a deformable mirror or an array of phase-modulating liquid crystals. A well-established technique, adaptive optics has already been successfully applied to many fields, including astronomy [25] and retinal imaging [26]. One limitation faced by adaptive optics, however, is the requirement of a physical guide star [27] situated close enough to the imaging area of interest such that it experiences similar aberrations, which is a condition that is not always available in practice. Alternatively, a virtual guide star [28] can be used, but these are difficult to create at greater depths.

Furthermore, adaptive optics is usually concerned with the correction of low order, smoothly varying aberrations, and is ill-equipped to deal with the more complex phase variations caused by scattering [29].

Feedback-based Wavefront Shaping

When light is incident on a static scattering medium, a speckle pattern is observed, both in transmission and reflection. This speckle is, in fact, an interference pattern caused by the superposition of many waves arriving at the observation plane, with different phases and amplitudes caused by scattering. By altering the incident wavefront, it is possible to manipulate this interference pattern, so that the transmitted or reflected light takes up a desired form, such as a focus. In 2007, this control of multiply scattered light was first demonstrated by Vellekoop *et al.* [30]. In their seminal paper, it was shown that by shaping an incident wavefront using a SLM, multiply scattered light can be made to interfere such that a focus, or even multiple foci, are formed after transmission through an opaque static scattering medium. The optimal wavefront to use was found by cycling the phase of each segment on the SLM through 2π, and choosing the phase that maximised a feedback signal - the intensity of the target distribution. Using the same technique, the authors later demonstrated focusing on a fluorescent bead embedded within a layer of zinc oxide pigment [31]. Cycling the phase for each segment may not be the most efficient means of wavefront shaping, and in view of time and signal to noise ratio (SNR) considerations, other algorithms for determining the optimal wavefront have also been proposed [32]. In addition, instead of phase modulation of the incident wavefront as initially implemented by Vellekoop *et al.*, amplitude modulation can also be used [33]. Though pure amplitude modulation theoretically results in a lower intensity enhancement at the focus [34], it allows for faster implementations based on digital micromirror devices (DMD), which have fast switching speeds [35].

Such wavefront shaping techniques have been further explored by many researchers using various feedback signals, such as two-photon fluorescence [36], the ultrasound signal generated via the photo-acoustic effect [37] and the frequency-shifted light induced by the acousto-optic effect [38]. Moreover, by choosing the appropriate

feedback signal, it has been shown that wavefront shaping techniques can be used to form foci with distinct polarisation [39, 40], spectral [41, 42] and temporal [43, 44] selectivity. Once these foci have been formed, they can be raster scanned to form images [45] of objects hidden behind the scattering medium through the use of the optical angular memory effect [46]. The angular memory effect, which is further discussed later in this section, is where the output speckle from a tilted incident wavefront is also tilted but remains otherwise unchanged. This effect occurs over a limited angular range, within which the optimised foci can be scanned. Other than imaging, the ability to form foci through scattering media can also be useful in other applications, such as for the optical trapping and manipulation of nanobeads behind a scattering layer [47].

At heart, these wavefront shaping techniques are based on the fact that the resulting scattered light is deterministic for any *fixed* instance of disorder. Thus, one challenge faced by these techniques is the continual re-optimisation of the incident wavefront that is required for dynamic scattering media, which result in scattered fields that change with time. Furthermore, the limited range of the optical memory effect limits the imaging field of view of these techniques. Outside of this field of view, or for a different target field distribution, the incident wavefront has to be reshaped.

Optical Phase Conjugation

An alternative technique to wavefront shaping, known as optical phase conjugation, makes use of the time reversal symmetry of light. The first use of time-reversal to recover an initial signal that had been scrambled by scattering was in the field of acoustics [48, 49], but it has since been applied to the optical regime. The key idea is that scattered light that is measured after propagation through the scattering medium can be "time-reversed" and sent back through the same scattering medium to recover the original incident field distribution, be it a focus or an image of a hidden object behind the scattering medium. For monochromatic light, time reversal is equivalent to phase conjugation, and can be achieved using phase conjugate mirrors based on photorefractive mirrors [50, 51]. Alternatively, phase conjugation can be

achieved digitally by first measuring the scattered field, for example by using digital phase-shifting holography, before forming the phase conjugate of the scattered field with a SLM and sending it back through the scattering medium [52, 53, 54]. Optical phase conjugation has already been successfully applied to imaging through various biological tissues in the multiple scattering regime [51, 55, 56], with one of its main advantages over wavefront shaping techniques being that the shaped wavefront is computed from a single measurement of the output speckle field. Optical phase conjugation methods, however, require access to both sides of the scattering medium. This obstacle may seem to render optical phase conjugation inutile for practical purposes, but solutions have been designed to overcome this problem. One example of such a solution is to use ultrasonically-encoded light [52, 57, 58], where light within an ultrasound focus is shifted in frequency due to the acousto-optic effect. The frequency-shifted light at the focus serves as a virtual guide star, so that when the scattered light at this shifted frequency is collected and "time-reversed", an optical focus within the scattering medium can be formed. Other sources have also been used as virtual guide stars, such as light produced by second harmonic generation [53], or even temporally incoherent fluorescence [54]. Nevertheless, similar to wavefront shaping techniques, the shaped wavefront is only valid for a fixed instance of disorder, which means that the applied wavefront has to be recomputed continuously for dynamic scattering media, or when the scattering medium is shifted in any way. Furthermore, true time reversal requires the measurement and manipulation of light amplitude, phase and polarisation over the full solid angle, and this is difficult to achieve given the finite size of the components involved, such as photorefractive mirrors, SLMs and charge-coupled device (CCD) or complementary metal oxide semiconductor (CMOS) cameras. As a result of this partial reconstruction of the "time-reversed" wavefront, a background is typically present with the recovered initial field [55, 59], which for imaging applications would imply a decrease in the signal-to-noise ratio.

Imaging with Speckle Correlations

A spatial basis consisting of a complete set of orthogonal spatial modes can be used to describe any arbitrary field at the input or output of a scattering medium. Various

definitions for this spatial basis are possible, for example a point basis, where each spatial mode corresponds to a point source or detector, or a Fourier basis, where spatial modes correspond to plane waves travelling at different angles. It has been shown that due to the existence of various correlations in the output speckle from different input spatial modes, information on the relative amplitude and phase of each input mode is preserved even upon propagation through a scattering medium [60]. As such, information about the object hidden behind the scattering medium is not completely lost and can be exploited for imaging. In particular, transmitted incident modes with a transverse wavevector difference of $\Delta k_\perp < \frac{1}{L}$ have been found to be highly correlated [46], where $\Delta k_\perp$ is the change in the transverse wavevector and L is the thickness of the scattering medium. If an incident plane wave is tilted within this angular range, the output speckle from the scattering medium is tilted but remains otherwise the same, resulting in a shift of the output speckle in the far-field. Thus, a change in the incident field (i.e. a tilt) is directly manifested in the output speckle, showing that information about the incident field persists even though it has been scattered by the medium. This is commonly known in literature as the angular memory effect. The angular range over which this tilt correlation persists is independent of the TMFP and the specific instance of disorder, and is only inversely related to the medium thickness [46]. The same phenomenon exists for the reflected modes, but the angular range is determined, instead, by the transport mean free path [61].

As discussed above, the angular memory effect has been used to scan foci formed via wavefront shaping or optical phase conjugation, so that an image can be formed by raster scanning [45]. A few works have opted for a different approach, making use of the memory effect directly for imaging. Bertolotti *et al.* [62] illuminated a fluorescent object placed behind a scattering medium using a collimated laser beam, and collected the fluorescence intensity in reflection through the scattering medium using a photodiode. As the illumination angle of the beam was changed within the range of the angular memory effect, the output speckle was shifted across the hidden object. Thus, the measured intensity, as a function of illumination angle, θ, is a convolution of the unchanging output speckle, S, and the object intensity

reflectance, O, which can be written as

$$I(\theta) = O(\theta^{'}) * S(\theta^{'}) \approx O\left(\frac{x^{'}}{z_0}\right) * S\left(\frac{x^{'}}{z_0}\right) \ , \tag{1.1}$$

where $*$ denotes a convolution and in the limit of small angles $\theta^{'} \approx \frac{x^{'}}{z_0}$. z_0 is the distance between the object and the front surface of the scattering medium and $x^{'}$ is the spatial co-ordinate in the object plane. Defining $\beta = \frac{x^{'}}{z_0}$, an autocorrelation of $I(\theta)$ as a function of θ, averaged over different instances of disorder, can be written as

$$\begin{aligned} \langle I(\theta) \star I(\theta) \rangle &= \langle (O(\beta) * S(\beta)) \star (O(\beta) * S(\beta)) \rangle. \\ &= (O(\beta) \star O(\beta)) * \langle S(\beta) \star S(\beta) \rangle \end{aligned} \tag{1.2}$$

where $\star$ denotes the autocorrelation and $\langle ... \rangle$ indicates an averaging over different instances of disorder. The width of the autocorrelation of S is usually peaked and narrow [63] and is often approximated to be a delta function such that $\langle I(\theta) \star I(\theta) \rangle \approx (O(\beta) \star O(\beta))$ [62, 64]. As such, the autocorrelation of the object can be directly obtained from an autocorrelation of the measured intensity. An image of the object can then be reconstructed from its autocorrelation using phase retrieval techniques [65].

Katz *et al.* [64] used a similar principle but implemented it using a spatially incoherent light source, which enabled $I(\theta)$ to be obtained in a single shot. This eliminated the need for multiple acquisitions over different angles of the incident laser beam. Since the speckle coming from each point of the object adds up incoherently, the output speckle from the scattering medium acts as an intensity point spread function. This can be contrasted to the point spread function from a lens. Imaging of blood cells [66] and moving objects [67] have also been successfully demonstrated via the same technique.

Unlike the imaging techniques that have been previously discussed, one key advantage of using the memory effect for imaging is that neither pre-calibration of the system nor the implementation of guide stars are required. Moreover, the object can be recovered from a single shot while the simple experimental design makes it

compatible with existing microscope systems, as demonstrated by Hofer *et al.* [68]. Unfortunately, this group of techniques faces a few important limitations.

One drawback of these techniques is that the finite width of the speckle autocorrelation function $\langle S(\beta) \star S(\beta) \rangle$, which is often neglected, could lead to some inaccuracies in the reconstruction for small or complex objects. The object complexity is also limited by the phase retrieval techniques that are commonly used [65]. An alternative method was proposed by Edrei *et al.* [69], who measured the point spread function of the system with the scattering medium present and applied deconvolution techniques to recover the hidden object from Equation 1.1. This, however, requires a pre-calibration step that negates one of the main benefits of these imaging techniques.

These techniques also suffer from a lack of depth resolution. Though some solutions have been proposed to extract depth information from these techniques [70, 71, 72, 73], each sacrifices some of the benefits afforded by imaging with the memory effect. For example, instead of a 2D autocorrelation, Yuka *et al.* [70] used a 3D autocorrelation to obtain a 3D image of the hidden object. In order to compute the 3D autocorrelation, the detector was moved axially to form a 3D image of the speckle. In this case, 3D information was obtained at the expense of increased computational intensity and an added requirement for sequential measurements. Singh *et al.* [72] added a guide star to the object plane so that the autocorrelation of the speckle would include cross-terms between the test object and the guide star that would be spatially shifted due to their separation distance. Since the guide star was assumed to be a point source, the spatially shifted cross-terms were then images of the hidden object. Though the object is recovered without the need for phase retrieval techniques, a guide star within the memory effect range is required.

Theoretically, the angular range of the memory effect, which effectively governs the field of view of these techniques, is given by the half angle, $\Delta\theta \approx \frac{\lambda_0}{\pi L}$ [64], where λ_0 is the light wavelength. For a fixed object distance, z_0, this corresponds to an object size of $h \approx \frac{2\lambda_0 z_0}{\pi L}$. As such, it can be seen that at close distances to the

scattering medium, as is the case for embedded objects that are typically encountered in practice, only small objects can be imaged. It should be noted, however, that these equations were formulated under the assumption that scattering is fully diffusive, that is, the direction of photons propagating through the medium is fully scrambled. In real scattering samples, such as biological tissue, it is often the case that scattering occurs mostly in the forward direction [17], such that the direction of incident light is preserved over longer distances. As a result, the theoretically predicted values for the field of view could be an underestimate of the true value, as was observed in measurements over 0.5mm thick slices of chicken breast by Katz *et al.* [64]. In their experiment, an angular correlation range of about 4° was observed, as determined from the point at which the correlation function dropped to $\frac{1}{e}$. This corresponded to a theoretical thickness of 7 microns, which is much smaller than the actual thickness of the chicken breast samples used. Nonetheless, the field of view related to these techniques remains small, particularly for samples close to the scattering medium. A translation memory effect was also identified by Judkewitz *et al.* [74], where a shift of an input point source results in a shift in the output speckle that remains otherwise unchanged. Though it has not been demonstrated, it was proposed that this shift correlation could be a means of extending the field of view [75].

Imaging with the Transmission Matrix

All of the above-mentioned techniques can be described using a scattering matrix formulation. Following the notation of Mello *et al.* [76], the scattering matrices, $\mathbf{S}$ and $\mathbf{R}$ can be defined as follows. Consider the system depicted in Figure 1.1 that consists of three regions, regions I, II and III. Regions I and III are the regions to the left and right of the scattering medium respectively, while the scattering medium is located in region II.

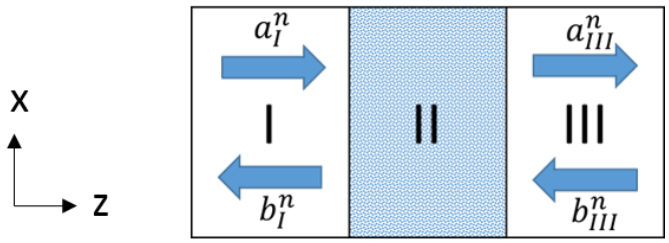

Figure 1.1: Geometry for the definition of the **S** and **R** matrices.

The transverse fields in each region can be decomposed as a sum of leftward and rightward propagating plane waves. For the i^{th} region, this can be written as

$$E_i = \sum_{n=1}^{N} \left[a_i^n \exp\left(i \left(\vec{k}_{r,i}^{\,n} \cdot \vec{r} - \left| k_{z,i}^n \right| z \right) \right) + b_i^n \exp\left(i \left(\vec{k}_{r,i}^{\,n} \cdot \vec{r} + \left| k_{z,i}^n \right| z \right) \right) \right] \ , \tag{1.3}$$

where a_i^n and b_i^n are the coefficients for the n^{th} rightward and leftward propagating wave respectively, and $\vec{k}_{r,i}^{\,n}$ and $k_{z,i}^n$ are the transverse and axial components of the wavevector, $\vec{k}$, for the n^{th} plane wave, so that $\left|\vec{k}_{r,i}^{\,n}\right|^2 + \left|k_{z,i}^n\right|^2 = \left|\vec{k}\right|^2 = \left(\frac{2\pi}{\lambda_0}\right)^2$. In addition, $\vec{r}$ represents the transverse co-ordinates, while the axial co-ordinate is denoted by z. With this notation, the **S** and **R** matrices of size $2N \times 2N$ can be defined as [76]

$$\begin{bmatrix} \vec{b}_I \\ \vec{a}_{III} \end{bmatrix} = \mathbf{S} \begin{bmatrix} \vec{a}_I \\ \vec{b}_{III} \end{bmatrix} = \begin{bmatrix} \mathbf{r}_L & \mathbf{t}_R \\ \mathbf{t}_L & \mathbf{r}_R \end{bmatrix} \begin{bmatrix} \vec{a}_I \\ \vec{b}_{III} \end{bmatrix} \ , \tag{1.4}$$

$$\begin{bmatrix} \vec{a}_{III} \\ \vec{b}_{III} \end{bmatrix} = \mathbf{R} \begin{bmatrix} \vec{a}_I \\ \vec{b}_I \end{bmatrix} \ .$$

In this thesis, matrices are denoted using a bold typeface, while vectors are denoted with an overlying arrow. In Equation 1.4, **r** and **t** are the reflection and transmission matrices respectively, for light that is incident on the scattering medium from the left (subscript L) and right (subscript R). In addition, for the i^{th} region, $\vec{a}_i$ and $\vec{b}_i$ are $N \times 1$ column vectors, formed from a concatenation of the a_i^n and b_i^n coefficients from Equation 1.3 respectively. From Equation 1.4, it can be seen that matrix **R** is a transfer matrix relating the fields to the left and the right of the medium, while matrix **S**, which is commonly known as the scattering matrix, relates the outgoing

and ingoing fields. The matrix $\mathbf{R}$ has found use in many theoretical studies for propagating light through discretised layers of the scattering media, but matrix $\mathbf{S}$, which consists of the transmission and reflection matrix of the scattering medium, is easier to measure experimentally. Regardless, a transformation exists between these two matrices [76], which implies they contain the same information. It is worth noting that though a plane wave basis has been used to describe the incident and outgoing fields in Equation 1.3, the choice of basis is by no means unique. The incident and output fields, for example, can also be described by a set of independent point sources and detectors. As such, the elements of the transmission matrix depend on the basis in which the matrix has been defined.

The transmission and reflection matrices can be defined in the context of Equation 1.4, as matrices that relate an input field to its transmitted and reflected output speckles respectively. Based on time-reversal invariance, it can be shown that the matrix $\mathbf{S}$ is unitary and symmetric, which in turn implies that $\mathbf{r}_L = \mathbf{r}_R = \mathbf{r}$ and $\mathbf{t}_L = \mathbf{t}_R^\top = \mathbf{t}$ [76], where the notation $\mathbf{A}^\top$ denotes the transpose of the matrix $\mathbf{A}$. The discussion in the rest of this section will focus mainly on the transmission matrix, though it is useful to note that energy conservation implies a relationship between the transmission and reflection matrices.

The eigenvalues of the Hermitian matrix $\mathbf{T} = \mathbf{t}^\dagger\mathbf{t}$, or equivalently the square of the singular values of $\mathbf{t}$, have been widely studied. Here, $\mathbf{A}^\dagger$ denotes the conjugate transpose of the matrix $\mathbf{A}$. These eigenvalues can be interpreted as the intensity transmittance of their corresponding eigenvectors. For scattering media in the diffusive regime, where the thickness of the scattering medium is large enough such that light is multiply scattered but is not confined within the material, the eigenvalues of $\mathbf{T}$ were found to follow a bimodal distribution with a large number of eigenvalues close to zero, but also with a small number of eigenvalues close to one [77, 78]. The eigenvalues close to one correspond to eigenvectors that are commonly known as "open" eigenchannels, as these eigenvectors can theoretically be transmitted through the scattering medium with close to no loss. Conversely, "closed" eigenchannels have eigenvalues that are approximately zero and are fully reflected

by the scattering medium. This phenomenon is exciting for imaging, as it suggests the possibility of imaging through multiply scattering media of arbitrary thicknesses in the diffusive regime.

Experimentally, the bimodal distribution of transmission eigenvalues has been demonstrated via the use of elastic waves travelling in a flat disordered waveguide [79]. In the optical regime, attempts have also been made to observe and propagate these eigenchannels through scattering media in transmission [80, 81, 82] and reflection [83]. Though significant transmission enhancement was achieved, the eigenchannels with close to unity transmission have not been observed in the optical regime. Practically, the fully transmitting eigenchannels are difficult to obtain because of incomplete control in the experiments, as not all of the independent input and transmitted modes are measured. This could be, for example, due to a finite illumination or collection numerical aperture or due to vignetting in the system. The statistical properties of transmission matrices measured under such circumstances were studied by Goetschy and Stone [84], using what they referred to as a "filtered random matrix ensemble", where only access to part of the full transmission matrix was available. It was found that the eigenchannels with transmittances close to one were highly sensitive to incomplete control, and consistent with experiments, these eigenchannels would not be present even if a small number of input or transmitted modes were not measured. In the extreme case, when only a small number of input and/or transmitted modes were acquired, correlations in the transmission matrix would become negligible and the singular values, normalised by their mean value, follow the Marcenko-Pastur law [85], which describes the distribution of singular values for uncorrelated Gaussian matrices. In the special case of square matrices, the Marcenko-Pastur law is also known as the "quarter-circle law". As such, the observation of the eigenchannels with unit transmission requires the measurement of all independent modes, which corresponds to a strikingly large transmission matrix that is difficult to measure in practice. As an indication of scale, a scattering sample with an illuminated surface area, A, contains $N = \frac{2\pi A}{\lambda_0^2}$ independent modes [86]. Consequently, an illuminated area of 1mm^2 contains about 15 million modes.

Despite the difficulty in accessing the theoretically predicted "open" eigenchannels, the measured transmission matrix can still be useful for imaging through scattering media. Since the scattered fields for a single instance of disorder are deterministic, once the transmission matrix is measured, the fields incident on the scattering medium can be computed from the transmitted fields through an inversion of the transmission matrix [87]. The transmission matrix can be obtained by measuring the transmitted speckle field over a set of independent input fields. One of the first experimental measurements of transmission matrices in the optical regime was made by Popoff *et al.* [81]. Full-field phase-shifting interferometry [88] was used to determine the amplitude and phase of the complex field, utilising speckle from a static portion of the wavefront as reference so that no additional reference arm is required in the setup. Later on, other measurement schemes were also proposed [82, 89, 90], mainly with variations in the interferometric methods used or the spatial basis used to obtain the transmission matrix. The works mentioned so far have measured monochromatic transmission matrices, which relate incident and transmitted fields of optical waves for a single wavelength and polarisation state, but other types of transmission matrices have also been defined and measured. For example, if polarisation elements are present, the vector transmission matrix can be measured, as was done by Tripathi *et al.* [91]. Katz *et al.* measured an acousto-optic transmission matrix [92], which relates the incident optical field to the ultrasonically tagged transmitted field that has been frequency-shifted, and used it to focus inside a scattering medium. Chaigne *et al.* demonstrated focusing onto several absorbers using the photoacoustic transmission matrix [93], which describes the relationship between the incident optical field and the acoustic wave detected by the ultrasonic transducers. Spatio-temporal control of light can also be obtained when a spectrally resolved [94, 95] or time-resolved transmission matrix is measured [96, 97].

Once the transmission matrix is measured, the scattering medium can effectively be used as a lens [98, 99, 100]. By placing the scattering medium with a known transmission matrix in between the test object and the imaging system, Choi *et al.* [100] showed that a larger field of view as well as enhanced resolution can be achieved. The enlarged field of view is due to light from outside of the field of

view, as defined by the imaging system, being scattered into the collection angle. Similarly, enhanced resolution is also caused by scattering, which re-directs highly oblique plane wave components, that would otherwise have not been collected, into the collection angle of the imaging system. These plane wave components correspond to high frequency information of the object [101], so their collection results in an increase in spatial resolution. Sub-diffraction limited imaging has also been achieved [99] by placing the scattering medium in the near-field of the object, thereby enabling the propagation of the evanescent waves to the far-field. Other than these advantages, using the scattering medium as a lens could also simplify imaging systems such as in endoscopes, where the optical fibre itself could be used as a lens [102, 103].

As mentioned above, the techniques that have been previously discussed can be described using the transmission matrix. Assuming that all of the transmitted light is collected and that there is negligible reflection, the shaped wavefronts used to form a focus in optical phase conjugation and wavefront shaping techniques are identical, and correspond to the complex conjugate of a column in the transmission matrix. The elements in this column are the complex amplitudes of the output speckle field originating from the target point. On the other hand, speckle correlation techniques make use of correlations that are present within the transmission matrix. As such, it can be seen that the use of the transmission matrix is a more general approach for imaging through scattering media. Unlike optical phase conjugation and wavefront shaping techniques, once the full transmission matrix has been measured, the optimal wavefront for focusing onto any target position can be computed from the transmission matrix without the need for any additional measurements, as long as the scattering medium remains static. Moreover, imaging using the transmission matrix does not depend on the memory effect, the range of which usually limits the field of view in speckle correlation techniques. A new measurement of the transmission matrix is necessary, however, whenever the instance of disorder is changed. In the case of dynamic scattering media, the measured transmission matrix is only valid within the speckle decorrelation time of the scattering medium, which for *in-vivo* tissues is typically on the order of a millisecond [104, 105]. In addition, at least for purely optical techniques, access to both sides of the scattering medium is required

for the measurement of the transmission matrix, which is a significant barrier to the application of these techniques to *in-vivo* samples. Correlations between the reflection and transmission matrix hint at a possible way of estimating the transmission matrix from reflection measurements [106], but this has yet to be achieved. Last but not least, in most practical applications, the goal is to image within rather than through scattering media. Though imaging up to a certain depth can be approximated as imaging through a scattering slab of the same thickness, the effect of light propagating backwards from deeper planes has not been accounted for.

Computational Approaches

Computational approaches have also been applied to image objects hidden behind scattering media. Techniques in machine learning have been successfully used in multiple works [107, 108, 109], but these methods are usually computationally-intensive and need large quantities of representative datasets. Moreover, as the algorithms basically function as "black boxes", the results are often difficult to interpret. Tajahuerce *et al* [110] proposed the use of a single pixel camera for imaging through scattering media. With this technique, the spatial information of the object is encoded via a sequential spatial modulation of the incident illumination *before* it propagates through the scattering medium. As such, intensities measured by a single pixel camera, each corresponding to a specific known spatial modulation of the incident illumination, can then be used to reconstruct an image of the hidden object. In contrast, for a spatially resolved camera, the spatial information is acquired directly by a multi-pixel detector, and only the scattered intensity can be observed. This technique is interesting as it does not require pre-calibration, and is also independent of the particular instance of disorder, which implies that it would work for both static and dynamic scattering media. Moreover, the use of single pixel cameras, such as photodiodes or spectrometers, raises the possibility of cost-efficient setups that can be easily adapted to include additional functionalities, such as hyperspectral imaging. One drawback, however, is that access to the illumination end of the object is required, and this is not usually available in practice. In addition, the number of measurements required for image reconstruction scales as N^2 for an image size of $N \times N$, which implies a significant increase in acquisition time for

increased resolution over the same field of view.

Polarimetric Imaging Methods

As can be seen from this discussion, most of the proposed techniques have focused on imaging in intensity. To date, there have been only a handful of works that have attempted to utilise scattered light in the recovery of both polarimetric and spatial information of objects hidden behind scattering media. The existing methods [91, 111] are based on the measurement of a transmission matrix, which as discussed previously, has to be pre-calibrated for the specific sample and needs access to both sides of the scattering medium. These requirements diminish the utility of these techniques in practical imaging applications.

Research Direction

Motivated by the benefits of polarimetric imaging and the lack of techniques available for it at greater depths, this work set out to find a solution for polarimetric imaging through scattering media. The single pixel camera solution proposed by Tajahuerce *et al.* [110] was particularly attractive, in view of its advantages that have been pointed out above. In terms of its drawbacks, the increase in acquisition time is alleviated by the availability of high speed DMDs [35] which can be used for the spatial modulation of the incident illumination, alongside photodiodes which can operate at high acquisition rates [112]. Furthermore, single pixel imaging is compatible with compressive sensing [113, 114], which reduces the number of measurements required to reconstruct the same image. On the other hand, the required access to one side of the object needs further investigation, and research to address this problem is still ongoing. For example, Escobet-Montalbán *et al.* [115] used temporal focusing to project Hadamard patterns at a selected plane within a sample, such that single pixel imaging can be used with multiphoton fluorescence microscopy.

Single pixel polarimetric imaging has previously been demonstrated by Soldevila *et al.* [116] without a scattering medium present. The polarimetric information decays as a function of the transport mean free path, compared to the decay of ballistic light which decays exponentially as a function of mean free path [16, 117].

Given the high scattering anisotropy in biological tissues (i.e. g close to 1), the transport mean free path is typically much longer than the mean free path. As such, polarisation information persists over longer length scales than the decay of ballistic light. Combining polarimetry with single pixel imaging, it is expected that polarimetric images can be recovered at the same length scales.

As such, this thesis is directed at investigating the feasibility of single pixel polarimetric imaging through scattering media, a technique which would open up possibilities for non-invasive, label-free, *in-vivo* polarimetric imaging through dynamic scattering media.

1.2 Thesis Structure and Overview

This section describes the layout of this thesis. Chapter 2 provides the necessary background knowledge, such as discussing the basics of single pixel imaging and polarimetry. Chapter 3 follows by introducing a theoretical model for single pixel polarimetric imaging, and proposes an imaging solution which is investigated using simulations based on a 2D Green's tensor formalism. To test the method experimentally, two types of scattering media were used - scattering phantoms made of microspheres embedded in epoxy resin and slices of chicken breast tissue. These samples are described in Chapter 4, which explains the experimental methods used for this work, including the implementation and calibration of the optical system, as well as sample preparation procedures. The characterisation of the optical system is then discussed in Chapter 5. The work culminates in Chapter 6, which presents the imaging results of a hidden test object obtained using the proposed method. Finally, conclusions are made in Chapter 7, with an examination of the limitations of the technique and the potential for future developments.

Chapter 2

Background

Having elucidated the motivation and aims of this work in Chapter 1, the current chapter introduces the relevant background knowledge required for the understanding of this thesis. Specifically, Section 2.1 gives a description of Maxwell's equations, which is fundamental to the description of scattered fields that is used in the numerical simulations conducted as part of this work. Moreover, since this thesis is concerned with polarimetric imaging, an introduction to the polarisation of light, along with the relevant tools used to describe and analyse it, is provided in Section 2.2. Key concepts and terminology related to scattering that are used in this work are then presented in Section 2.3, followed by an introductory description of single pixel imaging in Section 2.4. Finally, the chapter concludes with Section 2.5, which provides an outline of the assumptions made in this work.

2.1 Maxwell's Equations

Light is an electromagnetic wave and as such, light scattering is fundamentally described by Maxwell's equations, which have been well-discussed in many electromagnetism textbooks, such as [118, 119]. In this section, a brief overview of Maxwell's equations will be provided, along with some of the equations derived from it that are relevant for this work.

Maxwell's equations in their macroscopic and differential form can be written as

$$\nabla \cdot \vec{D}(\vec{r},t) = \rho_f(\vec{r},t) \tag{2.1}$$

$$\nabla \cdot \vec{B}(\vec{r},t) = 0 \tag{2.2}$$

$$\nabla \times \vec{H}(\vec{r},t) - \frac{\partial \vec{D}(\vec{r},t)}{\partial t} = \vec{J}_f(\vec{r},t) \tag{2.3}$$

$$\nabla \times \vec{E}(\vec{r},t) + \frac{\partial \vec{B}(\vec{r},t)}{\partial t} = 0 \ . \tag{2.4}$$

Equations 2.1 to 2.4, in order, are Gauss's law for the electric field, Gauss's law for the magnetic field, Ampère-Maxwell's law and Faraday's induction law. The vector fields in these equations are the electric field ($\vec{E}$), displacement current ($\vec{D}$), magnetic flux density ($\vec{B}$), magnetic field ($\vec{H}$), and current density ($\vec{J}_f$), while ρ_f denotes the free charge density. In order to provide a complete description of the fields, Maxwell's equations need to be supplemented by the constitutive relations

$$\vec{D}(\vec{r},t) = \epsilon(\vec{r})\vec{E}(\vec{r},t) \tag{2.5}$$

$$\vec{B}(\vec{r},t) = \mu(\vec{r})\vec{H}(\vec{r},t) \tag{2.6}$$

$$\vec{J}_f(\vec{r},t) = \sigma(\vec{r})\vec{E}(\vec{r},t) \ , \tag{2.7}$$

where σ denotes the conductivity, and $\epsilon = \epsilon_0\epsilon_r$ is the material permittivity, expressed in terms of the vacuum permittivity, ϵ_0, and the relative permittivity, ϵ_r. In addition, $\mu = \mu_0\mu_r$ denotes the permeability, similarly expressed in terms of the vacuum permeability, μ_0, and the relative permeability, μ_r. For an isotropic medium, as assumed here, σ, ϵ and μ are scalars, but it should be noted that in general, these quantities are tensors.

Under the assumption that the fields are time-harmonic, the electric field can be expressed as

$$\vec{E}(\vec{r},t) = \vec{E}(\vec{r})\exp(-i\omega t) \tag{2.8}$$

where ω denotes the angular frequency of the electromagnetic wave. The other fields, $\vec{D}$, $\vec{B}$, $\vec{H}$ and $\vec{J}_f$, can also be written in a similar manner. This assumption is

by no means limiting, since arbitrary functions can be formed from a superposition of harmonic functions. Furthermore, when no sources are present, $\vec{J}_f$ and ρ_f are zero. The insertion of these assumptions into Maxwell's equations (Equations 2.1 - 2.4) yields

$$\nabla \cdot \vec{D}(\vec{r}) = 0 \tag{2.9}$$

$$\nabla \cdot \vec{B}(\vec{r}) = 0 \tag{2.10}$$

$$\nabla \times \vec{H}(\vec{r}) + i\omega\vec{D}(\vec{r}) = \vec{0} \tag{2.11}$$

$$\nabla \times \vec{E}(\vec{r}) - i\omega\vec{B}(\vec{r}) = \vec{0}\ . \tag{2.12}$$

Taking the curl of Equation 2.12, one obtains

$$\nabla \times \nabla \times \vec{E}(\vec{r}) = i\omega(\nabla \times \vec{B}(\vec{r}))\ . \tag{2.13}$$

An alternative expression for the right side of Equation 2.13 can be found using Equation 2.11. Assuming a non-magnetic insulating dielectric medium, such that $\sigma = 0$ and $\mu(\vec{r}) = \mu_0$, Equation 2.11 can be written as

$$\nabla \times \vec{B}(\vec{r}) = -i\mu_0\omega\epsilon_0\epsilon_r(\vec{r})\vec{E}(\vec{r})\ . \tag{2.14}$$

Substituting Equation 2.14 in Equation 2.13 yields [120]

$$\nabla \times \nabla \times \vec{E}(\vec{r}) - k^2\vec{E}(\vec{r}) = i\omega\vec{j}(\vec{r}) \tag{2.15}$$

where $\vec{j}(\vec{r}) = -i\omega\epsilon_0\mu_0(\epsilon_r(\vec{r}) - 1)\vec{E}(\vec{r})$, $k = \frac{2\pi}{\lambda} = \frac{\omega}{c}$ is the free space wavevector and $c = \frac{1}{\sqrt{\mu_0\epsilon_0}}$ is the speed of light. In a typical electromagnetic scattering problem that considers a configuration of scatterers, the spatial variation of ϵ_r caused by the spatial distribution of the scatterers contributes directly to $\vec{j}(\vec{r})$. The computation of the resulting fields is then equivalent to finding the electric field, $\vec{E}(\vec{r})$, that satisfies Equation 2.15 for the specified scatterer configuration.

Equation 2.15 is a linear inhomogeneous equation that can be solved by consid-

ering the Green's function

$$\nabla \times \nabla \times \mathbf{G}^e(\vec{r}, \vec{r}^{\,'}) - k^2 \mathbf{G}^e(\vec{r}, \vec{r}^{\,'}) = \mathbb{I}\delta(\vec{r} - \vec{r}^{\,'}) \tag{2.16}$$

where $\mathbf{G}^e(\vec{r}, \vec{r}^{\,'})$ can be interpreted as the electric field at $\vec{r}$ from a point source at $\vec{r}^{\,'}$. Given the linearity of Equation 2.15, the total field, $\vec{E}(\vec{r})$, can be thought of as a superposition of the contributions from the individual point sources making up $\vec{j}(\vec{r})$, such that the general solution to Equation 2.15 can be formulated in terms of $\mathbf{G}^e(\vec{r}, \vec{r}^{\,'})$ as

$$\vec{E}(\vec{r}) = \vec{E}^{inc}(\vec{r}) + i\omega \int_V \mathbf{G}^e(\vec{r}, \vec{r}^{\,'}) \vec{j}(\vec{r}^{\,'}) \, d\vec{r}^{\,'} \ , \tag{2.17}$$

where $\vec{E}^{inc}(\vec{r})$ is the solution to the homogeneous equation obtained when no scatterers are present (i.e. $\vec{j}(\vec{r}) = \vec{0}$ in Equation 2.15). For scatterers in free space, which is the geometry considered in this work, the Green's function has a form given by [120]

$$\mathbf{G}^e(\vec{r}, \vec{r}^{\,'}) = \left(\mathbb{I} + \frac{1}{k^2} \nabla\nabla \right) \frac{\exp(ik|\vec{r} - \vec{r}^{\,'}|)}{4\pi|\vec{r} - \vec{r}^{\,'}|} \ . \tag{2.18}$$

Equation 2.17 presents a means of computing the scattered fields from randomly positioned particles. Techniques utilising these equations [121, 122] are considered later in Section 3.2.

Another way of computing the scattered fields is through the use of the vector Helmholtz equation. Through a standard vector identity [123] and the use of Equation 2.9, the left side of Equation 2.13 can be written as

$$\begin{aligned} \nabla \times \nabla \times \vec{E}(\vec{r}) &= \nabla(\nabla \cdot \vec{E}(\vec{r})) - \nabla^2 \vec{E}(\vec{r})) \\ &= -\nabla^2 \vec{E}(\vec{r})) \ . \end{aligned} \tag{2.19}$$

Making the further assumption that the scattering environment is piece-wise homogeneous, so that $\epsilon(\vec{r}) = \epsilon$ is independent of $\vec{r}$ within each homogeneous region, Equations 2.19 and 2.14 can be substituted into Equation 2.13 to yield the vector Helmholtz equation, which is given by

$$\nabla^2 \vec{E}(\vec{r}) + (nk)^2 \vec{E}(\vec{r}) = 0 \ , \tag{2.20}$$

where $n = \sqrt{\epsilon_r \mu_r} = \sqrt{\epsilon_r}$ is the medium's refractive index. Equation 2.20 holds in each of the homogeneous regions in the scattering environment with the appropriate value of n. For an isotropic medium, n is a scalar, and the scalar Helmholtz equation can be used to describe each component of the field. This can be written as

$$\nabla^2 \, E_i(\vec{r}) + (nk)^2 \, E_i(\vec{r}) = 0 \ , \tag{2.21}$$

where E_i denotes a component of the field.

It can be shown that if an arbitrary scalar field, U_i, fulfils the scalar Helmholtz equation in Equation 2.21, then the vector fields, $\vec{M}$ and $\vec{N}$, obtained as

$$\begin{aligned} \vec{M}(\vec{r}) &= \nabla \times (\vec{r} U_i(\vec{r})) \\ \vec{N}(\vec{r}) &= \frac{\nabla \times \vec{M}(\vec{r})}{k} \ , \end{aligned} \tag{2.22}$$

fulfil the vector Helmholtz equation in Equation 2.20 [124]. As such, for homogeneous isotropic media, the problem of finding a vector field that fulfils Equation 2.20 can be simplified to finding a scalar solution to Equation 2.21. As will be discussed in Section 3.2, by first finding a complete set of scalar basis functions that satisfy Equation 2.21 for the considered geometry (for spherical scatterers in a homogeneous background these consist of Legendre and spherical Bessel functions), the related set of vector basis functions that satisfy Equation 2.20 can be computed. These vector basis functions can then be used to describe the fields in the interior and exterior of the scatterer. The fields in the interior and exterior of the scatterer can then be described as a linear combination of these vector basis functions, with the related mode coefficients determined by a matching of the appropriate boundary conditions [124]. In this way, the scattered fields from spherical scatterers can be computed. Though spherical particles have been considered, this technique can also be adapted for non-spherical particles [125, 126].

2.2 Polarisation

Being an electromagnetic wave, propagating electric and magnetic fields of light oscillate perpendicularly to its direction of travel. Polarisation is a property of the wave, describing the evolution of the fields with time. This section does not attempt to provide a complete theoretical treatise, but focuses on the key concepts related to the polarisation of light, which will be used consistently throughout in this thesis. For further details, the reader is referred to the many excellent textbooks that have been written on the topic (e.g. [127, 128]).

Consider monochromatic light travelling in the z direction, with an electric field oscillation as depicted in Figure 2.1. A theoretical observer looking along the z axis towards the direction of the source will observe the tip of the electric field vector trace out certain shapes as the wave propagates. Examples of possible shapes are plotted at the bottom of Figure 2.1. If the oscillations are confined to a plane that is oriented at angle θ from the x axis, then the light is said to be linearly polarised at θ (see Figure 2.1(a)). In particular, when $\theta = 0°$, the oscillations of the field are confined to the x direction, which is commonly known as horizontally polarised light. Conversely, the oscillation plane for vertically polarised light is oriented at $\theta = 90°$, such that the field only oscillates in the y direction. Alternatively, if the oscillations rotate around the propagation direction as the wave travels, such that the tip of the field vector traces out a circle in the plane transverse to the direction of propagation (see Figure 2.1(b)), then the light is said to be circularly polarised. This rotation can be clockwise or anti-clockwise, and the corresponding light is known as right and left circularly polarised light respectively. More generally, however, light is elliptically polarised, with the tip of the electric field vector tracing out an ellipse with ellipticity angle ε and θ (see Figure 2.1(c)). It is straightforward to see that linear and circular polarisation states are special cases of elliptically polarised light. Similar to circularly polarised light, the rotation of light can occur in a clockwise or anti-clockwise manner, and the resulting light is termed as right and left elliptically polarised light. Finally, it is worth noting that for non-monochromatic light, it is possible that the electric field oscillates in a completely random manner, in which

case the resulting light is said to be unpolarised.

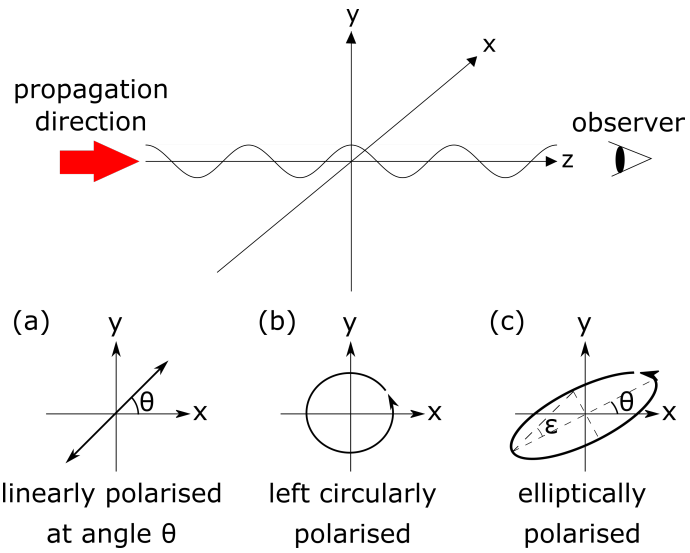

Figure 2.1: The top figure depicts a linearly polarised electromagnetic wave travelling in the z direction, and the four plots on the bottom are examples of common polarisation states.

The diagrams shown in Figure 2.1 are useful for an intuitive understanding of polarisation. Nevertheless, mathematical tools are required for a quantitative description of the polarisation state. In this respect, Jones and Mueller calculus have been widely used and are thus discussed below.

2.2.1 Jones Vectors

Consider, again, the same light wave propagating in the z direction, as depicted in the top of Figure 2.1. The electric field vector at any space and time can be described as [127]

$$\vec{E}(z,t) = \left(E_x\ \hat{i} + E_y\ \hat{j}\right) \exp\left(i(kz - \omega t)\right) \tag{2.23}$$

where $\hat{i}$ and $\hat{j}$ are unit vectors in the x and y directions respectively, while E_x and E_y are complex numbers describing the components of the electric field along the same directions. The polarisation of this wave can be concisely described in terms

of the complex Jones vector, which is defined as [127]

$$\vec{E} = \begin{bmatrix} E_x \\ E_y \end{bmatrix} \quad . \tag{2.24}$$

It should be pointed out that this representation of the field is limited to a single propagating plane wave. Plane waves travelling along directions other than z can also be described by choosing a reference frame with one of the axes along the propagation direction. In this work, as well as for the rest of this section, it is assumed that the light beam only has, at most, a small angular spread, such that it can be approximated as a collimated beam. As such, this limitation is not of consequence for this work. Note that, nonetheless, it is possible to extend this Jones vector formalism into three dimensions, and for arbitrary field distributions - a full discussion can be found in Ref. [129].

2.2.2 Coherency Matrices

Implicit in the definition of Jones vectors is the assumption that the light being described is fully polarised and coherent. In the case of partially polarised light, where E_x and E_y are not completely correlated, Jones vectors are unable to give a full description of the polarisation state, except at any specific point in time. As such, other representations of the field are required to describe partially (and fully) polarised light. One suitable representation is the coherency matrix, which is defined as [127]

$$\mathbf{C}_M = \langle \vec{E} \otimes \vec{E}^{\dagger} \rangle_t = \begin{bmatrix} \langle E_x E_x^* \rangle_t & \langle E_x E_y^* \rangle_t \\ \langle E_y E_x^* \rangle_t & \langle E_y E_y^* \rangle_t \end{bmatrix} \quad , \tag{2.25}$$

where $\otimes$ denotes the Kronecker product, otherwise known as the direct product, $\vec{E}^{\dagger}$ denotes the conjugate transpose of the Jones vector, $\vec{E}$, and A^* denotes the complex conjugate of A. Also, $\langle ... \rangle_t$ denotes a temporal average, over a time scale much longer than the fluctuations of the field. In the case of fully coherent light, the quantities within $\langle ... \rangle_t$ are constant with time and the temporal averaging may be dropped. The diagonal elements of $\mathbf{C}_M$ are real quantities, and describe the intensity ($I \propto \langle |\vec{E}|^2 \rangle_t$) of the x and y components of the light beam. The off-diagonal elements, on the

other hand, are generally complex and they describe the cross-correlation between the x and y components of the light beam. A coherency vector, consisting of the elements of $\mathbf{C}_M$, can also be defined as [127]

$$\vec{C} = \langle \vec{E} \otimes \vec{E}^* \rangle_t = \begin{bmatrix} \langle E_x E_x^* \rangle_t \\ \langle E_x E_y^* \rangle_t \\ \langle E_y E_x^* \rangle_t \\ \langle E_y E_y^* \rangle_t \end{bmatrix} . \tag{2.26}$$

2.2.3 Stokes Vectors

In spite of the benefits provided by coherency matrices and vectors, their complex elements make it cumbersome to directly measure them experimentally. The Stokes vector formulation provides a more convenient means of describing the polarisation state of light in terms of real quantities that are measurable in the lab, whilst also allowing the description of partially polarised light.

A Stokes vector consists of four real parameters that have the dimensions of intensity, and is defined as [127]

$$\vec{S} = \begin{bmatrix} S_0 \\ S_1 \\ S_2 \\ S_3 \end{bmatrix} = \begin{bmatrix} \langle |E_x|^2 \rangle_t + \langle |E_y|^2 \rangle_t \\ \langle |E_x|^2 \rangle_t - \langle |E_y|^2 \rangle_t \\ 2\langle \mathrm{Re}\{E_x E_y^*\} \rangle_t \\ -2\langle \mathrm{Im}\{E_x E_y^*\} \rangle_t \end{bmatrix} = \begin{bmatrix} I_x + I_y \\ I_x - I_y \\ I_{45} - I_{-45} \\ I_r - I_l \end{bmatrix} , \tag{2.27}$$

where the elements of the final vector are, respectively, the total intensity of the beam, the difference in intensities between components polarised in the x and y directions, the difference in intensities between the components polarised at $\pm 45°$ and the difference between the intensities of the left and right circularly polarised components of the beam. This formulation suggests that these parameters can be extracted through a simple series of laboratory measurements that are designed to determine the intensity of the relevant beam components. For example, $S_1 = I_x - I_y$ can be obtained by taking the difference between the two intensities transmitted through an ideal linear polariser with its transmittance axis oriented in x and y. Further-

more, aside from being able to describe partially polarised light, Stokes parameters allow the fraction of polarised light in the beam to be quantified through the degree of polarisation, $\mathbb{P}$, which is defined as [127]

$$\mathbb{P} = \frac{\sqrt{S_1^2 + S_2^2 + S_3^2}}{S_0} \ . \tag{2.28}$$

For fully unpolarised light, intensity measurements across different polarisation states are equal since no polarisation state is preferred. As such, $S_1 = S_2 = S_3 = 0$ and $\mathbb{P} = 0$. In contrast, considering a specific example of fully linearly polarised light at 45°, $S_2 = 1$ while S_1 and S_3 are equal to zero, such that $\mathbb{P} = 1$. It can be easily verified that the same result of $\mathbb{P} = 1$ is obtained when considering completely polarised light with other polarisation states. Values of $\mathbb{P}$ other than 0 and 1 correspond to partially polarised light.

The degree of polarisation specific to linear or circular polarisation states can also be defined as [128]

$$\begin{aligned} \mathbb{P}_L &= \frac{\sqrt{S_1^2 + S_2^2}}{S_0} \\ \mathbb{P}_C &= \frac{S_3}{S_0} \ , \end{aligned} \tag{2.29}$$

where $\mathbb{P}_L$ and $\mathbb{P}_C$ are the degree of linear polarisation (DOLP) and the degree of circular polarisation (DOCP) respectively.

Polarisation states can also be visualised by plotting the Stokes parameters, S_1, S_2 and S_3, along the Cartesian axes. Fully polarised states (i.e. $\mathbb{P} = 1$) corresponding to the same beam intensity, $S_0 = \sqrt{S_1^2 + S_2^2 + S_3^2}$, lie on a sphere with a radius of S_0. This sphere, which is illustrated in Figure 2.2, is known as the Poincaré sphere [127]. As examples, points on the sphere corresponding to the x, y and ±45° linearly polarised states, as well as right and left circularly polarised light, are indicated in Figure 2.2. All linearly polarised states lie along the equator of the Poincaré sphere, as indicated by the blue line in Figure 2.2, while the right and left circularly polarised states lie at the north and south pole of the sphere respectively. The rest of the sphere surface describes fully polarised elliptical states. Partially polarised

polarisation states (i.e. $\mathbb{P} < 1$) can also be described by the Poincaré sphere as points within the sphere. The Poincaré sphere, formed of the Stokes parameters, is a simple yet powerful graphical tool for the understanding of polarisation and its evolution as light passes through different media.

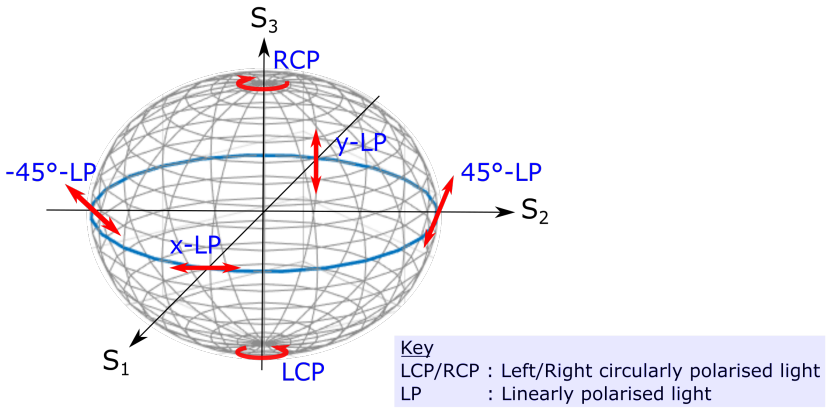

Figure 2.2: A diagram of the Poincaré sphere, showing the x, y and ±45° linearly polarised states, as well as right and left circularly polarised light.

The form of Equation 2.27 suggests that there is a relationship between Stokes vectors and their related coherency matrix/vector representation. Indeed, the elements of the Stokes vector can be related to the coherency matrix as

$$\mathbf{C}_M = \frac{1}{2}\sum_{j=0}^{3} S_j \sigma_j \ , \tag{2.30}$$

where

$$\sigma_0 = \begin{bmatrix} 1 & 0 \\ 0 & 1 \end{bmatrix} \ , \quad \sigma_1 = \begin{bmatrix} 1 & 0 \\ 0 & -1 \end{bmatrix} \ , \quad \sigma_2 = \begin{bmatrix} 0 & 1 \\ 1 & 0 \end{bmatrix} \ , \quad \sigma_3 = \begin{bmatrix} 0 & -i \\ i & 0 \end{bmatrix} \ , \tag{2.31}$$

are the well-known Pauli matrices. As such, it can be seen that the elements of the Stokes vector are the coefficients in the decomposition of the related coherency matrix into the matrices σ_j. Similarly, a conversion exists between the coherency and Stokes vectors, which can be written as

$$\vec{S} = \mathbf{\Gamma}\vec{C} \ , \tag{2.32}$$

where

$$\mathbf{\Gamma} = \begin{bmatrix} 1 & 0 & 0 & 1 \\ 1 & 0 & 0 & -1 \\ 0 & 1 & 1 & 0 \\ 0 & i & -i & 0 \end{bmatrix} . \tag{2.33}$$

As such, Stokes vectors can be related to the coherency matrix/vector representation, which in turn can be derived from the associated Jones vectors when light is fully polarised and coherent. For the case of partially polarised or incoherent light, the time-averaged elements of the Jones vector can be related to the coherency matrix/vector, as described previously in Equations 2.25 and 2.26. Equation Table 2.1 shows examples of how common polarisation states that are fully polarised can be expressed in the different representations.

	Jones	Coherency matrix	Stokes
Linearly polarised at angle θ	$e_0 \begin{bmatrix} \cos\theta \\ \sin\theta \end{bmatrix}$	$I_0 \begin{bmatrix} \cos^2\theta & \cos\theta\sin\theta \\ \cos\theta\sin\theta & \sin^2\theta \end{bmatrix}$	$S_0 \begin{bmatrix} 1 \\ \cos 2\theta \\ \sin 2\theta \\ 0 \end{bmatrix}$
Right circularly polarised	$e_0 \begin{bmatrix} 1 \\ i \end{bmatrix}$	$I_0 \begin{bmatrix} 1 & -i \\ i & 1 \end{bmatrix}$	$S_0 \begin{bmatrix} 1 \\ 0 \\ 0 \\ 1 \end{bmatrix}$
Elliptically polarised	$e_0 \begin{bmatrix} \cos\theta\cos\varepsilon - i\sin\theta\sin\varepsilon \\ \sin\theta\cos\varepsilon + i\cos\theta\sin\varepsilon \end{bmatrix}$	$I_0 \begin{bmatrix} 1+2\cos 2\theta\cos 2\varepsilon & \sin 2\theta\cos 2\varepsilon - i\sin 2\epsilon \\ \sin 2\theta\cos 2\varepsilon + i\sin 2\epsilon & 1-2\cos 2\theta\cos 2\varepsilon \end{bmatrix}$	$S_0 \begin{bmatrix} 1 \\ \cos 2\theta\cos 2\varepsilon \\ \sin 2\theta\cos 2\varepsilon \\ \sin 2\varepsilon \end{bmatrix}$
Unpolarised	-	$I_0 \begin{bmatrix} 1 & 0 \\ 0 & 1 \end{bmatrix}$	$S_0 \begin{bmatrix} 1 \\ 0 \\ 0 \\ 0 \end{bmatrix}$

Table 2.1: Examples of common polarisation states. e_0 denotes the a scalar complex amplitude and I_0 represents the light intensity, while the definition of θ and ε follows that of Figure 2.1.

2.2.4 Jones and Mueller matrices

When light interacts with matter, its polarisation state may be altered. The way that this effect is described depends primarily on the mathematical representation chosen to express the polarisation state. Here, only linear optical effects are considered.

As described previously, fully polarised light can be described in terms of Jones vectors. Consider an incident beam that is described by a Jones vector, denoted as $\vec{E}^{in}$. After propagation through a spatially homogeneous optical element, the polarisation of the resulting beam can be described by a second Jones vector, denoted as $\vec{E}^{out}$. The relationship between the two Jones vectors can be described in terms of the 2×2 Jones matrix, $\mathbf{T}$, such that

$$\vec{E}^{out} = \mathbf{T}\vec{E}^{in} \ . \tag{2.34}$$

In this way, the beam can be propagated through a train of N optical elements with known Jones matrices as $\vec{E}^{out} = \mathbf{T}_N\mathbf{T}_{N-1}...\mathbf{T}_2\mathbf{T}_1\vec{E}^{in}$, in order to determine the output polarisation state. Note that the exact physical mechanism affecting the polarisation state is inconsequential in this computation; the optical devices are treated as "black boxes" with the Jones matrix relating the input and output polarisation states.

Using Equation 2.25, it can be shown that the propagation of coherency matrices through a non-depolarising optical element with the Jones matrix, $\mathbf{T}$, can be described as

$$\mathbf{C}_M^{out} = \mathbf{T}\mathbf{C}_M^{in}\mathbf{T}^{\dagger} \ , \tag{2.35}$$

where the superscripts "in" and "out" denote input and output polarisation states. Similarly, it can be shown that coherency vectors can be propagated through optical elements as

$$\vec{C}^{out} = (\mathbf{T} \otimes \mathbf{T}^*)\vec{C}^{in} \ . \tag{2.36}$$

Given the relationship between coherency and Stokes vectors in Equation 2.32, it is straightforward to show that Stokes vectors can be propagated according to

$$\vec{S}^{out} = \mathbf{M}\vec{S}^{in} \ , \tag{2.37}$$

where $\mathbf{M}$ is the 4×4 Mueller matrix of the optical element, which can be related to the associated Jones matrix as

$$\mathbf{M} = \mathbf{\Gamma}(\mathbf{T} \otimes \mathbf{T}^*)\mathbf{\Gamma}^{-1} \ . \tag{2.38}$$

It is worth noting that depolarising systems cannot be described by a deterministic Jones matrix, and as such, Equations 2.35, 2.36 and 2.38 generally don't hold. Nevertheless, Equation 2.37 can still be used to describe propagation through depolarising systems. Table 2.2 shows examples of the Jones and Mueller matrices of ideal polarimetric elements. The linear polariser and waveplate have been specified with their transmission and fast axes at an angle $\theta = 0°$. Their corresponding matrices for an arbitrary angle to the x axis, α, can be obtained by using the relevant Jones or Mueller rotator matrices as

$$\begin{aligned} \mathbf{T}(\theta = \alpha) &= \mathcal{R}_J(-\alpha)\mathbf{T}(\theta = 0°)\mathcal{R}_J(\alpha) \\ \mathbf{M}(\theta = \alpha) &= \mathcal{R}_M(-\alpha)\mathbf{M}(\theta = 0°)\mathcal{R}_M(\alpha) \end{aligned} \tag{2.39}$$

where $\mathcal{R}_J$ and $\mathcal{R}_M$ respectively denote the Jones and Mueller rotator matrices that are specified in Table 2.2.

	Jones	Mueller matrix
Linear polariser with transmission axis at angle $\theta = 0°$	$\begin{bmatrix} 1 & 0 \\ 0 & 0 \end{bmatrix}$	$\begin{bmatrix} 1 & 1 & 0 & 0 \\ 1 & 1 & 0 & 0 \\ 0 & 0 & 0 & 0 \\ 0 & 0 & 0 & 0 \end{bmatrix}$
Waveplate with fast axis at angle $\theta = 0°$ with retardation φ	$\begin{bmatrix} \cos\frac{\varphi}{2} + i\sin\frac{\varphi}{2} & 0 \\ 0 & \cos\frac{\varphi}{2} - i\sin\frac{\varphi}{2} \end{bmatrix}$	$\begin{bmatrix} 1 & 0 & 0 & 0 \\ 0 & 1 & 0 & 0 \\ 0 & 0 & \cos\varphi & \sin\varphi \\ 0 & 0 & -\sin\varphi & \cos\varphi \end{bmatrix}$
Depolariser	-	$\begin{bmatrix} 1 & 0 & 0 & 0 \\ 0 & 0 & 0 & 0 \\ 0 & 0 & 0 & 0 \\ 0 & 0 & 0 & 0 \end{bmatrix}$
Rotator, rotating the co-ordinate axes counter-clockwise by angle θ	$\begin{bmatrix} \cos\theta & \sin\theta \\ -\sin\theta & \cos\theta \end{bmatrix}$	$\begin{bmatrix} 1 & 0 & 0 & 0 \\ 0 & \cos 2\theta & \sin 2\theta & 0 \\ 0 & -\sin 2\theta & \cos 2\theta & 0 \\ 0 & 0 & 0 & 1 \end{bmatrix}$

Table 2.2: Examples of Jones and Mueller matrices for some ideal polarimetric elements.

2.2.5 Polarimetry

Polarimetry is the measurement and analysis of polarisation, and it has been exploited in many applications, as highlighted in Chapter 1. Two categories of polarimetry can be identified, namely Stokes and Mueller polarimetry. In this section, the system models for both of these categories are introduced.

In Stokes polarimetry, the aim is to obtain the Stokes vector related to the polarisation state of the measured light. This can be done by measuring the transmitted intensity as the beam is passed through different polarimetric elements, otherwise known as polarisation analysers. Let d_i be the intensity measured when light is passed through a polarisation analyser that measures the polarisation state with a Stokes vector denoted as $\vec{a}_i^{\top} = [1, a_{i,1}, a_{i,2}, a_{i,3}]^{\top}/2$, where $\vec{a}_i$ has been normalised to ensure that the analyser is passive (i.e. $0 \leq d_i \leq S_0$). In fact, d_i is the projection of the incident Stokes vector, $\vec{S}$, on the analysed polarisation state. When N_A polarisation analysers are used, the related intensities measured can be concatenated in a $N_A \times 1$ vector, denoted as $\vec{D}$, which in turn can be related to the incident Stokes vector according to

$$\vec{D} = \mathbf{A}\vec{S} \; . \tag{2.40}$$

The matrix $\mathbf{A}$ is an $N_A \times 4$ instrument matrix describing the polarisation state analyser (PSA), with the i^{th} row of $\mathbf{A}$ corresponding to the Stokes vector describing the i^{th} analysed polarisation state (i.e. $\vec{a}_i$). From the linear equation in Equation 2.40, it can be seen that at least four analysed polarisation states are required to determine the four unknown Stokes parameters. Fewer polarisation analyser states will result in an underdetermined set of equations, which does not have a unique solution for the unknown Stokes vector. More than four analyser states can be used to produce an overdetermined set of equations, which in the case of noise could be useful for obtaining a least-squares estimate of the incident Stokes vector. As such, with a sufficient number of analysed polarisation states (that are known beforehand), it is theoretically possible to establish the Stokes vector of the incident beam through a matrix inversion, written as

$$\vec{S} = \mathbf{A}^{-1}\vec{D} \; . \tag{2.41}$$

If the matrix $\mathbf{A}$ is overdetermined or poorly conditioned (see below for a discussion on matrix conditioning), a least squares solution can, instead, be found by replacing the matrix inversion with the Moore-Penrose pseudo-inverse [130]. Various architectures for the PSA exist in literature, and will be described later in Section 4.1.

Mueller polarimetry, on the other hand, measures the full Mueller matrix, $\mathbf{M}$, of a test sample. This is done through the inclusion of a polarisation state generator (PSG), which generates incident illumination with different known input polarisation states. Various ways of generating the set of input polarisation states are discussed later in Section 4.1. The transmitted or reflected polarisation state is then collected and analysed by a PSA. For the j^{th} input polarisation state, the exiting Stokes vector is given by

$$\vec{S} = \mathbf{M}\vec{w}_j \ , \tag{2.42}$$

where $\vec{w}_j$ is the Stokes vector corresponding to the j^{th} input polarisation state. To determine the 16 elements in the Mueller matrix, at least 4 input polarisation states are, therefore, required, so that there are 16 simultaneous equations which form a fully determined set of linear equations. When N_G input polarisation states and N_A analysed polarisation states are used, the detector intensities can be expressed as

$$\mathbf{D} = \mathbf{AMW} \ , \tag{2.43}$$

where the i^{th} row of the $N_A \times 4$ matrix $\mathbf{A}$ is the Stokes vector describing the i^{th} polarisation analyser (i.e. $\vec{a}_i$) and the j^{th} column of the $4 \times N_G$ matrix $\mathbf{W}$ is the j^{th} input polarisation state (i.e. $\vec{w}_j$). The j^{th} column of $\mathbf{D}$ then corresponds to the detector intensities measured by the PSA for the j^{th} input polarisation state. Similarly to Equation 2.41, the Mueller matrix can be obtained as

$$\mathbf{M} = \mathbf{A}^{-1}\mathbf{D}\mathbf{W}^{-1} \ . \tag{2.44}$$

The data processing applied to obtain the Stokes vector in Stokes polarimetry, or the Mueller matrix in Mueller polarimetry, amplifies existing noise. The degree of noise amplification is often estimated using the condition number of the matrix, κ [131,

132]. For an arbitrary matrix $\mathbf{A}$, κ can be defined as $\kappa = ||\mathbf{A}^{-1}||_2||\mathbf{A}||_2$, with $||...||_2$ denoting the induced 2-norm of a matrix. A matrix with a low condition number is said to be well-conditioned, and the related matrix inverse can be reasonably estimated. The minimum condition number possible for arbitrary matrices is 1, in which case the maximum errors in the estimated quantity (i.e. $\vec{S}$ or $\mathbf{M}$) is no worse than the errors in the input dataset (i.e. the measured detector intensities). On the other hand, matrices with large condition numbers are said to be ill-conditioned, and noise in the data is likely to result in large errors in the estimated parameter. It should be added that since the elements of physical instrument matrices, $\mathbf{A}$ and $\mathbf{W}$, cannot be arbitrarily chosen, the minimum possible condition number for the instrument matrices is actually larger than 1 [133, 134]. To minimise errors in the estimated Stokes vector or Mueller matrix, it is important to consider architectures with low condition numbers in the design of PSG and PSA, as will be seen in Section 4.1.

2.2.6 Physicality of the Mueller Matrix

Physically realisable Mueller matrices form only a subset of all possible 4×4 real matrices. A physically realisable Mueller matrix is one that, for any given input Stokes vector, outputs a physically realisable polarisation state, which in turn satisfies physical constraints such as having a non-negative total intensity and a DOP≤ 1. Unfortunately, the estimate of the Mueller matrix computed by Equation 2.44 is not necessarily physically realisable. This is particularly true in the presence of noise which, as previously discussed, causes errors in the computed Mueller matrix that are potentially amplified by the data processing procedure. Many necessary conditions for a Mueller matrix to be physically realisable have been introduced in the literature [135, 136, 137], but there is not a definitive set of requirements that is commonly used. Examples of some of the proposed conditions are that [138]:

1. $tr(\mathbf{M}\mathbf{M}^\top) \leq 4m_{00}^2$,
2. $m_{00} \geq |m_{ij}|$ for $i, j \in \{0, 1, 2, 3\}$,
3. $m_{00}^2 \geq (m_{01}^2 + m_{02}^2 + m_{03}^2)$ and

4. the correlation matrix $\mathbf{H} = \frac{1}{4}\sum_{k,l=0}^{3} m_{kl}(\sigma_k \otimes \sigma_l)$ is positive semidefinite,

where $tr(\mathbf{A})$ and $\mathbf{A}^\top$ denote the trace and transpose of the matrix $\mathbf{A}$ respectively. Furthermore, m_{ij} denotes the $(i,j)^{th}$ element of the Mueller matrix and the matrices σ_k are the Pauli matrices defined in Equation 2.31. A method to ensure a physically realisable estimate of the Mueller matrix that fulfills these criteria will be presented later in Section 4.5.2.

2.2.7 Lu-Chipman Matrix Decomposition

The Mueller matrix is a simple and elegant means of characterising the effect of a test sample on an incident polarisation state but extracting the polarimetric properties of the sample (e.g. retardance, diattenuation and depolarisation, which will be explained below) from the Mueller matrix is not always a trivial task. Various matrix decompositions [139, 140, 141] have hence been proposed for the interpretation of the Mueller matrix. One of the most widely used decompositions is the Lu-Chipman matrix decomposition [139], which breaks down a Mueller matrix into a product of three matrices, each of which can be associated with a retarder, a diattenuator or a depolariser. A brief summary of the decomposition is given in this section, and the reader is referred to Ref. [139] for further details.

A pure diattenuator has an intensity transmission that is dependent on the incident polarisation state. The diattenuation of the diattenuator is defined as

$$\mathcal{D} = \frac{|\mathcal{T}_\alpha - \mathcal{T}_\beta|}{\mathcal{T}_\alpha + \mathcal{T}_\beta} \ , \tag{2.45}$$

with values of $\mathcal{D}$ lying in the range of 0 and 1, and $\mathcal{T}_\alpha$ and $\mathcal{T}_\beta$ being the transmittances of two orthogonal eigenpolarisations of the diattenuator. Eigenpolarisations of a polarising element pass through the element unaltered, except for a possible transmittance factor. The Mueller matrix of a diattenuator is given by

$$\mathbf{M}_D = T_u \begin{bmatrix} 1 & \vec{\mathcal{D}}^\top \\ \vec{\mathcal{D}} & \mathbf{m}_\mathcal{D} \end{bmatrix} \ , \tag{2.46}$$

where T_u is the transmittance of unpolarised light, and $\vec{\mathcal{D}}$ is the diattenuation vector whose magnitude is equal to $\mathcal{D}$. The direction of $\vec{\mathcal{D}}$ is described by the unit vector, $\hat{\mathcal{D}}$, which is related to the Stokes vector of the eigenpolarisation with the highest transmittance as $\vec{S} = [1, \hat{\mathcal{D}}^\top]^\top$. In addition, $\mathbf{m}_\mathcal{D}$ is a 3×3 matrix given by

$$\mathbf{m}_\mathcal{D} = \sqrt{1-\mathcal{D}^2}\,\mathbb{I} + (1-\sqrt{1-\mathcal{D}^2})\hat{\mathcal{D}}\hat{\mathcal{D}}^\top \ , \tag{2.47}$$

where $\mathbb{I}$ denotes the 3×3 identity matrix and $\hat{\mathcal{D}} = \vec{\mathcal{D}}/\mathcal{D}$ is the unit vector in the direction of $\vec{\mathcal{D}}$.

A pure retarder does not change the intensity of the incident light, but introduces different phase changes for its eigenpolarisations. The retardance of a retarder is defined as

$$\varphi = |\varphi_\alpha - \varphi_\beta| \ , \tag{2.48}$$

with values of φ lying between 0 and π, and φ_α and φ_β representing the phases of its two orthogonal eigenpolarisations. The Mueller matrix of a retarder has a structure given by

$$\mathbf{M}_R = \begin{bmatrix} 1 & \vec{0}^\top \\ \vec{0} & \mathbf{m}_R \end{bmatrix} \ , \tag{2.49}$$

where $\vec{0}$ denotes a 3×1 zero vector and $\mathbf{m}_R$ is a 3×3 unitary matrix with the $(i,j)^{th}$ element given by

$$(\mathbf{m}_R)_{ij} = \delta_{ij}\cos\varphi + a_i a_j(1-\cos\varphi) + \sum_{k=1}^{3} \epsilon_{ijk} a_k \sin\varphi \ , \ \text{with } i,j \in \{1,2,3\} \ , \tag{2.50}$$

where δ_{ij} is the Kronecker delta and ϵ_{ijk} is the Levi-Cività permutation symbol. Additionally, a_1, a_2 and a_3 are elements of the unit retardance vector, $\hat{R}$, such that the Stokes vector of the eigenpolarisation with the leading phase can be expressed as $\vec{S} = [1, \hat{R}^\top]^\top$.

A depolariser changes the degree of polarisation of the incident illumination, and

can be described by a Mueller matrix written as

$$\mathbf{M}_\Delta = \begin{bmatrix} 1 & \vec{0}^\top \\ \vec{P}_\Delta & \mathbf{m}_\Delta \end{bmatrix} , \tag{2.51}$$

where $\mathbf{m}_\Delta$ is a symmetric 3×3 matrix and $\vec{P}_\Delta$ denotes the 3×1 polarisance vector of the depolariser, which describes the possible polarising ability of the depolariser. The three principle axes of the depolariser and their corresponding depolarisation factors can be found through a diagonalisation of $\mathbf{m}_\Delta$. The average depolarisation caused by the depolariser can be quantified as

$$\Delta = 1 - \frac{|a| + |b| + |c|}{3} , \tag{2.52}$$

with values of Δ ranging from 0 to 1, and a, b, and c being the depolarisation factors of the depolariser.

In the Lu-Chipman matrix decomposition, an arbitrary Mueller matrix can be written as a product of the above mentioned matrices as

$$\mathbf{M} = \mathbf{M}_\Delta \mathbf{M}_R \mathbf{M}_D . \tag{2.53}$$

The polarisance vector of $\mathbf{M}$, denoted as $\vec{P}$, is fully determined by its first column, and describes the polarisation of the output light under unpolarised illumination. The magnitude of the polarisance is denoted as $\mathcal{P}$. When the product of the three matrices in the form of Equations 2.46, 2.49 and 2.51 is taken, it can be seen that T_u corresponds to the M_{00} element of $\mathbf{M}$, and the diattenuation vector $\vec{D}$ corresponds to the first row of the Mueller matrix normalised by M_{00}. With knowledge of $\vec{D}$, Equations 2.46 and 2.47 can then be used to compute $\mathbf{M}_D$. In this way, one of the matrices in the decomposition is retrieved. Under the assumption that $\mathbf{M}_D$ is not singular, multiplying Equation 2.53 by $\mathbf{M}_D^{-1}$ yields the modified Mueller matrix

$$\mathbf{M}' = \mathbf{M}\mathbf{M}_D^{-1} = \mathbf{M}_\Delta \mathbf{M}_R = \begin{bmatrix} 1 & \vec{0}^\top \\ \vec{P}_\Delta & \mathbf{m}_\Delta \mathbf{m}_R \end{bmatrix} . \tag{2.54}$$

As such, the polarisance of the depolariser, $\vec{P}_{\Delta}$, can be retrieved from the first column of $\mathbf{M}^{'}$. Finally, the remaining unknown matrices, $\mathbf{m}_{\Delta}$ and $\mathbf{m}_{R}$, can then be obtained through a polar decomposition of the 3×3 real matrix, $\mathbf{m}^{'} = \mathbf{m}_{\Delta}\mathbf{m}_{R}$. In this way, the various polarimetric parameters implicit in the Mueller matrix can be obtained, such as the magnitudes of the various polarimetric parameters provided by the quantities $\mathcal{D}$, φ, Δ and $\mathcal{P}$.

In the event the $\mathbf{M}_{D}$ is singular, the solution for $\mathbf{M}^{'}$, and consequently $\mathbf{M}_{\Delta}$ and $\mathbf{M}_{R}$, is not unique. This happens when $\mathcal{D}$ is equal to one, such that one eigenpolarisation is fully transmitted while its orthogonal polarisation state is completely blocked. Similarly, if $\mathbf{m}_{\Delta}$ is singular, then the polar decomposition of $\mathbf{m}^{'}$ has more than one possible solution for $\mathbf{m}_{R}$. This can happen when a scattering medium gets too thick, such that the output light becomes fully depolarised. This work considers scattering media at thicknesses such that some polarisation information is still preserved (i.e. not fully depolarising). Furthermore, most biological tissues do not fully block any particular polarisation state (i.e. $\mathcal{D} < 1$). As such, these scenarios are not particularly relevant to the work and will thus not be further expounded upon here. The interested reader can find more details in Ref. [139].

2.3 Electromagnetic Scattering

This section introduces key concepts in electromagnetic scattering that are relevant to this work. For the interested reader, further information can be found in detailed textbooks on the subject, such as [124, 142]. In this thesis, absorption is assumed to be negligible. In addition, only linear elastic scattering is considered, where the frequency of the incident light is maintained upon scattering. Inelastic scattering phenomena, such as the Raman or Brillouin scattering are not treated in this work. Furthermore, it is assumed that the incident illumination is fully coherent.

Consider a particle of arbitrary shape and size illuminated by a plane wave, as depicted in Figure 2.3.

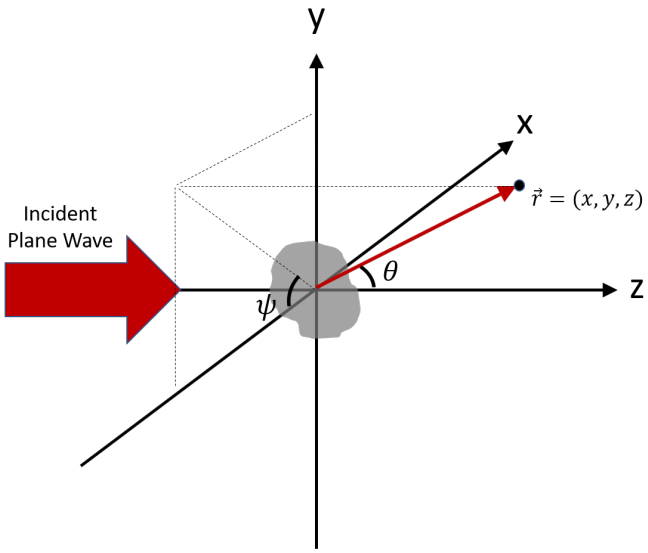

Figure 2.3: Figure showing the definition of the scattering angles, θ and ψ.

At large distances from the scatterer, the intensity of scattered light observed at the position $\vec{r} = [x, y, z]^\top$ in the direction defined by the scattering angles θ and ψ (see Figure 2.3), is given by [142]

$$I(\theta, \psi, \vec{r}) = \frac{I_0}{k^2 |\vec{r}|^2} F(\theta, \psi) \tag{2.55}$$

where $|\vec{r}| = \sqrt{x^2 + y^2 + z^2}$, I_0 is the intensity of the incident light and $F(\theta, \psi)$ is a dimensionless quantity which describes the modulation of light as a function of scattering angle. The origin of this modulation can be intuitively understood by considering the fundamental process underlying the emission of scattered light. Consider a theoretical subdivision of an arbitrary particle into many smaller regions. When an electromagnetic field, which oscillates in time, is incident on the particle, a dipole moment is induced in each of these small regions. These dipoles, in turn, oscillate at the frequency of the incident radiation and re-radiate in all directions. For any given direction in the far-field, the fields from each of these dipoles add up coherently. For a small particle, with dimensions smaller than the wavelength, it can be expected that the phase of the fields contributed by each dipole in any given direction is similar. Consequently, minimal variation in intensity is expected across all directions. In contrast, for larger particles, given the range of distances between the dipoles, a greater diversity in the phases contributed by each dipole in

each direction is expected. As a result, interference between the fields emitted by each dipole gives rise to intensities that vary with direction.

Let P^{tot} be the total scattered power that is obtained by integrating the scattered intensity, $I(\theta, \psi, \vec{r})$, over all directions. The scattering cross-section, C_{sca}, of the particle is defined as the equivalent area over which the power of the incident illumination is equal to P^{tot} [142]. By this definition, C_{sca} can be written mathematically as

$$C_{sca} = \frac{1}{k^2} \int_0^{2\pi} \int_0^{\pi} F(\theta, \psi) \sin\theta \; d\theta d\psi \; . \tag{2.56}$$

The scattering phase function, $p(\theta, \psi)$, describes the angular variation in the scattered intensity, and is defined as $F(\theta, \psi)$ normalised by the total scattered power, or equivalently, $p(\theta, \psi) = \frac{F(\theta,\psi)}{k^2 C_{sca}}$. From the scattering phase function, the scattering anisotropy factor, g, can be defined as [142]

$$g = \langle \cos(\theta) \rangle_\theta = \int_0^{2\pi} \int_0^{\pi} \cos\theta \; p(\theta, \psi) \sin\theta \; d\theta d\psi \; , \tag{2.57}$$

where it can be seen that $\langle ... \rangle_\theta$ is an average over θ and ψ that is weighted by $p(\theta, \psi)$. The scattering anisotropy factor describes the directionality of scattered light, such that particles that fully scatter light in the forward direction are described by $g = 1$. Conversely, $g = -1$ is associated with particles that cause light to be fully backscattered. In the case of isotropic scattering, where the same amount of light is scattered in every direction, $g = 0$.

When a collimated and monochromatic light beam travelling on axis is incident on a statistically homogeneous scattering medium[1] consisting of a random configuration of independent scatterers[2], the amount of unscattered light, otherwise known as ballistic light, decreases exponentially with depth in the medium. This is described

[1] A statistically homogeneous scattering medium means that there is an equal probability of the scatterer being located at any position in the scattering medium.

[2] The term "independent scatterers" implies that scattering from each particle can be considered individually without regard for other particles.

by the Beer-Lambert law, which can be written as

$$P(L) = P_o \exp\left(-\frac{L}{l}\right) \ , \tag{2.58}$$

where P_o is the power when no scattering medium is present and P is the power of the ballistic component at a depth of L. Equivalently, P is also the transmitted power of ballistic light in transmission measurements through a slab-shaped scattering medium of thickness L, which is the geometry considered in this work. The attenuation coefficient, l, is known as the scattering mean free path (MFP), and can be related to the scattering cross-section as [143]

$$l = \frac{1}{N_s C_{sca}} \ , \tag{2.59}$$

where N_s is the number density of the scatterers, defined as the number of scatterers per unit volume. The MFP describes the average distance between scattering events experienced by an incident photon, and its inverse is commonly termed as the scattering coefficient, denoted as μ_s. A closely related quantity to the MFP is the transport mean free path (TMFP), l_{tr}, which is defined as [8]

$$l_{tr} = \frac{l}{1-g} \ . \tag{2.60}$$

The TMFP describes the average distance it takes for the direction of the scattered photon to become completely randomised, and its inverse, denoted as $\mu_s^{'}$, is known as the reduced scattering coefficient. For scattering media consisting of scatterers that scatter predominantly in the forward direction (i.e. g close to 1), the directionality of light can be preserved over many scattering events, resulting in $l_{tr} > l$. On the other hand, if the scattering medium consists mainly of isotropic scatterers (i.e. g close to 0), then the directionality of light is lost even with a single scattering event, in which case, $l_{tr} = l$.

The Beer-Lambert law discussed above discusses the decay of the ballistic light intensity as a function of medium thickness. One would, perhaps naively, expect that degree of polarisation decays on the same length scale. Interestingly, for scat-

tering media with high g, studies have shown that the polarisation of the incident light persists over length scales much longer than the MFP [16, 117, 144]. By measuring the DOLP and DOCP (see Equation 2.29) of light transmitted through the scattering medium, it was shown that the decay length of linear or circular polarisation was generally different, and that the polarisation state with the longer decay length depended on the scatterer size [144]. Nevertheless, this decay length, otherwise known as the depolarisation length, for both linear and circular polarisation states was shown to be on the order of a few times the TMFP [16, 145], which for a high g can be equivalent to a decay length that is much longer than the MFP. This implies that for scattering media with a high g, the polarisation state of the incident light can still persist even after the intensity of ballistic light has been extinguished by many orders of magnitude.

2.4 Single Pixel Imaging

Single pixel imaging, as its name suggests, makes use of a detector with only a single pixel for imaging. This is in contrast to conventional cameras which typically utilise a detector with multiple pixels, such as CCD or CMOS cameras. The single pixel camera functions by probing the test object with a sequence of spatial patterns and collecting the corresponding intensities on a bucket detector containing only a single pixel [146, 147]. Taking intensity imaging in transmission as an example, the spatial patterns could be formed by a spatial modulation of the incident light field, while the intensity transmitted through the test object for each spatial pattern is captured on a photodiode. Each measured intensity is effectively the scalar projection of the spatial intensity transmittance of the test object on the associated spatial pattern. Note that the recovery of the spatial intensity transmittance of the test object is equivalent to forming its image.

Consider a test object illuminated by the i^{th} spatial mask, which is discretised into $N \times N$ pixels and has a spatial modulation that can be described by the $N^2 \times 1$ vector $\vec{\phi}$. The intensity measured by the detector, y_i is then given by $y_i = \vec{\phi}_i \cdot \vec{x}$, where $\cdot$ denotes the dot product and $\vec{x}$ is a $N^2 \times 1$ vector, such that the n^{th} element of

$\vec{x}$ corresponds to the spatially averaged intensity transmittance of the object across the n^{th} pixel of the spatial mask. If M spatial masks are sequentially projected onto the object, the associated measured intensities can be related to the intensity transmittance of the test object as

$$\vec{y} = \mathbf{\Phi}\vec{x} \ , \tag{2.61}$$

where the i^{th} element of the $M \times 1$ vector $\vec{y}$ is the intensity measured for the i^{th} projected spatial pattern (i.e. y_i) and the i^{th} row of the $M \times N$ measurement matrix $\mathbf{\Phi}$ corresponds to the spatial modulation of the i^{th} mask (i.e. $\vec{\phi}_i$). Thus, if the projected spatial patterns are known and the matrix $\mathbf{\Phi}$ is invertible, then the intensity transmittance of the object can be computed from a matrix inverse as

$$\vec{x} = \mathbf{\Phi}^{-1}\vec{y} \ , \tag{2.62}$$

from which it can be seen that the discretisation of the incident spatial patterns determines the image resolution of the single pixel camera. The advantages of single pixel imaging lie in its potential for building miniaturised imaging systems at low cost. This is particularly true when imaging outside of the visible spectrum, where economical silicon-based pixelated detectors are unavailable and any existing pixelated detectors come at a high price. In the visible spectrum, the availability of low-cost CCD and CMOS cameras means that the single pixel camera does not gain significantly in this respect. Yet, regardless of imaging wavelength, one key benefit of single pixel imaging is its inherent compatibility with compressive sensing [113, 114], which enables image recovery with fewer measurement samples than is typically needed for an accurate image reconstruction. As can be seen from Equation 2.61, at least N measurements are required in order to have a unique solution for the $N \times 1$ vector $\vec{x}$ (i.e., $M \geq N$). This reveals the main drawback of single pixel imaging - the image acquisition time scales with image resolution. If, however, the image of the object is "sparse" in some known basis (e.g. a wavelet basis), such that its decomposition in that sparse basis leads to only a small number of nonzero coefficients, then according to compressive sensing theory, it is possible to reconstruct the image with an undersampled set of measurements by measuring in a basis that

is "incoherent" with the sparse basis. Note that the "incoherence" between bases mentioned here is unrelated to the coherence of light, and is part of the terminology of compressive sensing literature referring to the strength of the correlation between the elements of the basis vectors in the sparse and measurement basis. As many natural signals have a sparse representation in an appropriately chosen basis [113], compressive sensing can be widely applied. Coupled with compressive sensing, single pixel imaging can provide high speed imaging at low cost, and also with a lower data volume, which is important for considerations of data storage. As this work aims to investigate the feasibility of single pixel polarimetric imaging, compressive sensing was not utilised in order to minimise any possible error sources. As such, further details on compressive sensing are not discussed, but can be found instead in Refs. [113, 114]. Nonetheless, it should be noted that compressive sensing is a possible means of significantly reducing the acquisition time for single pixel imaging. Finally, as mentioned in Chapter 1, another advantage of a single pixel camera is its resilience against the effects of scattering when imaging in intensity. Tajahuerce *et al.* [110] showed that when an object was hidden behind a scattering medium (i.e. a diffuser), spatially resolved cameras imaged a speckle pattern, while the single pixel camera was able to recover an image of the hidden object. This is possible because the spatial information of the object is encoded by the projected spatial patterns before light propagates through the scattering medium. This work aims to extend this capability to polarimetric imaging through scattering media.

2.5 Research Assumptions

Some of the assumptions made in this work have been introduced earlier in this Chapter. These assumptions are now summarised in this Section. The assumptions made are that:

- the scattering medium is statistically homogeneous, in that there is an equal probability of the scatterer being located at any position in the scattering medium.
- the scattering medium is in the shape of a slab.

- there is negligible absorption.
- the incident illumination is fully coherent.
- there is unimpeded access to the illumination side of the test object.
- scattered light maintains the frequency of the incident light (i.e. only elastic scattering is considered).
- the scattered light analysed by the PSA can be approximated to be collimated.
- the scattering medium is not fully depolarising for any given input polarisation state.

With these assumptions described, the next Chapter in this thesis presents the theoretical framework underlying single pixel polarimetric imaging. The impact of these assumptions on the conclusions made by this work is discussed in Chapter 7.

Chapter 3

Single Pixel Polarimetric Imaging

In Chapter 2, single pixel imaging and polarimetry have been introduced. In this chapter, the two are combined to give a description of single pixel polarimetric imaging. A method for single pixel polarimetric imaging through scattering media is then proposed and investigated using a 2D Green's tensor formalism.

3.1 Theoretical Model

3.1.1 Notation

Here, a summary of the notation utilised in this section is provided for the convenience of the reader.

General Notation	
Z_{β}^{α}	
Symbols, Z	
ψ	Amplitude modulation of spatial mask
I	Intensity measured by the photodiode
$\vec{E}$	Electric Field
$\vec{C}$	Coherency vector
$\vec{S}$	Stokes vector
$\vec{a}$	Stokes vector of an analysed polarisation state
$\vec{\Psi}$	Spatial basis vector
T	Jones matrix
M	Mueller matrix
Superscripts, α**, for** $\vec{E}$**,** $\vec{C}$ **and** $\vec{S}$	
I	Position before the object plane
II	Position after the object plane, before the scattering medium
III	Position at the detector plane
obj	Position after the object plane, under uniform illumination
inc	Position before the object plane, under uniform illumination
Subscripts, β	
i	Index of analysed polarisation state
j	Index of input polarisation state
k	Index of spatial mask projected
m	Index of input pixel
n	Index of output pixel

3.1.2 Without a Scattering Medium

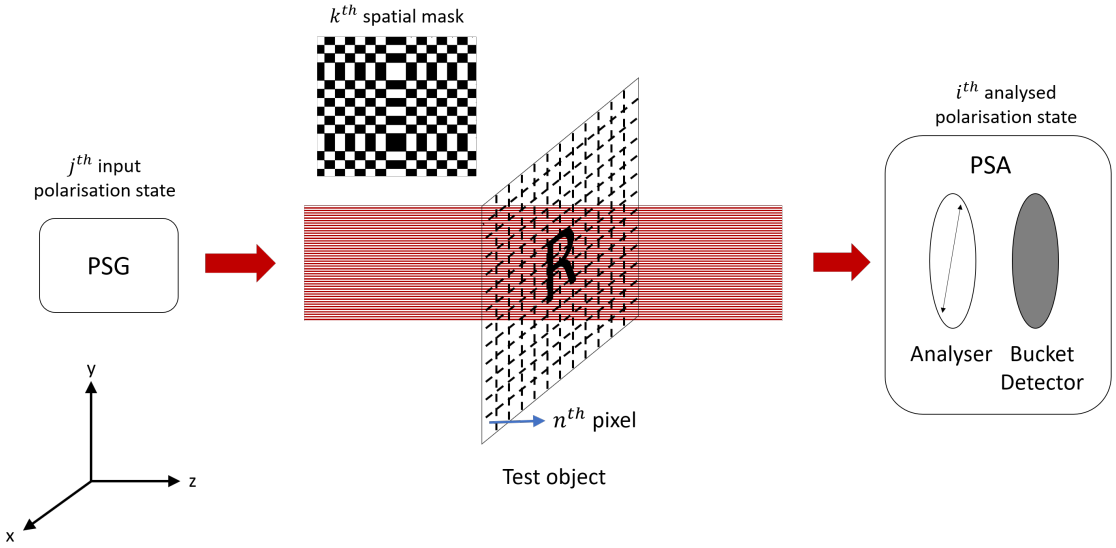

Figure 3.1: Illustration of single pixel polarimetric imaging. The polarised incident illumination, produced by a polarisation state generator (PSG), is spatially modulated such that a basis vector of the chosen measurement basis illuminates a test object with a spatially varying Jones matrix. The transmitted field is then analysed using a non-imaging polarisation state analyser (PSA), which extracts the polarimetric information.

Figure 3.1 presents a diagram that illustrates single pixel polarimetric imaging. The configuration without any scattering medium present is first considered. As in single pixel imaging, basis vectors from a chosen measurement basis are sequentially projected onto a test object, and the resulting intensity is collected using a bucket detector with no spatial resolution. As discussed in Section 2.4, the measured intensity is the scalar projection of the displayed spatial masks and the object intensity transmission, and Equation 2.62 can be used to reconstruct an intensity image of the object, with an image resolution determined by the discretisation of the spatial masks. In order to obtain a polarimetric image, or more specifically, the spatially resolved Mueller matrix of the test object, an additional step is required, where the input polarisation states are varied using a PSG, and the exiting light is analysed by a PSA, which consists of multiple measurements taken through different polarisation analysers. For the i^{th} analysed and j^{th} input polarisation state, the resulting

spatially varying field at the detector, $\vec{E}^{III}_{nijk}$, can be described as

$$\vec{E}^{III}_{nijk} = \mathbf{T}_i \mathbf{T}^{obj}_n \vec{E}^{I}_{njk} = \mathbf{T}_i \mathbf{T}^{obj}_n \left(\psi_{nk} \vec{E}^{inc}_{nj} \right) = \psi_{nk} \mathbf{T}_i \vec{E}^{obj}_{nj} \ , \tag{3.1}$$

where due to the discretised nature of the illumination, the spatial co-ordinate is also discretised into pixels with n being the corresponding index. For the n^{th} pixel, $\mathbf{T}_i$ and $\mathbf{T}^{obj}_n$ are the Jones matrices of the polarisation analyser and the object respectively, while $\vec{E}^{inc}_{nj}$ is the incident field without modulation and ψ_{nk} describes the amplitude modulation due to the k^{th} spatial mask such that the field right before the object is given by $\vec{E}^{I}_{njk} = \psi_{nk} \vec{E}^{inc}_{nj}$. Additionally, $\vec{E}^{obj}_{nj} = \mathbf{T}^{obj}_n \vec{E}^{inc}_{nj}$ can be understood as the field in a plane that is directly after the object when illuminated by an incident field without spatial modulation. Equation 3.1 can be converted into its Stokes-Mueller form by first writing it in terms of coherency vectors. The coherency vector at each output detector pixel, $\vec{C}^{III}_{nijk}$, is

$$\begin{aligned} \vec{C}^{III}_{nijk} &= \langle \vec{E}^{III}_{nijk} \otimes \vec{E}^{III,*}_{nijk} \rangle_t \\ &= |\psi_{nk}|^2 \left(\mathbf{T}_i \otimes \mathbf{T}^*_i \right) \langle \vec{E}^{obj}_{nj} \otimes \vec{E}^{obj,*}_{nj} \rangle_t \\ &= |\psi_{nk}|^2 \left(\mathbf{T}_i \otimes \mathbf{T}^*_i \right) \vec{C}^{obj}_{nj} \ , \end{aligned} \tag{3.2}$$

where $\langle ... \rangle_t$ denotes an averaging over time, and $\vec{C}^{obj}_{nj} = \langle \vec{E}^{obj}_{nj} \otimes \vec{E}^{obj,*}_{nj} \rangle_t$. For the rest of this section, it will be assumed that fully coherent light is utilised, such that $\langle ... \rangle_t$ is a constant and can therefore be omitted. Recalling Equation 2.32, the related output Stokes vector can then be shown to be

$$\vec{S}^{III}_{nijk} = |\psi_{nk}|^2 \mathbf{M}_i \vec{S}^{obj}_{nj} \ , \tag{3.3}$$

where $\vec{S}^{obj}_{nj} = \mathbf{\Gamma} \vec{C}^{obj}_{nj}$ is the Stokes vector incident on the PSA, $\mathbf{M}_i = \mathbf{\Gamma} \left(\mathbf{T}_i \otimes \mathbf{T}^*_i \right) \mathbf{\Gamma}^{-1}$ is the Mueller matrix of the i^{th} polarisation analyser and $\mathbf{\Gamma}$ is the transformation matrix relating coherency and Stokes vectors, as defined in Equation 2.32. The total Stokes vector summed across all output pixels is given by

$$\vec{S}^{tot}_{ijk} = \sum_n \vec{S}^{III}_{nijk} = \mathbf{M}_i \sum_n |\psi_{nk}|^2 \vec{S}^{obj}_{nj} \ . \tag{3.4}$$

The measurement by the bucket detector is a sum in intensity over all output pixels, and, by definition, is equal to the first element of $\vec{S}^{tot}_{ijk}$, which is denoted as $S^{tot}_{ijk,0}$. Using Equation 3.4, the measured intensity, I^{tot}_{ijk}, can be written in terms of the elements of $\vec{S}^{obj}_{nj}$ as

$$\begin{aligned} I^{tot}_{ijk} = S^{tot}_{ijk,0} &= \sum_n |\psi_{nk}|^2 \left(M_{i,00} S^{obj}_{nj,0} + M_{i,01} S^{obj}_{nj,1} + M_{i,02} S^{obj}_{nj,2} + M_{i,03} S^{obj}_{nj,3} \right) \\ &= \sum_n |\psi_{nk}|^2 \left(\vec{a}_i^{\top} \vec{S}^{obj}_{nj} \right) \\ &= \vec{\Psi}_k \cdot \vec{x}_{ij} \ , \end{aligned} \tag{3.5}$$

where $M_{i,pq}$ is the $(p,q)^{th}$ element of $\mathbf{M}_i$, and $S^{obj}_{nj,p}$ is the p^{th} element of $\vec{S}^{obj}_{nj}$. In addition, $\vec{x}_{ij}$ is a vector whose n^{th} element, $x_{ij,n} = \vec{a}_i^{\top} \vec{S}^{obj}_{nj}$, corresponds to the scalar projection of $\vec{S}^{obj}_{nj}$ on the Stokes vector corresponding to the analysed state, $\vec{a}_i = [M_{i,00}, M_{i,01}, M_{i,02}, M_{i,03}]^{\top}$. Note that although it has not been explicitly stated in this discussion, $\vec{a}_i$ (and also $\mathbf{M}_i$) are normalised to ensure that the analyser is passive, as explained in Section 2.2.5. Physically, $\vec{x}_{ij}$ is the intensity that would be observed by a spatially resolved detector. From Equation 3.5, it can be seen that I^{tot}_{ijk} is the scalar projection of the displayed spatial basis vector, $\vec{\Psi}_k$, and $\vec{x}_{ij}$. Thus, Equation 2.62 allows for $\vec{x}_{ij}$ to be reconstructed for each input and analysed polarisation.

Once $\vec{x}_{ij}$ has been reconstructed for all input and analysed polarisation states, the spatially resolved Mueller matrix can be computed by the application of Equation 2.44 on a pixel-wise basis, along with the matrices $\mathbf{A}$ and $\mathbf{W}$ that are obtained via calibration. For the n^{th} pixel, Equation 2.44 can be written as

$$\mathbf{M}_n = \mathbf{A}^{-1} \mathbf{D}_n \mathbf{W}^{-1} \ . \tag{3.6}$$

Equation 3.6 is explicitly related to the variables in Equation 3.5 as

$$\begin{aligned} D_{n,ij} &= x_{ij,n} \ , \\ \vec{A}_{i*} &= \vec{a}_i \ , \\ \vec{W}_{*j} &= \mathbf{\Gamma} \vec{C}^{inc}_{nj} = \vec{S}^{inc}_{nj} \ . \end{aligned} \tag{3.7}$$

where $D_{n,ij}$ is the $(i,j)^{th}$ element of the matrix $\mathbf{D}_n$. Moreover, the i^{th} row in the matrix $\mathbf{A}$, $\vec{A}_{i*}$, is the Stokes vector of the i^{th} analysed polarisation state, $\vec{a}_i$, while the j^{th} column of $\mathbf{W}$, $\vec{W}_{*j}$, is the incident Stokes vector corresponding to the j^{th} input polarisation state, $\vec{S}_{nj}^{inc}$. The use of Equation 3.6 completes the process of single pixel polarimetric imaging, returning a spatially resolved polarimetric image of the test object.

3.1.3 In the Presence of a Scattering Medium

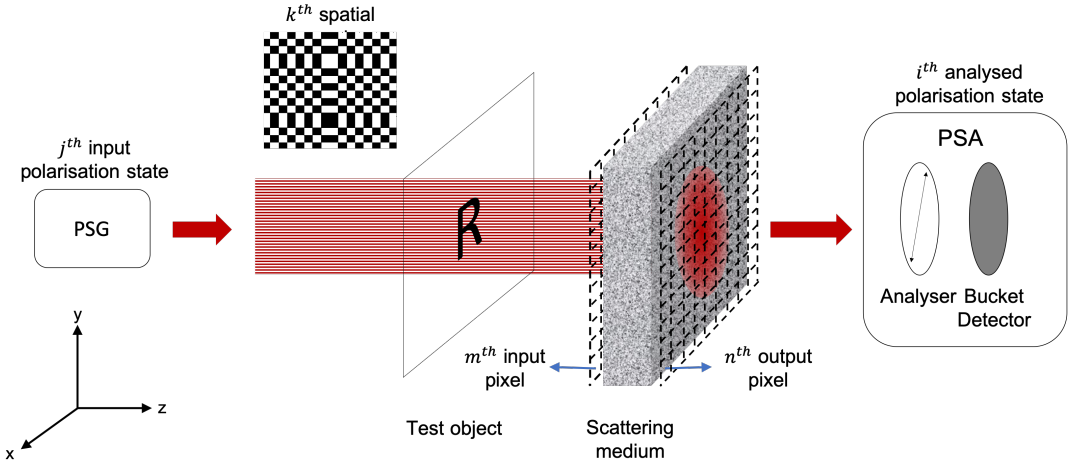

Figure 3.2: Illustration of single pixel polarimetric imaging with a scattering medium present. The polarised incident illumination, produced by a polarisation state generator (PSG), is spatially modulated such that a basis vector of the chosen measurement basis illuminates a test object with a spatially varying Jones matrix. The field then propagates through the scattering medium, and the transmitted light is analysed using a non-imaging polarisation state analyser (PSA), which extracts the polarimetric information.

Figure 3.2 shows an illustration of single pixel polarimetric imaging with a scattering medium present. In the presence of a scattering medium, transmission through the medium has to be taken into account. In this work, static scattering media are considered, such that the transmitted speckle patterns do not change with time. This can also be seen as a study of dynamic scattering media under the quasistatic approximation.

The vectorial electric field in the planes before and after a scattering medium are

related by the vectorial amplitude transmission matrix (VTM), $\mathbf{t}^{SM}$, as

$$\vec{E}^{out} = \mathbf{t}^{SM}\vec{E}^{in} \ , \tag{3.8}$$

where $\vec{E}^{in}$ and $\vec{E}^{out}$ are column vectors describing the vectorial fields for all input and output spatial modes respectively. As described in Chapter 1, a spatial basis consisting of a complete set of orthogonal spatial modes can be used to describe any arbitrary field at the input or output of a scattering medium. Here, a discretised pixel basis is assumed for both input and output modes. From Equation 3.8, it can be seen that the field in any given output pixel is a weighted sum of the fields over all input pixels. This can be written as

$$\vec{E}^{out}_{n} = \sum_{m} \mathbf{T}^{SM}_{nm}\vec{E}^{in}_{m} \ , \tag{3.9}$$

where $\mathbf{T}^{SM}_{nm}$ is a 2×2 sub-block of $\mathbf{t}^{SM}$, and is the Jones matrix relating the field for the m^{th} input pixel to the field for the n^{th} output pixel. As such, for the setup shown in Figure 3.2, the field at the bucket detector for the j^{th} input and the i^{th} analysed polarisation state is given by

$$\begin{aligned} \vec{E}^{III}_{nijk} &= \mathbf{T}_i \sum_{m} \mathbf{T}^{SM}_{nm}\vec{E}^{II}_{mj} \\ &= \mathbf{T}_i \sum_{m} \psi_{mk}\mathbf{T}^{SM}_{nm}\mathbf{T}^{obj}_{m}\vec{E}^{inc}_{mj} \\ &= \mathbf{T}_i \sum_{m} \psi_{mk}\mathbf{T}^{SM}_{nm}\vec{E}^{obj}_{mj} \ , \end{aligned} \tag{3.10}$$

where the notation follows that of Section 3.1.2. Comparing Equation 3.10 to Equation 3.1, it can be seen that in the presence of a scattering medium, each output pixel consists of field contributions from all input pixels. As such, the input field can be seen to be scrambled by the presence of the scattering medium. This is the reason why a hidden object cannot be seen when imaging with a spatially resolved camera. Yet, as the following discussion will demonstrate, single pixel imaging is still able to reconstruct an image of the hidden object. To see this, Equation 3.10

is first written in terms of coherency vectors as

$$\begin{aligned}
\vec{C}^{III}_{nijk} &= \vec{E}^{III}_{nijk} \otimes \vec{E}^{III,*}_{nijk} \\
&= \left(\sum_m \psi_{mk} \mathbf{T}_i \mathbf{T}^{SM}_{nm} \vec{E}^{obj}_{mj} \right) \otimes \left(\sum_l \psi_{lk} \mathbf{T}_i \mathbf{T}^{SM}_{nl} \vec{E}^{obj}_{lj} \right)^* \\
&= \sum_m \sum_l \psi_{mk} \psi^*_{lk} \left(\mathbf{T}_i \otimes \mathbf{T}^*_i \right) \left(\mathbf{T}^{SM}_{nm} \otimes \mathbf{T}^{SM,*}_{nl} \right) \left(\vec{E}^{obj}_{mj} \otimes \vec{E}^{obj,*}_{lj} \right) \\
&= \sum_m |\psi_{mk}|^2 \left(\mathbf{T}_i \otimes \mathbf{T}^*_i \right) \left(\mathbf{T}^{SM}_{nm} \otimes \mathbf{T}^{SM,*}_{nm} \right) \vec{C}^{obj}_{mj} \\
&\quad + \sum_m \sum_{\substack{l \\ l \neq m}} \psi_{mk} \psi^*_{lk} \left(\mathbf{T}_i \otimes \mathbf{T}^*_i \right) \left(\mathbf{T}^{SM}_{nm} \otimes \mathbf{T}^{SM,*}_{nl} \right) \vec{C}^{obj}_{mlj} \ ,
\end{aligned} \tag{3.11}$$

where the second equality follows from the mixed product property of the direct product [148] and $\vec{C}^{obj}_{mlj} = \vec{E}^{obj}_{mj} \otimes \vec{E}^{obj,*}_{lj}$. Also, the final expression in Equation 3.11 follows from the second equality by segmenting the terms with $m = l$. The total coherency vector, $\vec{C}^{tot}_{ijk}$, summed over output pixels is then given by

$$\begin{aligned}
\vec{C}^{tot}_{ijk} &= \sum_n \vec{C}^{III}_{nijk} \\
&= \sum_m |\psi_{mk}|^2 \left(\mathbf{T}_i \otimes \mathbf{T}^*_i \right) \mathbf{A}_m \vec{C}^{obj}_{mj} + \sum_m \sum_{\substack{l \\ l \neq m}} \psi_{mk} \psi^*_{lk} \left(\mathbf{T}_i \otimes \mathbf{T}^*_i \right) \mathbf{B}_{ml} \vec{C}^{obj}_{mlj} \ ,
\end{aligned} \tag{3.12}$$

where

$$\mathbf{A}_m = \sum_n \left(\mathbf{T}^{SM}_{nm} \otimes \mathbf{T}^{SM,*}_{nm} \right) , \ \mathbf{B}_{ml} = \sum_n \left(\mathbf{T}^{SM}_{nm} \otimes \mathbf{T}^{SM,*}_{nl} \right) \ . \tag{3.13}$$

Equation 3.12 shows that the total coherency vector consists of two contributions. The first term is an incoherent sum of the contributions from each input pixel, while the second term has a mixed contribution from different pixels, and can be interpreted as an interference term. $\mathbf{B}_{ml}$ can be written explicitly as

$$\mathbf{B}_{ml} = \sum_n \begin{bmatrix}
T_{nm,00} T^*_{nl,00} & T_{nm,00} T^*_{nl,01} & T_{nm,01} T^*_{nl,00} & T_{nm,01} T^*_{nl,01} \\
T_{nm,00} T^*_{nl,10} & T_{nm,00} T^*_{nl,11} & T_{nm,01} T^*_{nl,10} & T_{nm,01} T^*_{nl,11} \\
T_{nm,10} T^*_{nl,00} & T_{nm,10} T^*_{nl,01} & T_{nm,11} T^*_{nl,00} & T_{nm,11} T^*_{nl,01} \\
T_{nm,10} T^*_{nl,10} & T_{nm,10} T^*_{nl,11} & T_{nm,11} T^*_{nl,10} & T_{nm,11} T^*_{nl,11}
\end{bmatrix} , \tag{3.14}$$

where $T_{nm,pq}$ is the $(p,q)^{th}$ element in $\mathbf{T}_{nm}^{SM}$, and the superscript, 'SM', has been omitted for legibility. $\mathbf{A}_m$ has the same form as $\mathbf{B}_{ml}$, except that l is replaced by m (i.e. $\mathbf{A}_m = \mathbf{B}_{mm}$). The transmitted speckle at the n^{th} output pixel due to the incident field at the m^{th} input pixel can be computed as

$$\begin{bmatrix} E_n^{III,x} \\ E_n^{III,y} \end{bmatrix} = \begin{bmatrix} T_{nm,00} & T_{nm,01} \\ T_{nm,10} & T_{nm,11} \end{bmatrix} \begin{bmatrix} E_m^{II,x} \\ E_m^{II,y} \end{bmatrix} , \tag{3.15}$$

where $E_m^{II,x}$ and $E_m^{II,y}$ are the components of the incident electric field from the m^{th} input pixel along the x and y axis respectively, and $E_n^{III,x}$ and $E_n^{III,y}$ are defined in a similar fashion. In this way, it can be seen that the elements in $\mathbf{T}_{nm}^{SM}$ describe the different polarisation components of the output speckle for the n^{th} output pixel due to an incident field from the m^{th} input pixel with a polarisation state of $\vec{E}_m^{II} = \left[E_n^{II,x}, 0\right]^\top$ or $\vec{E}_m^{II} = \left[0, E_n^{II,y}\right]^\top$. Since the summation in Equation 3.14 is taken over all output pixels, the elements in $\mathbf{A}_m$ can therefore be interpreted as spatial correlations between polarised speckles from the same input pixel, while on the other hand, the elements of $\mathbf{B}_{ml}$ can be seen to be the correlations between polarised speckles produced from different input pixels. Let C_{r_1} denote the minimum distance between input points such that the speckle at any fixed output point is approximately uncorrelated. If the spatial extent of the input pixel is much larger than C_{r_1}, it can be expected that the correlations between speckles formed from different input pixels are much smaller than the correlations between speckles produced by fields from the same input pixel. Therefore, element-wise, $\mathbf{A}_m$ can be expected to be much larger than $\mathbf{B}_{ml}$, in agreement with the scalar formulation [110]. This allows Equation 3.12 to be approximated as

$$\vec{C}_{ijk}^{tot} \approx \sum_m |\psi_{mk}|^2 \left(\mathbf{T}_i \otimes \mathbf{T}_i^*\right) \mathbf{A}_m \vec{C}_{mj}^{obj} . \tag{3.16}$$

Using Equation 2.32, the total output Stokes vector is

$$\begin{aligned}\vec{S}_{ijk}^{tot} = \mathbf{\Gamma}\vec{C}_{ijk}^{tot} &= \mathbf{M}_i \sum_m |\psi_{mk}|^2 \mathbf{\Gamma}\mathbf{A}_m\mathbf{\Gamma}^{-1}\vec{S}_{mj}^{obj} \\ &= \mathbf{M}_i \sum_m |\psi_{mk}|^2 \mathbf{M}_m^{SM}\vec{S}_{mj}^{obj} \\ &= \mathbf{M}_i \sum_m |\psi_{mk}|^2 \mathbf{M}_m^{SM}\mathbf{M}_m^{obj}\vec{S}_{mj}^{inc} \ ,\end{aligned} \tag{3.17}$$

where $\mathbf{M}_i$, $\mathbf{M}_m^{SM} = \mathbf{\Gamma}\mathbf{A}_m\mathbf{\Gamma}^{-1}$ and $\mathbf{M}_m^{obj}$ are the Mueller matrices of the polarisation analyser, the scattering medium and the object respectively, and $\vec{S}_{mj}^{inc}$ is the Stokes vector corresponding to the j^{th} input polarisation state for the m^{th} input pixel.

If $\mathbf{M}_m^{SM}$ is assumed to be independent of m, then Equation 3.17 can be simplified as

$$\begin{aligned}\vec{S}_{ijk}^{tot} &= \mathbf{M}_i\mathbf{M}^{SM} \sum_m |\psi_{mk}|^2 \vec{S}_{mj}^{obj} \\ &= \mathbf{Q}_i \sum_m |\psi_{mk}|^2 \vec{S}_{mj}^{obj} \ ,\end{aligned} \tag{3.18}$$

where $\mathbf{Q}_i = \mathbf{M}_i\mathbf{M}^{SM}$ describes the combined effect of both the analyser and the scattering medium. The validity of this assumption (i.e. that $\mathbf{M}_m^{SM}$ is assumed to be independent of m) is discussed in the later part of this section. Comparing Equation 3.18 to Equation 3.4, it can be seen that the two equations have the same form, except for the contribution of the scattering medium, $\mathbf{M}^{SM}$. Therefore, similar to Equation 3.5, the intensity measured by the bucket detector is given by

$$\begin{aligned}I_{ijk}^{tot} = S_{ijk,0}^{tot} &= \sum_m |\psi_{mk}|^2 \left(Q_{i,00}S_{mj,0}^{obj} + Q_{i,01}S_{mj,1}^{obj} + Q_{i,02}S_{mj,2}^{obj} + Q_{i,03}S_{mj,3}^{obj}\right) \\ &= \sum_m |\psi_{mk}|^2 \left(\vec{a}_i^{\top}\mathbf{M}^{SM}\vec{S}_{mj}^{obj}\right) \\ &= \vec{\Psi}_k \cdot \vec{x}_{ij}^{\,\prime} \ ,\end{aligned} \tag{3.19}$$

where $Q_{i,pq}$ denotes the $(p,q)^{th}$ element of $\mathbf{Q}_i$. Note that, unlike Section 3.1.2, $\vec{x}_{ij}^{\,\prime} = \left(\vec{a}_i^{\top}\mathbf{M}^{SM}\vec{S}_{mj}^{obj}\right)$ does not correspond to the intensity image that would have been seen through the polarisation analyser by a spatially resolved camera, as $\mathbf{M}^{SM}$ is derived from $\mathbf{A}_m$, which consists of a sum over all output pixels. Nevertheless,

Equation 2.62 allows the reconstruction of $\vec{x}'_{ij}$, which can be understood as an image of the object as seen through the polarisation analyser, but with an additional optical element in between. Once $\vec{x}'_{ij}$ has been reconstructed for all input and analysed polarisation states, the set of obtained intensity values for the m^{th} input pixel can be related to its Mueller matrix as

$$\mathbf{D}_m = \mathbf{A}\mathbf{M}^{SM}\mathbf{M}_m^{obj}\mathbf{W} \ , \tag{3.20}$$

which is an altered form of Equation 4.31 that includes the effect of the scattering medium. The relationship between the matrices in Equation 3.20 and the variables in Equation 3.19 are as previously described in Equation 3.7. Finally, the spatially resolved Mueller matrix of the hidden object can be computed through an inversion of Equation 3.20 as

$$\mathbf{M}_m^{obj} = \mathbf{M}^{SM,-1}\mathbf{A}^{-1}\mathbf{D}_m\mathbf{W}^{-1} \ . \tag{3.21}$$

In the above discussion, $\mathbf{M}_m^{SM}$ was assumed to be independent of m, though in general, $\mathbf{M}_m^{SM}$ is a function of the position of the input pixel. In the general case, Equations 3.19 to 3.21 still hold, but $\mathbf{M}_m^{SM}$ at each input point needs to be known in order to reconstruct $\mathbf{M}_m^{obj}$. This would be inconvenient in practice, as the Mueller matrix of the scattering medium corresponding to each pixel has to be measured beforehand. There are, however, cases where it is possible that $\mathbf{M}_m^{SM}$ becomes independent of the input pixel position, thereby greatly simplifying the reconstruction process. One example is when I_{ijk}^{tot} is averaged over different instances of disorder in a statistically homogeneous scattering medium, which, as explained in Section 2.3, means that there is an equal probability of the scatterer being located at any position in the scattering medium. For such media, the related Jones matrix $\mathbf{T}_{nm}^{SM}$ is a statistically stationary random variable such that $\langle \mathbf{T}_{nm}^{SM} \rangle = \langle \mathbf{T}_{n-m}^{SM} \rangle$, that is, the ensemble-averaged Jones matrix only depends on the difference in position of the input and output pixels, rather than their absolute positions. Consequently, the ensemble-averaged speckle correlations $\langle \mathbf{T}_{nm}^{SM} \otimes \mathbf{T}_{nl}^{SM,\,*} \rangle$ are a function of the separation between input pixels, and do not depend on the absolute position of the input pixels. As such, it can be expected that through ensemble averaging, $\mathbf{A}_m$, and hence also $\mathbf{M}_m^{SM}$, is independent of m. Experimentally, a possible way that this

could be achieved is by imaging through dynamic scattering media over sufficiently long time scales. Averaging over time, however, sets a limitation on the minimum acquisition time required. Ensemble averaging can also be implemented by taking a spatial average over an input pixel. This will be investigated further in Section 3.2.2, where it will be shown that for a sufficiently large pixel size, $\mathbf{M}_m^{SM}$ becomes less dependent on the instance of disorder, which allows the same Mueller matrix to be used for different scatterer configurations. In this regime, each large pixel consists of many independent areas, with each area giving rise to a transmitted speckle pattern that is uncorrelated to the others, so that they can be considered to be related to a different instances of disorder. The Mueller matrix measured over a pixel is then equivalent to an average over different instances of disorder, and is, therefore, independent of the input pixel position. As such, even for a single instance of disorder, it is possible to use the same Mueller matrix for the scattering medium across all input pixels, so long as the pixel size is sufficiently large. In practice, the assumption of statistical homogeneity generally does not hold for biological tissues, for example when imaging across different tissue types. Nevertheless, it is possible to define a field of view over which the tissue can be approximated to be statistically homogeneous, such that the same Mueller matrix can be used for each input pixel.

A key assertion in the above derivation is that the interference term in Equation 3.11 is negligible (i.e. $\mathbf{A}_m \gg \mathbf{B}_{ml}$). The validity of this claim will be investigated in Section 3.2.3. Moreover, although 3D Stokes vectors can, in theory, be defined [149], most polarimeters only measure a 2D projection of the polarisation state (for e.g. [150, 151]). The experimental setup and data processing used in this work (see Chapter 4) are also based on the same approximation. This implies that only low numerical apertures (NA) should be used as the axial electric field that arises with light propagating at high angles is unaccounted for, and would cause an error in the measured polarisation state [152]. In Section 3.2.4, the effect of NA on single pixel imaging polarimetry is studied.

3.2 Simulations

In this section, the assumptions of the presented theoretical model are examined using numerical simulations. To this end, there are many techniques which have been developed for the simulation of electromagnetic scattering from randomly positioned particles, each one applying different strategies and assumptions to solve Maxwell's equations [120, 153, 154].

The first group of techniques approximates the differential operators in the differential form of Maxwell's equations (see Equations 2.1 to 2.4), through a discretisation of time and/or space [155, 156]. The main advantage of these techniques is their applicability to inhomogeneous, anisotropic particles of arbitrary shapes. In addition, implementations of these methods are available to the general public. Yet, computation time and power often becomes an issue for these techniques, such as in the simulation of particles that are much larger than the wavelength, or thick scattering media with a large number of scatterers. The second group of techniques describes the electric fields in terms of basis functions, which are themselves solutions to the vector Helmholtz equation (see Equation 2.20) [125, 126], as was described in Section 2.1. The related mode coefficients are then determined by a matching of the appropriate boundary conditions [124]. These methods have been shown to have high numerical accuracy and can be used for benchmarking. Another significant advantage is that with the coefficients in the expansion, one obtains full information about the scatterer so the computation does not have to be repeated for different particle orientations, or equivalently, different incident angles of illumination. This group of techniques, however, tends to be computationally intensive, particularly for simulations with a large number of scatterers. The third group of techniques approximates the solution to the inhomogeneous wave equation, Equation 2.15, by a discretisation of the integral taken over the scatterer volume in Equation 2.17 [121, 122]. By doing so, a set of linear equations can be solved to obtain the resulting field. As the computation is confined to the scatterer's volume, this relaxes the demand on computational resources in comparison to finite difference techniques. In addition, anisotropic, inhomogeneous and arbitrarily shaped particles can be simu-

lated. One disadvantage, however, is that, the computation has to be repeated for each new incidence angle of illumination and particle orientation. The last group of techniques solves the electromagnetic scattering problem stochastically. Examples of such techniques are Monte Carlo methods [157, 158], which model photon propagation in the scattering medium as a random walk, and random matrix theory [78], which generate elements of the scattering matrix from a pre-defined probability distribution that can then be used to compute the resulting light field. The flexibility of stochastic methods, such as in their ability to simulate, in principle, any incident light field, make them an attractive means of simulating electromagnetic light scattering, but the choice of a realistic probability distribution is not always clear-cut and affects the accuracy of the results. Furthermore, in particular for Monte Carlo methods, high accuracies can be achieved by launching a large number of photons, but this comes at high computational cost.

Each of these techniques have their strengths and drawbacks, and there isn't one technique that stands out as the best across all applications. The choice of technique is usually specific to the application. In this work, the field at a fixed detector plane is to be calculated over multiple scatterer configurations, for a constant illumination. Also, the thickness of the scattering medium should span a range of TMFPs (from less than one to a few). On the other hand, the transverse width of the medium needs to be a few times larger than the illumination spot so that edge effects from scattering off the boundary of the medium are negligible. A large number of scatterers is usually required to satisfy these conditions. Take for example, a three dimensional scattering medium with a transverse width of 1mm and a MFP of 200 microns. Assuming spherical scatterers in air, with a scatterer refractive index of 1.5 and a sphere diameter of 1 micron, a single instance of disorder contains circa one million scatterers. In view of the computational requirements of the simulations, the coupled dipole method was chosen for this work. In order to decrease the computational load further, the simulation was reduced to two dimensions, with the third dimension taken to extend to infinity. As such, the 2D coupled line dipole method based on the 2D Green's tensor was used to study the validity of the assumptions made in Section 3.1.3.

3.2.1 Numerical Methods

Simulation Geometry and Parameters

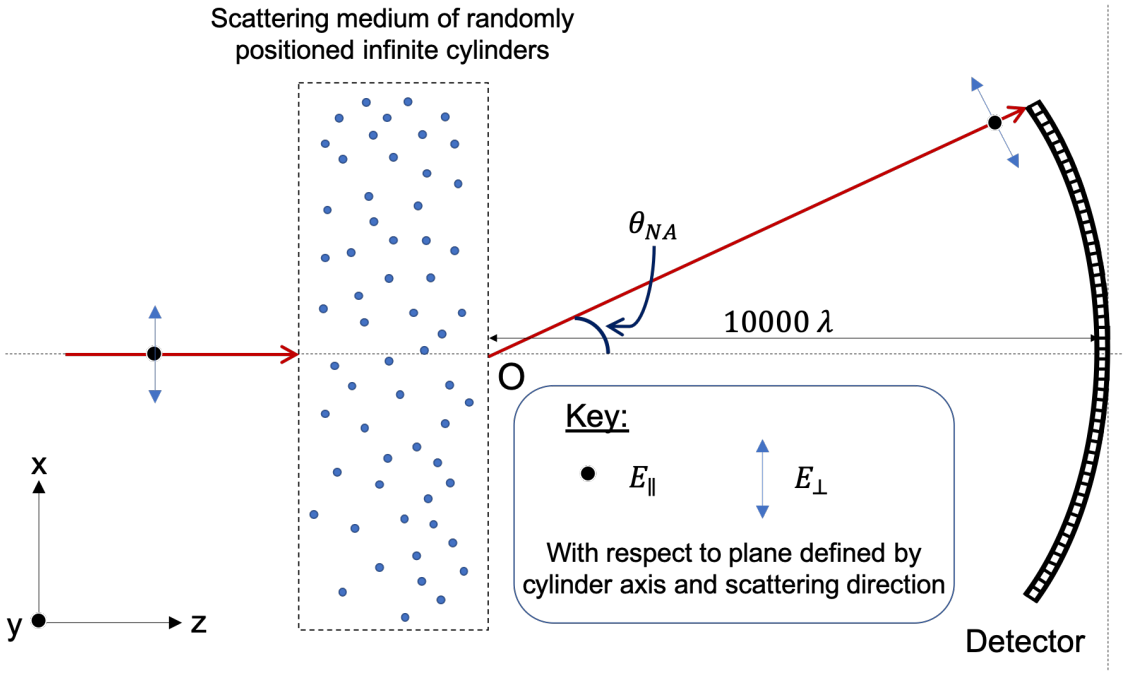

Figure 3.3: Simulation geometry showing the definition of the electric field in the far field.

The geometry of the simulation is shown in Figure 3.3, and the simulation parameters are defined in Table 3.1 below. Light travelling in the z-direction is incident on a 2D scattering medium of randomly positioned and non-overlapping cylinders in air. The cylinders are taken to be infinitely long in the y-direction, and their positions within the scattering medium are randomly chosen from a uniform distribution. In the transverse direction, the cylinders are assumed to be much smaller than the wavelength, such that they can be approximated as line dipoles. The dipole polarisability is governed by the radius and refractive index of the cylinders, which is described in Table 3.1 below.

In an experiment, the field within the numerical aperture of the collecting optics is collected and imaged onto the detector. In order to study the feasibility of the proposed method in a manner that is independent of the design of the collecting

optics, the resulting field is calculated in the far-field on a spherical detector with a radius of $10000\lambda_0$ that is centred on O, where λ_0 is the wavelength in free space. The computed field corresponds to the field within the numerical aperture of the collecting optics, before it is propagated through the lens. The detector pixels have an arc length separation of $\frac{\lambda_0}{2}$, and the full detector size corresponds to a numerical aperture of $NA = \sin\theta_{NA} \approx 0.1$. For each detector pixel, the perpendicular and parallel components of the field, $E_\perp$ and $E_\parallel$, are defined with respect to the plane defined by the cylinder axis and the scattering direction, as illustrated in Figure 3.3.

As biological samples have a MFP on the order of 100 microns [8, 17], similar MFPs were chosen for this simulation. Nevertheless, it is the ratio of thickness to MFP, $\zeta = \frac{L}{l}$, that is of importance as it defines the average number of scattering events experienced by a photon that enters the scattering medium. The MFP was computed using Mie theory [142] under the dipole approximation, using the refractive indices and cylinder radius specified in Table 3.1. The refractive index and radius of the cylinders affects their scattering cross-section, which in turn affects the density of scatterers required to achieve a desired MFP. Since the computational load increases with the number of scatterers, the refractive index and radius of the cylinders were selected in order to have a reasonable number of scatterers that could be managed by the available computational resources. Due to the cylindrical geometry of the scatterers, the MFP differs for incident fields polarised parallel ($\vec{E}_\parallel^{inc}$) and perpendicular ($\vec{E}_\perp^{inc}$) to the cylinder axis. For the scattering geometry considered, $\vec{E}_\parallel^{inc}$ has an electric field that oscillates in the y-direction while $\vec{E}_\perp^{inc}$ has an electric field that oscillates in the x-direction. ζ was defined with respect to the MFP corresponding to $\vec{E}_\perp^{inc}$ as $\zeta = \frac{L}{l_\perp}$, with $l_\perp$ denoting the relevant MFP. Values of ζ ranging from 1 to 3 were used.

Parameter	Value
Wavelength, λ_0	638 nm
Cylinder radius, a	220 nm
Transverse width, W	1 mm
Refractive index of cylinder, n_{cyl}	1.6
Refractive index of background, n	1
Mean free path ($\vec{E}_{\parallel}^{inc}$), $l_{\parallel}$	368 μm
Mean free path ($\vec{E}_{\perp}^{inc}$), $l_{\perp}$	200 μm
Scattering anisotropy factor, g	0
Mean spacing between cylinders	10.95μm
Ratio of thickness to mean free path, $\zeta = \frac{L}{l_{\perp}}$	$\{1, 2, 3\}$

Table 3.1: Simulation Parameters.

The Coupled Dipole Formalism

In this section, the coupled dipole technique used in this work is described. The methodology used in these simulations expands on the work previously done by A. Van de Nes [122]. As such, the main equations from the original formalism are first presented, from which a novel application is then formed in the ensuing sections. For further details and derivation, the reader is referred to Refs. [122, 159].

The 2D Green's tensor describing the electric field at $\vec{r} = (x, y, z)$ radiated by a single electric line dipole at $\vec{r}' = (x', y', z')$ can be written as

$$\begin{aligned}\mathbf{G}^e\left(\vec{r},\vec{r}'\right) &= \frac{i}{4}\begin{bmatrix} \cos^2\psi H_0 - \frac{\cos 2\psi}{k\rho}H_1 & 0 & \frac{\sin 2\psi}{2k\rho}\left(2H_1 - k\rho H_0\right) \\ 0 & H_0 & 0 \\ \frac{\sin 2\psi}{2k\rho}\left(2H_1 - k\rho H_0\right) & 0 & \sin^2\psi H_0 + \frac{\cos 2\psi}{k\rho}H_1 \end{bmatrix} \\ &= \frac{i}{4}\begin{bmatrix} \left(\frac{z-z'}{\rho}\right)^2 H_0 + \frac{\left(x-x'\right)^2 - \left(z-z'\right)^2}{k\rho^3}H_1 & 0 & \frac{\left(x-x'\right)\left(z-z'\right)(2H_1 - k\rho H_0)}{k\rho^3} \\ 0 & H_0 & 0 \\ \frac{\left(x-x'\right)\left(z-z'\right)(2H_1 - k\rho H_0)}{k\rho^3} & 0 & \left(\frac{x-x'}{\rho}\right)^2 H_0 - \frac{\left(x-x'\right)^2 - \left(z-z'\right)^2}{k\rho^3}H_1 \end{bmatrix},\end{aligned} \tag{3.22}$$

where ρ and ψ are the cylindrical co-ordinates defined as

$$\rho = \sqrt{(x-x')^2 + (z-z')^2},\ \psi = \tan^{-1}\left(\frac{x-x'}{z-z'}\right) . \tag{3.23}$$

Also, H_n denotes the Hankel function of the first kind of order n with an omitted argument of $k\rho$, where as defined previously, $k = \frac{2\pi}{\lambda_0}$ corresponds to the wavevector in free space. Since the line dipoles are infinite in the y-direction, the resulting fields are independent of the y co-ordinate, as can be seen from Equation 3.22. Nevertheless, all three co-ordinates have been specified for the sake of completeness. In the limit of large arguments, the H_n takes on the following form [160]

$$H_n(\xi) = \sqrt{\frac{2}{\pi\xi}} \exp\left(i\left(\xi - \frac{n\pi}{2} - \frac{\pi}{4}\right)\right) . \tag{3.24}$$

Therefore, to obtain the far-field expression of the Green's tensor, Equation 3.24 was used to evaluate the Hankel functions in Equation 3.22. The near-field expression of the Green's tensor was used for the computation of the dipole moments, while the far-field Green's tensor was used to compute the field at the detector (see below).

For a collection of N line dipoles, the electric field, $\vec{E}(\vec{r})$, at any point outside of the cylinders can be computed from the Green's tensor as

$$\begin{aligned} \vec{E}(\vec{r}) &= \vec{E}^{inc}(\vec{r}) + \omega^2\mu_o \sum_{n=1}^{N} \mathbf{G}^e(\vec{r},\vec{r}_n)\vec{p}_n \\ &= \vec{E}^{inc}(\vec{r}) + \vec{E}^{scat}(\vec{r}), \end{aligned} \tag{3.25}$$

where $\vec{E}^{inc}(\vec{r})$ is the unscattered incident field at $\vec{r}$ and $\vec{p}_n$ is the dipole moment of the n^{th} line dipole. The resulting field is thus a superposition of the incident field and the fields scattered by the line dipoles, $\vec{E}^{scat}(\vec{r})$. To compute $\vec{E}(\vec{r})$, it can be seen that the dipole moment of each line dipole must first be obtained. The dipole moment of the m^{th} line dipole that is located at $\vec{r}_m$, is given by

$$\vec{p}_m = \boldsymbol{\alpha}_m \vec{E}^{exc}(\vec{r}_m) \tag{3.26}$$

where $\boldsymbol{\alpha}_m$ is the polarisability of the line dipole and $\vec{E}^{exc}(\vec{r}_m)$ is the exciting field. An expression for the polarisability of a line dipole is derived in the next part of this section. Since identical particles were used in this simulation, $\boldsymbol{\alpha}_m$ was the same for all line dipoles. The exciting field, $\vec{E}^{exc}(\vec{r}_m)$, is the total field at $\vec{r}_m$ due to the incident field and all other line dipoles in the medium. It should be noted that the exciting field, $\vec{E}^{exc}(\vec{r}_m)$, is not the same as the actual field at $\vec{r}_m$, $\vec{E}(\vec{r}_m)$, as the latter includes a self-contribution term [159]. Thus, inserting Equation 3.25 in 3.26, $\vec{p}_m$ can be expressed as

$$\vec{p}_m = \boldsymbol{\alpha}_m \vec{E}^{exc}(\vec{r_m}) = \boldsymbol{\alpha}_m \vec{E}^{inc}(\vec{r}_m) + \omega^2 \mu_o \sum_{\substack{n=1 \\ n \neq m}}^{N} \boldsymbol{\alpha}_m \mathbf{G}^e(\vec{r}_m, \vec{r}_n) \vec{p}_n \ . \tag{3.27}$$

Equation 3.27 can be seen to form a set of $3N \times 3N$ linear equations, which can be solved to obtain $\vec{p}_m$. With the dipole moments known, Equation 3.25 can be used to obtain the electric field for any point exterior to the cylinders. As such, for a specified incident field, Equation 3.25 enables the computation of the resulting field, in a similar way as how $\mathbf{t}^{SM}$ provides the resulting field for a given incident field in Equation 3.8. Though not explicitly used in this work, it can be noted that there exists a relationship between $\mathbf{t}^{SM}$ and $\mathbf{G}^e$ [143].

As the resulting fields computed by Equation 3.25 were defined in terms of their Cartesian components, it was necessary to perform a co-ordinate transformation in order to compute the parallel and perpendicular components of the field as defined in Figure 3.3, with the components denoted as $E_{\parallel}$ and $E_{\perp}$ respectively. Under the paraxial approximation, each point (x, z) in the far-field corresponds to a plane wave travelling with an angle of $\beta = \tan^{-1}\left(\frac{x}{z}\right)$ from the z-axis [101]. Furthermore, the electric field oscillates in a plane that is orthogonal to the wavevector. Therefore, to obtain $E_{\parallel}$ and $E_{\perp}$, the field was converted to cylindrical components. The transformation matrix required can be written as

$$\begin{bmatrix} \hat{\rho} \\ \hat{\psi} \\ \hat{y} \end{bmatrix} = \begin{bmatrix} \sin\psi & 0 & \cos\psi \\ \cos\psi & 0 & -\sin\psi \\ 0 & 1 & 0 \end{bmatrix} \begin{bmatrix} \hat{x} \\ \hat{y} \\ \hat{z} \end{bmatrix} \ , \tag{3.28}$$

where $(\hat{\rho}, \hat{\psi}, \hat{y})$ and $(\hat{x}, \hat{y}, \hat{z})$ are the unit vectors of the cylindrical and Cartesian co-ordinate systems respectively. The field component along $\hat{\psi}$ is then $E_{\perp}$, while the component along $\hat{y}$ is $E_{\parallel}$.

An Expression for Dipole Polarisability

In order to solve Equation 3.27, an expression for the polarisability of a line dipole is needed. Figure 3.4 describes the considered geometry, where a single infinite cylinder, located at the origin, is normally illuminated by a plane wave, $\vec{E}^{inc}$. The resulting scattered field is observed in the direction of $\vec{E}^{scat}$, at an observation point $\vec{r} = (\rho, \psi, y)$, Since the cylinder is at the origin, $\rho = |\vec{r}|^2$.

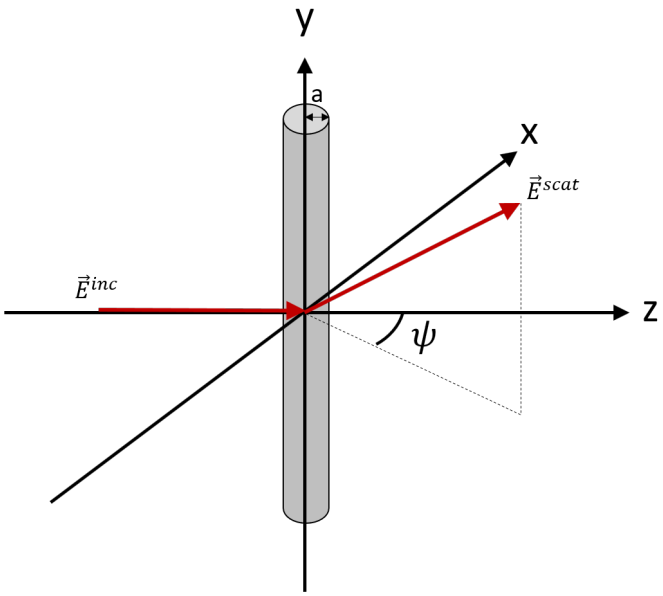

Figure 3.4: Illustration of an infinite cylinder of radius a that is illuminated by $\vec{E}^{inc}$, with the scattered field observed in the direction of $\vec{E}^{scat}$.

Given the geometrical anisotropy of the scatterer, the polarisability, $\boldsymbol{\alpha}$, is generally a tensor that can be written as

$$\boldsymbol{\alpha} = \begin{bmatrix} \alpha_{xx} & 0 & 0 \\ 0 & \alpha_{yy} & 0 \\ 0 & 0 & \alpha_{zz} \end{bmatrix} . \tag{3.29}$$

In addition, due to symmetry, $\alpha_{xx} = \alpha_{zz}$. To obtain an expression for the polaris-

ability, the far-field radiation by a single line dipole is first considered. There exists a known expression for the far-field scattered fields from a single infinite cylinder [124], which can be written, for an arbitrary cylinder radius, a, as

$$\begin{aligned}\vec{E}_{\parallel}^{scat}(\vec{r}) &= E_{\parallel}^{scat}(\vec{r})\ \hat{y} = \exp\left(i\frac{3\pi}{4}\right)\sqrt{\frac{2}{\pi k\rho}}\exp\left(ik\rho\right)T_1(\psi)\ E_{\parallel}^{inc}\ \hat{y} \\ \vec{E}_{\perp}^{scat}(\vec{r}) &= E_{\perp}^{scat}(\vec{r})\ \hat{\psi} = \exp\left(i\frac{3\pi}{4}\right)\sqrt{\frac{2}{\pi k\rho}}\exp\left(ik\rho\right)T_2(\psi)\ E_{\perp}^{inc}\ \hat{\psi}\ ,\end{aligned} \tag{3.30}$$

where $\vec{E}_{\parallel}^{scat}$ is the scattered field related to an incident plane wave polarised parallel to the cylinder axis, $\vec{E}_{\parallel}^{inc}$, while $\vec{E}_{\perp}^{scat}$ is defined similarly. In addition, $\hat{y}$ and $\hat{\psi}$ are the unit vectors that were previously defined in Equation 3.28. For light that is normally incident on the cylinder axis, no polarisation mixing occurs, such that incident fields parallel to the cylinder axis give rise to scattered fields that remain parallel to the cylinder axis, while incident fields perpendicular to the cylinder axis result in scattered fields that are also perpendicular to the cylinder axis [124]. The coefficients, $T_1(\psi)$ and $T_2(\psi)$, in Equation 3.30 can be expressed as

$$\begin{aligned}T_1(\psi) &= b_0 + 2\sum_{n=1}^{\infty} b_n\cos\left(n\psi\right) \\ T_2(\psi) &= a_0 + 2\sum_{n=1}^{\infty} a_n\cos\left(n\psi\right)\ ,\end{aligned} \tag{3.31}$$

such that a_n and b_n are the Mie coefficients that are defined as

$$\begin{aligned}a_n &= \frac{mJ_n^{'}(x)\,J_n(mx) - J_n(x)\,J_n^{'}(mx)}{mJ_n(mx)\,H_n^{'}(x) - J_n^{'}(mx)\,H_n(x)} \\ b_n &= \frac{J_n(mx)\,J_n^{'}(x) - mJ_n^{'}(mx)\,J_n(x)}{J_n(mx)\,H_n^{'}(x) - mJ_n^{'}(mx)\,H_n(x)}\ ,\end{aligned} \tag{3.32}$$

where primes denote derivatives with respect to the argument, $x = ka$ and $m = \frac{n_{cyl}}{n}$ is the refractive index of the cylinder relative to that of the background. In Equation 3.32, J_n denotes the n^{th} order Bessel function of the first kind.

Using Equations 3.22 to 3.25, for a field that is normally incident and polarised

parallel to the cylinder axis, i.e.

$$\vec{E}_{\parallel}^{inc} = \begin{bmatrix} 0 \\ E_y \\ 0 \end{bmatrix} , \tag{3.33}$$

the resulting scattered field at a point, $\vec{r}$, in the far-field can be shown to be

$$\begin{aligned} \vec{E}^{scat}(\vec{r}) &= \frac{i}{4}\omega^2\mu_o H_0 \alpha_{yy} E_y \ \hat{y} \\ &\approx -\exp\left(i\frac{3\pi}{4}\right)\sqrt{\frac{2}{\pi k\rho}}\exp(ik\rho)\left[\left(\frac{i}{4}\right)\omega^2\mu_o\alpha_{yy}\right] E_y \ \hat{y} \ , \end{aligned} \tag{3.34}$$

Thus, a field with an incident polarisation that is parallel to the cylinder axis results in a scattered field with the same polarisation, in agreement with Equation 3.30. Comparing Equation 3.34 and 3.30, it can be seen that α_{yy} can be computed as

$$\alpha_{yy} = i\frac{4}{\omega^2\mu_o}T_1(\psi) \ . \tag{3.35}$$

The derivation for α_{xx}, and thus also α_{zz}, is also conducted in a similar manner. For an incident field that is polarised perpendicularly to the cylinder axis, i.e.

$$\vec{E}_{\perp}^{inc} = \begin{bmatrix} E_x \\ 0 \\ 0 \end{bmatrix} , \tag{3.36}$$

the resulting scattered field can be calculated from Equations 3.22 to 3.25 to be

$$\vec{E}^{scat}(\vec{r}) = \frac{i}{4}\omega^2\mu_o\alpha_{xx}E_x \begin{bmatrix} c_1 H_0 + c_2 H_1 \\ 0 \\ c_3\left(2H_1 - k\rho H_0\right) \end{bmatrix} , \tag{3.37}$$

where $c_1 = \cos^2\psi$, $c_2 = -\frac{\cos(2\psi)}{k\rho}$ and $c_3 = \frac{\sin(2\psi)}{2k\rho}$. In order to have a representation of the field in terms of its $E_\perp$ and $E_\parallel$ components, a co-ordinate transformation is needed to convert Equation 3.37 from the Cartesian to cylindrical co-ordinates. The transformation matrix has been defined previously in Equation 3.28. Under this transformation, it can be shown that in the far-field, Equation 3.37 reduces to

the form

$$\begin{aligned}\vec{E}^{scat}(\vec{r}) &= \frac{i}{4}\omega^2\mu_o\alpha_{xx}E_x\begin{bmatrix}0\\H_0\cos\psi\\0\end{bmatrix}\\ &= \frac{i}{4}\omega^2\mu_o\cos\psi H_0\alpha_{xx}E_x\ \hat{\psi}\\ &\approx -\exp\left(i\frac{3\pi}{4}\right)\sqrt{\frac{2}{\pi k\rho}}\exp(ik\rho)\left[\omega^2\mu_o\cos\psi\alpha_{xx}\right]E_x\ \hat{\psi}\ .\end{aligned} \tag{3.38}$$

Since $\hat{\psi}$ corresponds to the direction of the perpendicular component of the field, it can be seen that an incident polarisation that is perpendicular to the cylinder axis results in a scattered field with the same polarisation, in agreement with Equation 3.30. A comparison of Equation 3.38 and 3.30 shows that α_{xx} and α_{zz} have the form

$$\alpha_{xx} = \alpha_{zz} = i\frac{4}{\omega^2\mu_o}T_2(\psi)\frac{1}{\cos\psi}\ . \tag{3.39}$$

In the small-particle limit, T_1 and T_2 can be expressed as [124]

$$T_1 = b_0,\ T_2 = 2a_1\cos\psi\ . \tag{3.40}$$

Substituting Equation 3.40 in Equations 3.35 and 3.39, the polarisability for a line dipole is hence given by

$$\begin{aligned}\alpha_{xx} = \alpha_{zz} &= i\frac{8}{\omega^2\mu_o}a_1\\ \alpha_{yy} &= i\frac{4}{\omega^2\mu_o}b_0\ .\end{aligned} \tag{3.41}$$

Computation of the Mueller Matrix

The Mueller matrix of the scattering medium at the n^{th} output pixel from an incident field at the m^{th} input pixel, can be obtained by first computing the corresponding Jones matrix, which is defined as

$$\mathbf{T}_{nm}^{SM} = \begin{bmatrix}T_{nm,00} & T_{nm,01}\\ T_{nm,10} & T_{nm,11}\end{bmatrix}\ , \tag{3.42}$$

such that

$$\begin{bmatrix} E^{III}_{n,\parallel} \\ E^{III}_{n,\perp} \end{bmatrix} = \begin{bmatrix} T_{nm,00} & T_{nm,01} \\ T_{nm,10} & T_{nm,11} \end{bmatrix} \begin{bmatrix} E^{II}_{m,\parallel} \\ E^{II}_{m,\perp} \end{bmatrix} . \tag{3.43}$$

Through the use of Equation 3.25, the Jones matrix related to each detector pixel can be formed by calculating separately the fields caused by the incident fields, $\vec{E}^{II}_{\parallel} = [E^{II}_{m,\parallel}, 0]^{\top}$ and $\vec{E}^{II}_{\perp} = [0, E^{II}_{m,\perp}]^{\top}$. For each input polarisation state, the resulting field at the detector forms a column in the Jones matrix, as can be seen from Equation 3.43. The Mueller matrix corresponding to each output pixel can then be computed using Equation 2.38.

Form of the Incident Field

In order to simulate a pixel, a spatially confined and physical field is required. The Gaussian beam is an attractive option as there exists a simple analytical form for the field (at least in the paraxial regime), which is advantageous from the point of view of computational efficiency. This is especially important as the field has to be computed not only at the detectors, but also at the position of each randomly positioned line dipole, so the choice of field has a direct impact on the computation time and complexity. Therefore, to simulate an input field of finite transverse extent, a Gaussian beam was used as the incident field. The diameter at the beam waist, $d = 2w_0$, was set to be equal to the pixel size at the input surface of the scattering medium, where w_0 denotes the beam waist radius. Under a paraxial approximation, the scalar Gaussian beam can be described at the transverse position, x and axial position, z, as [161]

$$E_{Gaussian}(x,z) = E_o \frac{w_o}{w(z)} \exp\left(-\frac{x^2}{w^2(z)}\right) \exp\left(\frac{ikr^2}{2R(z)}\right) \exp\left(i\left[kz - \tan^{-1}\left(\frac{z}{z_R}\right)\right]\right) , \tag{3.44}$$

where E_o is the amplitude of the wave, k is the free space wavevector and z_R is the Rayleigh distance. For a fixed axial position z, $w(z)$ and $R(z)$ are the beam radius and wavefront radius of curvature respectively. z_R, $w(z)$ and $R(z)$ can be computed

as

$$\begin{aligned} z_R &= \frac{kw_o^2}{2} \\ w(z) &= w_o\sqrt{1+\left(\frac{z}{z_R}\right)^2} \\ R(z) &= z\left(1+\left(\frac{z}{z_R}\right)^2\right) \ . \end{aligned} \tag{3.45}$$

The vector incident fields used to obtain the Mueller matrices are then

$$\vec{E}_{\parallel}(x,z) = \begin{bmatrix} 0 \\ E_{Gaussian}(x,z) \\ 0 \end{bmatrix}, \vec{E}_{\perp}(x,z) = \begin{bmatrix} E_{Gaussian}(x,z) \\ 0 \\ 0 \end{bmatrix} \ . \tag{3.46}$$

Equations 3.44 and 3.46 hold only under the paraxial approximation (i.e. $k_x \ll k$). Smaller beam waists have larger divergence, and a full vectorial description would be required. In view of computational efficiency, the analytical form of Equation 3.44 was used, as the field has to be calculated at the point of each dipole and detector. The half-angle divergence of the beam, $\Delta\theta$, for a given beam waist can be calculated as

$$\Delta\theta = \frac{\lambda_0}{\pi n w_o} \ , \tag{3.47}$$

where n is the refractive index of the medium of propagation. Using Equation 3.47 and the simulation parameters described in Section 3.2.1, the divergence angles corresponding to the beam waists used in this study were calculated and are shown in Table 3.2 below. It can be seen that the largest beam divergence is 0.004 radians. Given the small divergence angle, the paraxial approximation can be made, thus corroborating the use of Equations 3.44 and 3.46.

$d = 2w_o$ / μm	100	150	200	250	300
$\Delta\theta$ / rad	0.004	0.003	0.002	0.002	0.001

Table 3.2: Beam divergences computed using Equation 3.47 for the beam waists used in this study.

3.2.2 Spatial Invariance of the Scattering Medium's Mueller Matrix

In Section 3.1.3, it was proposed that for a large enough pixel size, the Mueller matrix of the scattering medium, $\mathbf{M}^{SM}$, is independent of the specific instance of disorder. For such pixel sizes, each pixel consists of contributions from many different instance of disorder, such that the measured Mueller matrix from each pixel is inherently an ensemble average. This, in turn, implies that $\mathbf{M}^{SM}$ is also pixel-independent. Here, this claim is investigated using numerical simulations based on the 2D coupled line dipole formalism introduced in Section 3.2.1.

Simulation Results

The Mueller matrix for each output pixel was computed for 200 random configurations of cylinders, which were simulated according to the simulation parameters in Table 3.1. A single input pixel was used, with varying pixel widths of $2w_o = \{100, 150, 200, 250, 300\}\mu$m. For each thickness, pixel size and instance of disorder, the Mueller matrix, as would have been measured by a photodiode, was then computed as the intensity sum over all output pixels. The change in the Mueller matrix over different instances of disorder was evaluated for each individual element of the Mueller matrix, by computation of the coefficient of variation (CV). For the $(i, j)^{th}$ Mueller matrix element, the CV is defined as

$$\mathrm{CV}_{ij} = \frac{\sigma_{ij}}{\langle M_{ij} \rangle} \tag{3.48}$$

where σ_{ij} and $\langle M_{ij} \rangle$ denote the standard deviation and mean of the $(i, j)^{th}$ Mueller matrix element respectively. An average CV across all matrix elements was also computed by taking the square root of the sum of squares of the CV for each Mueller matrix element. This result is shown in Figure 3.5, while Figure 3.6 shows the result for each Mueller matrix element as a function of pixel size. The empty elements in Figure 3.6 have a mean value of zero.

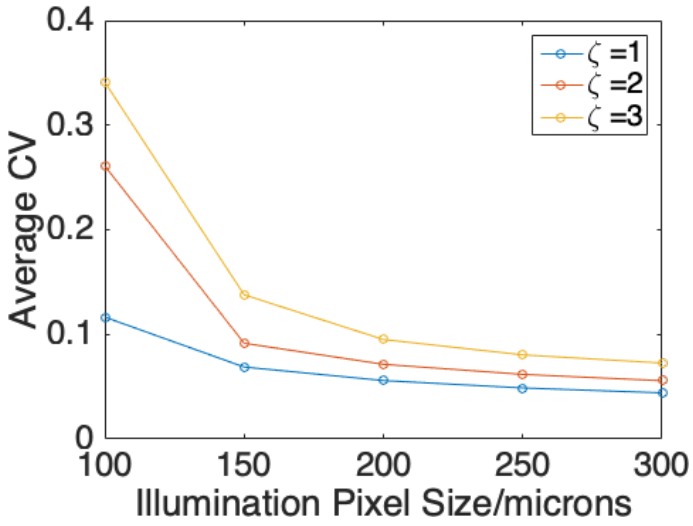

Figure 3.5: Average coefficient of variation across all Mueller matrix elements as a function of illumination pixel size for different medium thicknesses, ζ, calculated using 200 iterations.

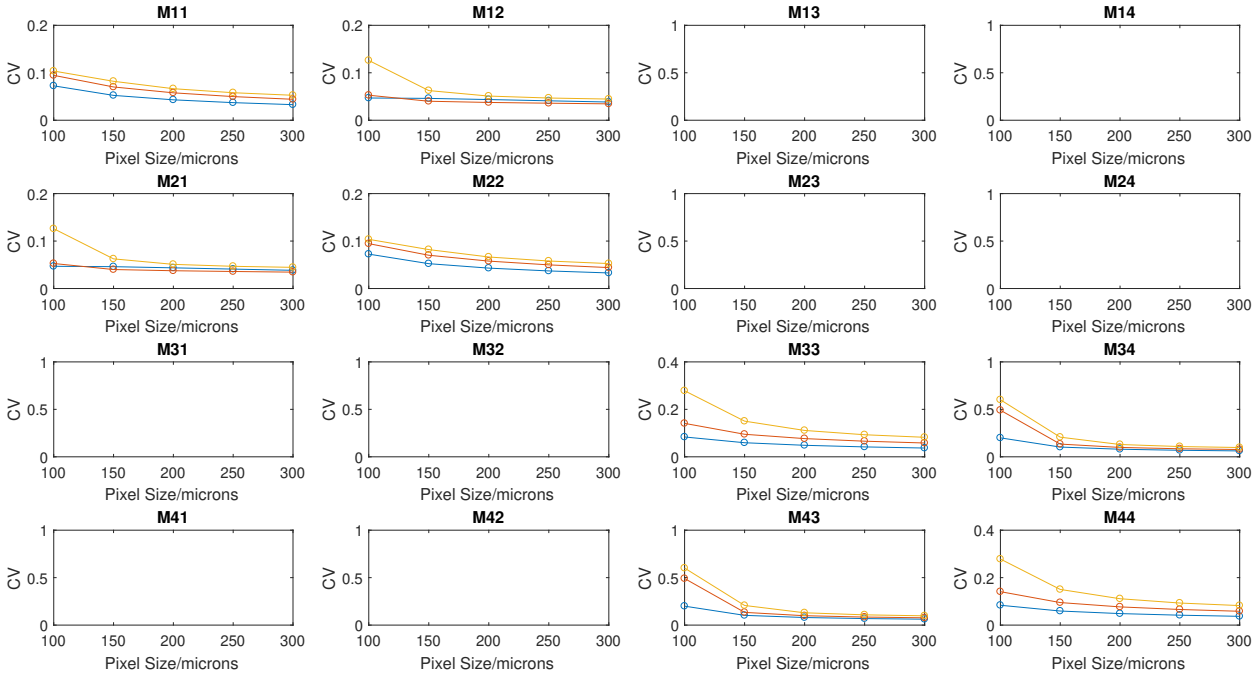

Figure 3.6: Coefficient of variation as a function of illumination pixel size for different medium thicknesses, ζ, calculated using 200 iterations. The empty elements have mean values of zero. Plot legend follows that of Figure 3.5.

Figure 3.6 shows that the coefficient of variance decreases non-linearly with pixel size, tailing off asymptotically at about 200 microns. Figure 3.5 demonstrates the

same trend, and shows that at the largest pixel size tested (300 microns), the average CV was between 0.05 to 0.1 across the three values of ζ. Therefore, as the pixel size increased, the Mueller matrix became less dependent on the instance of disorder. In addition, it was observed that thicker scattering media required larger pixel sizes to arrive at the same CV. In the next part of this section, the origin of this decrease is discussed.

One might be tempted to interpret this data quantitatively. For example, if a pixel size of 300 microns was used, an average variation of 5 to 10% can be expected in the scattering medium's Mueller matrix elements for the three thicknesses considered. It should be noted, however, that considering the differences between the scattering media used in the simulations and the experiments described in Chapter 4, these quantitative values obtained cannot be directly translated to the experimental results. This is discussed further in the final section of this chapter. Nevertheless, the trends observed in the simulation are still representative of what should be expected in the experiments.

Further Insights

A mathematical model is now proposed to provide further insight into the simulation results obtained. To begin, an expression for the measured Mueller matrix from a single input pixel and a *single* instance of disorder is first derived. The following analysis is generalised to a 3D geometry. Nevertheless, the conclusions also hold for the reduced 2D geometry of the simulation, where the scattering medium is taken to extend infinitely in the third dimension (i.e. y).

The electric fields at the front and back surfaces of the scattering medium, across all input and output pixels, are related by the vector transmission matrix according to Equations 3.9 and 3.10. To compute the outgoing fields from a single input pixel, the integral form of Equation 3.9 is used. This can be written as

$$\vec{E}^{out}(\vec{r}_2) = \int_{-\infty}^{\infty} \mathbf{T}(\vec{r}_1, \vec{r}_2)\vec{E}^{in}(\vec{r}_1)\, d\vec{r}_1 \ , \tag{3.49}$$

where $\vec{r}_1$ and $\vec{r}_2$ are the *transverse* spatial co-ordinates of the input and output surfaces of the scattering medium respectively, and $\vec{E}^{in}(\vec{r}_1)$ describes the incident field from the single input pixel being considered. As before, $\mathbf{T}(\vec{r}_1, \vec{r}_2)$ is a 2×2 matrix relating the field from a point source input at $\vec{r}_1$ to the transmitted field at the point $\vec{r}_2$, with the subscript "SM" suppressed for brevity. It should be noted that the two-dimensional transverse co-ordinates, $\vec{r}_1$ and $\vec{r}_2$, should not be confused with the three-dimensional vectors, $\vec{r}$ and $\vec{r}^{\,'}$, from earlier in this section. It follows that the coherency vector, $\vec{C}^{out}(\vec{r}_2)$, for each output point is

$$\begin{aligned} \vec{C}^{out}(\vec{r}_2) &= \langle \vec{E}^{out}(\vec{r}_2) \otimes \vec{E}^{out,*}(\vec{r}_2) \rangle_t \\ &= \iint_{-\infty}^{\infty} \left(\mathbf{T}(\vec{r}_1, \vec{r}_2) \otimes \mathbf{T}^*(\vec{r}_1^{\,'}, \vec{r}_2) \right) \left(\vec{E}^{in}(\vec{r}_1) \otimes \vec{E}^{in,*}(\vec{r}_1^{\,'}) \right) d\vec{r}_1 \, d\vec{r}_1^{\,'} \ , \end{aligned} \tag{3.50}$$

where the assumption of a static scattering medium illuminated by a fully coherent light source has been made. If, as in an experiment, the polarisation of the incident field is constant across the extent of the pixel, then

$$\begin{aligned} \vec{E}^{in}(\vec{r}_1) \otimes \vec{E}^{in,*}(\vec{r}_1^{\,'}) &= \sqrt{I(\vec{r}_1)} \ \vec{E}_0^{in} \otimes \sqrt{I(\vec{r}_1^{\,'})} \ \vec{E}_0^{in} \\ &= h\left(\vec{r}_1, \vec{r}_1^{\,'}\right) \left(\vec{E}_0^{in} \otimes \vec{E}_0^{in,*} \right) \ , \end{aligned} \tag{3.51}$$

where $\vec{E}_0^{in}$ is the Jones vector of the incident field that has been normalised to unit intensity, $I(\vec{r}_1) = \left| \vec{E}^{in}(\vec{r}_1) \right|^2$ is the intensity at $\vec{r}_1$, and $h(\vec{r}_1, \vec{r}_1^{\,'}) = \sqrt{I(\vec{r}_1) I(\vec{r}_1^{\,'})}$ accounts for a spatial variation of the incident intensity. With Equation 3.51, Equation 3.50 becomes

$$\begin{aligned} \vec{C}^{out}(\vec{r}_2) &= \left(\iint_{-\infty}^{\infty} \left(\mathbf{T}(\vec{r}_1, \vec{r}_2) \otimes \mathbf{T}^*(\vec{r}_1^{\,'}, \vec{r}_2) \right) h(\vec{r}_1, \vec{r}_1^{\,'}) \, d\vec{r}_1 \, d\vec{r}_1^{\,'} \right) \left(\vec{E}^{in} \otimes \vec{E}^{in,*} \right) \\ &= \left(\iint_{-\infty}^{\infty} \left(\mathbf{T}(\vec{r}_1, \vec{r}_2) \otimes \mathbf{T}^*(\vec{r}_1^{\,'}, \vec{r}_2) \right) h(\vec{r}_1, \vec{r}_1^{\,'}) \, d\vec{r}_1 \, d\vec{r}_1^{\,'} \right) \ \vec{C}^{in} \ . \end{aligned} \tag{3.52}$$

Converting from coherency to Stokes vectors using Equation 2.32,

$$\begin{aligned} \vec{S}^{out}(\vec{r}_2) &= \mathbf{\Gamma} \left(\iint_{-\infty}^{\infty} \left(\mathbf{T}(\vec{r}_1, \vec{r}_2) \otimes \mathbf{T}^*(\vec{r}_1^{\,'}, \vec{r}_2) \right) h(\vec{r}_1, \vec{r}_1^{\,'}) \, d\vec{r}_1 \, d\vec{r}_1^{\,'} \right) \mathbf{\Gamma}^{-1} \vec{S}^{in} \\ &= \mathbf{m}(\vec{r}_2) \vec{S}^{in} \ . \end{aligned} \tag{3.53}$$

Thus, the Mueller matrix for each output position, $\mathbf{m}(\vec{r}_2)$, can be written as

$$\mathbf{m}(\vec{r}_2) = \mathbf{\Gamma} \left(\iint_{-\infty}^{\infty} \Big(\mathbf{T}(\vec{r}_1, \vec{r}_2) \otimes \mathbf{T}^*(\vec{r}_1^{'}, \vec{r}_2) \Big) \, h(\vec{r}_1, \vec{r}_1^{'}) \, d\vec{r}_1 \, d\vec{r}_1^{'} \right) \mathbf{\Gamma}^{-1} \ . \tag{3.54}$$

The measured Mueller matrix is an integration over all output points. Therefore, for a single input pixel, the measured Mueller matrix is given by

$$\begin{aligned} \mathbf{M}^{SM} &= \int_S \mathbf{m}(\vec{r}_2) \, d\vec{r}_2 \\ &= \mathbf{\Gamma} \left(\int_S \int_{-\infty}^{\infty} \int_{-\infty}^{\infty} \Big(\mathbf{T}(\vec{r}_1, \vec{r}_2) \otimes \mathbf{T}^*(\vec{r}_1^{'}, \vec{r}_2) \Big) \, h(\vec{r}_1, \vec{r}_1^{'}) \, d\vec{r}_1 \, d\vec{r}_1^{'} \, d\vec{r}_2 \right) \mathbf{\Gamma}^{-1} \ , \end{aligned} \tag{3.55}$$

where S is the integration area on the output surface of the scattering medium. If $\mathbf{m}(\vec{r}_2)$ was a statistically stationary random variable, that is, $\langle \mathbf{m}(\vec{r}_2) \rangle = \langle \mathbf{m}(\vec{r}_2 - \Delta r) \rangle = \langle \mathbf{m} \rangle$, then $\mathbf{M}^{SM}$, for a sufficiently large S, can be seen to approximate $\langle \mathbf{m} \rangle$ under an ergodic assumption. Here, $\langle ... \rangle$ denotes an ensemble average, or in other words, an average over instances of disorder. In such a situation, $\mathbf{M}^{SM}$ is thus independent of the instance of disorder, and in turn, the input pixel position. This investigation, therefore, turns to the stationarity of $\mathbf{m}(\vec{r}_2)$.

Taking the ensemble average of Equation 3.54, $\langle \mathbf{m}(\vec{r}_2) \rangle$ is given by

$$\langle \mathbf{m}(\vec{r}_2) \rangle = \mathbf{\Gamma} \left(\iint_{-\infty}^{\infty} \Pi(\vec{r}_1) \Pi(\vec{r}_1^{'}) \langle \mathbf{T}(\vec{r}_1, \vec{r}_2) \otimes \mathbf{T}^*(\vec{r}_1^{'}, \vec{r}_2) \rangle \, d\vec{r}_1 \, d\vec{r}_1^{'} \right) \mathbf{\Gamma}^{-1} \ . \tag{3.56}$$

where $\Pi(\vec{r}_1) = \sqrt{I(\vec{r}_1)}$. Furthermore, assuming that $\mathbf{T}$ is a statistically stationary random variable, such that $\langle \mathbf{T}(\vec{r}_1, \vec{r}_2) \rangle = \langle \mathbf{T}(\vec{r}_1 - \Delta r, \vec{r}_2 - \Delta r) \rangle = \langle \mathbf{T}(\vec{r}_1 - \vec{r}_2, 0) \rangle$, Equation 3.56 can be written as

$$\langle \mathbf{m}(\vec{r}_2) \rangle = \mathbf{\Gamma} \left(\iint_{-\infty}^{\infty} \Pi(\vec{r}_1) \Pi(\vec{r}_1^{'}) \langle \mathbf{T}(\vec{r}_1 - \vec{r}_2, 0) \otimes \mathbf{T}^*(\vec{r}_1^{'} - \vec{r}_2, 0) \rangle \, d\vec{r}_1 \, d\vec{r}_1^{'} \right) \mathbf{\Gamma}^{-1} \ . \tag{3.57}$$

In an extreme scenario, if the incident illumination was a plane wave (i.e. an infinitely large pixel), then Π would just be a constant function, and Equation 3.56

would be reduced to

$$\langle \mathbf{m}(\vec{r}_2) \rangle = \mathbf{\Gamma} \left(\iint_{-\infty}^{\infty} \langle \mathbf{T}(\vec{r}_1 - \vec{r}_2, 0) \otimes \mathbf{T}^*(\vec{r}_1^{'} - \vec{r}_2, 0) \rangle \, d\vec{r}_1 \, d\vec{r}_1^{'} \right) \mathbf{\Gamma}^{-1} \ , \tag{3.58}$$

which is independent of $\vec{r}_2$. In this case, $\mathbf{m}(\vec{r}_2)$ is stationary and $\mathbf{M}^{SM}$ is independent of the instance of disorder and input pixel location. At the other extreme, if the illumination was a point source at $\vec{r}_o$ (i.e. an infinitely small pixel), Π would be a delta function, such that Equation 3.57 becomes

$$\begin{aligned} \langle \mathbf{m}(\vec{r}_2) \rangle &= \mathbf{\Gamma} \left(\iint_{-\infty}^{\infty} \delta(\vec{r}_1 - \vec{r}_o) \delta(\vec{r}_1^{'} - \vec{r}_o) \langle \mathbf{T}(\vec{r}_1 - \vec{r}_2, 0) \otimes \mathbf{T}^*(\vec{r}_1^{'} - \vec{r}_2, 0) \rangle \, d\vec{r}_1 \, d\vec{r}_1^{'} \right) \mathbf{\Gamma}^{-1} \\ &= \mathbf{\Gamma} \ \langle \mathbf{T}(\vec{r}_o - \vec{r}_2, 0) \otimes \mathbf{T}^*(\vec{r}_o - \vec{r}_2, 0) \rangle \ \mathbf{\Gamma}^{-1} \ , \end{aligned} \tag{3.59}$$

which is not independent of $\vec{r}_2$. From these observations, a natural question then arises - is there a pixel size above which $\mathbf{m}(\vec{r}_2)$ is, or can at least be approximated to be, stationary?

Via a change of variables, Equation 3.57 can be re-written as

$$\begin{aligned} \langle \mathbf{m}(\vec{r}_2) \rangle &= \mathbf{\Gamma} \left(\iint_{-\infty}^{\infty} \Pi(\vec{r}_1) \Pi(\vec{r}_1^{'}) \langle \mathbf{T}(\vec{r}_1 - \vec{r}_2, 0) \otimes \mathbf{T}^*(\vec{r}_1^{'} - \vec{r}_2, 0) \rangle \, d\vec{r}_1 \, d\vec{r}_1^{'} \right) \mathbf{\Gamma}^{-1} \\ &= \mathbf{\Gamma} \left(\iint_{-\infty}^{\infty} \Pi(\vec{r}_1) \Pi(\vec{r}_1^{'}) \mathbf{C}(\vec{r}_1 - \vec{r}_2, \vec{r}_1^{'} - \vec{r}_2) \, d\vec{r}_1 \, d\vec{r}_1^{'} \right) \mathbf{\Gamma}^{-1} \\ &= \mathbf{\Gamma} \left(\iint_{-\infty}^{\infty} \Pi(\vec{\rho}_{12} + \vec{r}_2) \Pi(\vec{\rho}_{12}^{'} + \vec{r}_2) \mathbf{C}(\vec{\rho}_{12}, \vec{\rho}_{12}^{'}) \, d\vec{\rho}_{12} \, d\vec{\rho}_{12}^{'} \right) \mathbf{\Gamma}^{-1} \\ &= \mathbf{\Gamma} \left(\int_{-\infty}^{\infty} \Pi(\vec{\rho}_{12}^{'} + \vec{r}_2) \left[\int_{-\infty}^{\infty} \Pi(\vec{\rho}_{12} + \vec{r}_2) \mathbf{C}(\vec{\rho}_{12}, \vec{\rho}_{12}^{'}) \, d\vec{\rho}_{12} \right] \, d\vec{\rho}_{12}^{'} \right) \mathbf{\Gamma}^{-1} \ , \end{aligned} \tag{3.60}$$

where $\vec{\rho}_{12} = \vec{r}_1 - \vec{r}_2$ and $\vec{\rho}_{12}^{'} = \vec{r}_1^{'} - \vec{r}_2$. In addition, $\mathbf{C}(\vec{r}_1 - \vec{r}_2, \vec{r}_1^{'} - \vec{r}_2) = \langle \mathbf{T}(\vec{r}_1 - \vec{r}_2, 0) \otimes \mathbf{T}^*(\vec{r}_1^{'} - \vec{r}_2, 0) \rangle$ can be interpreted as the correlation between the speckle field at a fixed output point, $\vec{r}_2$, from two input points, $\vec{r}_1$ and $\vec{r}_1^{'}$. Equation 3.60 can be seen to be a double cross-correlation integral between $\mathbf{C}$ and Π.

To gain further intuition about the shape of $\langle \mathbf{m}(\vec{r}_2) \rangle$, the integral

$$f(x_2) = \int_{-\infty}^{\infty} \Pi(\Delta_x + x_2) C_{ij}(\Delta_x, 0)\, d\Delta_x \ , \tag{3.61}$$

was plotted. This 1D cross-correlation function can be seen to be a simplified version of Equation 3.60, relating to the cross-correlation integral enclosed within the square brackets in the final expression of Equation 3.60 in the plane $(y_1 - y_2) = 0$, such that $\vec{\rho}_{12} = [x_1 - x_2, y_1 - y_2]^\top = [x_1 - x_2, 0]^\top = [\Delta_x, 0]^\top$. In addition, Equation 3.61 corresponds to taking the integral in the square brackets of Equation 3.60 at $\vec{\rho}'_{12} = [x_1^{'} - x_2, y_1^{'} - y_2]^\top = \vec{0}$. Furthermore, as $\mathbf{C}$ is a matrix, the result of the integral is also a matrix, and Equation 3.61 can be understood as plotting only one of the elements of that matrix.

The correlation function C_{ij} was assumed to be a Gaussian with a standard deviation of σ, corresponding to the decay of the correlation function as Δ_x departs from $\Delta_x^{'} = x_1^{'} - x_2 = 0$. On the other hand, the pixel was assumed to be uniformly illuminated, such that $\Pi(\Delta_x)$ is given by

$$\Pi(\Delta_x) = \begin{cases} 1 & (\Delta_x + x_2) \in \Omega \\ 0 & \text{otherwise,} \end{cases} \tag{3.62}$$

where Ω denotes the pixel area. The resulting cross-correlation is shown in Figure 3.7.

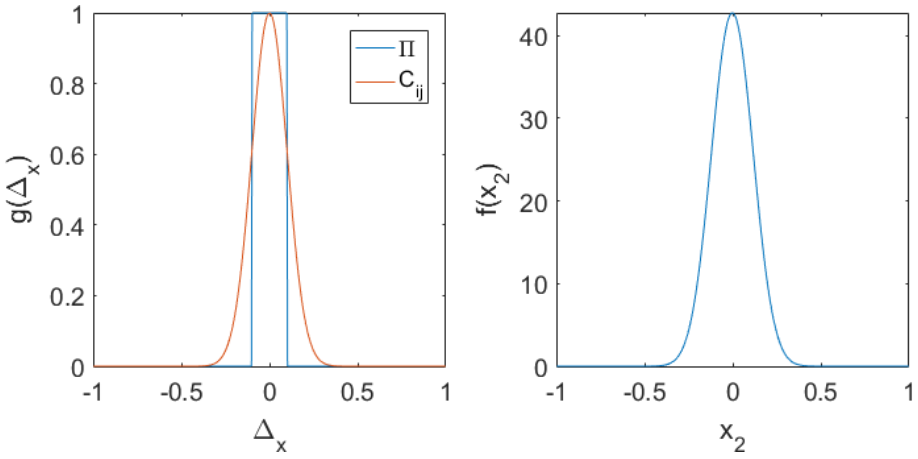

(a) Width of $\Omega = 0.1$, $\sigma = 0.1$

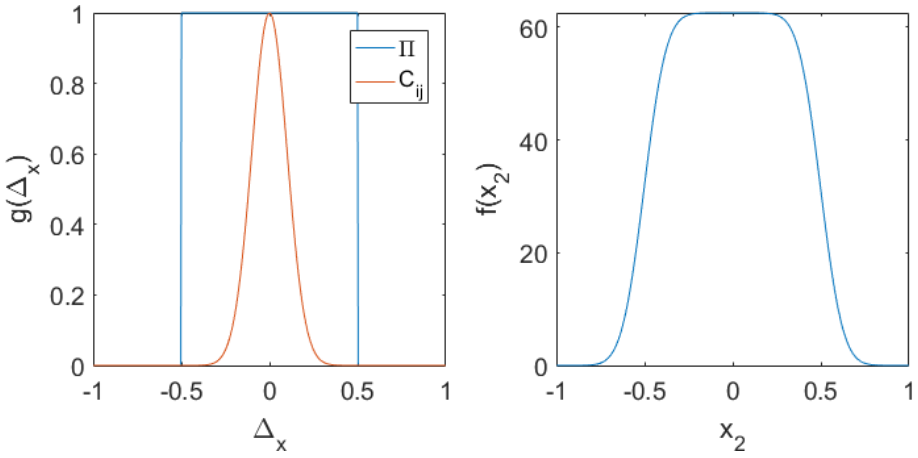

(b) Width of $\Omega = 0.5$, $\sigma = 0.1$

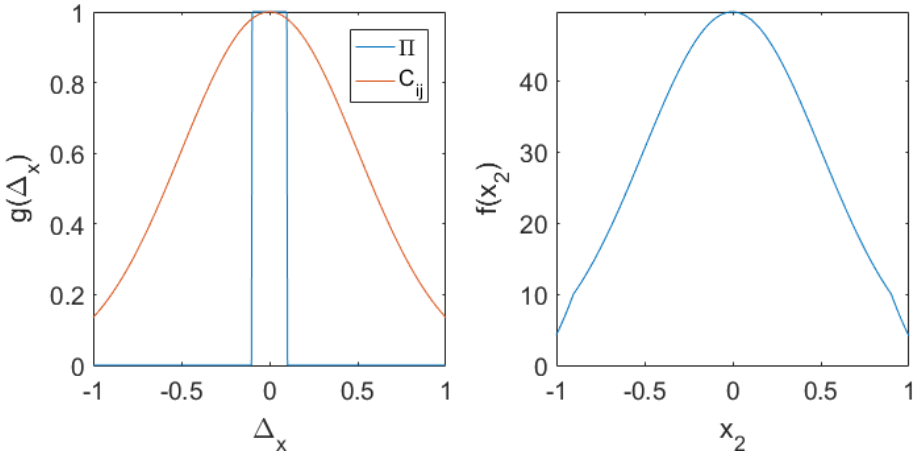

(c) Width of $\Omega = 0.1$, $\sigma = 0.5$

Figure 3.7: Illustration showing the shape of $f(x_2)$ for different widths (in arbitrary units) of Π and C_{ij}. Left: Original functions, Right: Cross-correlation result.

From Figure 3.7, it can be seen that the wider function dominates the shape of the cross-correlation. The 1D plots shown in Figure 3.7 can be generalised to Equation

3.60, so that the same behaviour can be expected from the described double cross-correlation. As such, if the width of Π is much larger than the width of each matrix element in $\mathbf{C}$, it can be expected that the shape of $\langle \mathbf{m}(\vec{r}_2) \rangle$ is similar to the shape of Π. In this regime, $\mathbf{C}(\vec{\rho}_{12}, \vec{\rho}_{12}^{'})$ can be approximated as a delta function, so that Equation 3.60 becomes

$$\begin{aligned} \langle \mathbf{m}(\vec{r}_2) \rangle &\approx \mathbf{\Gamma} \iint_{-\infty}^{\infty} \Pi(\vec{\rho}_{12} + \vec{r}_2)\Pi(\vec{\rho}_{12}^{'} + \vec{r}_2)\delta(\vec{\rho}_{12}^{'} - \vec{\rho}_{12})\delta(\vec{\rho}_{12})\mathbf{C}_o \, d\vec{\rho}_{12} \, d\vec{\rho}_{12}^{'} \mathbf{\Gamma}^{-1} \\ &= \mathbf{\Gamma} \left|\Pi(\vec{r}_2)\right|^2 \mathbf{C}_o \mathbf{\Gamma}^{-1} \ , \end{aligned} \tag{3.63}$$

where $\mathbf{C}_o$ is a matrix without any dependence on $\vec{r}_2$. From this equation, it can be seen that when the width of Π is much larger than the width of $\mathbf{C}$, the dependence of $\langle \mathbf{m}(\vec{r}_2) \rangle$ on $\vec{r}_2$ comes wholly from the scalar amplitude variation of the illumination. This implies that

$$\langle \mathbf{m}(\vec{r}_2) \rangle = b_o(\vec{r}_2, \vec{r}_2 + \Delta r) \langle \mathbf{m}(\vec{r}_2 + \Delta r) \rangle = b_o(\vec{r}_2, 0) \langle \mathbf{m}(\vec{0}) \rangle = b_o(\vec{r}_2) \langle \mathbf{m} \rangle \tag{3.64}$$

where b_o is a position-dependent scalar constant. The scalar constant only affects the unpolarised intensity transmission, while polarimetric properties, such as diattenuation, retardance and depolarisation, are derived from the Mueller matrix $\langle \mathbf{m} \rangle$. As such, $\langle \mathbf{m}(\vec{r}_2) \rangle$ can be considered to be stationary in terms of its polarisation properties. Consequently, it can be deduced that the use of Equation 3.55 gives an estimate of the $\langle \mathbf{m} \rangle$, but with a scalar proportionality factor depending on the intensity variation of the incident illumination. As a result, for a large enough pixel size, $\mathbf{M}^{SM}$ is independent of instance of disorder and input pixel position.

Factors Affecting the Minimum Pixel Size

But how large does the pixel (i.e. the width of Π) have to be? As discussed, this is governed by the width of $\mathbf{C}$, which is, in turn, dependent on two factors. The first factor is how far apart two input points can be before the individual contributions to the speckle field at the same output point becomes uncorrelated. This distance is denoted as C_{r_1}. If this distance is small with respect to the pixel size, then the approximation $\mathbf{C}(\vec{r}_1 - \vec{r}_2, \vec{r}_1^{'} - \vec{r}_2) \approx \delta(\vec{\rho}_{12}^{'} - \vec{\rho}_{12})\mathbf{C}(\vec{\rho}_{12})$ can be made, such that the

double integral in Equation 3.60 can be written as

$$\begin{aligned}\langle \mathbf{m}(\vec{r}_2)\rangle &\approx \mathbf{\Gamma}\left(\iint_{-\infty}^{\infty}\Pi(\vec{\rho}_{12}+\vec{r}_2)\Pi(\vec{\rho}_{12}^{'}+\vec{r}_2)\delta(\vec{\rho}_{12}^{'}-\vec{\rho}_{12})\mathbf{C}(\vec{\rho}_{12})\,d\vec{\rho}_{12}\,d\vec{\rho}_{12}^{'}\right)\mathbf{\Gamma}^{-1}\\ &=\mathbf{\Gamma}\left(\int_{-\infty}^{\infty}\Pi(\vec{\rho}_{12}+\vec{r}_2)\Pi(\vec{\rho}_{12}+\vec{r}_2)\mathbf{C}(\vec{\rho}_{12})\,d\vec{\rho}_{12}\right)\mathbf{\Gamma}^{-1}\\ &=\int_{-\infty}^{\infty}\Pi(\vec{\rho}_{12}+\vec{r}_2)\Pi(\vec{\rho}_{12}+\vec{r}_2)\mathbf{m}_p(\vec{\rho}_{12})\,d\vec{\rho}_{12}\ ,\end{aligned} \tag{3.65}$$

where

$$\begin{aligned}\mathbf{m}_p(\vec{\rho}_{12}) &= \mathbf{\Gamma}\mathbf{C}(\vec{\rho}_{12})\mathbf{\Gamma}^{-1}\\ &=\mathbf{\Gamma}\langle\mathbf{T}(\vec{r}_1-\vec{r}_2,0)\otimes\mathbf{T}^*(\vec{r}_1-\vec{r}_2,0)\rangle\mathbf{\Gamma}^{-1}\\ &=\mathbf{\Gamma}\langle\mathbf{T}(0,\vec{r}_2-\vec{r}_1)\otimes\mathbf{T}^*(0,\vec{r}_2-\vec{r}_1)\rangle\mathbf{\Gamma}^{-1}\ ,\end{aligned} \tag{3.66}$$

where the equivalence of the second and third expressions comes from the previous assumption made, that $\mathbf{T}$ is a statistically stationary random variable. Comparing the form of $\mathbf{m}_p(\vec{\rho}_{12})$ in Equation 3.66 to Equation 3.59, it can be seen that $\mathbf{m}_p$ can be interpreted as the ensemble averaged Mueller matrix for the output point at $\vec{r}_2-\vec{r}_1$, due to a point source at $\vec{0}$. The $(0,0)$ element of any Mueller matrix is its unpolarised transmittance [139]. As such, for any input point source, the $(0,0)^{th}$ element of $\mathbf{m}_p(\vec{\rho}_{12})$ describes the intensity profile of the diffused spot at the output surface of the scattering medium, which modulates all elements of $\mathbf{m}_p(\vec{\rho}_{12})$. Thus, the second factor affecting the minimum pixel width is the width of the ensemble-averaged intensity profile from an incident point source, denoted as C_{r_2}. If the pixel width is much larger than C_{r_2}, then $\mathbf{m}_p(\vec{\rho}_{12})$ can be approximated as $\mathbf{m}_p(\vec{\rho}_{12})\approx\delta(\vec{\rho}_{12})\mathbf{m}_0$, such that Equation 3.65 can be written as

$$\begin{aligned}\langle \mathbf{m}(\vec{r}_2)\rangle &\approx \int_{-\infty}^{\infty}\Pi(\vec{\rho}_{12}+\vec{r}_2)\Pi(\vec{\rho}_{12}+\vec{r}_2)\delta(\vec{\rho}_{12})\mathbf{m}_0\,d\vec{\rho}_{12}\\ &=|\Pi(\vec{r}_2)|^2\,\mathbf{m}_0\\ &=\mathbf{\Gamma}\,|\Pi(\vec{r}_2)|^2\,\mathbf{C}_0\mathbf{\Gamma}^{-1}\ ,\end{aligned} \tag{3.67}$$

thereby arriving back at Equation 3.63, with $\mathbf{m}_0=\mathbf{\Gamma}\mathbf{C}_0\mathbf{\Gamma}^{-1}$. Thus, for a single instance of disorder, the smallest pixel size required such that the measured Mueller matrix becomes independent of the specific instance of disorder depends on two correlation lengths - the smallest distance between input points such that the speckle at

a given output point becomes uncorrelated and the width of the ensemble-averaged Mueller matrix from a point source. The requirement of a pixel size larger than C_{r_2} may seem overly restrictive, particularly for thick scattering media. Nonetheless, for scattering media that demonstrate a high degree of forward scattering, as in the case of most biological tissues [8], only a small divergence of the scattered beam is expected, so it is possible that a reasonable combination of depth and pixel size can still be achieved. Moreover, as discussed in Section 3.1.3, the minimum pixel size can potentially be reduced further by combining spatial and temporal averaging over different instances of disorder.

The width of C_{r_1} for the scattering media corresponding to the results shown in Figures 3.5 and 3.6 was investigated using the 2D coupled line dipole simulation described in Section 3.2.1. The simulation geometry is summarised in Figure 3.8.

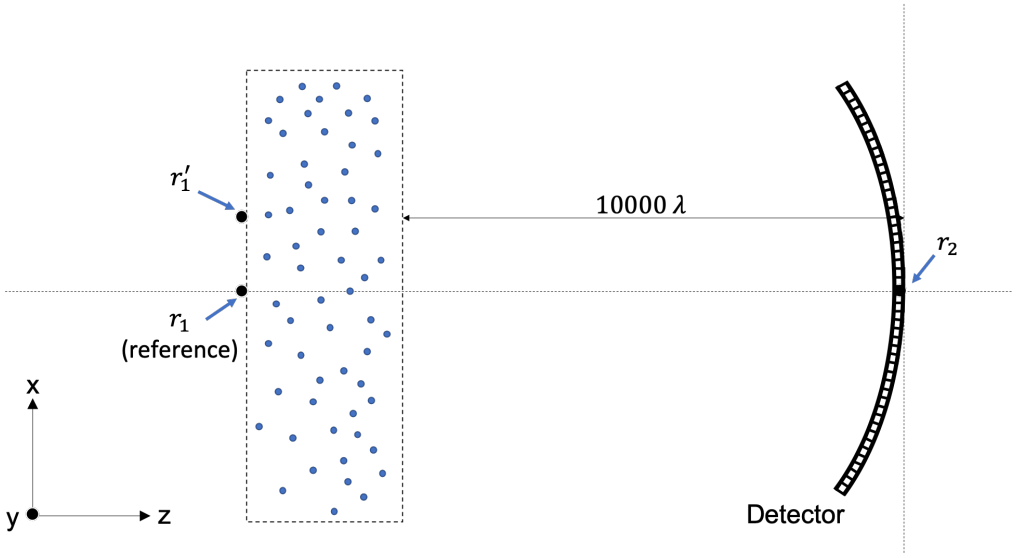

Figure 3.8: Simulation geometry used to investigate the width of C_{r_1}.

In two dimensions, the correlation function, $\mathbf{C}$, can be written as

$$\begin{aligned}\mathbf{C}(\Delta_x, \Delta_x^{'}) &= \langle \mathbf{T}(x_1 - x_2, 0) \otimes \mathbf{T}^*(x_1^{'} - x_2, 0) \rangle \\ &= \langle \mathbf{T}(x_1, x_2) \otimes \mathbf{T}^*(x_1^{'}, x_2) \rangle\end{aligned} \tag{3.68}$$

where $\Delta_x = x_1 - x_2$ and $\Delta_x^{'} = x_1^{'} - x_2$. To compute $\mathbf{C}$, the output far-field speckle was firstly computed as a line dipole was moved transversely across the front

surface of the medium. Two incident polarisations, parallel and perpendicular to the cylinder axis, were simulated by setting the dipole moments to $\vec{p}_{\parallel}^{inc} = [1, 0, 0]^{\top}$ and $\vec{p}_{\perp}^{inc} = [0, 1, 0]^{\top}$ respectively. The Jones matrix was then computed for each input position from the obtained speckle fields, for a fixed output point on axis (i.e. $x_2 = 0$). Then, taking the input point on axis as reference (i.e. $x_1 = 0$), $\mathbf{C}(\Delta_x, \Delta_x^{'})$ was calculated from the elements of the Jones matrices as an average over 250 configurations of cylinders. Figure 3.9 shows the elements of the resulting matrix as a function of the separation between input points, where for each value of ζ, each element has been normalised to the maximum correlation value across all elements.

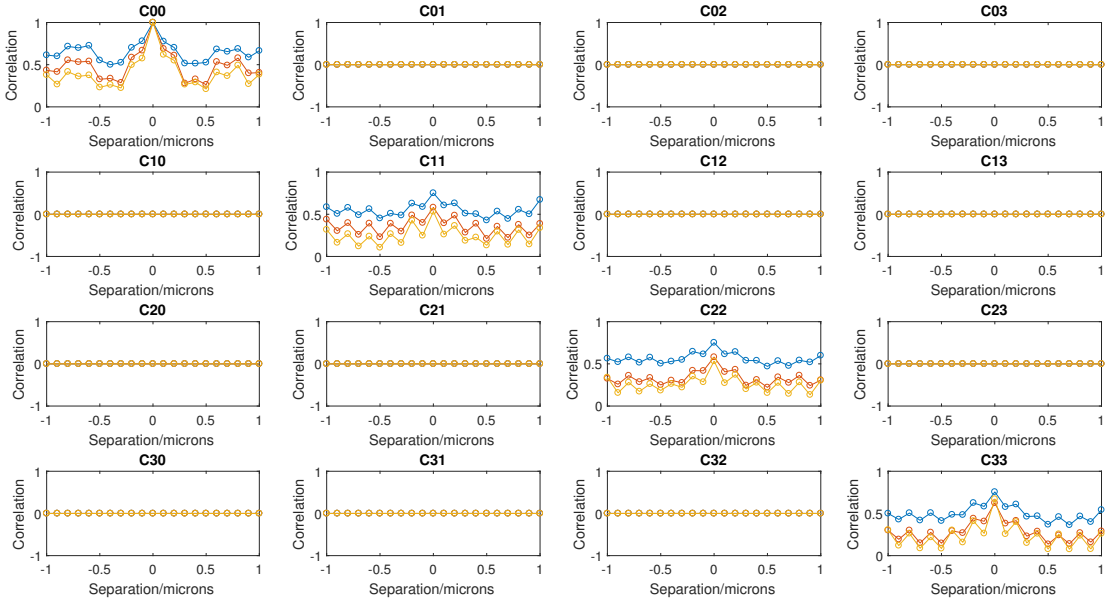

Figure 3.9: $\mathbf{C}(\Delta_x, \Delta_x^{'})$ at a fixed output point ($x_2 = 0$) as a function of separation between input points for $\zeta = 1$ (blue), $\zeta = 2$ (red) and $\zeta = 3$ (yellow).

From this Figure 3.9, it can firstly be seen that some of the elements in $\mathbf{C}(\Delta_x, \Delta_x^{'})$ are zero. This is because, as discussed in Section 3.2.1, when incident light is travelling at normal incidence to the cylinder axis, no cross-polarisation between the field components that are parallel and perpendicular to the cylinder axis occurs. As such, the Jones matrix is inherently diagonal with off-axis elements that are equal to zero, and elements in $\mathbf{C}(\Delta_x, \Delta_x^{'})$ with contributions from these off-axis elements of the Jones matrix would also be equal to zero. The second observation from Figure

3.9 is that there is a non-zero background in the correlation function for the non-zero elements of $\mathbf{C}(\Delta_x, \Delta_x^{'})$. This can be attributed to the presence of a ballistic component that decreases with medium thickness. Finally, the non-zero elements of $\mathbf{C}(\Delta_x, \Delta_x^{'})$ display a peaked behaviour, with a width of about 0.6 microns for all three thicknesses tested, which is much smaller than the pixel widths used to obtain the plots in Figure 3.6 (from 166 to 500 times smaller). As the pixel size gets larger, the approximation $\mathbf{C}(x_1 - x_2, x_1^{'} - x_2) \approx \delta(\Delta_x - \Delta_x^{'})\mathbf{C}(\Delta_x)$ becomes more valid, so it can be expected that the variation in the Mueller matrix due to different instances of disorder decreases with larger pixel sizes. This agrees with the observations of Figure 3.6.

In the discussion for Figure 3.6, it was noted that for thicker scattering media, larger pixel sizes are required for the measured Mueller matrix to be independent of instance of disorder. This is consistent with the second factor that has been discussed, where the pixel size has to be larger than C_{r_2}, the ensemble-averaged intensity profile of a point source. Since the size of the emerging scattered spot increases with medium thickness, a larger pixel size will be required for the approximation $\mathbf{C}(x_1 - x_2, x_1^{'} - x_2) \approx \delta(\Delta_x^{'} - \Delta_x)\delta(\Delta_x)\mathbf{C}_o$ to be valid.

In summary, the results from numerical simulations demonstrated a decrease in the variation of the Mueller matrix over different instances of disorder with increasing pixel size. In addition, for thicker scattering media, a larger pixel size was required in order to achieve the same decrease in the variation in the Mueller matrix. Using a mathematical model, it was shown that at pixel sizes larger than the width of the correlation function of the scattering medium, the Mueller matrix for each output point can be considered as a stationary random variable, such that the measured Mueller matrix is an estimate of an ensemble-averaged quantity. Therefore, for a large enough pixel size, the measured Mueller matrix can be considered to be independent of disorder. Being an ensemble-averaged quantity, the measured Mueller matrix is also independent of the input pixel position even for a single instance of disorder. Finally, two factors affecting the required pixel size were identified. Firstly, the pixel size has to be larger than the furthest distance between input points that

preserves the output field correlation. Secondly, the pixel size also has to be larger than the ensemble-averaged intensity profile from a point source.

3.2.3 Neglecting Interference

In this section, the assumption that interference can be neglected (i.e. that $\mathbf{B}_{ml} \ll \mathbf{A}_m$) is studied using the coupled dipole formalism.

In separate simulations, the speckle field in the far-field from two adjacent input pixels was simulated over 200 instances of disorder. Figure 3.10 shows the intensity of the incident illumination at the front surface of a scattering medium for the two pixels. The pixel widths were set to 200 microns, and the pixels were placed 400 microns apart. From the simulated speckle fields, $\mathbf{A}_m$ and $\mathbf{B}_{ml}$ were computed, according to Equation 3.13. For each instance of disorder, $\mathbf{A}_m$ and $\mathbf{B}_{ml}$ were normalised by the sum of the $(1,1)^{th}$ and $(4,4)^{th}$ element of $\mathbf{A}_m$, which corresponds to the total intensity transmission from the m^{th} pixel across the two input polarisation states (see Equation 3.14). The magnitude of the elements of both matrices for each realisation was then plotted in a histogram. Figure 3.11 show the results for the three thicknesses, $\zeta = \{1, 2, 3\}$. In all three cases, the values for $\mathbf{A}_m$ can be seen to be much greater than those of $\mathbf{B}_{ml}$. As discussed in Section 3.1.3, similar results can be expected for other pixel sizes, as long as their widths are larger than the width of the correlation function, $\mathbf{C}$, of the scattering medium. When the pixel size is smaller than C_{r_1}, for example, the output speckle from two adjacent input pixels is correlated across different instances of disorder. As such, the correlations estimated by the elements of $\mathbf{B}_{ml}$ will not be negligible. Thus, for all the cases tested, the effect of interference can be considered to be negligible.

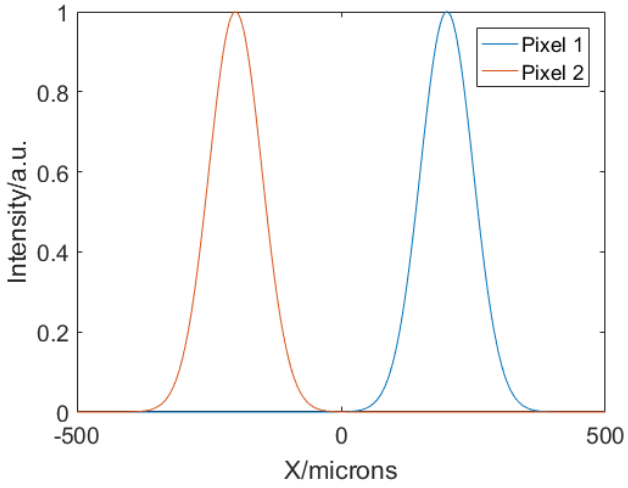

Figure 3.10: Intensity of the two pixels used for the simulation.

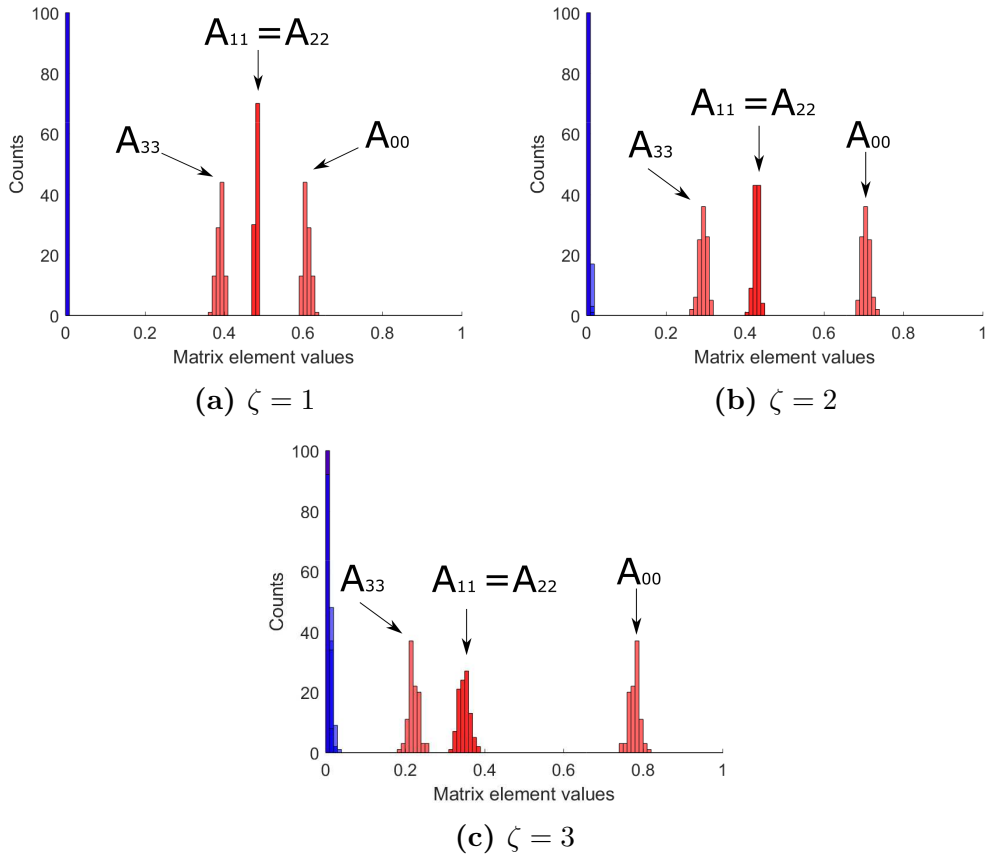

(a) $\zeta = 1$

(b) $\zeta = 2$

(c) $\zeta = 3$

Figure 3.11: $\mathbf{A}_m$ (red bars) versus $\mathbf{B}_{ml}$ (blue bars). Other than the matrix elements in the labels of this plot, all other elements lie within the blue part of the histogram.

It should be noted, however, that there could be cases where $\mathbf{B}_{ml}$ could become comparable to $\mathbf{A}_m$. One example would be when the illumination corresponding to

adjacent input pixels overlap. Figure 3.12 shows a histogram generated by the same simulation parameters as those of Figure 3.11, but this time with the two pixels spaced only 100 microns apart (see Figure 3.12). It can be seen that the magnitude of the elements in $\mathbf{B}_{ml}$ are comparable with some of the elements in $\mathbf{A}_m$, implying that the correlations between different input pixels become more significant with the pixel overlap.

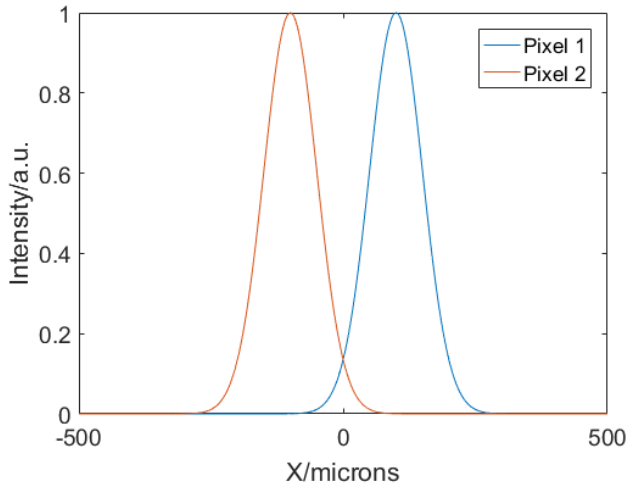

Figure 3.12: Intensity of the two overlapping pixels used for the simulation.

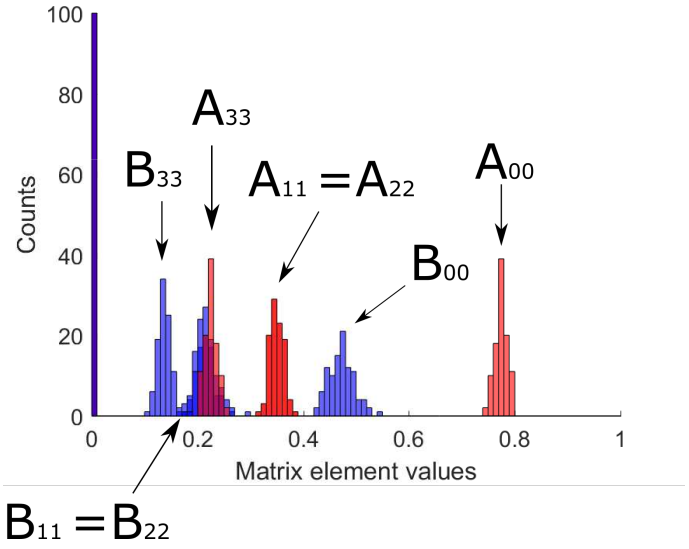

Figure 3.13: $\mathbf{A}_m$ (red bars) versus $\mathbf{B}_{ml}$ (blue bars) for $\zeta = 3$ and overlapping pixels.

Pixel overlap could occur, for example, when significant aberrations are present, such that the resulting point spread function becomes comparable to the size of

a pixel. In single pixel polarimetric imaging, the spatial masks on the DMD are imaged onto the test object which is located right next to the scattering medium. Significant aberrations in the plane of the test object would cause a spreading of the point spread function, which would cause the pixels to partially overlap. Therefore, minimising aberrations is important, in order to ensure that the interference term, $\mathbf{B}_{ml}$, remains negligible. The optical design of the imaging optics used to image the DMD onto the object plane in this work is discussed in Section 4.2.

3.2.4 Effect of Numerical Aperture

In Sections 3.2.2 and 3.2.3, the validity of the assumptions made in the proposed model was investigated for a fixed collection numerical aperture (NA) of 0.1. In this section, the effect of NA on the obtained results is studied.

The simulations presented in Section 3.2.2 were repeated for various values of NA, for the medium thickness corresponding to $\zeta = 3$. As the speckle was computed in the far-field, the field at each detector pixel can be interpreted as the plane wave component propagating in the direction $\theta \approx \frac{x}{z}$, or equivalently, different spatial frequencies [101]. Therefore, the results for each NA were obtained by reducing the size of the full detector correspondingly.

Figure 3.14 compares the average CV that was computed for each NA. In all cases, the CV was seen to reach an asymptotic value, but it can be seen that this value is higher for lower values of NA. This is further elucidated in Figure 3.15, which plots the average CV as a function of NA for the largest pixel size tested (i.e. $2w_o = 300$ microns). It can be seen that as the NA is reduced, the CV remains constant until the NA is approximately 0.02, at which point the CV increases sharply. This turning point can be better understood by looking at Figure 3.16, which shows the detector cut-off for different NA compared to the far-field intensity speckle from a single instance of disorder for a pixel size of 300 microns. The intensity speckle was plotted as a function of the detector angle, θ, which as explained above can be related to different spatial frequencies. From this plot, it can be seen that the spatial frequencies with the largest amplitudes lie within the NA cut-off of 0.02. Therefore,

reducing the NA up to 0.02 did not have much effect. When the NA is reduced past 0.02, less of the significant spatial frequencies are sampled. Since spatial frequencies can be interpreted as spatial modes in the Fourier basis, this implies that there are less independent spatial modes being collected. As much of the proposed model depends on the computation of spatial correlations, the reduction of spatial modes collected has an adverse impact on the validity of the assumptions. In particular, the assumption that $\mathbf{B}_{ml}$ is negligible may not hold. This can be seen in Figure 3.17, which is a histogram that was generated with the same parameters as that of Figure 3.11c, except this time the collection NA is decreased to 0.01. The interference term, $\mathbf{B}_{ml}$, becomes comparable to $\mathbf{A}_m$. As such, in single pixel polarimetric imaging, the NA of the collection optics has to be large enough so that there is sufficient sampling of the spatial modes. Yet, on the other hand, a low collection NA is favoured for polarimetry so as to minimise the transverse wavevector of the measured electric field, as the inclusion of light travelling at higher angles would cause an error in the measured Mueller matrix [152]. A balance, therefore, has to be reached between these two requirements in the system design.

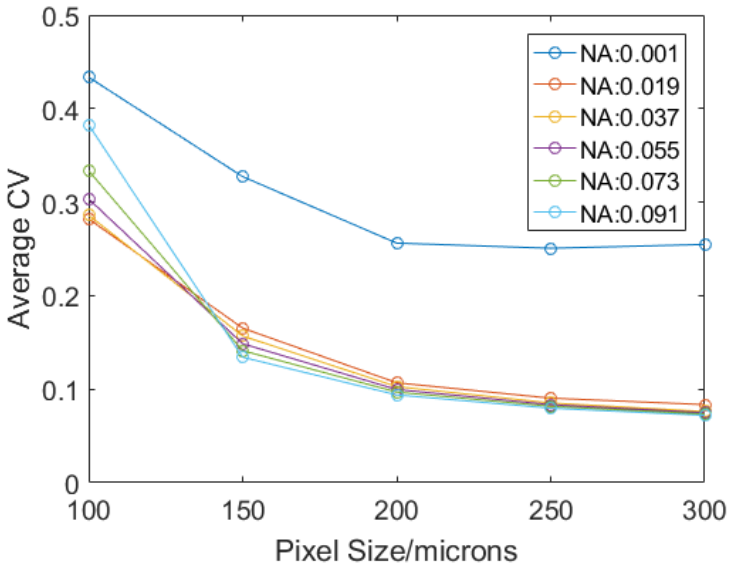

Figure 3.14: Average coefficient of variation as a function of pixel size for different values of NA, for the scattering medium with a thickness corresponding to $\zeta = 3$.

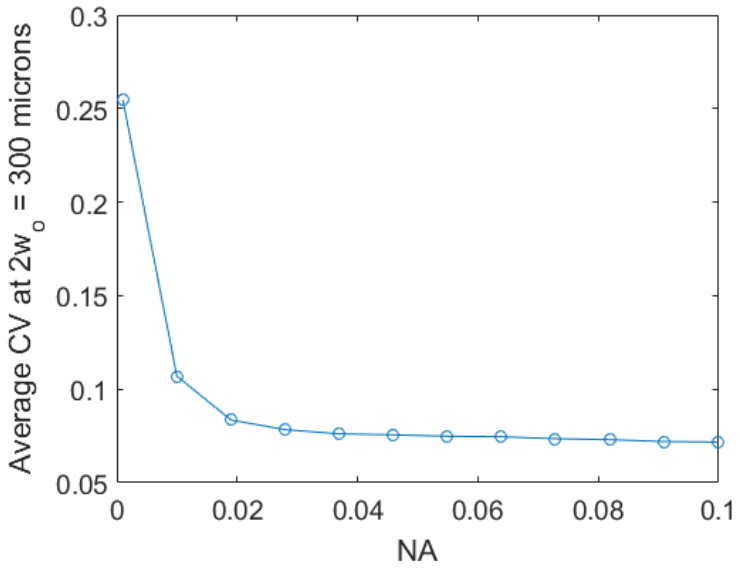

Figure 3.15: Average coefficient of variation as a function of NA for a pixel size of 300 microns incident on a scattering medium with a thickness corresponding to $\zeta = 3$.

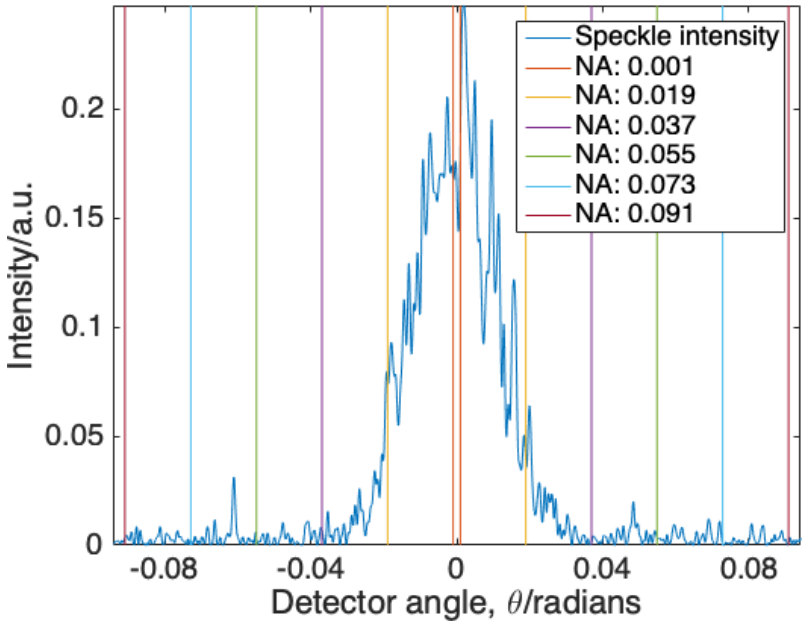

Figure 3.16: Plot to illustrate the detector cut-off for different NA over a sample intensity speckle for a pixel size of 300 microns incident on a scattering medium with a thickness corresponding to $\zeta = 3$. The vertical bars indicate cut-offs for different choices of detector NA.

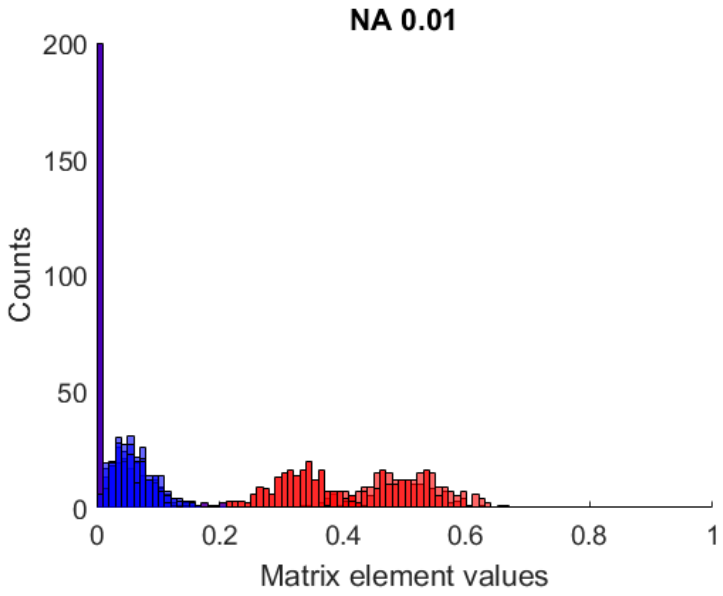

Figure 3.17: $\mathbf{A}_m$ (red bars) versus $\mathbf{B}_{ml}$ (blue bars) for $\zeta = 3$, with a collection NA of 0.01.

3.3 Discussion

In this chapter, a theoretical imaging model for single pixel polarimetric imaging was discussed. When the effects of interference are negligible, the detector intensity is shown to take a form similar to that of single pixel imaging in intensity. Using a 2D coupled line dipole simulation, negligible interference was observed in the cases tested. It was also demonstrated, however, that in the presence of significant aberrations or when the collection optics has a NA that is too low, the effect of interference can become more significant. Furthermore, the Mueller matrix of the scattering medium, which in general is a function of input pixel position, was shown to become less dependent on the instance of disorder as the pixel size increased. All of these are important factors that should be considered in the system design.

Given that the simulations were conducted in 2D with line dipoles scatterers, and with different scattering parameters to those of the experiments (see Section 4.6), one might ask, fairly, how the conclusions of the numerical simulations would relate to the experiment. For example, the matrix elements of $\mathbf{C}(\Delta_x, \Delta_x^{'})$ that are equal to zero in Figure 3.9 would not be zero in a 3D geometry, since polarisation mixing

would occur. Nevertheless, since the 2D simulation is but a 3D simulation with an invariance in one of the dimensions (due to scatterers that extend to infinity in said dimension), it is expected that the physical trends observed in the simulation should still be representative of the experiment. Nonetheless, given the differences between the simulation and the experiment, the length scales at which these trends occur, as well as the absolute values obtained in the simulations, such as the minimum CV attained, and would likely be different from those of the experiment. For example, in 2D, the measured Mueller matrix from a "line pixel" is an average over N instances of disorder, where N is the number of independent input modes contained within the "line pixel". In contrast, in the 3D geometry, the measured Mueller matrix from a square pixel with a width equal to the length of the "line pixel" is an average over N^2 instances of disorder. As such, for a fixed thickness, a smaller pixel size may be required in the 3D geometry to have a spatially invariant Mueller matrix of the scattering media.

Chapter 4

Experimental Methods

In the previous chapter, an imaging model for single pixel polarimetric imaging through scattering media was discussed and investigated via numerical simulations. This chapter discusses the experimental methods that were used for the practical implementation of the proposed technique.

Firstly, Section 4.1 presents the single pixel polarimetry imaging setup. The optical design of the setup is then explained in Section 4.2, while the calibration process is detailed in Section 4.3. The procedures for acquiring and processing the data obtained from the imaging system are then described in Section 4.4 and 4.5 respectively. In particular, measures taken to improve the system's SNR are discussed. Given the low light levels associated with transmission measurements of scattering media, such measures are important to reduce the uncertainty in the obtained results. Finally, in Section 4.6 the preparation and characterisation of the scattering samples used in the experiments, biological phantoms and chicken breast, are detailed.

4.1 Single Pixel Polarimetry Setup

The experimental setup used for this work is shown in Figure 4.1, followed by a description of the lenses used in Table 4.1. Following the terminology of Section 2.2, the system can be classified into four main parts - the PSG, the object, the PSA

and the detectors. In this section, the components within each of these parts are described in detail.

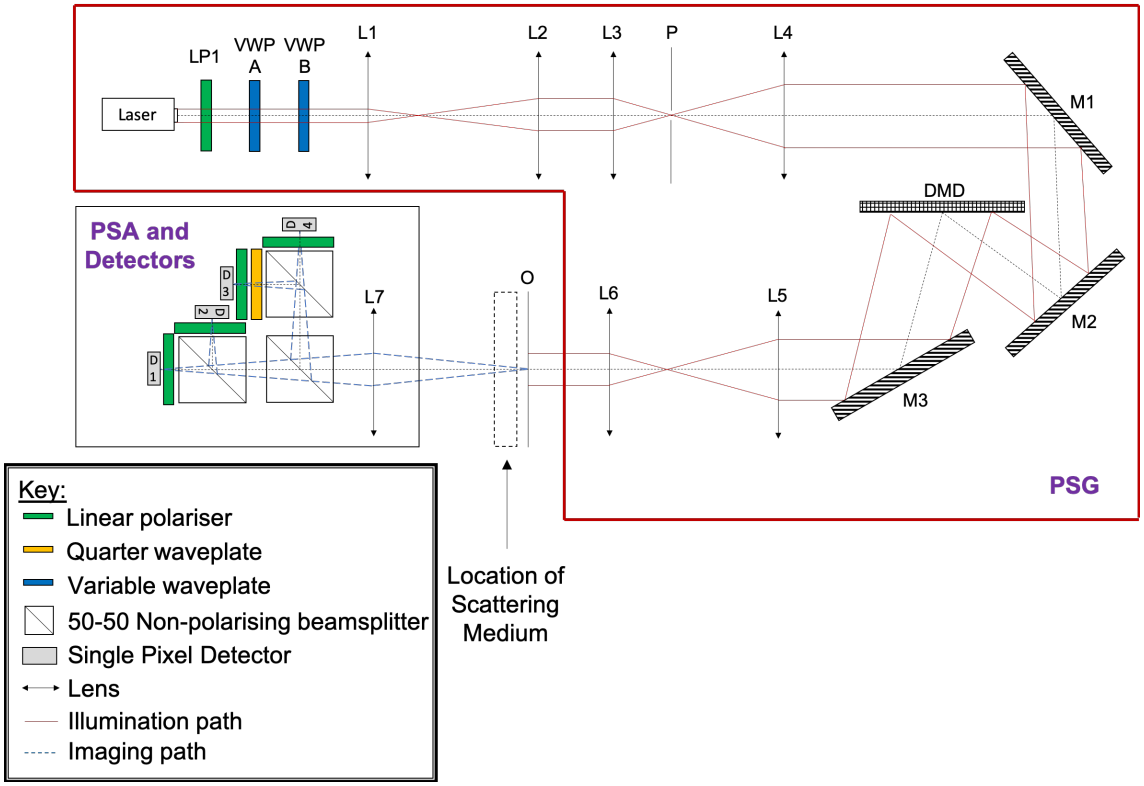

Figure 4.1: Experimental setup. Key: variable waveplate (VWP), beamsplitters (BS), lens (L), pinhole (P), quarter waveplate (QWP), linear polariser (LP), detectors (D), mirror (M), digital micromirror device (DMD). Details about the lenses, such as their focal length and model number, can be found in Table 4.1.

Lens number	Focal length/mm	Component details
L1	50	Linos Photonics 322339000
L2	200	Linos Photonics 322353000
L3	30	Thorlabs AC254-030-A-ML
L4	200	Thorlabs AC254-200-A-ML
L5	100	Thorlabs AC254-100-A-ML
L6	50	Thorlabs AC254-50-A-ML
L7	120	Linos Photonics 322309322

Table 4.1: Focal length of the lenses used. All lenses used were achromatic doublets.

4.1.1 The Polarisation State Generator

The PSG generates the input polarisation states used for polarimetry, and can be described by the matrix **W**. The columns in **W** correspond to the Stokes vectors of the input polarisation states. These different input polarisation states are time-modulated and can be generated in many ways, such as through the use of rotating polarisers and/or retarders [151, 162, 163], photo-elastic modulators [164], Pockel's cells [165, 166], or liquid crystal variable waveplates (LCVWP) [131, 167, 168]. In particular, LCVWPs have been widely employed in Mueller matrix polarimeters, as they offer an easy and affordable means of automating the setup. LCVWPs make use of optically anisotropic liquid crystals. The application of an external electric field causes individual molecules in the liquid crystal to change in orientation, which in turn modifies the birefringence of the liquid crystal cells. Consequently, depending on the applied voltage and the orientation of the incident polarisation relative to the fast axis of the liquid crystal cell, light travelling through the cell experiences different phase shifts. As such, the input polarisation state can be changed simply by altering the applied voltage. LCVWPs also have the advantage of possessing no mechanically moving parts, and also require only low driving voltages (typically tens of volts). As such, in this work, LCVWPs were chosen for the modulation of the input polarisation state.

The input states were generated by passing a y-polarised beam (*Cobolt, MLD638*) through two LCVWP (*Arcoptix, 20mm aperture*), denoted VWP A and VWP B. The intensity of the y-polarised beam was temporally modulated for lock-in detection, as detailed in Section 4.4. The variable waveplates introduce a changeable phase shift along their fast axis depending on the voltage applied. Before use, the waveplates were individually calibrated to obtain the relationship between the applied voltage and the induced phase shift [169, 170]. This was done by placing each variable waveplate between crossed polarisers, with the fast axis of the waveplate oriented at 45°. The transmittance, T, of a light beam propagating through this setup can be related to the induced phase shift, δ, as

$$T(\delta) = \frac{I(\delta)}{I^{max}} = \frac{1}{2}\left(1 - \cos(\delta)\right) \ , \tag{4.1}$$

where I is the intensity measured by a detector when a phase shift of δ is applied, and I^{max} is the maximum intensity, which is obtained when $\delta = \pi$. Hence, by changing the applied voltage in a known manner and measuring the corresponding intensities, the related phase shifts can be obtained using Equation 4.1. In this way, the calibration of the waveplates was accomplished.

In theory, any arbitrary polarisation state can be generated by the pair of variable waveplates, but, as discussed in Chapter 2, the input polarisation states used for polarimetry need to be chosen carefully in order to optimise the polarimeter performance. In the literature, it has been shown that the minimum condition number of $\mathbf{W}$ that can be obtained using two variable waveplates is $\sqrt{3}$ [131]. This can be achieved when

(i) the fast axes of VWP A and VWP B are oriented at 27.4° and 72.4° respectively, with respect to the transmission angle of the incident polarisation, and

(ii) the phase shifts applied by VWP A and VWP B to generate the four input polarisation states are as shown in Table 4.2.

	Input 1	Input 2	Input 3	Input 4
VWP A	$\frac{3\pi}{4}$	$\frac{3\pi}{4}$	$\frac{7\pi}{4}$	$\frac{7\pi}{4}$
VWP B	$\frac{3\pi}{4}$	$\frac{7\pi}{4}$	$\frac{3\pi}{4}$	$\frac{7\pi}{4}$

Table 4.2: VWP phase shifts applied to generate the optimal set of four input polarisation states.

Therefore, to minimise the condition number of $\mathbf{W}$, these settings were used in the PSG for this work. With this configuration, the theoretical form of $\mathbf{W}$ is given by

$$\mathbf{W}^{\mathbf{theory}} = \begin{bmatrix} 1.00 & 1.00 & 1.00 & 1.00 \\ 0.94 & 0.00 & -0.47 & -0.47 \\ 0.33 & -1.00 & 0.33 & 0.33 \\ 0.00 & 0.00 & -0.82 & 0.82 \end{bmatrix}. \tag{4.2}$$

After passing through the two waveplates, the polarised beam was prepared for illumination onto a SLM to generate the spatial masks needed for single pixel imaging.

SLMs are devices that enable the variation of light amplitude, phase or polarisation in space and time. In single pixel imaging, liquid crystal based SLMs (LCSLM) and DMDs are commonly used as SLMs. LCSLMs are based on the same working principle as LCVWPs, with the optically anisotropic liquid crystal molecules allowing the birefringence of the cell to be varied depending on the input voltage. Unlike a LCVWP, however, LCSLM consists of many independent liquid crystal cells. As the voltage to each cell on a LCSLM can be independently controlled, spatially varying phase modulation of the incident beam can be achieved. If amplitude modulation is desired, additional polarisers have to be used before and after the LCSLM, typically in a cross-polarised arrangement. In contrast, a DMD chip consists of many microscopic mirrors that can be electronically rotated to two discrete angles, typically $\pm 10 - 12°$, corresponding to an "ON" or "OFF" state [35, 171]. Depending on the state of the mirror, light is directed in one of two directions, thereby enabling binary amplitude modulation of the incident light field. Comparing the two technologies, LCSLMs offer more flexibility in modulation than DMDs, both in terms of modulation depth and modulation modes. In addition, LCSLMs have a higher diffraction efficiency, which directly affects the throughput of the optical system. For example, Turtaev *et al.* [172] measured a diffraction efficiency of 8% from a DMD, compared to 42% by a LCSLM. Yet, DMDs are able to operate at much faster speeds with typical binary pattern rates of tens of kilohertz, compared to only hundreds of hertz in LCSLMs [172, 173]. The rate at which spatial masks can be applied is directly correlated with the acquisition time for single pixel imaging, and is thus an important factor to consider in relation to practicality, particularly for biological applications, which exhibit variations at millisecond timescales [104, 105]. Moreover, DMDs are more cost effective than LCSLMs, therefore making them an attractive choice for building economical yet functional imaging platforms. In view of these advantages, alongside the consideration that binary modulation is sufficient for single pixel polarimetric imaging, this work employs a DMD (*Texas Instruments, DLP4500*) as a SLM.

It is important to ensure that the beam illuminating the DMD is spatially homogeneous to minimise SNR ratio differences across pixels in the final image, in order

to avoid a variation in the polarisation sensitivity for different pixels. As the diode laser used in this experiment did not demonstrate good beam quality, the laser beam had to be expanded and spatially filtered before it could be used to illuminate the DMD. Unfortunately, this meant that the throughput of the setup was decreased. Beam magnification was achieved via two beam expanders (Lenses L1 to L4), which provided a combined magnification of $m = 26$. To spatially filter the beam, a pinhole with a diameter of 15μm was included at the focal point of L3, which has a diffraction limited focal spot size of 13.67 microns. These steps resulted in a maximum to minimum intensity difference of 50% across the field of view (see Section 5.2 for experiment results). The expanded and filtered beam was then directed towards the DMD. As the DMD consists of a periodic array of micromirrors, it behaves similarly to a blazed diffraction grating. The interference between the reflected light from each mirror causes the light to appear in different diffraction orders, with the intensity of each order dependent on the angle of the incident illumination. In order to maximise the light transmitted to a single diffraction order, the laser beam was directed towards the DMD at an incident angle of 31°, with the angle of incidence adjusted via mirrors M1 and M2. This maximised the light transmitted to the third diffraction order [174]. Residual light in other orders were eliminated using beam blocks. The third diffraction order was then reflected by mirror M3 and imaged onto the object plane using lenses L5 and L6. Details on the lenses used in the PSG are shown in Table 4.1.

4.1.2 The Objects

Both spatially homogeneous and heterogeneous objects were utilised in this work to test the single pixel polarimetric setup. During measurement, the test object in use was placed in the object plane. The spatially homogeneous objects used were a linear polariser (*Thorlabs, LPVISE2×2*) and a quarter waveplate (*Thorlabs, WPQ10E-546*). After verifying the proposed polarimetric imaging technique on these test objects, the technique was further tested on a spatially inhomogeneous test object, which was a letter R that was printed on a soda lime glass substrate using low-reflectivity chrome (*Thorlabs, Multi-Frequency Grid Distortion Target R1L3S3P*). A sheet linear polariser (*Thorlabs, LPVISE2×2*) and scotch tape (*3M, Scotch© Easy*

tear tape), which acts as a retarder, was adhered to opposite sides (see Figure 4.2). This test object was chosen because of its spatial variation as well as the distinct and known polarisation properties of the three regions, which facilitates the assessment of the spatially resolved Mueller matrix. The images obtained with and without the scattering medium can be compared, while the letter R further highlights the setup's ability in retrieving the spatial information of the object.

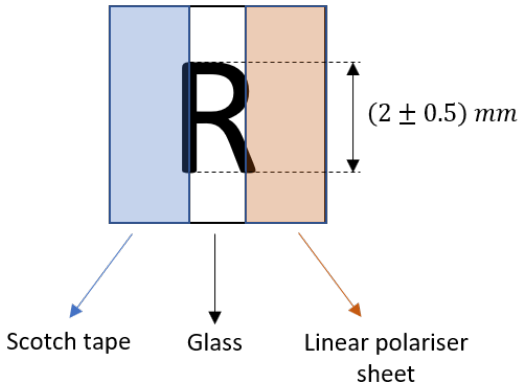

Figure 4.2: Test target used for proof-of-concept experiments.

4.1.3 The Polarisation State Analyser and Detectors

The PSA measures the output polarisation state, and can be described by the instrument matrix, **A**, whose rows are the Stokes vectors corresponding to the output polarisation states analysed. As discussed in Section 2.2, multiple measurements of different analyser states are required to determine the polarisation state of the measured light field. To obtain these measurements, many configurations for the PSA have been proposed in literature (see [175] for a review). These can be broadly classified into a few categories based on their operating principle. The first category consists of division of wavefront polarimeters (DOWP) [176, 177, 178], which spatially subdivide the incoming wavefront into different segments, such that light in each segment passes through separate polarisation analysers and detectors. In this way, DOWPs allow measurements to be taken simultaneously, thus avoiding potential errors caused by temporal discrepancies in the acquired data. Moreover, DOWPs are compact, thereby allowing for easier miniaturisation of the system. Nevertheless, DOWPs tend to require specialised optics, such as a microarrays of

lenses or polarimetric elements, and as such can be more costly to build.

Instead of dividing the incident wavefront, division of amplitude polarimeters (DOAP) [179, 180, 181] obtain the multiple measurements needed by splitting the light using optical components, such as prisms and beamsplitters . Similar to DOWPs, the main advantage of DOAPs is that synchronous measurements of the incident polarisation state can be made. In addition, DOAPs can be built economically, using off-the-shelf components such as beamsplitters, polarisers and waveplates. Yet, alignment with DOAPs can be tricky, particularly when imaging detectors are used, to ensure good spatial registration of the acquired images in each analyser arm.

Finally, division of time polarimeters (DOTP) [4, 131, 151, 163] function by modulating the analysed polarisation state in time, for example through the use of rotating analysers. The obvious drawback to DOTPs is that the incident polarisation has to remain static over the observation time, but this comes with the benefit of less hardware, making them easier and potentially more cost-effective to build, especially in a small package.

Real scattering media, such as biological tissue, are dynamic. Therefore, due to the temporal variability of their scattering properties, synchronous measurements are generally preferred to minimise the temporal misregistration between different measurements. Between DOWP and DOAP, the latter is attractive due to its simplicity and cost-effectiveness. Furthermore, in single pixel polarimetric imaging, the constraint on alignment is relaxed due to the use of single pixel detectors with no spatial resolution. As such, this work opted for the use of a DOAP.

A schematic of the PSA used is shown below in Figure 4.3. As explained in Section 2.2, at least four output analyser states are necessary to determine the incoming Stokes vector. More than four analyser states can also be used to form an overdetermined set of linear equations, which can be useful in the case of noise [133]. This comes, however, at the cost of signal strength, as the incident light would have to be divided into more parts. Therefore, in this work, four output polarisation states

were analysed. These were, specifically, linearly polarised light in x, y and 45°, as well as left circularly polarised light. The advantage of such a setup is that it can be implemented easily with just beamsplitters, quarter waveplates and linear polarisers. The incident beam was split into four paths through the use of three 50-50 non-polarising beamsplitters. Beamsplitters of equal splitting power were used to minimise the condition number of the related instrument matrix [129, 182]. To analyse the x and y linearly polarised states, linear polariser sheets were used (*Thorlabs, LPVISE2×2*), while the 45° linear polarisation state was analysed using a mounted linear polariser (*Thorlabs, LPVISE100-A*). The analyser optics for left circularly polarised light consisted of a quarter waveplate (*Thorlabs, WPQ10M-633*) in a horizontal orientation, followed by a linear polariser (*Thorlabs, LPVISE100-A*) at −45°. This configuration results in a theoretical instrument matrix given by

$$\mathbf{A}^{\mathbf{theory}} = \begin{bmatrix} 1.00 & 1.00 & 0.00 & 0.00 \\ 1.00 & -1.00 & 0.00 & 0.00 \\ 1.00 & 0.00 & 1.00 & 0.00 \\ 1.00 & 0.00 & 0.00 & -1.00 \end{bmatrix}, \tag{4.3}$$

which has a condition number of 3.23. For comparison, Tyo *et al.* showed that the minimum condition number for a PSA measuring four output analyser states was $\sqrt{3} \approx 1.73$ [183]. Although other PSA architectures with lower condition numbers are possible, this design was chosen as it can be constructed economically with off-the-shelf components.

Light from the object passed through the PSA, and was imaged onto the four detectors (*Thorlabs, PDA100A*) via lens L7 (see Table 4.1 for lens details). The design distances from the object plane to lens L7 and from lens L7 to each detector were equally 240 mm. A low collection NA is necessary to minimise the axial component of the electric field, or equivalently the transverse component of the wavevector, in the light collected, as it is not well accounted for by typical polarising elements, such as those that have been used in the PSA. On the other hand, the results of Section 3.2.4 showed that the variance in the Mueller matrix across different instances of disorder and across different pixels is higher for lower NA. A balance between these

two factors is needed in the selection of the NA. To this end, the values of NA used in the simulation in Section 3.2.4 can serve as guide, but the absolute values are unlikely to correspond to the experiment due to the two-dimensional nature of the simulation. For this setup, the NA was empirically chosen to be 0.05. Equivalently, Lens L7 had a collection half-angle of 3°.

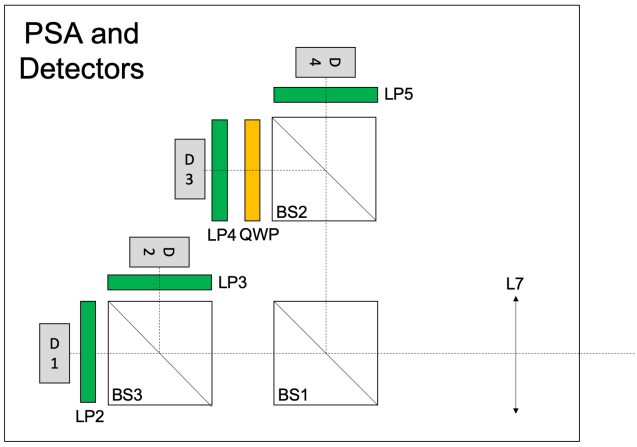

Component	Model*	Orientation/°
LP2	LPVISE2X2	90
LP3	LPVISE2X2	0
LP4	LPVISE100-A	45
LP5	LPVISE100-A	-45
QWP	WPQ10M-633	0
BS1/BS2/BS3	CCM-BS013/M	-

*All components from Thorlabs

Figure 4.3: The layout of the PSA. Key: beamsplitters (BS), quarter waveplate (QWP), linear polariser (LP), detectors (D), lens (L).

Finally, the detectors measured the resulting intensity after propagation through the analysing optics. These measured intensities form the matrix $\mathbf{D}$, where each column corresponds to the data collected for a single input polarisation state generated by the PSG. The measurement was done using lock-in detection, as detailed in Section 4.4.

4.2 Optical Design

As discussed in Section 3.2.3, the presence of large aberrations when imaging the DMD onto the object plane would adversely affect single pixel imaging polarimetry. Other than a reduction in image quality and resolution, interference effects between pixels also become more significant. Moreover, the point spread function of the imaging system is a key parameter that determines the spatial resolution of the single pixel polarimetric imaging system, because for any fixed DMD, it sets a limit on the smallest pixel size of the spatial masks that can be projected onto the sample

plane. These considerations aside, given the low NA of L7, the lenses also have to be chosen so as to minimise the angular spread of the beam impinging on the object plane, thus maximising the light efficiency. In other words, the imaging system has to be able transmit all spatial frequencies in a displayed spatial pattern to the object plane while keeping the divergence of the beam low enough to minimise vignetting by the collection lens L7. Therefore, careful selection of the imaging components by means of optical design is essential, and is presented in this section.

The components involved in imaging the DMD onto the object plane can be grouped into two parts - the illumination optics, which consists of all the components from the laser up to the DMD, and the imaging optics, which is composed of lenses L5 and L6. The plane mirrors used in this setup are assumed to be ideal and free from aberrations. In reality, if the mirrors are not perfectly flat, it is possible that some astigmatism may be present [184], which may be a problem for more demanding imaging applications.

For a few reasons that will be discussed here, it is expected that the illumination optics contributes weakly to the total aberrations in the system. Firstly, the pinhole, which is of a similar size to the diffraction-limited focal spot size of L3, spatially filters the beam. As a result, the zero-frequency component of the field is isolated, while the higher frequency components are mostly rejected. Since, ideally, the laser beam entering L3 is collimated and on axis, the removal of the higher frequency components aids in minimising aberrations in the incident beam. Secondly, only achromatic doublets were used in both beam expanders. Achromatic doublets are usually designed to have minimum coma, spherical and chromatic aberrations. Combined with the consideration that the laser beam is aligned on axis, the aberrations caused by the lenses are not expected to be large. For these reasons, the optical design of the system has mainly focused on the imaging optics, lenses L5 and L6.

The design of the system was done using the simulation software *Zemax OpticStudio* 16.5, and was conducted in the following manner. First, two achromatic doublets

were selected based on a design magnification of -0.5. This magnification was chosen so that the spatial masks projected by the DMD (full height of 6.614mm) would fully cover the letter R in the heterogeneous test object (full height of 2mm). The selected magnification only controls the ratio between the focal lengths of lenses L5 and L6. The absolute focal lengths were picked by testing different configurations, and choosing an option which provided a balance between the system footprint and image aberrations. The focal lengths chosen were $f = 100$mm and $f = 50$mm for L5 and L6 respectively, as described in Table 4.1. The two lenses were initially placed in an afocal setup, where both the object and image distances are at infinity, to resemble the illumination path, and the distance between them was optimised for minimum root-mean-squared error in the resulting wavefront. Once optimised, the separation of the two lenses was fixed, and the setup was switched to finite image and object distances. The object height was set to 3mm, corresponding to approximately half of the height of the DMD, since the DMD is centred on the optical axis. Finally, the object and image distances were optimised for the smallest spot size at the image plane.

The final design layout for L5 and L6 is shown in Figure 4.4. The paraxial magnification of the system was reported by the software to be -0.5. The red, green and blue rays in Figure 4.4 originate from object points at heights of 3mm, 2mm and on axis respectively. The predicted spot sizes at said object heights are shown in Figure 4.5, and show that the system is expected to be diffraction limited with an Airy radius of 7.35μm. The Seidel coefficients [185] are shown in Figure 4.6. It can be seen that the largest aberration in the system is spherical abberation, with a corresponding Seidel coefficient of 0.086 waves.

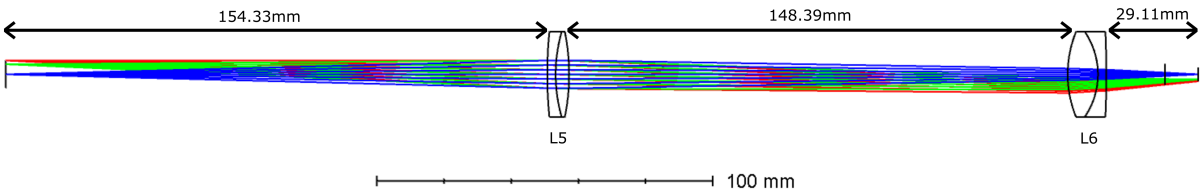

Figure 4.4: Layout for optical system for imaging DMD onto the object plane.

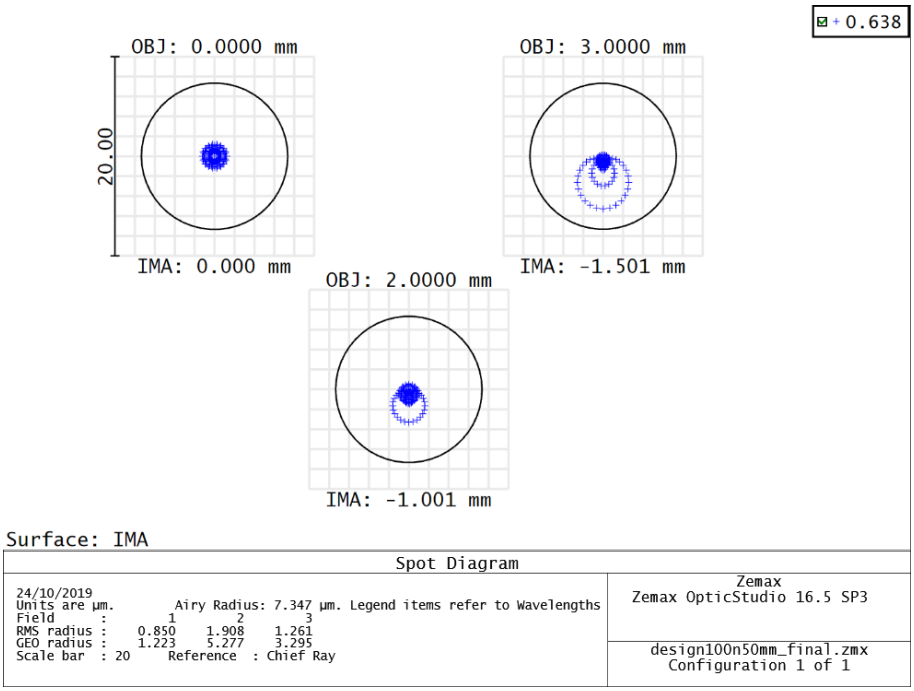

Figure 4.5: Spot diagram for optical system for imaging DMD onto the object plane, showing the image plane spot sizes for the three object distances tested.

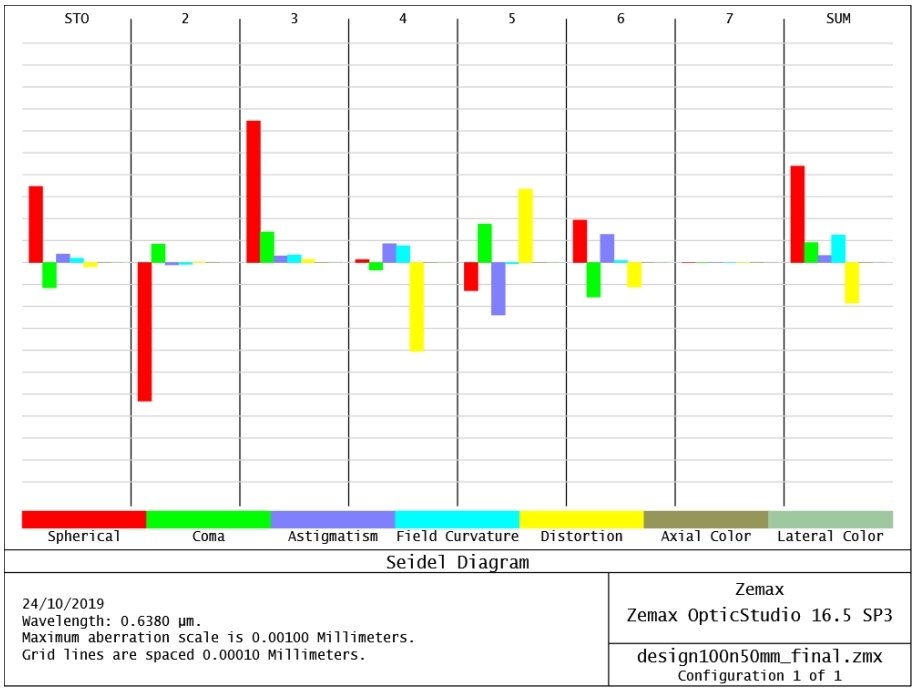

Figure 4.6: Seidel coefficients at each surface in the system.

The system was set up in the laboratory according to the design distances, as shown in Figure 4.4. As the height of the letter R in the heterogeneous object was measured with a ruler to be (2 ± 0.5)mm, the image magnification was estimated using the height of the letter in a reconstructed intensity image obtained using the system (see Section 4.4 and 4.5 for details of image reconstruction). The resulting image had a pixel resolution of 16×16, and is shown in Figure 4.7. The letter R was found to be 10 pixels in height, so the size of each pixel was computed to be $\frac{2\pm0.5}{10\pm0.5} = (0.2 \pm 0.05)$mm. The height of the illuminated patch at the object plane was thus concluded to be $\frac{2\pm0.5}{10\pm0.5} \times 16 = (3.2 \pm 0.8)$mm. Since the spatial mask covered the full height of the DMD, the imaging system was found to have a magnification of $\frac{3.2\pm0.8}{6.614} = 0.5 \pm 0.1$. Seeing that the magnification is close to the design magnification, it was inferred that the separation of the lenses in the actual arrangement was similar to the design distances. Consequently, the spatial resolution predicted by the simulations is expected to be representative of the physical setup.

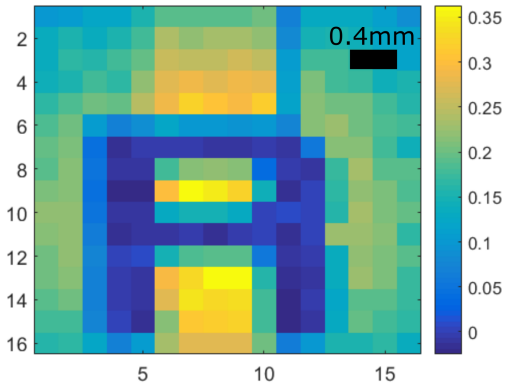

Figure 4.7: Intensity image of letter R obtained using the system. The x and y axes correspond to pixel indices.

The last lens in the system, L7, images the object plane onto each photodiode in the PSA, with the collected light passing through beamsplitters and polarising elements on the way. Since the photodiode has a single pixel and only measures an integrated intensity, the aberrations caused by L7 and the optical elements in the PSA are inconsequential, so long as all the light is still collected by the detector. Moreover, due to the low NA of L7, the collected light propagates through the optics at low angles, so instrumental polarisation can be assumed to be negligible. Nevertheless, the changes in polarisation due to the various optical elements in the setup are intrinsically accounted for in the calibration of the polarimeter, which is discussed in the next section of this chapter.

4.3 Polarimetric Calibration

Polarimeter calibration is required before the system is used, in order to obtain the true instrument matrices of the PSG and PSA. Once the instrument matrices, **A** and **W** are known, the Mueller matrix of any test object can be computed using Equation 4.32 (see Section 2.2 or 4.5). Since the determination of the Mueller matrix of the object depends on these two matrices, it is important that the calibration is done accurately.

Many techniques for polarimeter calibration have been reported in literature [186, 187, 188, 189]). Though usually adapted to the specific setup, the procedure gener-

ally consists of measuring the detector intensities corresponding to different orientations of optical elements that have known polarimetric responses. A theoretical form for the expected detector intensities can then be derived, and this, combined with the measurements, allows the instrument matrices to be computed. For instance, for the calibration of the four-detector photopolarimeter by Azzam [187, 190], a Glan-Thompson polariser was rotated around the beam axis. From theory, the related detector measurements were shown to follow a simple Fourier series, with the Fourier components corresponding to the first three columns of the PSA instrument matrix. Thus, these columns could be obtained by a least square fit to the theoretically derived function. The fourth column of the instrument matrix was obtained similarly by rotating a Glan-Thompson polariser and a quarter waveplate in two orientations, such that right and left circularly polarised light was directed into the PSA. It was then demonstrated that by taking the difference of the two measurements, the final column of the instrument matrix could be obtained. Though well-established, these techniques are sensitive to errors in the measurement, and require meticulous alignment of the optical components with high precision. Moreover, the optical components themselves are often imperfect, and further measurements are required in order to reduce the resulting uncertainties. Making use of the same example as before of the four-detector photopolarimeter, the production of perfectly circular polarisation states used for calibration is a highly challenging task. As quarter waveplates tend to be flawed, it is more likely that elliptical near-circular polarisation states are produced instead, thus leading to errors in the resulting instrument matrix. To overcome this, other than the original measurement taken for each circularly polarised state, the authors took an additional measurement by jointly rotating the Glan-Thompson polariser and the quarter waveplate by 90°. Assuming that imperfections in the quarter waveplate are small, the sum of the two measurements was shown to approximate a perfect circularly polarised state. Thus, as this example illustrates, having to account for the imperfections of the optical components further complicates the calibration process. These drawbacks aside, these calibration procedures also exclude the contribution of other optical elements in the system, such as lenses and mirrors, which also modify the polarisation state of light.

The eigenvalue calibration method (ECM) offers a means of overcoming these limitations. Instead of making assumptions about $\mathbf{W}$, both matrices $\mathbf{A}$ and $\mathbf{W}$ are derived from measurements over multiple calibration samples, with the Mueller matrix for each sample, $\mathbf{M}_i$, also recovered in the process. As a result, system imperfections are included within the calibrated matrices. In view of these advantages, ECM was adopted as the means of calibration for this work. A full description of the method can be found in [191, 192]. Here, a brief summary of the method and its implementation is discussed.

4.3.1 Eigenvalue Calibration Method

The assumptions made in the ECM are that

1. there is negligible noise in the system,
2. the calibration samples used are non-depolarising,
3. the calibration samples have known Mueller matrices.

To conduct ECM, measurements over K calibration samples are first taken. As discussed in Chapter 2.2, the corresponding detector intensities for the i^{th} calibration sample are described by

$$\mathbf{D}_i = \mathbf{A}\mathbf{M}_i\mathbf{W} \ , \tag{4.4}$$

for $i = \{1, 2, ..., K\}$. A measurement with no calibration sample present is also taken, with the resulting detector intensities given by

$$\mathbf{D}_{air} = \mathbf{A}\mathbf{W} \ . \tag{4.5}$$

Here, the Mueller matrix for air is taken to be the identity matrix. Multiplying the measurements for each calibration sample with $\mathbf{D}_{air}^{-1}$ gives the set of matrices

$$\mathbf{C}_i = \mathbf{D}_{air}^{-1}\mathbf{D}_i = \mathbf{W}^{-1}\mathbf{M}_i\mathbf{W} \ . \tag{4.6}$$

The matrices $\mathbf{C}_i$ and $\mathbf{M}_i$ can be seen to be similar matrices, which consequently have shared eigenvalues [148]. This property enables the reconstruction of $\mathbf{M}_i$, which is

done as follows.

In the absence of depolarisation, a general Mueller matrix can be written in the form [127]

$$\mathbf{M}_i = \tau_i R(-\theta_i) \begin{bmatrix} 1 & -\cos 2\Psi_i & 0 & 0 \\ -\cos 2\Psi_i & 1 & 0 & 0 \\ 0 & 0 & \sin 2\Psi_i \cos \Delta_i & \sin 2\Psi_i \sin \Delta_i \\ 0 & 0 & -\sin 2\Psi_i \sin \Delta_i & \sin 2\Psi_i \cos \Delta_i \end{bmatrix} R(\theta_i) \ , \tag{4.7}$$

where τ_i is equal to half of the maximum transmission, Δ_i is the retardance of the sample and $\tan \Psi_i$ describes the ratio between the maximum and minimum amplitude transmission of the sample. Also, $R(\theta_i)$ is the rotation matrix describing a counter-clockwise rotation about the optical axis by θ_i, defined with respect to an observer facing towards the source, given by

$$R(\theta_i) = \begin{bmatrix} 1 & 0 & 0 & 0 \\ 0 & \cos 2\theta_i & \sin 2\theta_i & 0 \\ 0 & -\sin 2\theta_i & \cos 2\theta_i & 0 \\ 0 & 0 & 0 & 1 \end{bmatrix} \ . \tag{4.8}$$

From Equation 4.7, the four eigenvalues of $\mathbf{M}_i$ can be computed as

$$\begin{aligned} \mu_1 &= 2\tau_i \sin^2 \Psi_i \\ \mu_2 &= 2\tau_i \cos^2 \Psi_i \\ \mu_3 &= \tau_i \sin 2\Psi_i \exp(i\Delta_i) \\ \mu_4 &= \tau_i \sin 2\Psi_i \exp(-i\Delta_i) \ . \end{aligned} \tag{4.9}$$

Therefore, for each calibration sample, the eigenvalues of $\mathbf{C}_i$ can be used to obtain τ, Ψ_i and Δ_i through Equation 4.9. This means that the Mueller matrix for each calibration sample can be reconstructed using Equation 4.7, up to an unknown rotation as described by $R(\theta_i)$.

In order to obtain the matrix $\mathbf{W}$, Equation 4.6 is used. Multiplying both sides

of the equation by $\mathbf{W}$, one obtains

$$\mathbf{M}_i\mathbf{W} - \mathbf{W}\mathbf{C}_i = \mathbf{0} \ . \tag{4.10}$$

From Equation 4.10, the matrix $\mathbf{W}$ lies in the nullspace of the operator $\mathbb{H}_M$, which is defined as

$$\mathbb{H}_{M_i} : \mathbf{X} \rightarrow \mathbf{M}_i\mathbf{X} - \mathbf{X}(\mathbf{A}\mathbf{W})^{-1}(\mathbf{A}\mathbf{M}_i\mathbf{W}) \tag{4.11}$$

where $\mathbf{C}_i$ has been substituted using Equations 4.5 and 4.6. Hence, if the dimension of the nullspace of $\mathbb{H}_{M_i}$ is 1, the unique matrix in the nullspace must be the desired matrix $\mathbf{W}$. Unfortunately, as the following discussion will show, this is not the case when only a single calibration sample (i.e. $K = 1$) is used. The key idea is then to use multiple calibration samples, such that the intersection of their nullspaces has a dimension of 1, corresponding to the instrument matrix $\mathbf{W}$.

Substituting $\mathbf{X}^{'} = \mathbf{X}\mathbf{W}^{-1}$, and multiplying by $\mathbf{W}^{-1}$, a second operator can be defined from Equation 4.11 as

$$\mathbb{H}^{'}_{M_i} : X \rightarrow \mathbf{M}_i\mathbf{X}^{'} - \mathbf{X}^{'}\mathbf{M}_i \ . \tag{4.12}$$

Since $\mathbf{W}$ is, by definition, invertible and not a zero matrix, $\mathbb{H}_{M_i}$ and $\mathbb{H}^{'}_{M_i}$ share the same nullspace. With this in mind, a few observations can be made from Equation 4.12. Firstly, the nullspace of the operator $\mathbb{H}^{'}_{M_i}$, and consequently $\mathbb{H}_{M_i}$, is fully determined by the Mueller matrices of the calibration samples, and is independent of the instrument matrices $\mathbf{A}$ and $\mathbf{W}$. Thus, the choice of calibration samples is universal, and does not depend on the experiment setup. Secondly, it can be observed that $\mathbb{H}^{'}_{M_i}$ is also the commutator of $\mathbf{M}_i$, in the sense that matrices in the nullspace of $\mathbb{H}^{'}_{M_i}$ are all possible matrices that commute with $\mathbf{M}_i$. Accordingly, the nullspace of $\mathbb{H}^{'}_{M_i}$ and the commutator of $\mathbf{M}_i$ are of equal dimension. From matrix theory, it can be derived that a square matrix, $\mathbf{A}$, of dimension $n \times n$, is commutable with at least n matrices [191]. Hence, given that Mueller matrices have a size of 4×4, the use of a single calibration sample will mean that there are at least 4 solutions to Equations 4.11 and 4.12. At least two calibration samples are required in order to ensure that

there is a unique solution for $\mathbf{W}$. In this work, as proposed by De Martino *et al.* [131], linear polarisers at 0° and 90°, along with a quarter waveplate at 30° were used.

With a set of appropriate calibration samples, the equation

$$\mathbf{MW} - \mathbf{W}(\mathbf{AW})^{-1}(\mathbf{AMW}) = \mathbf{0} \ , \ \mathbf{M} \in \{\mathbf{M}_1, \mathbf{M}_2, ...\mathbf{M}_K\} \tag{4.13}$$

forms an overdetermined linear system, whose unique solution for $\mathbf{W}$ can be found as follows. Equation 4.10 is first vectorised as

$$\begin{aligned} \left(\mathbf{I} \otimes \mathbf{M}_i - \mathbf{C}_i^\top \otimes \mathbf{I}\right) \mathrm{vec}(\mathbf{W}) &= \vec{0} \\ \mathbf{H}_i \mathrm{vec}(\mathbf{W}) &= \vec{0} \ , \end{aligned} \tag{4.14}$$

where $\mathbf{H}_i = \left(\mathbf{I} \otimes \mathbf{M}_i - \mathbf{C}_i^\top \otimes \mathbf{I}\right)$ and vec(...) denotes the vectorisation operation. Multiplying both sides of Equation 4.14 by $\mathbf{H}_i^\top$, Equation 4.14 can be combined for the K calibration samples as

$$\mathbf{L}\mathrm{vec}(\mathbf{W}) = \vec{0}, \text{ where } \mathbf{L} = \sum_{i=1}^{K} \mathbf{H}_i^\top \mathbf{H}_i \ . \tag{4.15}$$

As $\mathbf{L}$ is a real symmetric matrix, it can be diagonalised, with the diagonal values being equal to its eigenvalues. vec($\mathbf{W}$) is then the eigenvector corresponding to the single null eigenvalue of $\mathbf{L}$, which has been made to be unique through the choice of calibration samples. In this way, the instrument matrix, $\mathbf{W}$ is obtained. In practice, due to noise and experimental precision, the smallest eigenvalue is not exactly zero, but should still be close to this ideal value.

Equation 4.15 utilises the Mueller matrices of the calibration samples, whose rotation angle, θ_i, has so far been undetermined. The rotation angles of the calibration samples relative to each other can be obtained from $\mathbf{L}$ by minimising the ratio between the smallest eigenvalue, λ_{16}, and second smallest eigenvalue, λ_{15}, of $\mathbf{L}$,

$$\epsilon = \sqrt{\frac{\lambda_{16}}{\lambda_{15}}} \ , \tag{4.16}$$

The absolute rotation angle for each calibration sample can be obtained by setting a reference axis to the optical system, such as an axis of a calibration sample, or an axis corresponding to a fixed polariser placed directly after the source. With the rotation angle of each calibration sample determined, $\mathbf{M}_i$, and hence $\mathbf{L}$, can be computed. This, in turn, allows $\mathbf{W}$ to be obtained as the eigenvector corresponding to the null eigenvalue of $\mathbf{L}$. Finally, $\mathbf{A}$ can be obtained from Equation 4.5 as

$$\mathbf{A} = \mathbf{D}_{air}\mathbf{W}^{-1} \tag{4.17}$$

This completes the calibration process, and the matrices $\mathbf{A}$, $\mathbf{W}$ and $\mathbf{M}_i$ are known. It is worth noting that the method is sensitive to noise, as can be seen from Equations 4.5 and 4.6. In the presence of noise, $\mathbf{D}_{air}$ in Equation 4.5 has an added noise term that is amplified by the matrix inversion in Equation 4.6. This is propagated through the calibration process into errors in the obtained matrices.

4.3.2 Calibration Results

Here, the calibration results used to obtain the images in Chapter 6 are discussed. The ECM calibration procedure discussed in Section 4.3.1 was used. As mentioned previously, a quarter wave plate at 30° (*Thorlabs WPQ10M-546*) and a linear polariser (*Thorlabs LPVISE100-A*) at 0° and 90° were used as calibration samples. Lock in-detection (see Section 4.4.2) was used to increase the measurement SNR. In addition, to prevent saturation of the photodiodes, neutral density (ND) filters (*Thorlabs NE10A and NE20A*) were used to attenuate the incident illumination.

The two linear polariser samples are each crossed with at least one output analyser in the PSA. ECM is sensitive to experimental noise, and with poor SNR, as is the case for these linear polarisers, the eigenvalues of $\mathbf{C}_i$ could be complex. If the eigenvalues of $\mathbf{C}_i$ were found to be complex for the two linear polariser samples, the ideal polarimetric parameters, $\{\Psi, \Delta\} = \{\frac{\pi}{2}, 0\}$, were used instead in Equation 4.7 to generate their Mueller matrices. τ remains unchanged, and is computed from the trace of $\mathbf{C}_i$.

Due to experimental uncertainties, the exact orientation angles of the calibration samples may differ slightly in practice, but ECM estimates the actual angles used as part of the calibration process, as discussed in Section 4.3.1. A comparison of the recovered angles and the polarimetric parameters, Ψ, Δ and τ, with their expected values therefore serves as a first verification of the calibration.

Using the above mentioned calibration samples, the polarimetric parameters and orientation angles estimated by ECM were

Calibration Sample	Ψ/radians	Δ/radians	τ	$\theta/^\circ$
Linear polariser (0°)	1.57	0.00	0.40	−2.00
Linear polariser (90°)	1.57	0.00	0.39	90.00
Quarter waveplate (30°)	0.78	1.19	0.99	25.93

Table 4.3: Polarimetric parameters and orientation angles of the calibration samples obtained by ECM. The reference axis is defined to be that of the linear polariser at 90°.

The final column of Table 4.3 shows that the retrieved orientation angles for the three calibration samples are close to the design angles. With regards to the estimated polarimetric parameters, a check of the manufacturer's datasheet [193] shows that the linear polariser has a maximum transmission of 79.25%, which implies that ideally, $\tau = 0.395$. It can be seen that this is close to the values obtained through ECM for both linear polariser samples. The polarimetric parameters for an ideal quarter waveplate are $\{\Psi, \Delta, \tau\} = \{\frac{\pi}{4}, \frac{\pi}{2}, 1\}$. It can be seen that other than Δ, the obtained values are close to the ideal parameters. The lower value of Δ is to be expected as the quarter waveplate used is not designed for the laser wavelength used in this work. The manufacturer datasheet for the waveplate [194] reports a typical retardance of 0.2151 waves at the laser wavelength of 638nm, which corresponds to $\Delta = 1.35$. This is closer to the obtained result by ECM, although a small discrepancy of 0.03 waves remains. The manufacturer quotes a retardance accuracy of 0.01 waves, so part of this discrepancy could stem from differences in the fabrication of each waveplate. The slight deviation could also be caused by some spatial inhomogeneity of the waveplate. Thus, the estimated values in Table 4.3 are seen to agree with expectation.

The calibration matrices obtained from ECM were

$$\mathbf{W}_{ECM} = \begin{bmatrix} 0.37 & 0.35 & 0.35 & 0.32 \\ 0.37 & 0.03 & -0.01 & -0.14 \\ 0.03 & 0.11 & 0.20 & -0.27 \\ -0.04 & 0.34 & -0.30 & 0.14 \end{bmatrix}, \tag{4.18}$$

$$\mathbf{A}_{ECM} = \begin{bmatrix} 6.33 & 6.32 & 0.67 & -0.32 \\ 14.20 & -14.19 & -2.88 & -0.09 \\ 12.45 & -1.76 & -4.96 & -11.33 \\ 11.28 & 0.07 & 11.01 & 0.49 \end{bmatrix}. \tag{4.19}$$

The matrices $\mathbf{W}_{ECM}$ and $\mathbf{A}_{ECM}$ have condition numbers of 2.57 and 5.52 respectively. These are slightly larger than the condition numbers expected from theory, which is to be expected due to non-ideal experimental conditions.

As mentioned previously, each column in $\mathbf{W}$ is a Stokes vector corresponding to an input polarisation state. As such, the first row of $\mathbf{W}$ describes differences between the intensity of the four input polarisation states. Theoretically, the four input polarisations should have the same intensity. However, it can be seen from $\mathbf{W}_{ECM}$ that there is a slight variation across the four input states. On the other hand, each row in $\mathbf{A}$ is a Stokes vector relating to an output analyser state, which implies that the first column of $\mathbf{A}$ shows differences between the transmittance of the four output analyser arms of the PSA. In theory, the four arms should have equal transmittance, but it can be seen from $\mathbf{A}_{ECM}$ that in reality, there is a variation in transmittance across the four arms. Both of these variations are likely due to non-ideal polarisation elements, such as the variable waveplates and the non-polarising beamsplitters which were employed.

$\mathbf{W}_{ECM}$ and $\mathbf{A}_{ECM}$ can be better compared to the matrices expected from theory by first normalising them such that each polarisation state has equal intensity or transmittance. In other words, $\mathbf{W}_{ECM}$ is normalised by its first row, while $\mathbf{A}_{ECM}$ is normalised by its first column. The resulting matrices are shown in Equations 4.21

and 4.20 below.

$$\mathbf{W}_{ECM}^{norm} = \begin{bmatrix} 1.00 & 1.00 & 1.00 & 1.00 \\ 0.98 & 0.08 & -0.02 & -0.43 \\ 0.07 & 0.31 & 0.59 & -0.85 \\ -0.12 & 0.95 & -0.86 & 0.44 \end{bmatrix} \tag{4.20}$$

$$\mathbf{A}_{ECM}^{norm} = \begin{bmatrix} 1.00 & 1.00 & 0.11 & -0.05 \\ 1.00 & -1.00 & -0.20 & -0.01 \\ 1.00 & -0.14 & -0.40 & -0.91 \\ 1.00 & 0.01 & 0.98 & 0.04 \end{bmatrix} \tag{4.21}$$

Comparing Equation 4.20 to Equation 4.2, it can be seen that the values in $\mathbf{W}_{ECM}^{norm}$ are significantly different from the theoretical prediction. Possible causes for the difference are inaccuracies in the orientation of the fast axes of the VWP and the applied phase differences, as well as the additional components in the optical path, such as mirrors and lenses, that are unaccounted for in the theoretical matrix. Comparing Equation 4.21 to Equation 4.3, it can be seen that there are also some differences between the theoretically and experimentally obtained matrix, particularly in the last two rows. One possible reason for the deviation could be imperfect non-polarising beamsplitters, which could have small differences between the Fresnel coefficients of the s and p polarisations. In addition, secondary reflections could explain the larger deviation in the third and fourth rows of $\mathbf{A}_{ECM}^{norm}$, which correspond to the analyser arms measuring linearly polarised light at 45° and left circularly polarised light respectively. As the two analysed polarisation states are not orthogonal, secondary reflections from one arm could still arrive at the detector of the other arm, and thus contribute to the calibrated matrix. In contrast, the first two rows, which correspond to the analyser arms measuring x and y linearly polarised light respectively, show a smaller deviation from theory. As the two analyser arms are measuring crossed polarisation states, secondary reflections from one arm would not be detected at the output of the other arm. In all, although there were discrepancies between the instrument matrices obtained and their theoretical counterparts, the deviations observed were deemed to be reasonable.

The obtained matrices, $\mathbf{A}$ and $\mathbf{W}$, were further verified by measuring the Mueller matrices of a Glan-Thompson prism and a quarter waveplate (*Thorlabs WPQ10M-561*) at different orientation angles. Specifically, the orientation angles used ranged from 0° to 180°, in step sizes of 10°. As a first check, the experimentally obtained Mueller matrices, $\mathbf{M}^{exp}$, of these two test samples, were multiplied with a known input Stokes vector, and the output intensities were qualitatively compared to the results obtained using the theoretical Mueller matrices, $\mathbf{M}^{theory}$, at each orientation angle. The quantitative difference between the two Mueller matrices, $\mathbf{M}^{exp}$ and $\mathbf{M}^{theory}$, was also computed, by first normalising each matrix by their respective $(1,1)$ matrix elements. The difference between the normalised matrices for each orientation angle was then calculated using two measures - the Frobenius norm and an element-wise root-mean-square error (RMSE). The Frobenius norm is defined as

$$\left\|\Delta\mathbf{M}(\theta_n)\right\|_F = \sqrt{\sum_{i,j} \left|\Delta M_{ij}(\theta_n)\right|^2}\,, \tag{4.22}$$

where $\Delta\mathbf{M} = \mathbf{M}^{exp,n} - \mathbf{M}^{theory,n}$, with $\mathbf{M}^{exp,n}$ and $\mathbf{M}^{theory,n}$ denoting the normalised experimental and theoretical Mueller matrices respectively. ΔM_{ij} is the $(i,j)^{th}$ element of the $\Delta\mathbf{M}$, θ_n is the n^{th} orientation angle and the summation is taken over all elements of $\Delta\mathbf{M}$. The Frobenius norm provides a quantitative measure of the difference across the entire Mueller matrix and can be interpreted as an estimate of the total error across all matrix elements for a single orientation angle. The average error across Mueller matrix elements for each orientation angle is related to the Frobenius norm by a multiplicative factor of $\frac{1}{4}$. On the other hand, the element-wise RMSE is computed as

$$\mathrm{RMSE}_{ij} = \sqrt{\frac{1}{N}\sum_{n=1}^{N} \left|\Delta M_{ij}(\theta_n)\right|^2}\,. \tag{4.23}$$

Here, N is the total number of orientation angles used. The element-wise RMSE calculates the error for each Mueller matrix element across all tested orientation angles, and provides further insight, highlighting any matrix elements which potentially demonstrate larger error.

For the Glan-Thompson prism, a Stokes vector corresponding to an input beam that is linearly polarised in the x direction was used. Theoretically, the output intensity should be governed by Malus's law,

$$I(\theta) = I_o \cos(\theta) \ , \tag{4.24}$$

where θ is the orientation angle of the prism and I_o is the maximum intensity across all orientation angles. This behaviour was observed in both the theoretical and experimental results, which are compared in the left figure of Figure 4.8. Both experimental and theoretical results have been normalised by their respective I_o.

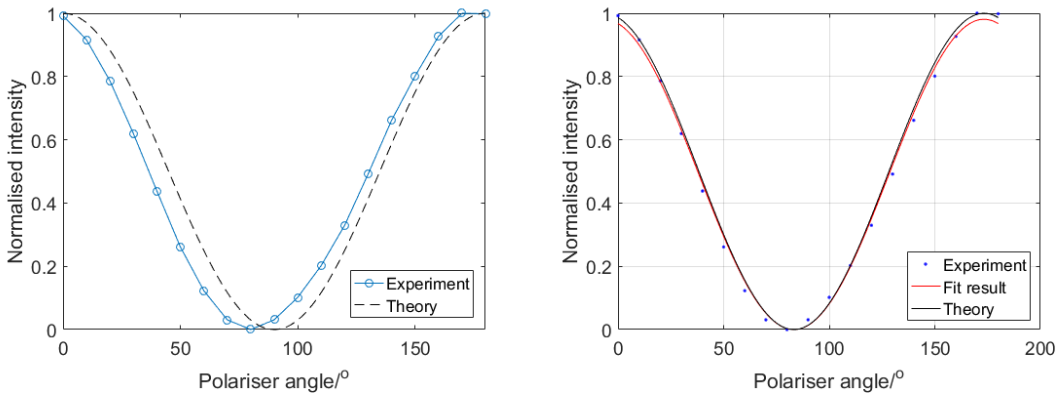

Figure 4.8: Verification of calibration using a Glan-Thompson prism Comparison of intensity simulated using the experimental and theoretical Mueller matrices before (left) and after (right) fitting and correcting for offset.

From Figure 4.8, it can also be seen that the experimental result shows a systematic offset of about 10°, which can be attributed to an offset in the starting orientation of the Glan-Thompson. This offset has to be accounted for in the theoretical Mueller matrices before any quantitative comparison can be made. In order to obtain a better estimation of the offset, the experimental data was fit with the function

$$I(\theta) = a \cos^2(\theta - b) + c \ , \tag{4.25}$$

where a, b and c are constants determined by the fit. The determined constants were $a = 0.98$, $b = -6.73°$ and $c = -6.01 \times 10^{-6}$ with a R-squared value of 0.996, and a plot showing the fit is shown on the right of Figure 4.8. As expected, a is close to 1 and c is small, and b shows an offset of 6.73°, which was used to

adjust the theoretical Mueller matrices. The Frobenius norm and the element-wise RMSE of the difference between the theoretical and experimental matrices were also computed, and are shown in Figure 4.9 and Table 4.4 respectively. The largest Frobenius norm observed was 0.27, and the largest element-wise RMSE of 0.064 was observed for matrix elements $(3, 1)$ and $(4, 1)$.

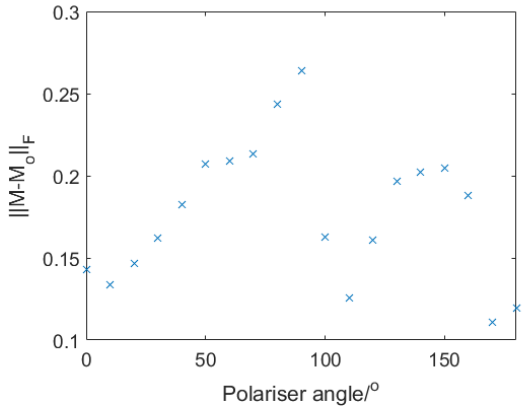

Figure 4.9: Frobenius norm of the difference between the theoretical and experimental Mueller matrices for the Glan-Thompson prism as a function of the transmission axis.

0	0.042	0.059	0.030
0.050	0.049	0.060	0.020
0.063	0.057	0.049	0.025
0.064	0.038	0.051	0.008

Table 4.4: Element-wise RMSE of the difference between the theoretical and experimental Mueller matrices for the Glan-Thompson prism.

For the quarter wave plate, a Stokes vector corresponding to an input beam that is linearly polarised in the x direction was also used. To detect changes in the output polarisation state, the ideal Mueller matrix of a linear polariser with its transmission axis oriented parallel to the x-direction was also multiplied by the experimental Mueller matrices. The output intensities are then the first element of the output Stokes vector that was computed as

$$\vec{S}_{out}(\theta) = \mathbf{M}^{LP}\mathbf{M}^{QWP,exp}(\theta_n)\vec{S}_{in} \tag{4.26}$$

Here, $\vec{S}_{in}$ and $\vec{S}_{out}$ are the input and output Stokes vectors respectively, $\mathbf{M}^{LP}$ is the Mueller matrix of the ideal linear polariser and $\mathbf{M}^{QWP,exp}(\theta_n)$ is the Mueller matrix of the quarter waveplate measured at the orientation angle θ_n. Theoretically, the intensity variation as a function of orientation angle is given by

$$I(\theta) = \frac{I_o}{2}\left(1 + \cos^2 2\theta\right) \ . \tag{4.27}$$

The plot on the left of Figure 4.10 shows the comparison between the intensities calculated from the experimental and theoretical Mueller matrices, once again normalised by I_o. Both intensities exhibit the behaviour predicted by Equation 4.27, although a systematic offset can be seen in the experimental results. As was the case for the Glan-Thompson prism, this systematic offset can be attributed to an experimental uncertainty in the starting orientation of the test quarter waveplate.

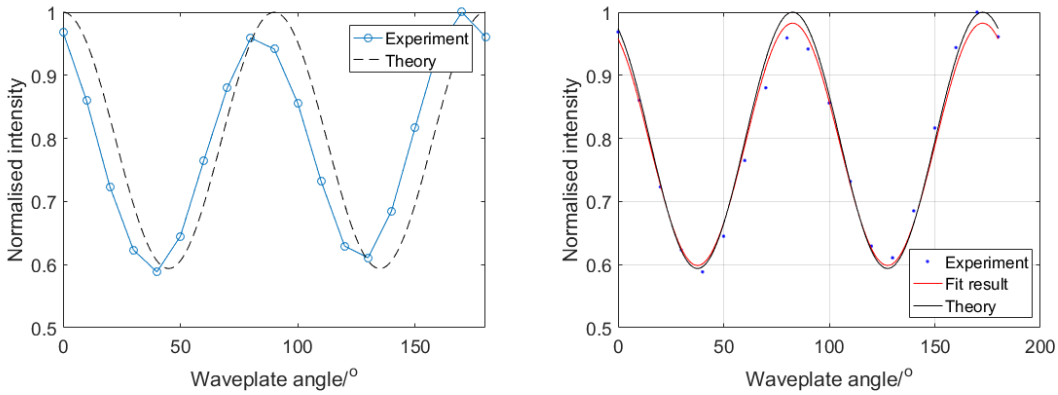

Figure 4.10: Verification of calibration using a quarter waveplate
Comparison of intensity simulated using the experimental and theoretical Mueller matrices before (left) and after (right) fitting and correcting for offset.

As before, a fit was conducted in order to determine the offset, but this time the fit was done with the function

$$I = a\cos^2(2(\theta - b)) + c \ , \tag{4.28}$$

where a, b and c are constants determined by the fit. The determined constants were $a = 0.38$, $b = -7.362°$ and $c = 0.5986$ with a R-squared value of 0.98, and a plot showing the fit is shown on the right of Figure 4.10. The offset of 7.362° was used to correct the theoretical matrices, and the difference between the theoretical

and experimental matrices were computed. The Frobenius norm of the difference and the element-wise RMSE are shown in Figure 4.11 and Table 4.5 respectively. The largest Frobenius norm was 0.11 and the largest RMSE of 0.038 was observed for the matrix element $(2, 3)$.

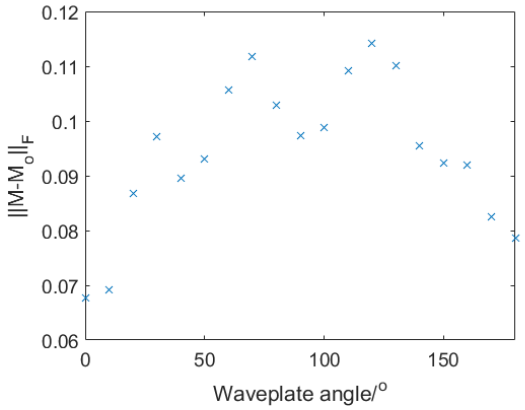

Figure 4.11: Frobenius norm of the difference between the theoretical and experimental Mueller matrices for the quarter waveplate.

0	0.022	0.021	0.024
0.013	0.020	0.036	0.025
0.010	0.033	0.017	0.026
0.028	0.023	0.020	0.023

Table 4.5: Element-wise RMSE of the difference between the theoretical and experimental Mueller matrices for the quarter waveplate.

From these measurements, the calibration matrices obtained from ECM are seen to provide reasonable results, and have thus been verified. Furthermore, there are no matrix elements that consistently demonstrate a larger error. ECM is not a perfect technique - though it accounts for all elements in the optical path, noise can still lead to errors in the calibration. Inaccuracies in the calibration matrices would in turn result in a systematic error in the computed Mueller matrices. Yet, the observed differences between the experimental and theoretical Mueller matrices could also originate from other sources other than calibration errors. For example, non-ideal test samples would also lead to a systematic error while experimental noise would cause random errors in the computed Mueller matrix. It is challenging to separate

the contributions from various systematic errors, but it is possible to estimate the amount of random fluctuations in the Mueller matrix based on the fluctuations in the detector signal. The propagation of experimental noise to the Mueller matrix is discussed further in Section 5.

For conciseness, in the rest of this thesis, the matrices obtained from ECM will simply be denoted as **A** and **W**.

4.4 Data Acquisition

4.4.1 Acquisition Procedure

Using the setup described in Section 4.1, spatial masks for single pixel imaging were sequentially projected onto the sample plane using the DMD for each input polarisation state. The four detectors in the PSA then acquired the data, which was recorded by a data acquisition system (*National Instruments, DAQ 6341*) with a sampling rate of 100Hz and an acquisition time of 30ms. The resulting dataset, consisting of 30 datapoints, was averaged to form the intensity recorded in one measurement sample. The sampling rate and acquisition time were determined based on the parameters used for lock-in detection, which was employed to increase the SNR of the measurements and will be detailed further in Section 4.4.2. Before each image acquisition, a dark measurement was also taken for all four detectors with the same acquisition parameters, and these recorded values were subtracted from subsequent measurements taken by each detector.

A close examination of multiple measurements acquired over an unchanging incident illumination showed the presence of spikes, which seemed to occur randomly across any one of the four detectors. An example is shown in Figure 4.12, which shows 1000 measurement samples taken by detector D3 under constant illumination, without any polarimetric elements in front of the detector. The dataset corresponding to the spike (dataset number 712 in the left plot of Figure 4.12) is shown on the right of Figure 4.12, compared to a different dataset which did not exhibit a

spike (specifically the dataset corresponding to sample 500 in the left plot of Figure 4.12).

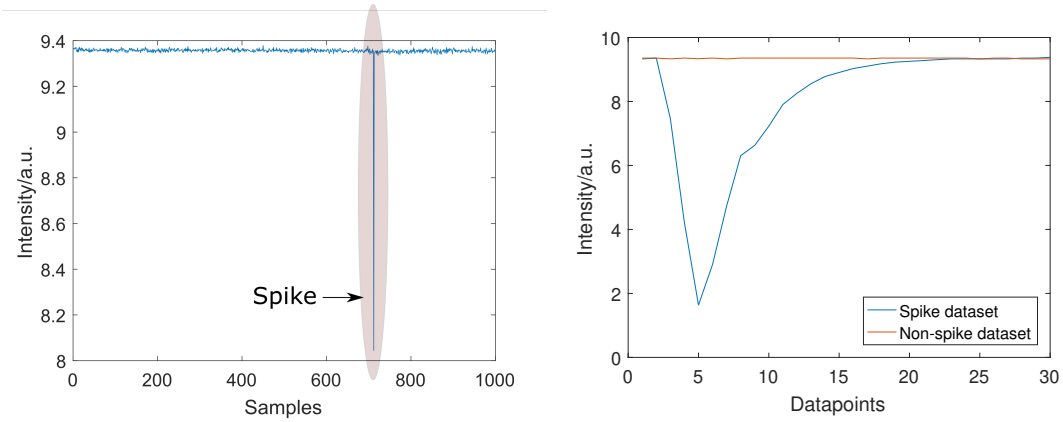

Figure 4.12: (left) Measurement samples, where each sample was an average over 30 datapoints, taken by detector D3 under constant illumination showing a spike in the data, (right) the datapoints making up the sample corresponding to the observed spike compared to a sample that did not exhibit a spike.

It can be seen that the datapoints making up the spiked measurement sample were highly anomalous. The source of this anomaly was not clear, but since no polarimetric elements were present in the measurements shown in Figure 4.12 and spikes have been observed to occur randomly in all four of the detectors, it was hypothesised that the spikes were due to instability of the laser source. In order to reject anomalous data, the standard deviation for each measurement sample was computed. The resulting standard deviation corresponding to the measurements in Figure 4.12 is shown below in Figure 4.13, and it is obvious that the anomalous dataset has a large standard deviation, as can be expected given the fluctuations observed in the right plot of Figure 4.12. Checking the values of the standard deviation in other instances where spikes have occurred, a threshold on the standard deviation was empirically set to be 0.03. Thus, measurement samples that had a standard deviation larger than 0.03 were rejected and the measurement was repeated.

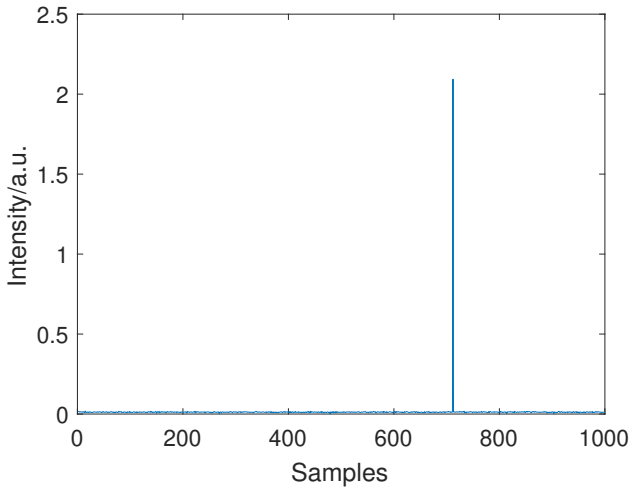

Figure 4.13: Standard deviation for each measurement sample in Figure 4.12.

As discussed in Section 2.4 (see Equation 2.61), for the j^{th} input polarisation state and the i^{th} analysed polarisation state, the related output intensity corresponding to each spatial mask can be concatenated into a vector, $\vec{y}_{ij}$, which can be related to the object transmission, $\vec{x}_{ij}$, as

$$\vec{y}_{ij} = \mathbf{\Phi}\vec{x}_{ij} \ , \tag{4.29}$$

where the rows in $\mathbf{\Phi}$ correspond to the projected basis vectors. As discussed in Section 2.4, any complete set of basis vectors (i.e. $\mathbf{\Phi}$ is invertible) can be used for single pixel imaging. In this work, a spatial basis formed by the rows of a 256×256 scrambled Hadamard matrix was used [195]. Such a matrix is obtained by a randomisation of the rows and columns of the conventional (i.e. not scrambled) Hadamard matrix, which consists of -1 and $+1$ elements. In the context of compressive sensing, it was proposed that the additional randomisation step applied to the Hadamard matrix would result in a matrix that is universally incoherent with any chosen sparsifying basis [195], thereby minimising the number of measurements required for an exact reconstruction. Though compressive sensing was not utilised in this work, the scrambled Hadamard matrix was chosen as the spatial basis in view of potentially incorporating this method in the future. Each row of the scrambled Hadamard basis was reshaped into a square, resulting in a spatial mask consisting of 16×16 pixels. The full set of 256 masks was used.

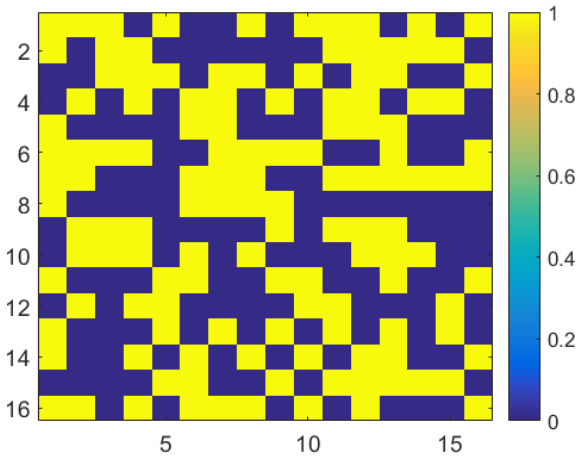

Figure 4.14: An example of a positive Hadamard mask used in the experiment.

In order to project the spatial masks, the DMD was set to mirror the computer screen, and a MATLAB code utilising the PsychToolBox extension [196, 197, 198] was written to project the spatial masks onto the screen. As the DMD is only able to provide binary modulation, in practice, it is necessary to project two spatial masks per basis vector - a positive mask displaying the $+1$ elements, and a negative mask consisting of the -1 elements. An example of a positive spatial mask used in the experiment is shown in Figure 4.14. The difference between the two corresponding detector intensities is then a measurement of the true projection of the object intensity transmission and the Hadamard basis mask. Figure 4.15 illustrates this process using a basis vector from a 4×4 Hadamard matrix, that has been reshaped to be a 2×2 matrix. As such, for each of the four input and analysed polarisation states, $2 \times 256 = 512$ measurements were taken.

1	-1	=	1	0	-	0	1
-1	1		0	1		1	0

Figure 4.15: Illustration showing how two non-zero spatial masks can be used to obtain the projection between the object transmission and the Hadamard basis mask.

4.4.2 Lock-in Detection

Lock-in detection [199] was employed to improve the SNR of the measurements. Before implementing lock-in detection, it is useful to first study the power spectrum of the noise in the data as this would enable the identification of suitable modulation frequencies. Asquare illumination area covering the full height of the DMD was projected onto the empty sample plane and the resulting signal was measured 1000 times by the PSA over an acquisition time of 1s, with a sampling frequency of 20kHz. The same measurement was taken without any illumination on the DMD. A Fourier transform of both datasets was then performed, and the power spectrum was computed as the square of the Fourier amplitudes averaged over the 1000 acquisitions. The resulting power spectra are shown in Figures 4.16 and 4.18, with the zero-order frequency set to zero for readability. It can be seen that in both cases, the noise is mainly concentrated within ±1kHz. In view of these observations, the modulation frequency for lock-in detection was set to 5kHz.

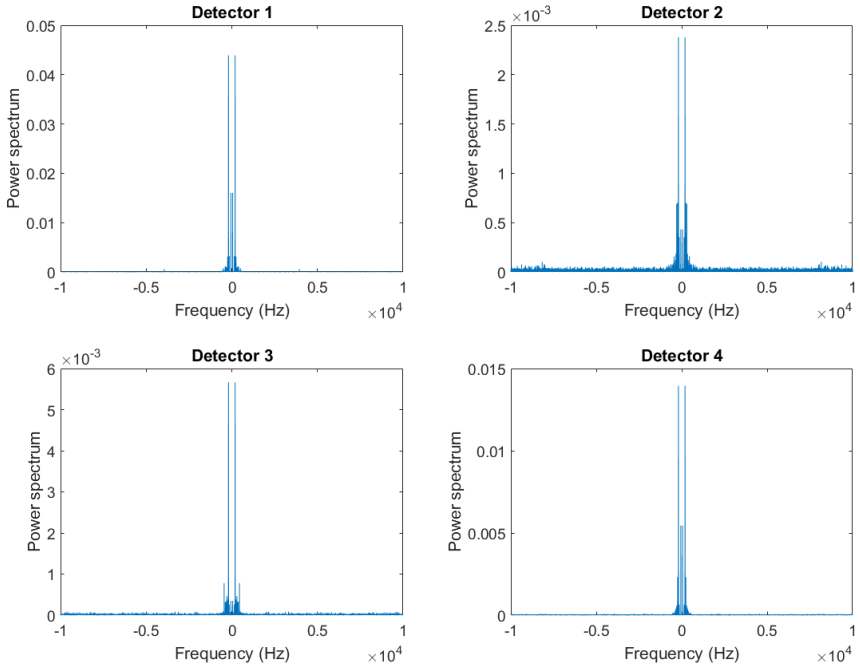

Figure 4.16: The power spectrum of the noise obtained when the detectors were illuminated. For readability, the zero-order frequency has been set to zero.

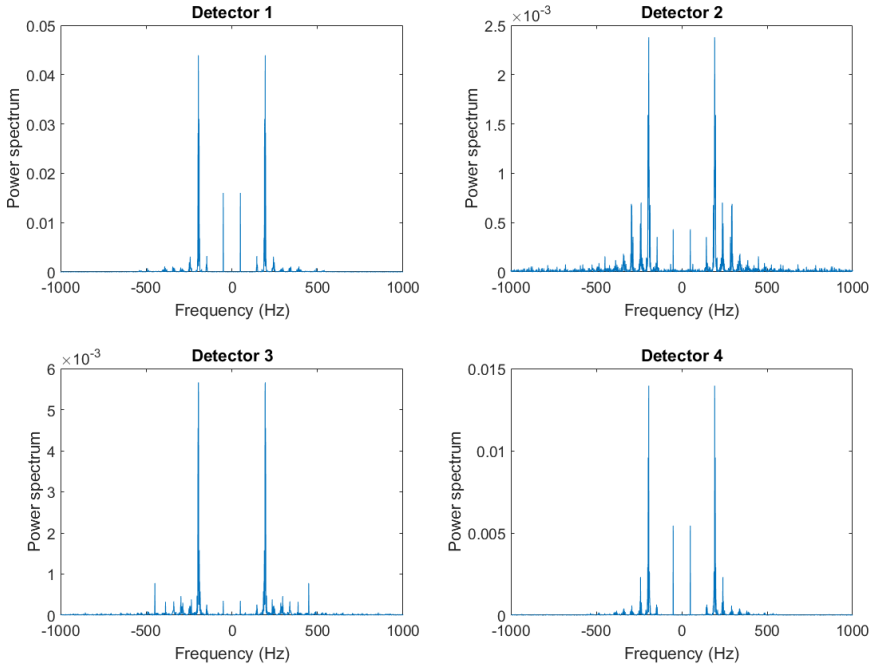

Figure 4.17: Same as Figure 4.16, but zoomed in on the central region of the plot.

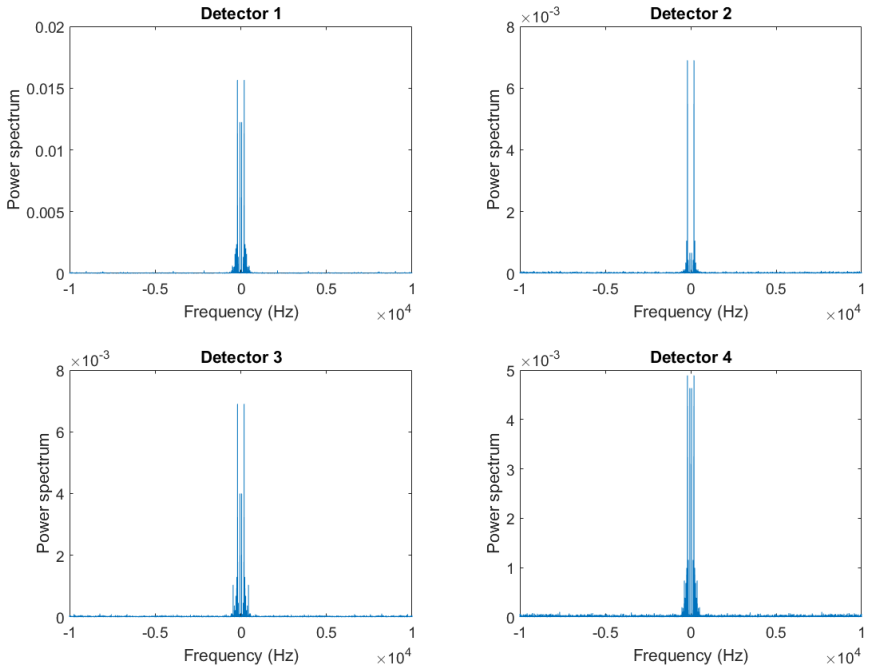

Figure 4.18: Log of the noise spectrum obtained without any illumination on the detectors. For readability, the zero-order frequency has been set to zero.

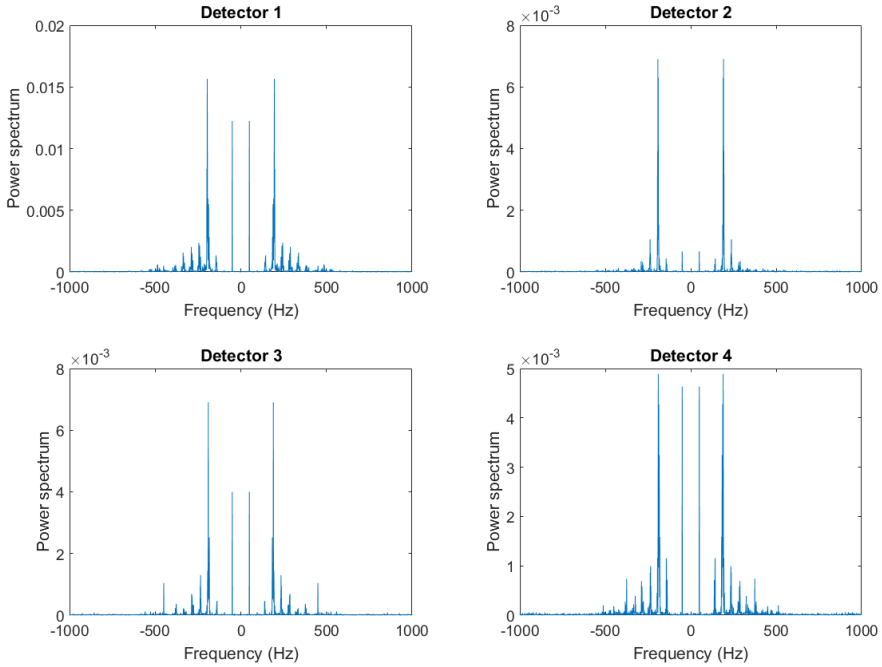

Figure 4.19: Same as Figure 4.18, but zoomed in on the central region of the plot.

Lock-in detection was then implemented as follows. The laser intensity was first modulated using a frequency generator (*TTi, TG330*), at a frequency of 5kHz. For each input polarisation state, the four detector outputs were sequentially forwarded to a lock-in amplifier (*Stanford Research Systems, Model SR530*), through the use of an analog multiplexer (*Texas Instruments, MPC509*). The lock-in amplifier was set to a time constant of $\tau = 30$ms and a sensitivity of 5mV. With these settings, the output signal was filtered and amplified within a range of $f_{\text{cutoff}} = \frac{1}{2\pi\tau} \approx 5$Hz around the modulation frequency. These settings were selected such that with a scattering medium (specifically the scattering phantom SM4, see Section 4.6) present in the sample plane illuminated by one of the Hadamard masks used for single pixel imaging, the maximum signal from the four detectors is close to the limit of the dynamic range of 10V without saturating the detectors. The resulting signal output from the lock-in amplifier was then recorded using a data acquisition system (*National Instruments, DAQ 6341*) at a sampling rate of 100Hz. Finally, 30 samples were acquired and averaged to provide the measured data for each detector.

The advantage of using lock-in detection can be clearly seen by a comparison of

the SNR of a typical measurement before and after its implementation. 1000 measurements were taken with a scattering medium present, with and without lock-in detection. For this experiment, all pixels on the DMD were set to be on, and the first input polarisation, with a Stokes vector corresponding to the first column of **W** (see Equation 4.18), was used. In addition, since the four detectors were identical, only detector 4 was studied. For a fair comparison, the same sampling rate of 100Hz and acquisition time of 30ms were used for both measurements. Figure 4.20 shows the results. A low frequency modulation seems to be present in the dataset taken with lock-in detection, and this is thought to be caused by temporal instability in the frequency generator. This was not investigated further because qualitatively, the signal with lock-in detection still showed smaller fluctuations with respect to the mean signal. This can be quantified in terms of the SNR, computed as the ratio of the mean to the standard deviation of the acquired data. When lock-in detection was used, the mean and standard deviation were found to be 5.6235 and 0.0083 respectively, resulting in a SNR of 682. Conversely, when lock-in detection was not used, the mean and standard deviation were found to be 0.0143 and 0.0001 respectively, such that the SNR was 105. Thus, it can be seen that lock-in detection has provided close to seven-fold improvement to the measured SNR.

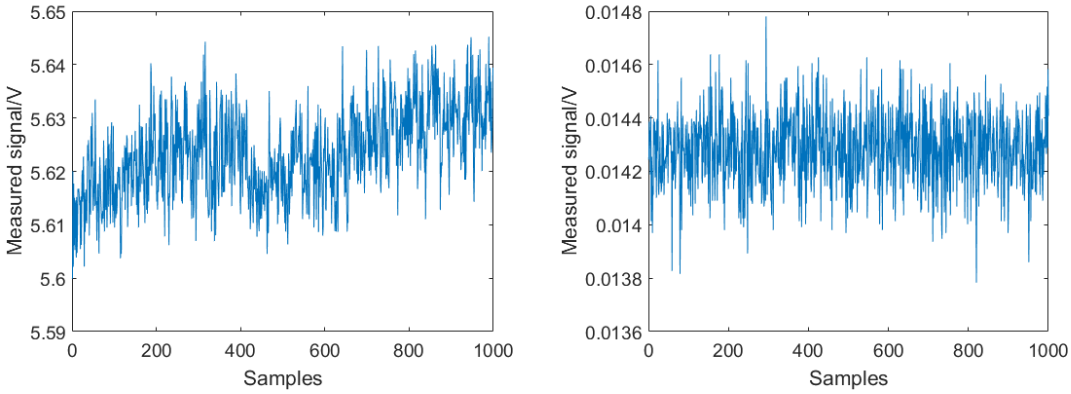

Figure 4.20: Acquired data using detector 4 with SM4 present (left) With lock-in detection (right) Without lock-in detection.

The improvement in SNR has a significant effect on the intensity images reconstructed by single pixel imaging, and as a consequence, the resulting polarimetric images. As an example, intensity images of the test object hidden behind the scattering medium were taken using single pixel imaging, with and without using

lock-in detection. The results are presented in Figure 4.21, where the letter R is clearly seen the image taken with lock-in detection. In stark contrast, the image taken without lock-in detection is heavily corrupted by noise and the letter R can no longer be seen. Further matrix inversions required to retrieve the polarimetric images can only exacerbate the problem. Thus, it can be seen that lock-in detection significantly increases the SNR, which is important considering the low light levels involved in measurements of scattering media. As such, lock-in detection was employed in this work.

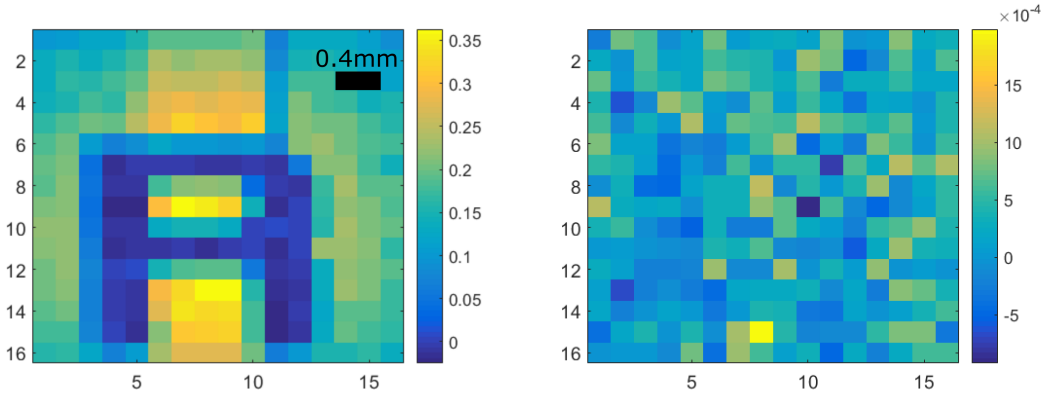

Figure 4.21: Single pixel images of the test object taken (left) with lock-in detection (right) without lock-in detection.

4.5 Data Processing

4.5.1 Obtaining the Spatially Resolved Mueller Matrix

For each input and output polarisation state, the detected intensities corresponding to the project spatial masks were used to reconstruct an image of the object. This was done using Equation 2.62, which for the i^{th} analysed and the j^{th} input polarisation state can be written as

$$\vec{x}_{ij} = \mathbf{\Phi}^{-1}\vec{y}_{ij} \ , \tag{4.30}$$

which follows from Equation 4.29. The set of reconstructed intensity images, $\vec{x}_{ij}$, for all input and analysed polarisation states then provides the detector matrix $\mathbf{D}$ for

each pixel. As discussed in Section 4.1, the four parts of the system can be described in terms of their corresponding matrices, **D**, **A**, **M** and **W**. These four matrices are related via a matrix product, which can be written for the n^{th} pixel as

$$\mathbf{D}_n = \mathbf{A}\mathbf{M}_n\mathbf{W} \ , \tag{4.31}$$

when no scattering medium is present. Since four input and analysed polarisation states were used, each of these matrices has a size of 4×4. The instrument matrices, **A** and **W**, which have been obtained using ECM (see Section 4.3), can then be used to compute **M** via a matrix inversion on a pixel-by-pixel basis as

$$\mathbf{M}_n = \mathbf{A}^{-1}\mathbf{D}_n\mathbf{W}^{-1} \ . \tag{4.32}$$

When a scattering medium is present, Equation 4.32 is altered to adjust for the contribution of the scattering medium in the manner described in Section 3.1.3, and can be written as

$$\mathbf{M}_n = \mathbf{M}^{SM,-1}\mathbf{A}^{-1}\mathbf{D}_n\mathbf{W}^{-1} \ , \tag{4.33}$$

where, as in Section 3.1.3, $\mathbf{M}^{SM,-1}$ denotes the Mueller matrix of the scattering medium. It was assumed that the utilised pixel size of 0.2mm was sufficiently large such that the $\mathbf{M}^{SM,-1}$ did not vary significantly across the image pixels. As such, unless otherwise stated, the same correction for the contribution of the scattering medium was applied to all pixels.

As explained in Section 2.2.5, in practice, obtaining $\mathbf{M}_n$ via matrix inversions, as written in Equations 4.32 and 4.33, does not ensure the physicality of the obtained Mueller matrix, especially in the presence of noise [200]. In this work, a Constrained Least Squares algorithm is used instead, and this is discussed further in the next sub-section. Finally, once $\mathbf{M}_n$ has been computed for each pixel, the spatially resolved Mueller matrix is obtained.

4.5.2 Constrained Least Squares Algorithm

As discussed, a direct inversion of the instrument matrices (see Equation 4.32) is not guaranteed to provide a physically acceptable Mueller matrix [200]. In this work, a constrained least squares algorithm (CLSQR) was used to ensure the physicality of the Mueller matrices (see Section 2.2.6) computed from experimental data. Here, the CLSQR algorithm is detailed and tested on simulated data. The results are compared to those obtained using a direct inversion, as well as an algorithm based on maximum likelihood estimation (MLE) that was previously proposed by Aiello *et al.* [201].

The CLSQR algorithm seeks to find the physical Mueller matrix, $\mathbf{M}'$, that minimises the function

$$\mathcal{F}(\mathbf{M}') = \left\| \mathbf{D} - \mathbf{A}\mathbf{M}'\mathbf{W} \right\|_2 \ . \tag{4.34}$$

In other words, the obtained $\mathbf{M}'$ is a physical estimate of the ideal Mueller matrix, $\mathbf{M}$, that minimises the difference between the theoretical and experimental detector intensities.

$\mathbf{M}'$ is constrained to be physical by making use of its related $\mathbf{H}$ matrix (see Section 2.2.6)), which can be obtained from $\mathbf{M}'$ as

$$\mathbf{H} = \frac{1}{4} \sum_{k,l=0}^{3} m_{kl} \left(\sigma_k \otimes \sigma_l^* \right) \ , \tag{4.35}$$

where m_{kl} denotes the $(k,l)^{th}$ element of $\mathbf{M}'$, and σ_k are the 2×2 Pauli matrices (see Equation 2.31). Writing out the elements of $\mathbf{H}$ explicitly, it can be shown that the elements of $\mathbf{H}$ can be expressed in terms of Jones matrix elements as

$$\mathbf{H} = \begin{bmatrix} \langle T_{00}T_{00}^* \rangle_t & \langle T_{00}T_{01}^* \rangle_t & \langle T_{00}T_{10}^* \rangle_t & \langle T_{00}T_{11}^* \rangle_t \\ \langle T_{01}T_{00}^* \rangle_t & \langle T_{01}T_{01}^* \rangle_t & \langle T_{01}T_{10}^* \rangle_t & \langle T_{01}T_{11}^* \rangle_t \\ \langle T_{10}T_{00}^* \rangle_t & \langle T_{10}T_{01}^* \rangle_t & \langle T_{10}T_{10}^* \rangle_t & \langle T_{10}T_{11}^* \rangle_t \\ \langle T_{11}T_{00}^* \rangle_t & \langle T_{11}T_{01}^* \rangle_t & \langle T_{11}T_{10}^* \rangle_t & \langle T_{11}T_{11}^* \rangle_t \end{bmatrix} \ , \tag{4.36}$$

where T_{ij} denotes the $(i,j)^{th}$ component of the Jones matrix. As such, it can be seen that $\mathbf{H}$ is the complex correlation matrix of the underlying Jones matrix elements. Hence, any $\mathbf{H}$ that is related to a physically acceptable Mueller matrix is required to be a positive semidefinite matrix [137], which allows it to be represented using the Cholesky decomposition,

$$\mathbf{H} = \mathbf{L}\mathbf{L}^{\dagger} \ , \tag{4.37}$$

where $\mathbf{L}$ is a lower triangular matrix containing 16 real parameters of the form [201]

$$\mathbf{L} = \begin{bmatrix} l_1 & 0 & 0 & 0 \\ l_5 + il_6 & l_2 & 0 & 0 \\ l_{11} + il_{12} & l_7 + il_8 & l_3 & 0 \\ l_{15} + il_{16} & l_{13} + il_{14} & l_9 + il_{10} & l_4 \end{bmatrix} \ . \tag{4.38}$$

Using Equations 4.34, 4.35 and 4.37, an optimal set of parameters $\{l_1, l_2, ..., l_{16}\}$ that minimises the function $\mathcal{F}$ can be found through a minimisation algorithm. Here, the `fminsearch` function in MATLAB was applied. An optimised $\mathbf{H}$ matrix, $\mathbf{H}^{opt}$, can then be reconstructed using Equation 4.37, and the final Mueller matrix, that is now guaranteed to be physical, can be computed element-wise as

$$m_{kl} = \mathrm{tr}\{\mathbf{H}^{opt}\left[\sigma_k \otimes \sigma_l^*\right]\} \ . \tag{4.39}$$

The CLSQR algorithm follows closely to the MLE algorithm proposed by Aiello *et al.* [201], except that the optimisation function used in the latter is given by

$$\mathcal{L}(\mathbf{M}) = \sum_{a,b} f_{ab} \ln\left[p_{ab}(\mathbf{M})\right] \ , \tag{4.40}$$

where f_{ab} and $p_{ab}(\mathbf{M}) = \vec{a}_a^{\top}\mathbf{M}\vec{w}_b$ are the experimental and theoretical probabilities of measuring a non-zero intensity value at the detector, for an analysed polarisation state, $\vec{a}_a^{\top}$, and an input polarisation state, $\vec{w}_b$. In addition, the summation is taken over all input and analysed polarisation states. In this approach, the Mueller matrix is the solution that maximises the likelihood function in Equation 4.40. This work had initially tested the MLE algorithm using simulated data, but it was found that the retrieved Mueller matrices were incorrect, even when no noise was present.

Each simulated dataset was generated by using the theoretical Mueller matrix of either a quarter waveplate or linear polariser, whose Mueller matrices have a known form. The detector intensities were then obtained using Equation 4.31 and the theoretical instrument matrices for the setup used in this work, $\mathbf{A}_{theory}$ and $\mathbf{W}_{theory}$ (see Equations 4.2 and 4.3). As an example, the results obtained by the MLE algorithm when using the Mueller matrix for a linear polariser with its transmission axis at 25° is shown here. The groundtruth Mueller matrix is given by

$$\mathbf{M}^{GT} = \begin{bmatrix} 1.00 & 0.64 & 0.77 & 0.00 \\ 0.64 & 0.41 & 0.49 & 0.00 \\ 0.77 & 0.49 & 0.59 & 0.00 \\ 0.00 & 0.00 & 0.00 & 0.00 \end{bmatrix}, \tag{4.41}$$

but the Mueller matrix retrieved by the MLE algorithm using ideal noiseless data was

$$\mathbf{M}^{MLE} = \begin{bmatrix} 1.00 & 0.64 & 0.77 & 0.00 \\ 0.45 & 0.29 & 0.35 & 0.00 \\ 0.89 & 0.57 & 0.68 & 0.00 \\ 0.00 & 0.00 & 0.00 & 0.00 \end{bmatrix}. \tag{4.42}$$

These two matrices can be seen to be very different, with the largest difference between elements of 0.189. As the groundtruth Mueller matrix was used as the initial guess for the algorithm, this suggests that the difference cannot be explained by the algorithm finding a local maximum. Interestingly, a lower value was obtained for the optimisation function (see Equation 4.40) when the groundtruth Mueller matrix was used. One possible explanation behind this discrepancy could be that the instrument matrices used by Aiello *et al.* are different from those used in this work. Aiello *et al.* utilised the same set of six polarisation states for the PSA and the PSG, namely linearly polarised light at 0°, 90°, 45° and 135°, along with left and right circularly polarised light. The instrument matrices corresponding to these

polarisation states are

$$\mathbf{A}_{Aiello} = \mathbf{W}_{Aiello}^{\top} = \begin{bmatrix} 1.00 & 1.00 & 0.00 & 0.00 \\ 1.00 & -1.00 & 0.00 & 0.00 \\ 1.00 & 0.00 & 1.00 & 0.00 \\ 1.00 & 0.00 & -1.00 & 0.00 \\ 1.00 & 0.00 & 0.00 & -1.00 \\ 1.00 & 0.00 & 0.00 & 1.00 \end{bmatrix} . \tag{4.43}$$

Using ideal noiseless data that was simulated using $\mathbf{A}_{Aiello}$ and $\mathbf{W}_{Aiello}$, the groundtruth Mueller matrix, $\mathbf{M}^{GT}$, was obtained exactly by the MLE algorithm. A third set of instrument matrices was also tested, defined as

$$\mathbf{A}_{tetra} = \mathbf{W}_{tetra}^{\top} = \sqrt{\frac{2}{3}} \begin{bmatrix} \sqrt{\frac{3}{2}} & 1 & 0 & -\frac{1}{\sqrt{2}} \\ \sqrt{\frac{3}{2}} & -1 & 0 & -\frac{1}{\sqrt{2}} \\ \sqrt{\frac{3}{2}} & 0 & 1 & \frac{1}{\sqrt{2}} \\ \sqrt{\frac{3}{2}} & 0 & -1 & \frac{1}{\sqrt{2}} \end{bmatrix} , \tag{4.44}$$

where the polarisation states used form a regular tetrahedron within the Poincaré sphere with an edge length of $\frac{2\sqrt{2}}{\sqrt{3}}$. With this third set, it was also found that the Mueller matrix retrieved by the MLE algorithm matched the groundtruth result. The observations from these tests seem to suggest that the instrument matrices used in this work introduce a bias in the optimisation function described in Equation 4.40 whereas those used by Aiello *et al.* represent a mutually unbiased basis [201]. At the point of writing, the reason behind this phenomenon was still unclear, but it was surmised that it could be due to an unequal distribution of the polarisation states sampled by the PSA across the Poincaré sphere. Figure 4.22 shows the distribution of the polarisation states on the Poincaré sphere for the PSG and the PSA used in this work. In contrast, the polarisation states used by Aiello *et al.* and the polarisation states forming the regular tetrahedron are shown in Figure 4.23.

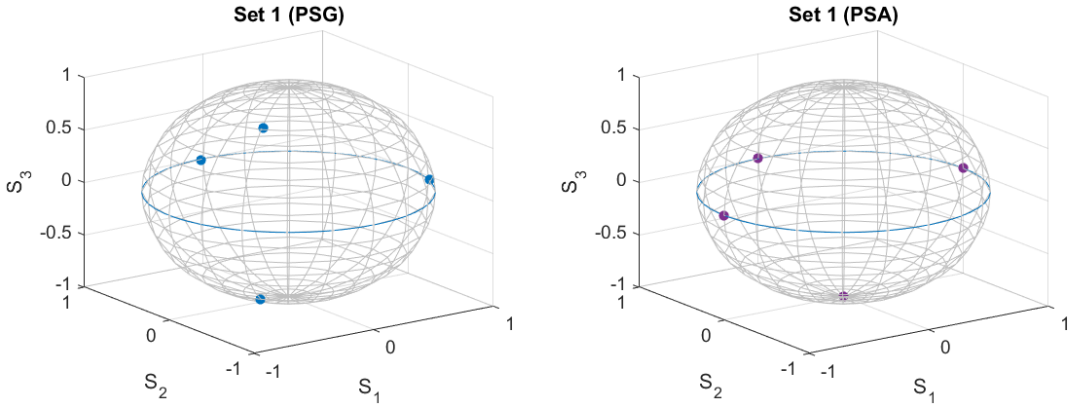

Figure 4.22: Distribution of polarisation states on the Poincaré sphere for the (left) PSG and the (right) PSA used in this work.

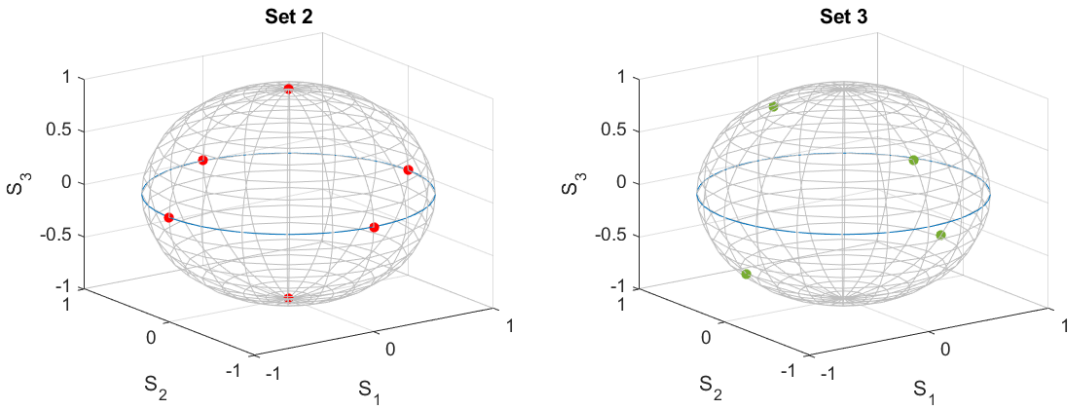

Figure 4.23: Distribution of polarisation states on the Poincaré sphere for the instrument matrices used by (left) Aiello *et al.* [201] and (right) that formed using polarisation states forming a regular tetrahedon within the Poincaré sphere.

Comparing the four sets of polarisation states, it can be seen that those corresponding to $\mathbf{A}_{theory}$ are exclusively located in the bottom hemisphere, while the polarisation states in the other three sets are more equally spaced about the sphere surface. As such, the set of all possible polarisation states, as represented by the Poincaré sphere, is not equally sampled by the PSA, and polarisation states in the bottom hemisphere can be determined more accurately than those in the top hemisphere. This hypothesis was further corroborated by an additional experiment, where $\mathbf{A}_{tetra}$ and $\mathbf{W}_{theory}$ was used to produce the simulated dataset. In this case, the MLE algorithm computed a Mueller matrix that matched the groundtruth Mueller matrix in Equation 4.42. Since the MLE algorithm was seen to be unsuitable for the PSA utilised in this work, the CLSQR algorithm, whose optimisation function is shown

in Equation 4.34, was used instead. As will be demonstrated next, the CLSQR algorithm was successful in retrieving the groundtruth Mueller matrix in the ideal noiseless datasets, and was furthermore shown to provide better performance over a simple matrix inversion for noisy data.

The CLSQR algorithm was tested using simulated detector intensities for an ideal linear polariser and quarter waveplate at five orientation angles that spanned 0° to 180°. The theoretical Mueller matrices corresponding to these test objects (see Section 2.2) were combined with $\mathbf{A}_{theory}$ and $\mathbf{W}_{theory}$ (see Equations 4.2 and 4.3) using Equation 4.31 to simulate a noiseless dataset. Random Gaussian noise was then added to the noiseless data such that the standard deviation corresponded to a desired SNR value. In this simulated experiment, it was assumed that $\mathbf{A}$ and $\mathbf{W}$ were known and ideal, and that noise came solely from the detector. In addition, it was further assumed that the measurements were Gaussian noise-limited, and that the standard deviation of the noise was, σ_N, independent of the detector signal. SNR was then defined based on the expected signal at the four detectors when the incident light is unpolarised. Specifically, if the incident Stokes vector was $\vec{S}^{in} = [1\ 0\ 0\ 0]^\top$, the detected intensity at each of the four detectors is $\vec{D} = \mathbf{A}_{theory}\vec{S}^{in} = [0.125\ 0.125\ 0.125\ 0.125]^\top$. Therefore, the SNR was defined as $\text{SNR} = \frac{0.125}{\sigma_N}$. Datasets with a SNR of 100 and 50 were tested, alongside a noiseless dataset. The CLSQR algorithm was used on these datasets to compute $\mathbf{M}'$, and the difference between $\mathbf{M}'$ and the ideal Mueller matrix, $\mathbf{M}$, was quantified by computing the Frobenius norm of the difference matrix. The Frobenius norm for the noiseless dataset is shown in Figure 4.24, while the mean Frobenius norm for the two noisy datasets, averaged over 100 instances of noise, are presented in Figures 4.25 and 4.26. For comparison, the results were compared to those obtained via a matrix inversion, as well as the MLE algorithm.

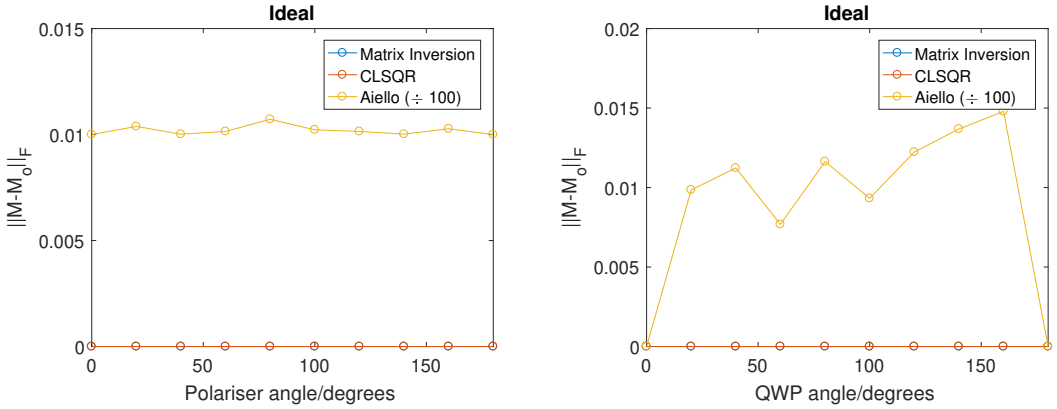

Figure 4.24: Mean Frobenius norm obtained when using ideal noiseless data for the (left) linear polariser and (right) quarter waveplate. For ease of comparison, the results for the MLE algorithm have been divided by 100.

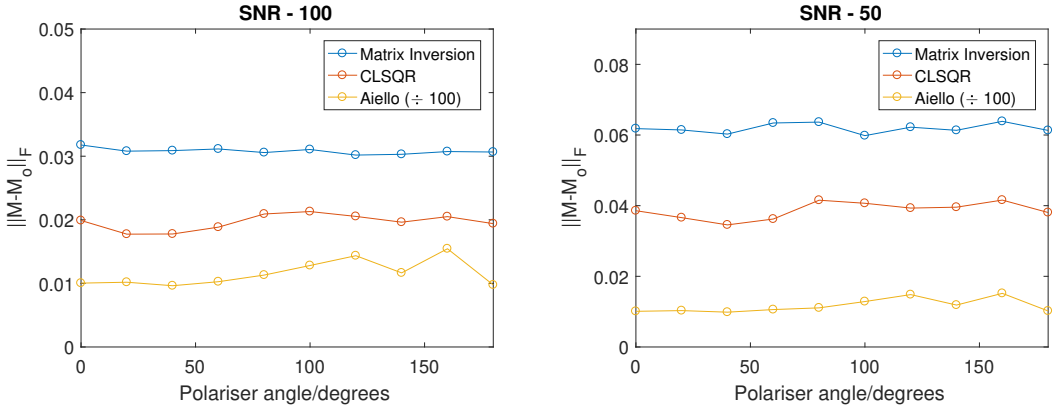

Figure 4.25: Mean Frobenius norm obtained with the linear polariser. For ease of comparison, the results for the MLE algorithm have been divided by 100.

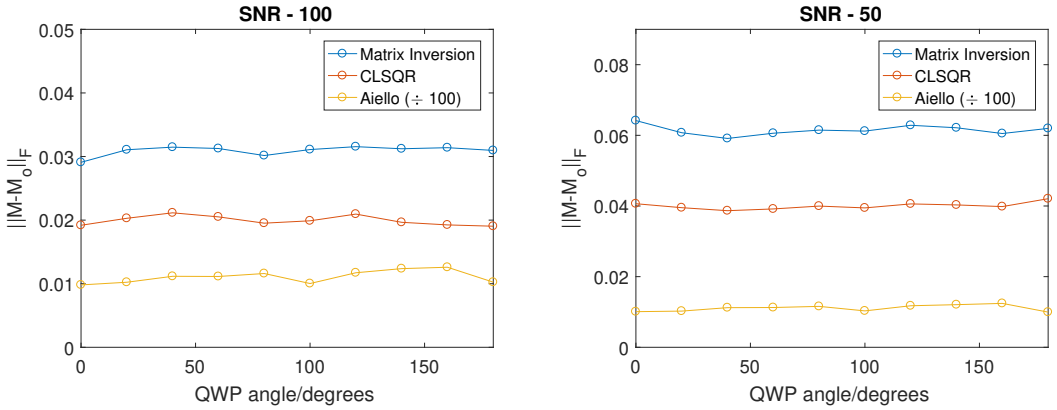

Figure 4.26: Mean Frobenius norm obtained with the quarter waveplate. For ease of comparison, the results for the MLE algorithm have been divided by 100.

It can be seen that in all test cases, the CLSQR algorithm had the best performance out of the three algorithms tested. Since this was tested over different noise levels, it can be seen that the algorithm provides some resilience to noise. Along with its guarantee of a physical Mueller matrix, the CLSQR algorithm is therefore the superior option for computing the Mueller matrix from the measured detector signals, given the PSA and PSG used in this work, and was thus the algorithm implemented for the computation of the Mueller matrix.

4.6 Scattering Sample Preparation and Characterisation

4.6.1 Scattering Phantoms

In order to have test scattering media with known scattering properties, scattering phantoms were prepared. The preparation and characterisation of these phantoms is now discussed.

Preparation

Biological tissues typically have a MFP on the order of 100μm, and a scattering anisotropy factor, g, that is close to 1 [8, 18]. To have phantoms that closely mimic the scattering behaviour of tissues, the target scattering parameters for the phantoms were a MFP of 200μm and g that is close to 1.

Scattering phantoms consisting of silica microspheres (*Merck, Monospher 1000E*) embedded in epoxy resin were chosen. The microspheres had a diameter of 1μm. Refractive indices of both the silica microspheres and the epoxy resin were not available from the manufacturers, therefore, the refractive index of the microspheres was assumed to be 1.457 at the wavelength of $\lambda = 638$nm that was used for this work [202]. For initial calculations, a refractive index of 1.55 was taken for the background epoxy, given that typical refractive indices for epoxy range between 1.50 to 1.57 [203]. The actual refractive index of the epoxy resin was measured after the phantoms were made. Therefore, given these parameters, the expected value

for g was computed using Mie theory [142] to be 0.95 at the laser wavelength of $\lambda = 638$nm. The thickness of the phantoms were chosen such that combinations of the scattering phantoms would be able to provide thicknesses on the order of 3 to 4 transport MFP (TMFP). In cases where the phantoms were combined, immersion oil, with a refractive index of 1.517 ± 0.001, was applied to the surfaces in contact so as to minimise surface reflections. These thicknesses were chosen because it was previously shown that for suspensions of similarly sized microspheres, light becomes fully depolarised at similar thicknesses [144, 145]. Table 4.6 shows a summary of the target parameters.

Parameter	Value
Mean free path (MFP), l/μm	200
Transport mean free path (TMFP), l_{tr}/mm	4.37
Scattering anisotropy factor, g	0.95
Thickness, L/mm	2,4,6,8,10
$\frac{L}{l}$	10,20,30,40,50
$\frac{L}{l_{tr}}$	0.46,0.92,1.37,1.83,2.29

Table 4.6: Design parameters for the scattering phantoms.

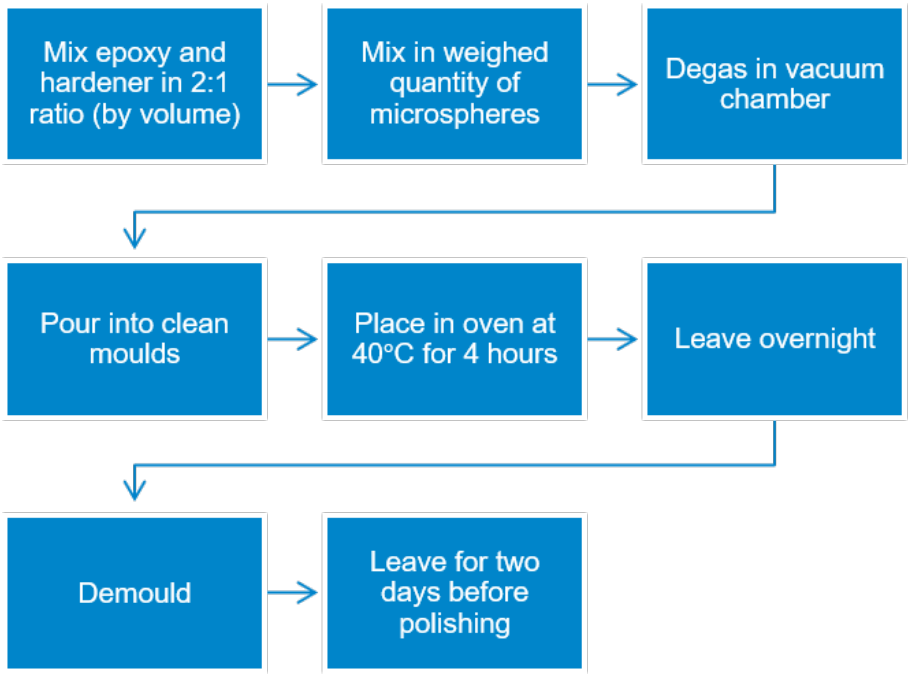

Figure 4.27: Flowchart describing the preparation of the scattering phantoms.

Figure 4.27 describes the preparation protocol of the scattering phantoms, which followed closely the procedure described in [204]. First, the epoxy and hardener (*Easy Composites, GlassCast 50 Clear Epoxy Casting Resin*) were mixed in a ratio of 2:1 by volume. (63 ± 0.25)ml of the epoxy mixture was then mixed with (1.251 ± 0.001)g of microspheres, which were weighed using a laboratory balance (*Oxford Balances, A1204*). This resulted in 1.421×10^7 spheres per mm^3, or equivalently a scatterer fraction by volume of 0.0074. The proportions of spheres to epoxy were pre-calculated using the planned scattering parameters. Unfortunately, due to a bug in the code that was only discovered and corrected for later, the proportions used corresponded to a theoretical MFP of 231μm rather than the originally planned value of 200μm. Since the MFP did not differ from the planned value by a large margin, the samples were left unchanged. Moreover, the actual MFP was measured after the samples were made, and it is the measured MFP that is used for subsequent analysis. The combined mixture was then left to stand for half an hour, after which it was degassed in a vacuum chamber until air bubbles stopped appearing at the surface. The degassed mixture was poured into cube-shaped silicone moulds, up to the desired thicknesses, and the moulds were then placed in a pre-heated oven at 40°C. The oven was switched off after four hours and the samples were left to stabilise

overnight. The scattering samples were removed from the moulds on the following day, but were left to harden further for another two days before polishing. Figure 4.28 shows the final de-moulded scattering samples before they were polished, with a clear control sample on the top left that was made without any microspheres so that the refractive index of the epoxy could be determined. The samples were then characterised after polishing was complete. Before polishing, clumps of spheres were observed on the bottom surface suggesting that sphere aggregation had occurred during the fabrication process. This could cause the final MFP of the scattering phantoms to differ from the design MFP. As such, the actual MFP of the phantoms was characterised after fabrication, and this value was used for subsequent analysis of the experimental results.

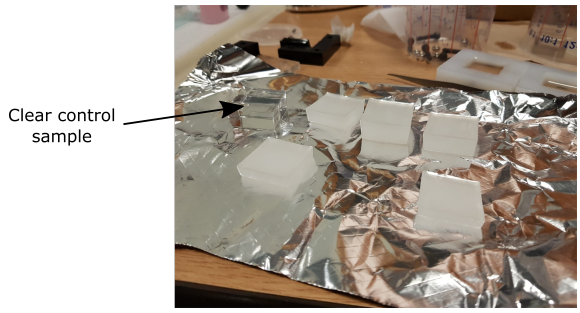

Figure 4.28: The scattering phantoms after de-moulding.

Phantom Background Refractive Index and Thickness

The refractive index of the background epoxy resin was determined by measuring the clear control sample using an Abbe refractometer (*Bellingham&Stanley, Abbe 5 Refractometer*). The refractive index was found to be 1.5500±0.0005 at a wavelength of 589nm. The thickness of the phantoms were measured using a vernier caliper at the centre of the four edges. The resulting thicknesses are presented in Table 4.7 below. The phantoms are denoted as SM1 to SM5, in order of ascending thickness.

	Thickness/mm				
Phantom	Edge 1	Edge 2	Edge 3	Edge 4	Average
Clear	10.32	10.25	10.26	10.36	10.30
SM1	1.93	1.92	1.93	1.94	1.93
SM2	3.82	3.74	3.68	3.82	3.77
SM3	5.33	5.32	5.33	5.32	5.33
SM4	7.33	7.34	7.33	7.34	7.34
SM5	9.81	9.58	9.60	9.81	9.70

Table 4.7: Average and range of the measured thickness of each scattering phantom. The measurements had a precision of 0.01mm.

Phantom Mean Free Path

The total transmitted ballistic power, P, for a scattering medium of a given thickness, L, and MFP, l, is described by the Beer Lambert law, which is given by Equation 2.58. This equation provides a means of determining the MFP of the scattering phantoms. By measuring P and L for each scattering medium, as well as P_o, l can be established through a linear fit to the function

$$L = -l \ln\left(\frac{P}{P_o}\right) \quad . \tag{4.45}$$

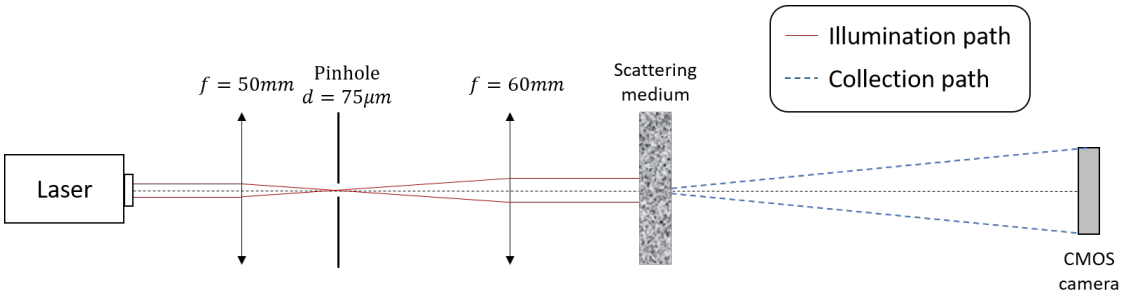

Figure 4.29: Experimental setup used to measure the MFP of the scattering phantoms.

Figure 4.29 shows the setup used for measuring the MFP of the scattering phantoms. A HeNe laser (λ = 632.8nm, *JDS Uniphase, Model 1103P*) was used for illumination. As the beam was observed to have a poor spatial profile, it was first

directed through a beam expander, consisting of lenses L8 and L9. To spatially filter the beam, a pinhole, with a diameter of 75μm, was placed at the focal point of L8, which has a diffraction-limited spot size of 90μm. Lens L9 then collimated the light emerging from the pinhole. The resulting beam was incident on the front surface of the scattering medium, and the output intensity was recorded with a CMOS camera (*Ximea, MQ013MG-ON*) that was placed (26.5$\pm$0.5)cm away from the back surface of the scattering medium. As can be inferred from Table 4.7, the two transverse surfaces of the scattering phantoms are not completely parallel. This small wedge angle causes the ballistic part of the transmitted beam to change slightly in position for different phantoms due to refraction. As such, in order to spatially isolate the ballistic part of the beam, it was not possible to use a fixed spatial filter, such as a pinhole. Instead, a CMOS camera was used to image the output speckle and an average over multiple uncorrelated speckle patterns was used to discriminate the ballistic component. This was done as follows.

To determine the ballistic part of the transmitted beam in the acquired images, images of the output speckle for each phantom was taken with the exposure of the camera kept constant at 6.5ms for all phantoms. ND filters were placed before the beam expander to adjust the incident illumination to ensure that the signal remained unsaturated. The resulting images for the case without any phantom present, and for SM1 and SM2 are shown in Figure 4.30 below. Unfortunately, no clear ballistic component was observed for the thicker phantoms. This is demonstrated by the mean speckle intensity obtained for SM3 on the bottom right of Figure 4.30, which was computed as an average over 15 images. When the phantoms were shifted by 0.5mm, it was observed that the output speckle intensities before and after the shift were spatially uncorrelated. As such, the phantom was moved by 0.5mm transversely between each image. Since the addition of uncorrelated intensity speckle patterns reduces the speckle contrast [63], any ballistic component present should be made more distinct by averaging the 15 images. Nonetheless, no clear ballistic component was observed.

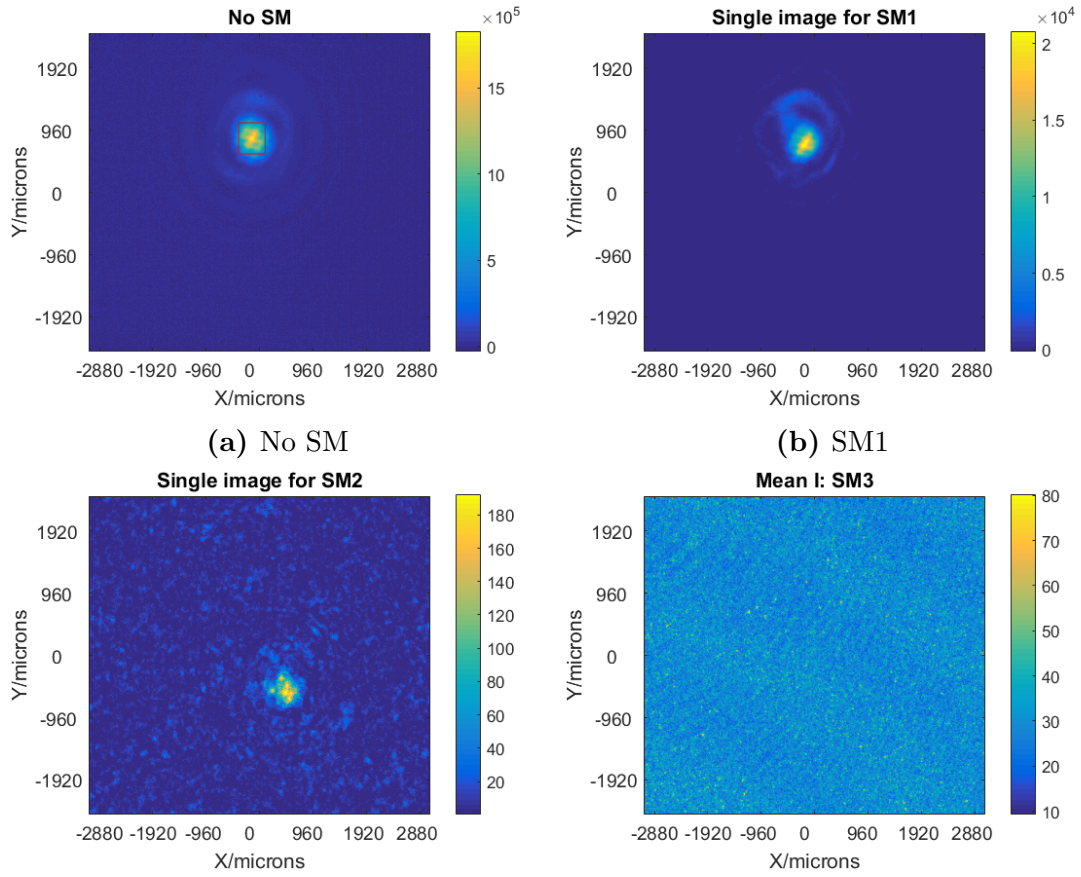

(a) No SM **(b)** SM1

(c) SM2 **(d)** SM3 (Average of 15 images)

Figure 4.30: Intensity images recorded by the CMOS camera.

The ballistic intensity measured for SM1 and SM2 was taken from an average over 15 intensity images, with each phantom moved by 0.5mm transversely between images. The use of ND filters was necessary to prevent saturation of the signal because for a fixed incident power, the difference in the range of intensity values when no phantom was present, and when SM1 and SM2 were present, was too large for the dynamic range of the camera. In order to account for the different incident power used for each image, the intensity of the beam before and after the ND filters in each case was measured using a power meter (*Thorlabs PM100*). The recorded data is presented in Table 4.8, and was used to normalise the acquired images to the right intensities.

	Phantoms		
	None	SM1	SM2
With ND, $P/\mu W$	0.016 ± 0.002	1.060 ± 0.003	-
Without ND, $P/\mu W$	163 ± 1	162 ± 1	172 ± 1

Table 4.8: Measured power before the scattering phantoms.

It was empirically determined that the observed ballistic spot had an approximate size of 100 × 100 pixels, as indicated by the red box in Figure 4.30. Hence, to obtain the MFP of the scattering phantoms, the total power within a 100 × 100 pixel window around the maximum of the averaged image was computed for SM1 and SM2, which were normalised by the total power observed when no phantom was present, P_o. A linear fit was then conducted using the natural logarithm of the computed ratios and the corresponding thicknesses, resulting in the results shown in Figure 4.31. The gradient of the fit then corresponds to the measured MFP. It can be seen that the function was a good fit to the acquired data, and that the resulting MFP was 395μm .

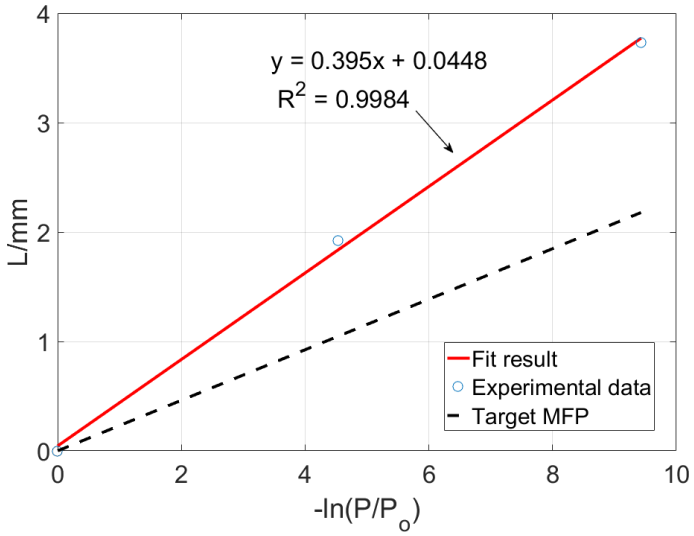

Figure 4.31: Fit of the function $L = -l \ln\left(\frac{P}{P_o}\right)$ to the experimentally obtained ratios for the computation of the MFP, compared to the plot that would have been obtained with the target MFP of 231μm.

The measured MFP of the scattering phantoms is approximately twice that of the target MFP. Despite thorough mixing and careful measurements being made in the

fabrication process, it was inevitable that there would be some deviation from the target parameters. For example, as it took time for the epoxy to set, it is possible that the microspheres could drift downwards due to gravity. Further polishing of the surfaces of the phantoms would also remove some of the microspheres that settled near the surface. Nevertheless, as the MFP has been characterised, the scattering phantoms can still be utilised in the experiments. The final ratios of $\frac{L}{l}$ and $\frac{L}{l_{tr}}$ based on the measured MFP and thickness are shown in Table 4.9 below.

	Phantoms				
	SM1	SM2	SM3	SM4	SM5
$\frac{L}{l}$	4.89	9.53	13.48	18.57	24.56
$\frac{L}{l_{tr}}$	0.22	0.44	0.62	0.85	1.12

Table 4.9: Ratios of $\frac{L}{l}$ and $\frac{L}{l_{tr}}$ of the phantoms computed from measured MFP and thickness.

Average Mueller Matrices of the Phantoms

The Mueller matrices of the phantoms were measured to understand how their polarimetric properties, such as retardance, diattenuation and depolarisation, change with thickness.

Using the setup that was previously described in Section 4.1, the Mueller matrix of the phantoms were measured without single pixel imaging. The phantoms were placed at the location indicated in Figure 4.1. A square illumination area, the same size as a 16×16 Hadamard mask, was incident on the back surface of the phantoms, and the object plane was empty. The detector intensities measured for all input and analysed polarisation states was then used with Equation 2.44 to obtain the Mueller matrix of each phantom. 20 measurements were taken for each phantom, and as was done for the measurement of MFP, the sample was moved by 0.5mm in between each measurement so as to acquire data over different instances of disorder. An average Mueller matrix for each phantom was then computed from the 20 measurements. For comparison, the Mueller matrix of the clear control sample that was made with pure epoxy was also measured.

A Lu-Chipman matrix decomposition (see Section 2.2) was conducted on the average Mueller matrices to obtain the retardance, diattenuation, depolarisation and polarisance of each sample. These four quantities were plotted as a function of the phantom thickness, and the result is shown in Figure 4.32. The four values corresponding to the clear control sample are also indicated as a solid red line in each plot for reference.

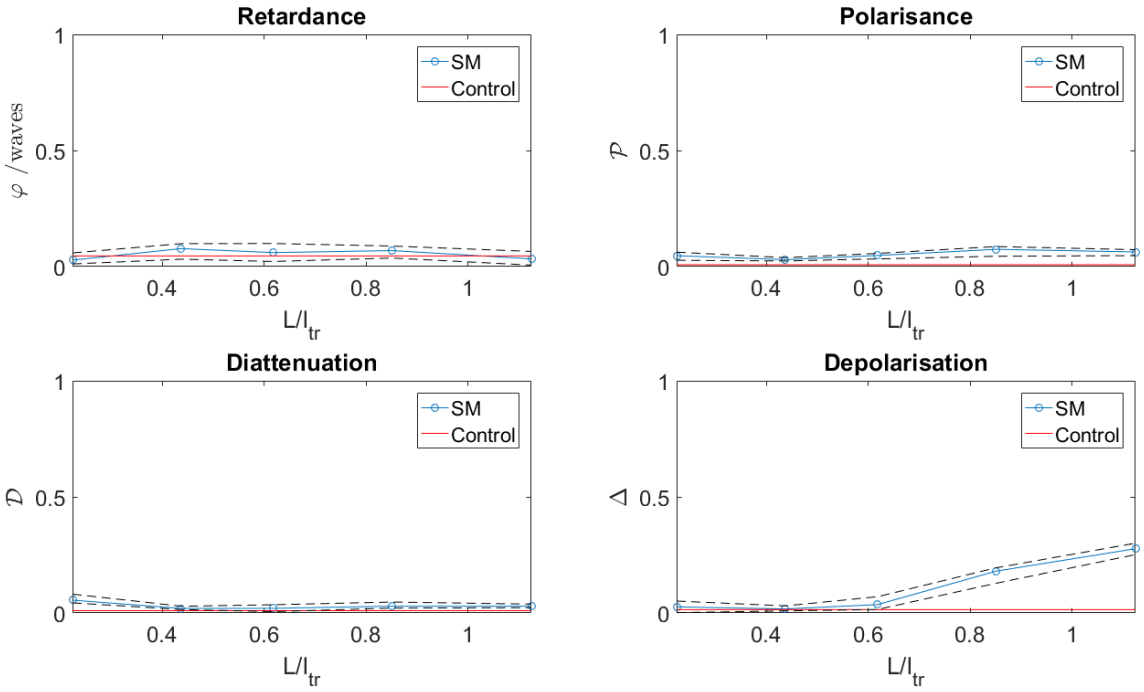

Figure 4.32: Parameters from the Lu-Chipman decomposition as a function of phantom thickness. The dotted black lines indicate the maximum and minimum values for each parameter over the 20 measurements.

Since the phantoms consist of randomly positioned microspheres, whose positions are assumed to be uncorrelated, no particular polarisation state is expected to be favoured. As such, it is expected that the main effect of an increase in medium thickness is depolarisation. For incident linearly polarised light, depolarisation is caused by the scrambling of scattering planes with each scattering event. On the other hand, for incident circularly polarised light, depolarisation is due to randomisation of both the propagation direction and helicity upon scattering [117, 144]. From the four plots, it is evident that, consistent with expectation, depolarisation was the main phenomenon observed as the medium thickness increased, with the

amount of depolarisation reaching about 0.27 for the thickest scattering phantom, SM5. Retardance was close to the control values, and can thus be attributed mainly to the background epoxy. The non-zero value of the retardance for both the control and the phantoms could be due to the three-dimensional cross-linked structure of the cured epoxy resin. The polarisance and diattenuation of the phantoms were also slightly larger than those of the control, though the cause of this polarisance was still unknown at the time of writing.

4.6.2 Biological Samples

This work opted to use slices of chicken breast as the biological scattering samples, as chicken breast is a cost-efficient sample that is widely available. At the wavelength of $\lambda = 638$nm used in this work, chicken breast has been reported to have a scattering anisotropy factor of 0.96 and a TMFP of about 1.25mm [17, 205]. These scattering parameters were required to estimate the ratio of thickness to TMFP of the chicken breast samples. As only an approximation of this ratio is required, the scattering parameters from literature were used. Needless to say, the accuracy and comparability of these reported values depends on the experimental conditions and procedures, but they are sufficient for use as a rule of thumb. As mentioned previously, it has been shown that light becomes fully depolarised at thicknesses of a few TMFPs. Therefore, this ratio provides an intuition for the amount of depolarisation expected. Moreover, it allows for a comparison between chicken breast samples and scattering phantoms with similar TMFP ratios.

Preparation

Chicken breast fillets purchased from mainstream supermarkets were stored in the fridge. Right before the measurements were taken, the chicken breast was removed from the fridge and sliced with a meat slicer (*Ital Stresa 250 Standard*). As the meat slicer was not a precision instrument, the settings on the meat slicer were simply set to the minimum possible thickness, resulting in sample thicknesses of about 1mm. The actual thicknesses and polarimetric parameters of the samples used were measured at the end of each experiment, and are specified in Chapter 6. The chicken breast slice was mounted in a custom-made holder (see Figure 4.33), which had an

open square window of size 1" × 1", and was held in place with mounting screws. The holder was also covered in a layer of matte black paint to minimise reflections.

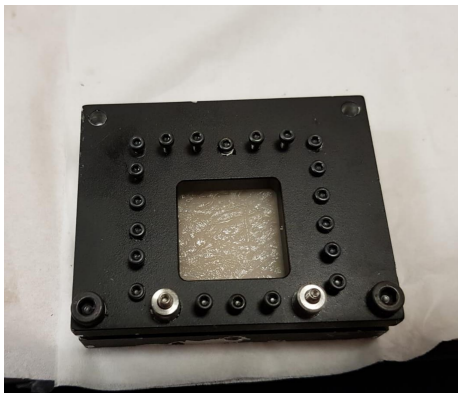

Figure 4.33: Chicken breast sample mounted in the custom-made holder.

Chapter 5

System Characterisation

In this Chapter, the system described in Chapter 4 is characterised. In Section 5.1, the polarimetric resolution of the system is first studied. The spatial homogeneity of the incident beam is then investigated in Section 5.2. Finally, a discussion on the factors affecting the spatial resolution and imaging depth that is achievable by the proposed technique is given in Section 5.3.

5.1 Polarimetric Resolution

The polarimetric sensitivity of the system, defined in this work as the smallest change in the Mueller matrix elements which can be reliably detected, depends on the amount of noise present in the measurements. Noise in the measurements can come from various sources, such as laser intensity fluctuations, electronic noise, and detector noise. If the amount of measurement noise is known, it is possible to estimate the polarimetric sensitivity of the setup by propagating the measured fluctuations to the spatially resolved Mueller matrices. The resulting variance in the elements of the spatially resolved Mueller matrix is then an estimate of the polarimetric sensitivity of the setup, as it describes the random fluctuations in the Mueller matrix elements that are due solely to noise. In this section, a method for error propagation through the single pixel polarimetry setup is outlined, and an estimate of the polarimetric sensitivity of the system is computed.

The computation of the spatially resolved Mueller matrix begins with single pixel imaging. Assuming a direct inversion of Equation 4.29 is used, the object intensity transmission is computed via Equation 4.30. As discussed in Section 4.4, to obtain $\vec{y}$, the acquired data by the photodiodes is processed by taking the difference in the signal measured for the positive and negative masks projected for single pixel imaging. This can be written mathematically as

$$\vec{y}_{ij} = \vec{y}_{ij,+} - \vec{y}_{ij,-} \ , \tag{5.1}$$

where $\vec{y}_{ij,+}$ and $\vec{y}_{ij,-}$ are the photodiode measurements corresponding to the positive and negative masks respectively. Consequently, the variance of $\vec{y}$ can be computed as

$$\mathrm{Var}(\vec{y}_{ij}) = \mathrm{Var}(\vec{y}_{ij,+}) + \mathrm{Var}(\vec{y}_{ij,-}) - \mathrm{Cov}(\vec{y}_{ij,+}, \vec{y}_{ij,-}) \ , \tag{5.2}$$

where Var(...) and Cov(...) denote the variance and covariance respectively. Assuming uncorrelated noise in the two measurements for each spatial mask, the variance of $\vec{y}_{ij}$ can then be computed as a sum of the variances of the individual measurements.

The covariance matrix describing the fluctuations in the resulting image, for the j^{th} input and i^{th} analysed polarisation state, can be defined as

$$\mathbf{K}_{x,ij} = \langle \Delta\vec{x}_{ij} \Delta\vec{x}_{ij}^{T} \rangle \ , \tag{5.3}$$

where $\Delta\vec{x}_{ij} = \vec{x}_{ij} - \langle\vec{x}_{ij}\rangle$, with $\langle ... \rangle$ denoting an averaging over different instances of noise. Substituting Equation 4.30 into Equation 5.3, the covariance matrix of the computed image pixels, $\mathbf{K}_{x,ij}$, can be related to the covariance matrix of the measured projections, $\mathbf{K}_{y,ij}$, as

$$\begin{aligned} \mathbf{K}_{x,ij} &= \langle \mathbf{\Phi}^{-1} \Delta\vec{y}_{ij} \Delta\vec{y}_{ij}^{T} (\mathbf{\Phi}^{-1})^{T} \rangle \\ &= \mathbf{\Phi}^{-1} \mathbf{K}_{y,ij} (\mathbf{\Phi}^{-1})^{T} \ . \end{aligned} \tag{5.4}$$

Assuming that the noise between different measurements is independent, $\mathbf{K}_{y,ij}$ in Equation 5.4 is a diagonal matrix, with the variance of each measured projection

along the diagonal.

The reconstructed intensity images are then processed on a pixel-wise basis to obtain the final polarimetric image, as described by Equation 4.32. For the n^{th} image pixel, the covariance of the computed Mueller matrix elements can be described in terms of the 16×16 element covariance matrix, $\mathbf{K}_{M,n}$, as

$$\mathbf{K}_{M,n} = \langle \text{vec}(\mathbf{\Delta M}_n)\text{vec}(\mathbf{\Delta M}_n)^T \rangle = \langle (\Delta \vec{M}_n)(\Delta \vec{M}_n)^T \rangle \ . \tag{5.5}$$

Here, $\mathbf{\Delta M}_n = \mathbf{M}_n - \langle \mathbf{M}_n \rangle$ and $\Delta \vec{M}_n$ is the vectorised form of $\mathbf{\Delta M}_n$. Vectorising Equation 4.32 gives

$$\vec{M}_n = \text{vec}(\mathbf{A^{-1}} \mathbf{D}_n \mathbf{W}^{-1}) = ((\mathbf{W^{-1}})^{\mathbf{T}} \otimes \mathbf{A^{-1}}) \vec{D}_n \ , \tag{5.6}$$

where $\vec{D}_n$ is the vectorised form of $\mathbf{D}_n$. Combining Equations 5.5 and 5.6, it can be shown that

$$\mathbf{K}_{M,n} = (\mathbf{W^T} \otimes \mathbf{A})^{-1} \mathbf{K}_{D,n} (\mathbf{W} \otimes \mathbf{A^T})^{-1} \ , \tag{5.7}$$

where $\mathbf{K}_{D,n} = \langle \Delta \vec{D}_n \Delta \vec{D}_n^T \rangle$, and $\Delta \vec{D}_n = \vec{D}_n - \langle \vec{D}_n \rangle$. Equation 5.7 describes the relationship between the covariance matrix of the pixel-wise detector measurements, $\mathbf{K}_{D,n}$ and the covariance matrix of the Mueller matrix elements, $\mathbf{K}_{M,n}$. If it is assumed that the noise across different detectors and different input polarisation states is independent, $\mathbf{K}_{D,n}$ is a diagonal matrix, with the variances of each detector for each input polarisation state along the diagonal. For single pixel polarimetry, these diagonal elements in $\mathbf{K}_{D,n}$ are related to $\mathbf{K}_{y,ij}$ in the previous analysis as

$$\text{diag}\left(\mathbf{K}_{D,n}\right) = \text{vec} \begin{bmatrix} K_{x,11,n} & K_{x,12,n} & K_{x,13,n} & K_{x,14,n} \\ K_{x,21,n} & K_{x,22,n} & K_{x,23,n} & K_{x,24,n} \\ K_{x,31,n} & K_{x,32,n} & K_{x,33,n} & K_{x,34,n} \\ K_{x,41,n} & K_{x,42,n} & K_{x,43,n} & K_{x,44,n} \end{bmatrix} \ , \tag{5.8}$$

where $\text{diag}(\mathbf{K}_{D,n})$ represents the elements on the diagonal of $\mathbf{K}_{D,n}$, and $K_{x,ij,n}$ is the n^{th} element on the diagonal of $\mathbf{K}_{x,ij}$. When the assumption of independent noise across detectors and input polarisation states is not made, then $\mathbf{K}_{D,n}$ has to be

computed from its definition, $\mathbf{K}_{D,n} = \langle \Delta\vec{D}_n \Delta\vec{D}_n^T \rangle$.

For single pixel polarimetry, Equations 5.4 and 5.7 allow $\mathbf{K}_M$ to be computed from the measurement noise. The variance of the Mueller matrix elements can then be extracted from the diagonal of $\mathbf{K}_M$. As a note, when the optical system is used in non-imaging mode (i.e. without single pixel imaging), then Equation 5.7 alone describes the covariance matrix of the final Mueller matrix.

To estimate the polarimetric sensitivity of the system, the standard deviation of the measurements was investigated. Due to the polarimetric elements in front of the detectors in the PSA, the data acquired by the four photodiodes depends on both the intensity as well as the polarisation state of the incident beam. This makes it difficult to compare the noise characteristics across the four photodiodes. Hence, in this experiment, the polarimetric elements in front of the detectors were removed so that only intensity fluctuations were measured. As the four detectors were the same model, it was expected that they showed similar noise characteristics. This was verified by checking the noise characteristics over two photodiodes, specifically, detectors 3 and 4. The experiment was conducted at different illumination levels covering the full detector range of $10V$, with the different illumination levels implemented by projecting squares of different sizes onto an empty sample plane. As the parameters utilised for lock-in detection had been optimised for the low light levels associated with the presence of a scattering medium (see Section 4.4.2), ND filters (*Thorlabs NE10A and NE20A*) were used to ensure that the detector signal remained unsaturated for all illumination levels. 1000 datapoints were acquired for each illumination level, and the mean and standard deviation of the collected data were computed. For brevity, the mean of the data at illumination level p is hereby denoted as $\langle D_p \rangle$, while the standard deviation is denoted as σ_p.

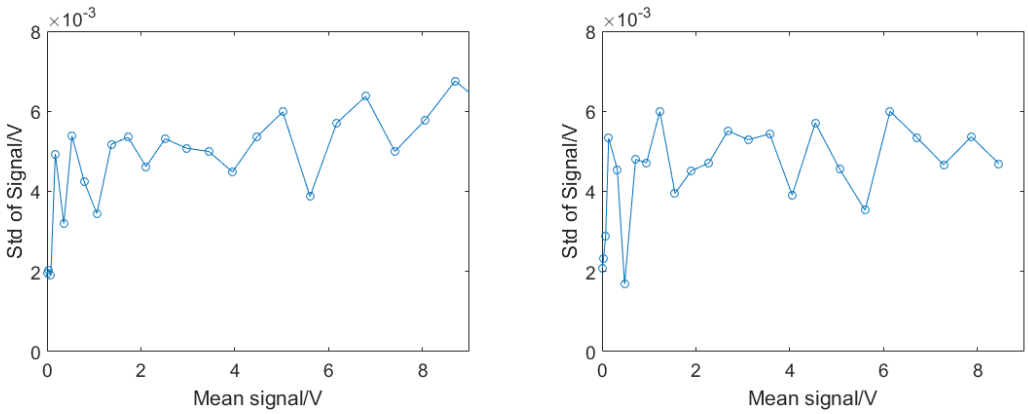

Figure 5.1: Standard deviation as a function of mean signal level for (left) Detector 3 (right) Detector 4.

Figure 5.1 shows the results for both detectors. It can be seen that for both detectors, the standard deviation of the data is approximately constant at about 0.005 across the full detector range. This suggests that the noise is independent of the illumination level. Under this assumption, a plot of $\beta = \log_{10}\left(\frac{\sigma_p}{\langle D_p \rangle}\right)$ versus $\langle D_p \rangle$ can be fitted by the function $\beta = \log_{10}\left(\frac{c}{\langle D_p \rangle}\right)$, where c is an estimate of the standard deviation to be determined by the fit. This fit was conducted for both datasets and the results are shown in Figure 5.2.

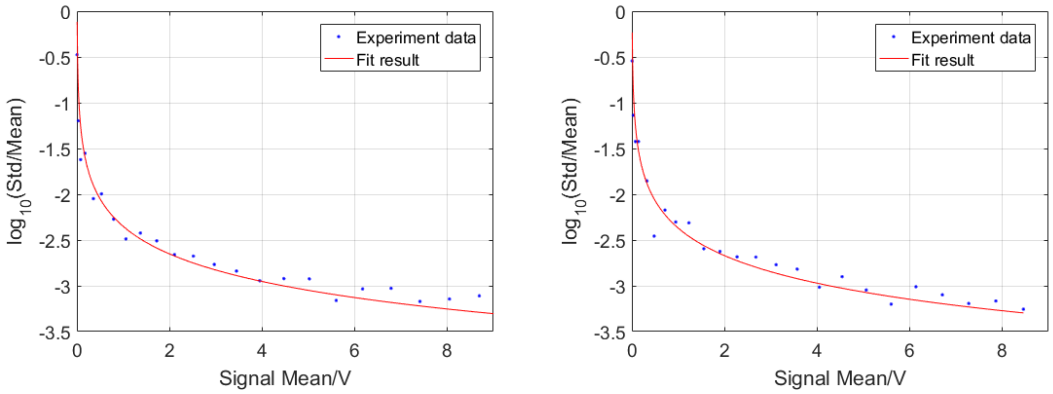

Figure 5.2: Fit results for (left) Detector 3 (right) Detector 4.

c was found to be 0.0045 for detector 3 and 0.0043 for detector 4, with corresponding R-squared values of 0.95 and 0.96 respectively. Considering Figures 5.1 and 5.2, as well as the goodness of fit, it can be concluded that the standard deviation of the data is, as initially assumed, independent of intensity level. Moreover, given the similarity of the two results shown in Figures 5.1 and 5.2, the detectors can also be

concluded to have similar noise characteristics, with an average standard deviation of $0.0044V$ computed from the two detectors tested.

Based on these measurements, the covariance matrix of the Mueller matrix elements obtained via single pixel imaging polarimetry was calculated using Equations 5.4 and 5.7. This was done for both imaging and non-imaging experiments using the experimental instrument matrices determined from calibration. For imaging experiments, since noise was observed to be independent of illumination level, it follows that the diagonal elements of $\mathbf{K}_{x,ij}$ are equal with a value of $\sqrt{(2 \times \sigma_p^2)} = 0.0064$. It was further assumed that noise across detectors and input polarisations was independent. As such, $\mathbf{K}_{D,n}$ was also a diagonal matrix, with diagonal elements of 0.0064. For the non-imaging experiments, the diagonal elements of $\mathbf{K}_D$ were identically equal to $\sigma_p = 0.0044$. The resulting standard deviations are shown in Tables 5.1 and 5.2.

0.0008	0.0015	0.0016	0.0012
0.0009	0.0017	0.0019	0.0014
0.0012	0.0022	0.0025	0.0018
0.0015	0.0028	0.0030	0.0022

Table 5.1: Predicted standard deviation in the Mueller matrix elements with single pixel imaging.

0.0006	0.0010	0.0011	0.0008
0.0006	0.0012	0.0013	0.0010
0.0008	0.0016	0.0017	0.0013
0.0010	0.0020	0.0021	0.0016

Table 5.2: Predicted standard deviation in the Mueller matrix elements without single pixel imaging.

To see how these predictions compare to experiment, using the same instrument matrices as the above, the Mueller matrix of air was measured 1000 times. The experiment was done without single pixel imaging. In addition, for a fair comparison, the Mueller matrices were obtained without using the CLSQR algorithm, which

is expected to reduce the resulting fluctuations due to noise. The mean and standard deviation of the computed Mueller matrices are shown in Tables 5.3 and 5.4 respectively.

1.0000	0.0010	0.0032	0.0007
−0.0065	1.0057	0.0287	0.0123
0.0008	0.0100	0.9900	0.0145
−0.0131	0.0236	−0.0193	1.0099

Table 5.3: Mean of the measured (un-normalised) Mueller matrices from 1000 measurements of air.

0.0036	0.0021	0.0017	0.0012
0.0023	0.0041	0.0068	0.0033
0.0029	0.0056	0.0053	0.0038
0.0031	0.0040	0.0050	0.0027

Table 5.4: Standard Deviation of the measured Mueller matrices from 1000 measurements of air.

The average measured Mueller matrix can be seen to be close to the expected identity matrix. On the other hand, the standard deviation of the measured Mueller matrices is seen to be larger than the predicted values in Table 5.2. This difference suggests the presence of other noise sources which have not been accounted for in the analysis. The presence of unaccounted noise sources is further evidenced by Table 5.5, which shows the standard deviation of the four detector outputs for each input polarisation from the 1000 measurements of air. It can be seen that these values are larger than the standard deviation of $0.0044V$ measured in the previous experiment (see Figure 5.1). Furthermore, the standard deviation in the Mueller matrix elements was recomputed using the detector noise covariance matrix that was directly calculated from the measurements as $\mathbf{K}_D = \langle \Delta\vec{D}\Delta\vec{D}^T \rangle$, and the results were found to be identical to those in Table 5.4, thereby validating the method of error propagation. The computed matrix $\mathbf{K}_D$ was observed to have significant off-diagonal elements, as shown in Figure 5.3. This suggests the presence of a common-mode noise, which

causes the noise across detectors to become dependent on each other. One possible unaccounted noise source that is consistent with these findings could be variations in the polarisation states produced by the voltage-controlled variable waveplate. Such variations would not cause a change in intensity when polarisation elements in front of the detectors are removed, and would thus not be apparent in the results shown in Figure 5.1. As this is a noise on the illumination, the noise across the four detectors can no longer be assumed to be independent. Furthermore, variations in the input polarisation state would cause the resulting noise measured by four detectors in the PSA to become sample-dependent.

	Input Polarisation States			
Detectors	Input 1	Input 2	Input 3	Input 4
D1	0.011	0.013	0.007	0.011
D2	0.003	0.013	0.029	0.053
D3	0.012	0.004	0.033	0.012
D4	0.017	0.014	0.024	0.012

Table 5.5: Standard deviation of the detector measurements from 1000 measurements of air. Each row corresponds to a detector, while each column corresponds to an input polarisation.

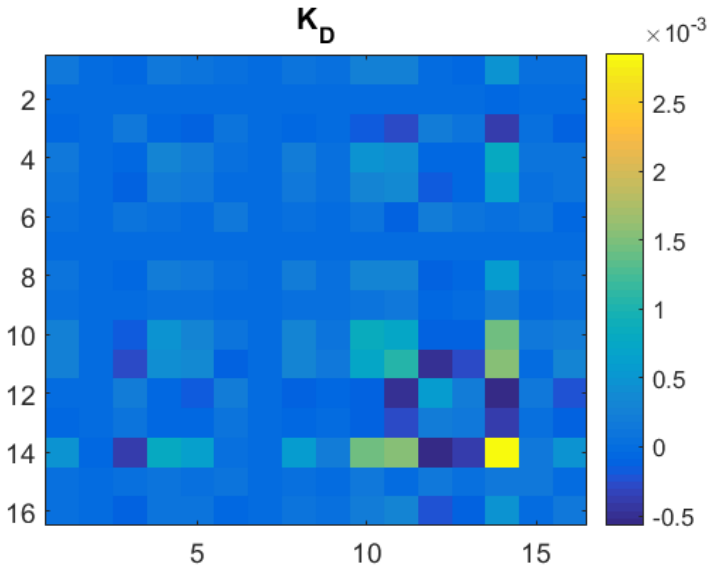

Figure 5.3: Plot of $\mathbf{K}_D$ for the 1000 measurements of air.

In summary, a method for error propagation through the single pixel polarimetric setup was presented. From the analysis, it can be seen that under the sole consideration of intensity noise, the elements of the Mueller matrix obtained through single pixel polarimetry are expected to have fluctuations less than 0.003 when single pixel imaging is used, and 0.002 when single pixel imaging is not used. However, the experimentally measured fluctuations were larger than this expected value, with a maximum standard deviation observed of 0.007 when single pixel imaging was not used. This was shown to be caused by other noise sources that were not accounted for in the analysis, probably noise due to the variability of the input polarisation state generated by the LCVWPs. Nevertheless, the measured standard deviation of the Mueller matrix in Table 5.4 gives an indication of the magnitude of the fluctuations that can be expected in the Mueller matrix for the experimental setup used.

5.2 Illumination Homogeneity

To check the spatial homogeneity of the illumination, single pixel imaging was conducted using the setup presented in Chapter 4 with an empty object plane. Figures 5.4 to 5.7 show the resulting reconstructed images for each input polarisation state, normalised to the maximum value of each image.

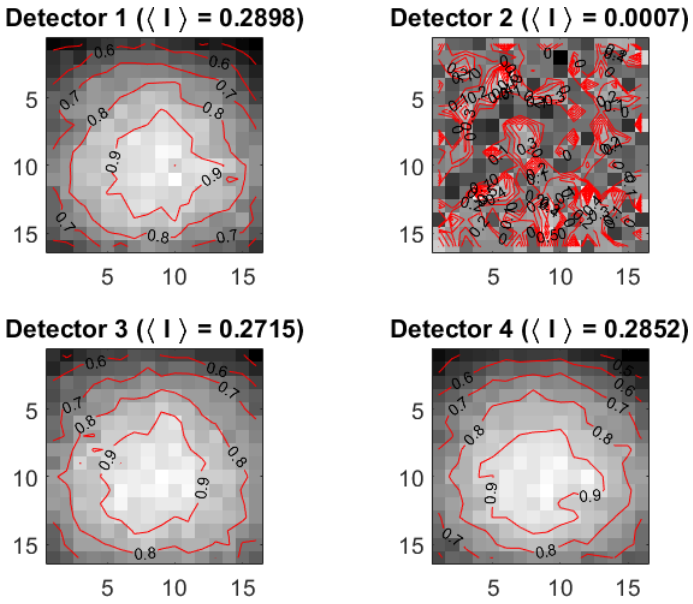

Figure 5.4: Intensity at each detector for the first input polarisation state, reconstructed using single pixel imaging. The intensity values for each detector have been normalised by their respective maximum values. Average (un-normalised) intensity for each detector is provided in the title for reference

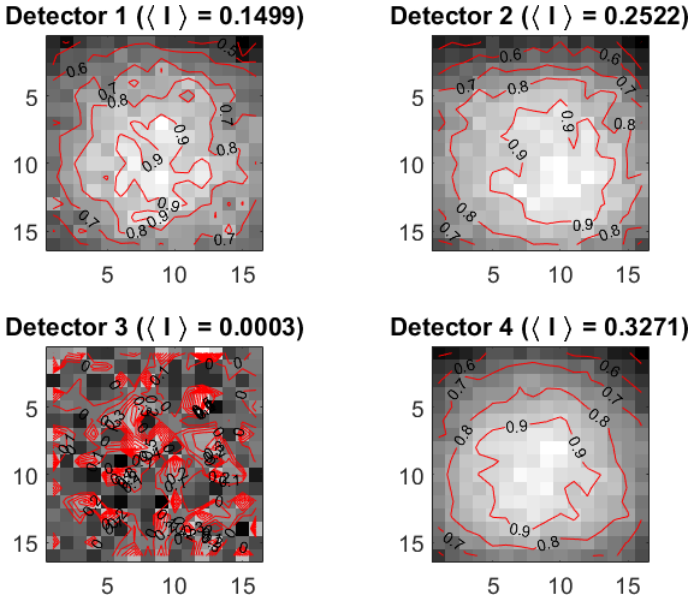

Figure 5.5: Intensity at each detector for the second input polarisation state, reconstructed using single pixel imaging. Refer to caption of Figure 5.4 for details.

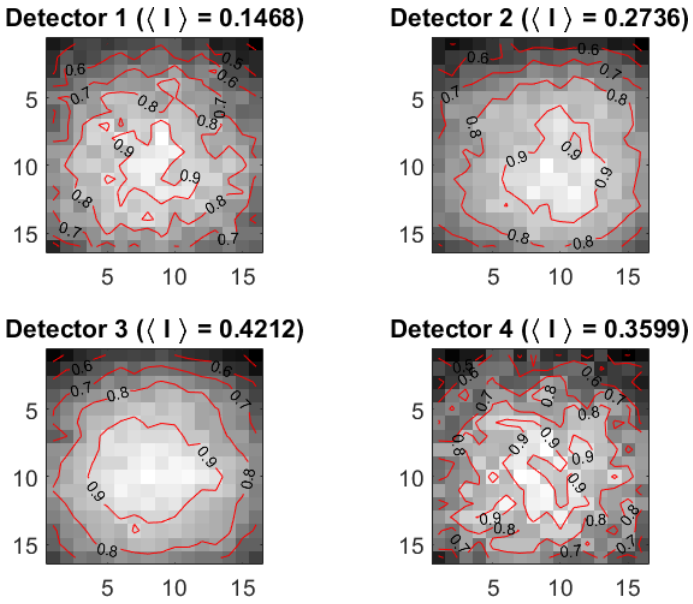

Figure 5.6: Intensity at each detector for the third input polarisation state, reconstructed using single pixel imaging. Refer to caption of Figure 5.4 for details.

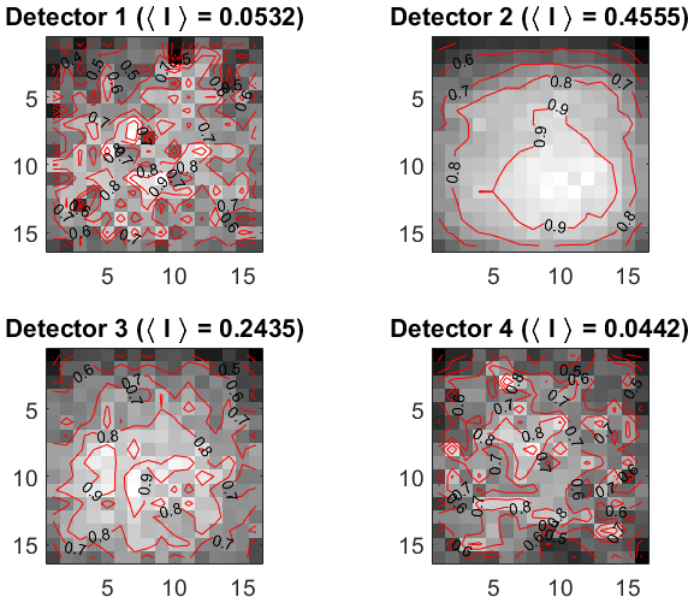

Figure 5.7: Intensity at each detector for the fourth input polarisation state, reconstructed using single pixel imaging. Refer to caption of Figure 5.4 for details.

It can be seen that the ratio of the minimum to maximum intensity in each image is minimally 0.5. In addition, it can be observed that the spatial profile of the beam is not close to the ideal Gaussian profile expected for the incident laser beam. Furthermore, it can be seen that the spatial variation in intensity is dependent on the incident and analysed polarisation state (c.f. images for detector 4 in Figures

5.5 and 5.6). This suggests that the spatial variation measured by the detectors is caused by a spatial inhomogeneity in the incident polarisation state, which could be caused by a non-ideal spatial inhomogeneity in the VWPs, a known problem for LCVWPs [206]. Another possible cause of the spatial inhomogeneities seen in Figures 5.4 to 5.7 could be detector noise which is propagated to the reconstructed images. From Table 5.5, it can be seen that the highest recorded standard deviation for non-imaging polarimetric measurements over air was 0.05. Taking an extreme example that all measurements exhibited this maximum standard deviation of 0.05, Equation 5.4 predicts that the reconstructed images from single pixel imaging would have a standard deviation of $\sqrt{2(0.05)^2} = 0.071$. This value is about 15% of the highest intensity measured in Figures 5.4 to 5.7 (i.e. $\langle I \rangle = 0.4555$ in Figure 5.7). As such, it is possible that detector noise is one of the causes behind the spatial inhomogeneities observed in Figures 5.4 to 5.7.

5.3 Factors Affecting Spatial Resolution and Imaging Depth

This section discusses the factors influencing the best achievable spatial resolution and the maximum imaging depth for single pixel polarimetric imaging.

As discussed in Section 2.4, the spatial resolution of single pixel polarimetric imaging is basically determined by the size of the pixels projected onto the object plane. As such, the best achievable spatial resolution depends on two factors. The first factor is the width of the PSF related to the imaging optics used to image the SLM onto the object plane. The second factor is the minimum pixel size required such that the Mueller matrix of the scattering medium becomes independent of the instance of disorder, as well as the location of the input pixel. As discussed in Section 3.2.2, this second factor is important when considering the practicality of the technique. The minimum pixel size required to ensure the independence of the Mueller matrix has been shown to be determined by the width of the correlation function $\mathbf{C}(\vec{\rho}_{12}, \vec{\rho}'_{12})$ (see Section 3.2.2). In turn, $\mathbf{C}(\vec{\rho}_{12}, \vec{\rho}'_{12})$ is reliant on how far two input point sources can be before the speckle field observed at a common output point becomes uncor-

related, as well as the width of the ensemble-averaged intensity profile from a point source. As such, it is necessary that the pixel size implemented is larger than both of these quantities. As a consequence, it was seen in Section 3.2.2 that the pixel size required is larger for thicker scattering media. The smaller the width of $\mathbf{C}(\vec{\rho}_{12}, \vec{\rho}'_{12})$ and the PSF, the better the spatial resolution that can be expected from single pixel polarimetric imaging.

For the setup used in this work, the PSF related to the imaging optics used to image the SLM onto the object plane had a radius of $7.35\mu m$ (see Section 4.2). On the other hand, the width of $\mathbf{C}(\vec{\rho}_{12}, \vec{\rho}'_{12})$ depends on the scattering sample, and was, unfortunately, challenging to quantify, both experimentally and computationally. Nevertheless, this implies that the minimum achievable pixel size for the setup described in Chapter 4 is, at best, $7.35\mu m$. Higher NA lenses could potentially be used in the design to reduce the size of the PSF. This, however, increases the angular spread of plane waves propagating through the system, which would result in a depolarisation of the applied input polarisation state due to an averaging of the Mueller matrices corresponding to each plane wave component [152].

The imaging depth that the technique can be applied to depends on the pixel size used, the level of noise in the system and the depolarisation length of the scattering medium. The smallest imaging depth required by these three elements is then the maximum imaging depth attainable with the proposed technique. As mentioned above, the minimum pixel size required to minimise the variance of the Mueller matrix across instances of disorder is larger for thicker scattering media. Consequently, the imaging depth is affected by the choice of pixel size. The noise level of the system is also a factor because the amount of scattered light that is collected for a fixed NA decreases as a function of scattering medium thickness. As such, for any given noise level, there will be a limit on the maximum thickness after which the collected signal becomes indistinguishable from noise (i.e. SNR = 1). Systems with less noise can thus image at larger imaging depths. For an arbitrary noise level, the limit on imaging depth depends on the scattering properties of the medium itself. Specifically, a higher scattering anisotropy factor would allow for greater imaging

depths, as more of the incident light would be scattered in the forward direction. A medium with a longer mean free path would also allow deeper imaging, since the incident photons would undergo less scattering for any given thickness. Finally, single pixel polarimetric imaging can only work if the scattering medium does not fully depolarise the incident light. In an extreme scenario, if the depolarisation factor, Δ, of the Mueller matrix, obtained from a Lu-Chipman decomposition (see Section 2.2.7), is one, then the exiting light is completely depolarised for all input polarisation states. The related Mueller matrix is non-invertible and single pixel polarimetric imaging would not work as the non-invertibility of the Mueller matrix implies that there are many solutions for the input polarisation state for any measured output polarisation state, which is logical since any input polarisation state would give the same unpolarised output. It should be noted that the converse is not generally true - a Δ less than one does not necessarily imply an invertible Mueller matrix, as one of the principle axes of the associated depolariser could still be fully depolarising. The depolarisation length of the scattering medium provides an indication of the thicknesses at which incident light becomes fully depolarised. The proportion of light emerging from the scattering medium that is still polarised can be quantified in terms of the DOP, DOLP and DOCP, as defined in Section 2.2. The DOLP and DOCP have been used to study the depolarisation rate of incident linearly and circularly polarised light respectively [144, 145]. In these studies, the depolarisation length was determined as the scattering medium thickness after which the DOLP or DOCP decreased past a minimum threshold, for example $\frac{1}{e}$, beyond which the exiting light can be considered depolarised. It was found that the depolarisation lengths varied depending on the input polarisation state and the specific properties of the scatterers (e.g. scatter concentration, size), and was generally on the order of a few transport mean free paths. Since linear and circular states form a basis for any arbitrary polarisation states, these depolarisation lengths give an indication of the thicknesses at which single pixel polarimetric imaging can work.

The DOLP and DOCP of light transmitted by the scattering phantoms used in this work were computed from their corresponding Mueller matrices, which were measured using the setup described in Chapter 4. As was done for the measure-

ments of mean free path (see Section 4.6), 20 measurements of the Mueller matrix were taken for each phantom, with the sample translated by $0.5mm$ transversely between each measurement. The output speckle related to each sample translation were observed to be uncorrelated, therefore each measurement was considered to be of a different instance of disorder. The average Mueller matrix, computed from the 20 measurements, was then used to compute the DOLP and DOCP corresponding to incident light with the relevant polarisation state. This was accomplished by multiplying the average Mueller matrix with the input Stokes vectors for x and y linearly polarised light, as well as left and right circularly polarised light, which can be written respectively as

$$\begin{aligned} \vec{S}^{in,x} &= [1\ ,1\ ,0\ ,0]^T\ , \\ \vec{S}^{in,y} &= [1\ ,-1\ ,0\ ,0]^T\ , \\ \vec{S}^{in,R} &= [1\ ,0\ ,0\ ,1]^T\ , \\ \vec{S}^{in,L} &= [1\ ,0\ ,0\ ,-1]^T\ . \end{aligned} \tag{5.9}$$

For each incident linearly polarised Stokes vector, the DOLP was computed from the exiting Stokes vector using Equation 2.29. Similarly, the DOCP was computed for each incident circularly polarised Stokes vector. The results for the four input Stokes vectors are plotted in Figure 5.8 as a function of medium thickness. The top horizontal axis shows the ratio of the medium thickness to mean free path, while the bottom axis shows the medium thickness normalised by the transport mean free path. The depolarisation length cannot be determined based on this data as there is a lack of datapoints at lower DOLP/DOCP, and the plot does not necessarily follow a linear trend [16]. Nevertheless, the minimum degree of polarisation observed was 0.679, which implies that single pixel polarimetric imaging is possible for these scattering phantoms, provided that there is sufficient SNR and a large enough pixel size.

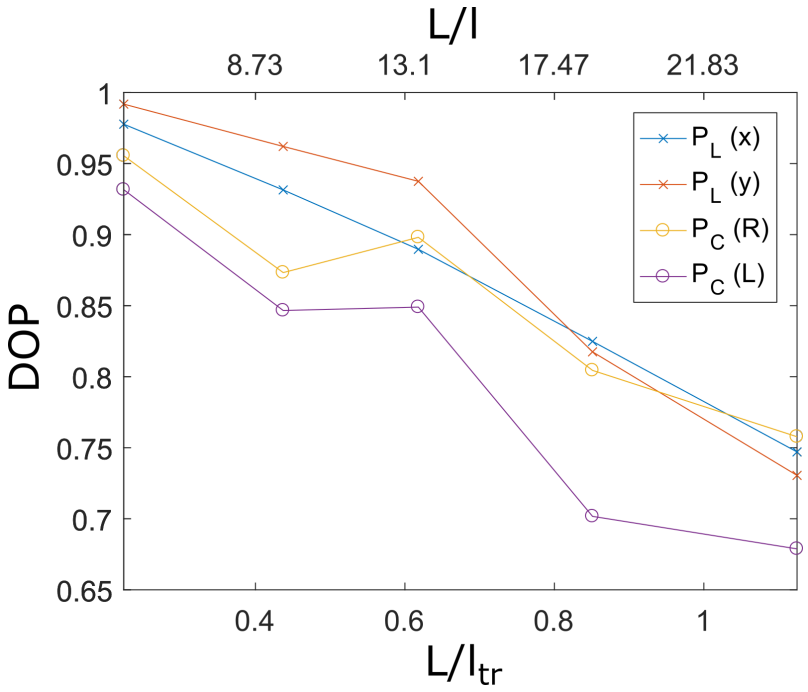

Figure 5.8: Plot of the degree of polarisation as a function of sample thickness for different input polarisation states. The top and bottom axes shows the ratio of thickness and mean free path and the ratio of thickness and transport mean free path respectively. Key: $P_L(x)$: DOLP for input x linearly polarised light, $P_L(y)$: DOLP for input y linearly polarised light, $P_C(R)$: DOCP for input right circularly polarised light and $P_C(L)$: DOCP for input left circularly polarised light.

Chapter 6

Imaging results with a pre-calibrated scattering medium

The proposed imaging technique discussed in Section 3.1.3 was used to image the test objects described in Section 4.1.2, through the various scattering samples detailed in Section 4.6. This chapter presents the imaging results with a pre-calibrated scattering medium, that is, when the Mueller matrix of the scattering medium is measured beforehand. Section 6.1 and Section 6.2 show the results from the prepared scattering phantoms and chicken breast respectively.

6.1 Scattering Phantoms

As mentioned in Section 2.3, the TMFP corresponds to an average distance past which the direction of the propagating photon can be considered to be fully randomised. Past this distance, spatial information of the light incident on the scattering medium is fully scrambled, but polarimetric information can still persist [144, 145]. As such, the proposed method was tested on the scattering phantoms with thickness to TMFP ratios that were greater than or approximately equal to one TMFP. Out of the five scattering phantoms (see Section 4.6.1), SM4, SM5 and their combination (denoted as SM6), were chosen to test the proposed method. The corresponding thicknesses to MFP and TMFP ratios are shown in Table 6.1.

	Phantoms		
	SM4	SM5	SM6
$\frac{L}{l}$	18.57	24.56	43.13
$\frac{L}{l_{tr}}$	0.85	1.12	1.97

Table 6.1: Ratios of $\frac{L}{l}$ and $\frac{L}{l_{tr}}$ of the phantoms used to test the proposed method.

In this section, to demonstrate the proposed technique, the reconstructed images of the test objects hidden behind SM4 are first presented and analysed. The results are then extended to the thicker scattering media, SM5 and SM6.

6.1.1 Measured Mueller Matrix for SM4

The Mueller matrix of SM4 was measured using the setup presented in Figure 4.1, with the DMD was set such that an illumination area matching the size of the 16×16 Hadamard masks was incident on the input surface of the scattering medium. This measured Mueller matrix was used to correct for the contribution of the scattering medium, as described previously in Section 4.5. The CLSQR algorithm (see Section 4.5.2), along with the calibrated instrument matrices (see Section 4.3) were used to compute the Mueller matrix. Normalising the computed Mueller matrix to its M_{00} component yields

$$\mathbf{M}^{SM} = \begin{bmatrix} 1.00 & -0.02 & 0.00 & 0.01 \\ -0.01 & 0.83 & 0.10 & -0.14 \\ -0.05 & 0.02 & 0.75 & 0.10 \\ 0.04 & 0.16 & -0.09 & 0.84 \end{bmatrix} . \tag{6.1}$$

The polarimetric properties of SM4 have been discussed previously in Section 4.6.1. It should be noted that this Mueller matrix was for a single instance of disorder and was not an average over multiple measurements. In addition, $\mathbf{M}^{SM}$ can be seen to be largely diagonal, which is typical for ensembles of microspheres in the multiple scattering regime [207].

6.1.2 Spatially Homogeneous Objects

The proposed technique was first tested on spatially homogeneous objects, specifically a linear polariser with its transmission axis at $-20°$, and a quarter wave plate with its fast axis at $40°$. These test objects have been detailed previously in Section 4.1.2. For reference, the theoretical Mueller matrix for a linear polariser with its transmission axis at $-20°$ is given by

$$\mathbf{M}^{LP,theory} = \begin{bmatrix} 1.00 & 0.77 & -0.64 & 0.00 \\ 0.77 & 0.59 & -0.49 & 0.00 \\ -0.64 & -0.49 & 0.41 & 0.00 \\ 0.00 & 0.00 & 0.00 & 0.00 \end{bmatrix}, \tag{6.2}$$

while that for a quarter wave plate with its fast axis at $40°$ is

$$\mathbf{M}^{QWP,theory} = \begin{bmatrix} 1.00 & 0.00 & 0.00 & 0.00 \\ 0.00 & 0.24 & 0.13 & -0.96 \\ 0.00 & 0.13 & 0.98 & 0.17 \\ 0.00 & 0.96 & -0.17 & 0.22 \end{bmatrix}. \tag{6.3}$$

Note that the manufacturer-listed retardance of 0.2151 waves at the laser wavelength was used to compute $\mathbf{M}^{QWP,theory}$. Each test object was placed in the object plane, as depicted in Figure 4.1, and measurements were first taken for each test object without the scattering medium present, using the data acquisition procedures described in Section 4.4. In order to avoid saturating the photodiodes, ND filters (*Thorlabs NE10A and NE20A*) were used to attenuate the incident illumination. After the measurement was complete, the ND filters were removed and the scattering medium, SM4, was placed in between the object and the PSA, as shown in Figure 4.1, and the measurement was repeated. The two acquired datasets were then processed using the methods discussed previously in Section 4.5 to yield the spatially resolved polarimetric images.

Before comparing the results with and without the scattering medium present, the validity of the Mueller matrices obtained without the scattering medium was first

verified. This was done by averaging each Mueller matrix element across all pixels, and comparing the resulting averaged Mueller matrix for each test object to the Mueller matrix of the same test object that was obtained without single pixel imaging (i.e. non-imaging polarimetry). Both Mueller matrices were normalised to their respective M_{00} elements before comparison. Usually, the M_{00} element can be interpreted as the unpolarised transmittance of the sample (see Section 2.2.7), but as the illumination intensity during the calibration was attenuated by ND filters (see Section 4.3) that were not used in the experiments with the scattering medium present, the M_{00} element is, instead, directly proportional to the unpolarised transmittance of the sample. This distinction is important as it is then possible to have M_{00} values that are greater than 1. Nevertheless, normalising each Mueller matrix to their respective M_{00} elements is equivalent to an intensity normalisation, so that the polarimetric parameters can be better compared. As the Mueller matrices obtained in the non-imaging polarimetry setup have previously been validated in Section 4.3, this comparison would highlight any additional errors caused by single pixel imaging. For the linear polariser, the spatially averaged Mueller matrix, normalised to the M_{00} element, was

$$\mathbf{M}^{LP,SPI} = \begin{bmatrix} 1.00 & 0.66 & -0.71 & -0.04 \\ 0.72 & 0.48 & -0.51 & -0.02 \\ -0.67 & -0.44 & 0.48 & 0.04 \\ -0.11 & -0.08 & 0.08 & 0.01 \end{bmatrix}, \tag{6.4}$$

while the Mueller matrix obtained from non-imaging polarimetry was

$$\mathbf{M}^{LP,no\ SPI} = \begin{bmatrix} 1.00 & 0.65 & -0.75 & -0.03 \\ 0.72 & 0.48 & -0.54 & -0.01 \\ -0.68 & -0.44 & 0.52 & 0.03 \\ -0.11 & -0.08 & 0.08 & 0.01 \end{bmatrix}. \tag{6.5}$$

As explained in Section 4.3, differences between experimental and theoretical Mueller matrices can be expected due to experimental uncertainties and imperfections in the optical element under test. Since the non-imaging single pixel polarimeter has previously been verified (see Section 4.3), to validate the single pixel polarimeter, it

is more instructive to consider differences between $\mathbf{M}^{LP,SPI}$ and $\mathbf{M}^{LP,no\ SPI}$ than to compare them to their theoretical counterparts. The values in these two matrices can be seen to be similar, with a maximum difference of 0.04. For the quarter waveplate, the spatially averaged Mueller matrix, normalised to the M_{00} element, was

$$\mathbf{M}^{QWP,SPI} = \begin{bmatrix} 1.00 & -0.02 & -0.02 & -0.01 \\ 0.00 & 0.24 & 0.30 & -0.88 \\ -0.02 & 0.13 & 0.90 & 0.34 \\ -0.01 & 0.94 & -0.17 & 0.19 \end{bmatrix}, \tag{6.6}$$

while the Mueller matrix obtained from non-imaging polarimetry was

$$\mathbf{M}^{QWP,no\ SPI} = \begin{bmatrix} 1.00 & -0.02 & -0.02 & -0.01 \\ 0.00 & 0.24 & 0.31 & -0.90 \\ -0.02 & 0.12 & 0.91 & 0.34 \\ 0.00 & 0.96 & -0.18 & 0.19 \end{bmatrix}. \tag{6.7}$$

The maximum difference between these two matrices was 0.02. The differences observed for both test objects were similar to the deviations observed in Section 4.3. As such, single pixel imaging did not introduce significant error, and the Mueller matrices obtained by single pixel polarimetry were deemed to be reasonable.

The imaging results computed for the linear polariser, without and with SM4 present, are shown in Figures 6.1 and 6.2 respectively, while those for the quarter waveplate are presented in Figures 6.3 and 6.4. For all imaging results shown in this chapter, pixels in the spatially resolved Mueller matrices are normalised to their respective M_{00} values, which as previously explained, allows for an easier comparison of the polarimetric properties across pixels. The M_{00} matrix element, however, is presented in its original form as it is directly proportional to the unpolarised transmittance of the sample, and hence shows the intensity image recovered by single pixel polarimetric imaging.

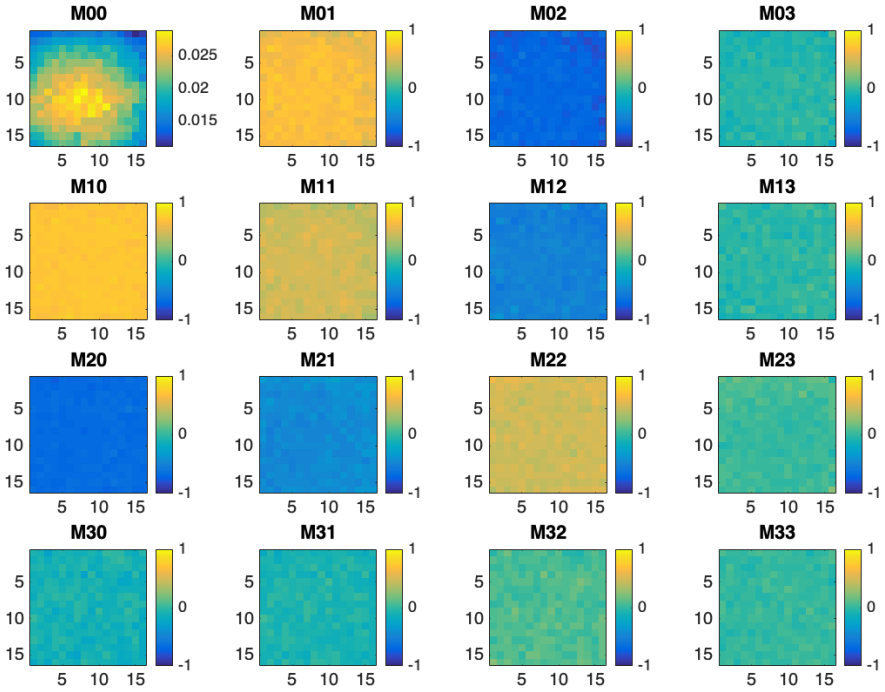

Figure 6.1: Spatially resolved Mueller matrix for an unobscured linear polariser with its transmission axis at $-20°$. Matrix elements, other than M_{00}, are normalised to their respective M_{00} values. The x and y axes for each plot correspond to pixel indices.

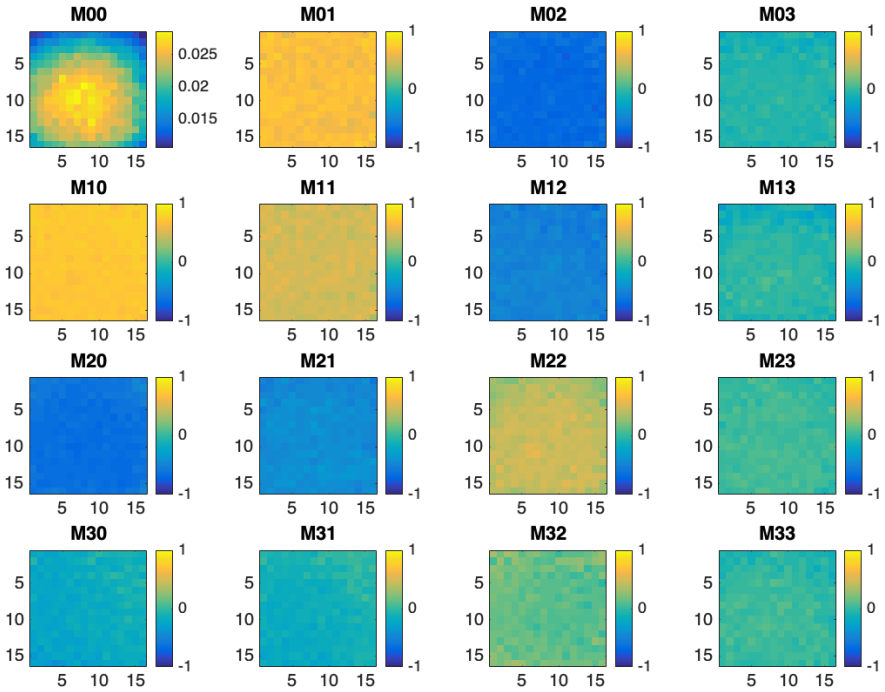

Figure 6.2: Spatially resolved Mueller matrix for a test linear polariser with its transmission axis at $-20°$, hidden behind SM4. Matrix elements, other than M_{00}, are normalised to their respective M_{00} values. The x and y axes for each plot correspond to pixel indices.

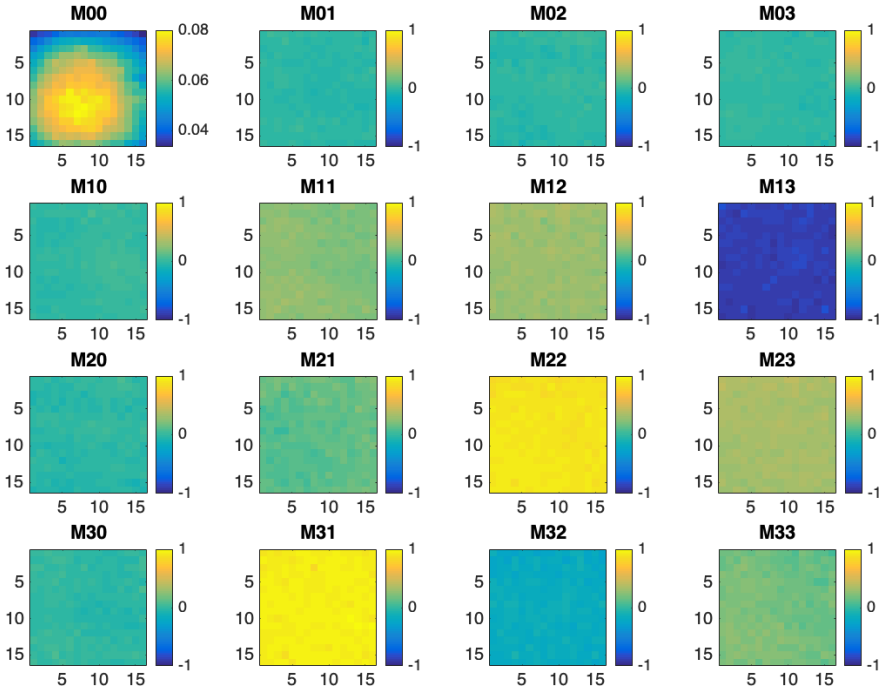

Figure 6.3: Spatially resolved Mueller matrix for an unobscured quarter waveplate with its fast axis at 40°. Matrix elements, other than M_{00}, are normalised to their respective M_{00} values. The x and y axes for each plot correspond to pixel indices.

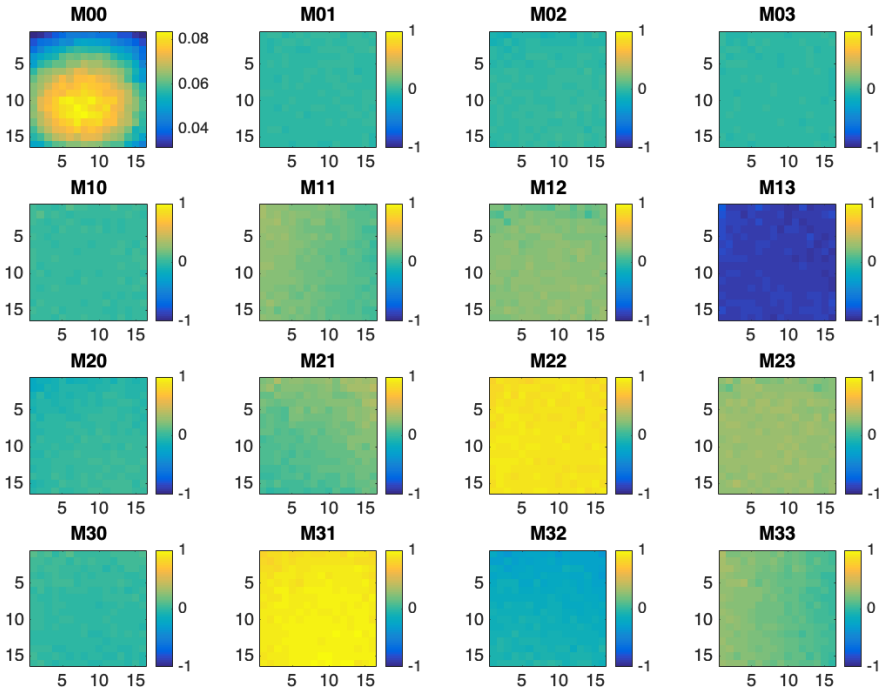

Figure 6.4: Spatially resolved Mueller matrix for a test quarter waveplate with its transmission axis at 40°, hidden behind SM4. Matrix elements, other than M_{00}, are normalised to their respective M_{00} values. The x and y axes for each plot correspond to pixel indices.

Qualitatively, it can be seen that for both test objects, the images obtained with and without SM4 present are generally similar, which indicates the feasibility of the proposed technique. For each test object, the similarity between the two images was quantified using an element-wise RMSE for each Mueller matrix element. As the illumination intensity was changed between the two measurements, the element-wise RMSE was computed after normalising each pixel in the obtained polarimetric images by their respective M_{00} value. Mathematically, the element-wise RMSE of the $(i,j)^{th}$ Mueller matrix element was computed as

$$\mathrm{RMSE}_{ij} = \sqrt{\frac{1}{256}\sum_{k=1}^{256}\left(M_{ijk}^{O} - M_{ijk}^{O,SM}\right)^2}, \tag{6.8}$$

where M_{ijk}^{O} and $M_{ijk}^{O,SM}$ are, respectively, the $(i,j)^{th}$ Mueller matrix elements for the k^{th} pixel without and with the scattering medium present.

Comparing the reconstructed images with and without SM4 present, the resulting element-wise RMSE values computed for the linear polariser and quarter waveplate, denoted as RMSE^{LP} and RMSE^{WP} respectively, were

$$\mathrm{RMSE}^{LP} = \begin{bmatrix} 0.00 & 0.08 & 0.07 & 0.07 \\ 0.04 & 0.07 & 0.06 & 0.10 \\ 0.07 & 0.06 & 0.11 & 0.07 \\ 0.12 & 0.10 & 0.10 & 0.07 \end{bmatrix}. \tag{6.9}$$

$$\mathrm{RMSE}^{WP} = \begin{bmatrix} 0.00 & 0.03 & 0.04 & 0.03 \\ 0.04 & 0.09 & 0.09 & 0.03 \\ 0.05 & 0.08 & 0.03 & 0.07 \\ 0.04 & 0.04 & 0.07 & 0.07 \end{bmatrix}. \tag{6.10}$$

The maximum RMSE in both cases was about 0.1, which is slightly larger than the deviations observed in Section 4.3. One possible source of error could be spatial variations in $\mathbf{M}^{SM}$ caused by spatial inhomogeneities in SM4 that were unaccounted for in the data processing, such as spatial variations in the density of the formed crosslinks in the background epoxy [208] in SM4. Errors due to spatial variations

in the scattering medium can be accounted for by correcting for its contribution on a pixel-wise basis, by using the spatially resolved Mueller matrix for the scattering medium without any test object present. The maximum RMSE values computed in this manner for the linear polariser and the quarter waveplate were 0.14 and 0.13 respectively. Since the RMSE did not improve by a pixel-wise correction for the scattering medium, it was concluded that spatial inhomogeneities in SM4 were not the main cause of the increased error.

Other possible sources of error could be experimental uncertainties in the measured $\mathbf{M}^{SM}$ and experimental noise (see discussion in Section 5.1). The latter, along with a spatially varying illumination (see Section 5.2), results in a spatially varying SNR. For a fixed input and analysed polarisation state, the detector noise related to each projected spatial mask used for single pixel imaging can be considered to be independent and equal in magnitude. As such, according to Equation 5.4, this results in the same magnitude of uncertainty for each pixel. This implies that the SNR varies with the illumination level, and is lowest at the edges of the image where the intensity of the beam is also at its lowest. This variation in SNR leads to spatially varying uncertainties in the determined spatially resolved Mueller matrix, which are worsened by the normalisation of the Mueller matrix by its M_{00} element. The effect of a spatially varying SNR on the obtained polarimetric image is evidenced in Figure 6.5, which, for each test object, shows the absolute difference between the Mueller matrices obtained with and without SM4 present, averaged across all 16 Mueller matrix elements. The differences can be seen to be largest at the edges of the image, which are the image regions with the lowest SNR. This suggests that experimental noise is likely a significant factor behind the errors observed.

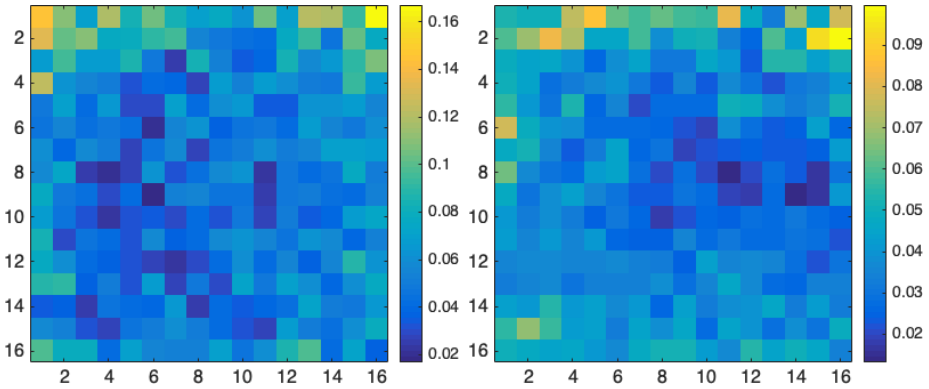

(a) Linear polariser **(b)** Quarter waveplate

Figure 6.5: Absolute of the difference between the Mueller matrices obtained with and without SM4 present for the two homogeneous test objects, averaged across all Mueller matrix elements. The x and y axes of the plot correspond to pixel indices.

6.1.3 Spatially Inhomogeneous Test Object

Having seen the feasibility of the proposed method on spatially homogeneous test objects, the natural next step was to test the same method on a test object exhibiting spatial inhomogeneity. The spatially inhomogeneous test object, depicted in Figure 4.2, was placed in the object plane, as shown in Figure 4.1. For reference, measurements were first taken without the scattering medium present using the data acquisition procedures described in Section 4.4. As was done for the spatially homogeneous test objects, ND filters (*Thorlabs NE10A and NE20A*) were used to attenuate the incident illumination to prevent saturation of the photodiodes. The resulting polarimetric image, obtained through the data processing methods discussed previously in Section 4.5, is shown in Figure 6.6.

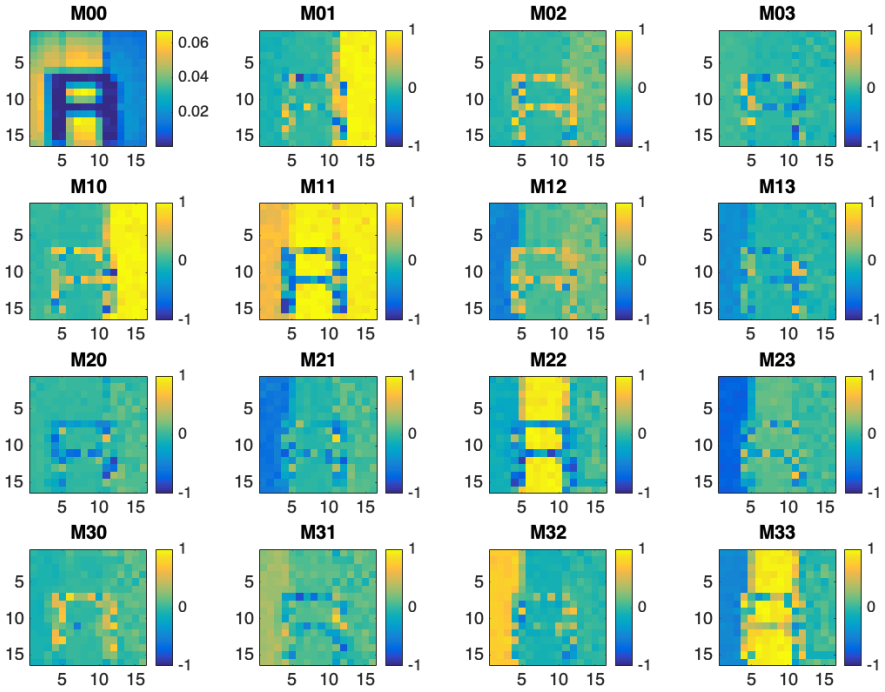

Figure 6.6: Spatially resolved Mueller matrix for the spatially inhomogeneous test object without any scattering medium present. Matrix elements, other than M_{00}, are normalised to their respective M_{00} values. The x and y axes for each plot correspond to pixel indices.

The letter R is clearly visible in the image. In addition, three distinct regions can be seen in the left, centre and right of the image shown in Figure 6.6, corresponding respectively to the regions covered by the scotch tape, glass and linear polariser. SM4 was then inserted in between the object and the PSA, as shown in Figure 4.1, and the ND filters were removed. Figure 6.7 shows an intensity image that was taken of the obscured test object using a spatially resolved CMOS camera located at the position of the photodiode D1. It can be observed that no features of the test object are visible in the image.

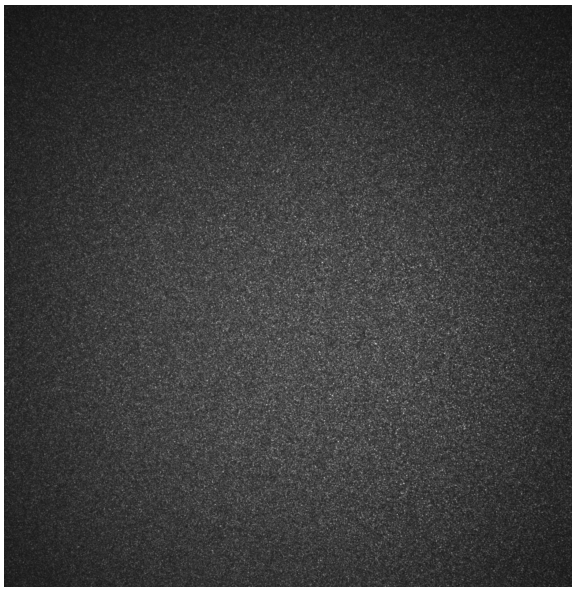

Figure 6.7: Intensity image of the spatially inhomogeneous test object with SM4 present, taken with a spatially resolved CMOS camera.

Using the procedures detailed in Sections 4.4 and 4.5, along with the measured Mueller matrix for SM4 in Equation 6.1, the measured detector intensities for each input and analysed polarisation state were processed to obtain the spatially resolved Mueller matrix, which is shown in Figure 6.8.

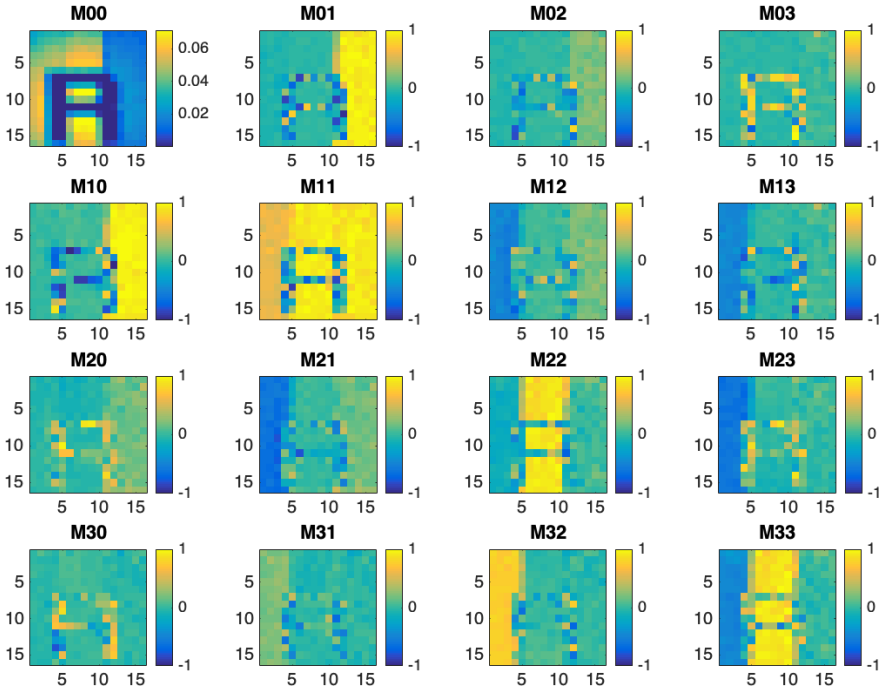

Figure 6.8: Spatially resolved Mueller matrix for the spatially inhomogeneous test object with SM4 present. Matrix elements, other than M_{00}, are normalised to their respective M_{00} values. The x and y axes for each plot correspond to pixel indices.

The results in Figure 6.8 look similar to those in Figure 6.6 that were taken without SM4 present. Compared to Figure 6.7, it can be seen that the spatial characteristics of the object have been faithfully reconstructed using single pixel polarimetric imaging, though some small discrepancies can be observed, such as in the matrix elements M_{21} and M_{31}. Nevertheless, keeping in mind the intensity image measured by a spatially resolved detector in Figure 6.7 which bore no resemblance to the hidden test object whatsoever, the similarity of Figures 6.6 and 6.8 demonstrates the feasibility of the proposed approach.

As was done for the spatially homogeneous test objects, the similarity of the images in Figures 6.6 and 6.8 was quantified by the element-wise RMSE that was specified in Equation 6.8. Before comparison, each pixel in both Figures 6.6 and 6.8 was normalised by their respective M_{00} values, which as explained previously, is equivalent to removing the effect of intensity variation for a better comparison of the polarimetric properties. Since the pixels corresponding to the opaque letter R consisted mainly of noise which was amplified by the normalisation of the Mueller

matrix, these pixels were identified by setting an empirically determined threshold of 0.008 to the pixel values in the M_{00} image of Figure 6.6 and were not included in the comparison. A mask consisting of the excluded pixels is shown in Figure 6.9.

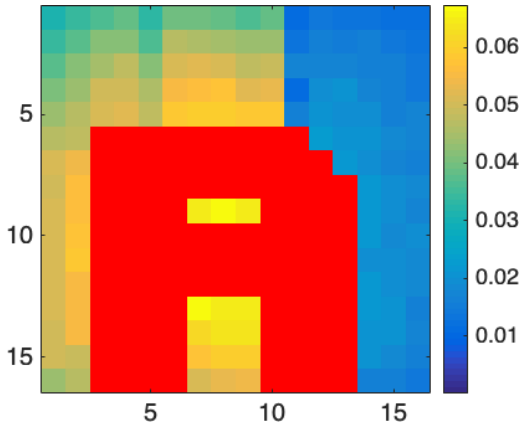

Figure 6.9: A figure illustrating the pixels excluded from the quantitative comparison, which are indicated in red.

The element-wise RMSE computed was

$$\mathrm{RMSE}^{letterR} = \begin{bmatrix} 0.00 & 0.06 & 0.12 & 0.11 \\ 0.06 & 0.07 & 0.11 & 0.15 \\ 0.07 & 0.08 & 0.10 & 0.09 \\ 0.08 & 0.10 & 0.12 & 0.09 \end{bmatrix}, \tag{6.11}$$

with a maximum RMSE value of 0.15. The RMSE values obtained cannot be directly compared to those computed for the spatially homogeneous objects, because as described in Chapter 5, possible fluctuations in the input polarisation state imply that the noise is sample-dependent. Nevertheless, the RMSE values for the spatially homogeneous and inhomogeneous objects are on the same order of magnitude. Possible sources of error contributing to the RMSE have been discussed previously in Section 6.1.2.

6.1.4 Thicker Scattering Media

The results so far have discussed the performance of the proposed technique with the various test objects hidden behind SM4. The same data acquisition and processing methods were used to reconstruct images of the same test objects hidden behind

the thicker scattering phantoms, SM5 and SM6. As before, the Mueller matrices of the scattering media were measured beforehand, to be used for the reconstruction of the hidden object as described in Section 4.5. The polarimetric properties of these measured Mueller matrices, as computed from a Lu-Chipman decomposition (see Section 2.2.7), are plotted in Figure 6.10. Similar to the results of Section 4.6.1, the scattering phantoms are seen to behave mainly as depolarisers, with the thickest scattering medium, SM6, having an average depolarisation factor of 0.6.

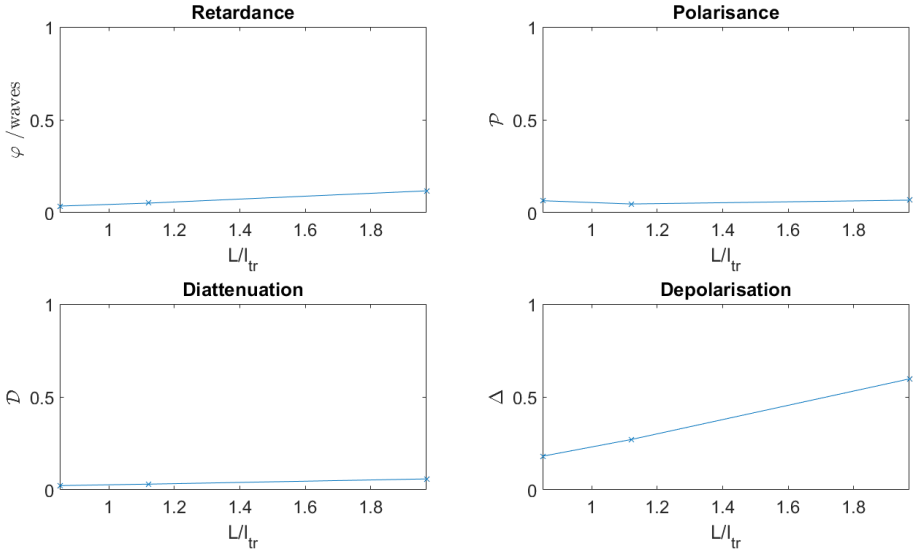

Figure 6.10: Lu-Chipman parameters of diattenuation ($\mathcal{D}$), polarisance ($\mathcal{P}$), depolarisation (Δ) and retardance in waves (φ) for SM4, SM5 and SM6.

Figures 6.11 and 6.12 show the polarimetric images of the spatially inhomogeneous test object when hidden behind SM5 and SM6 respectively.

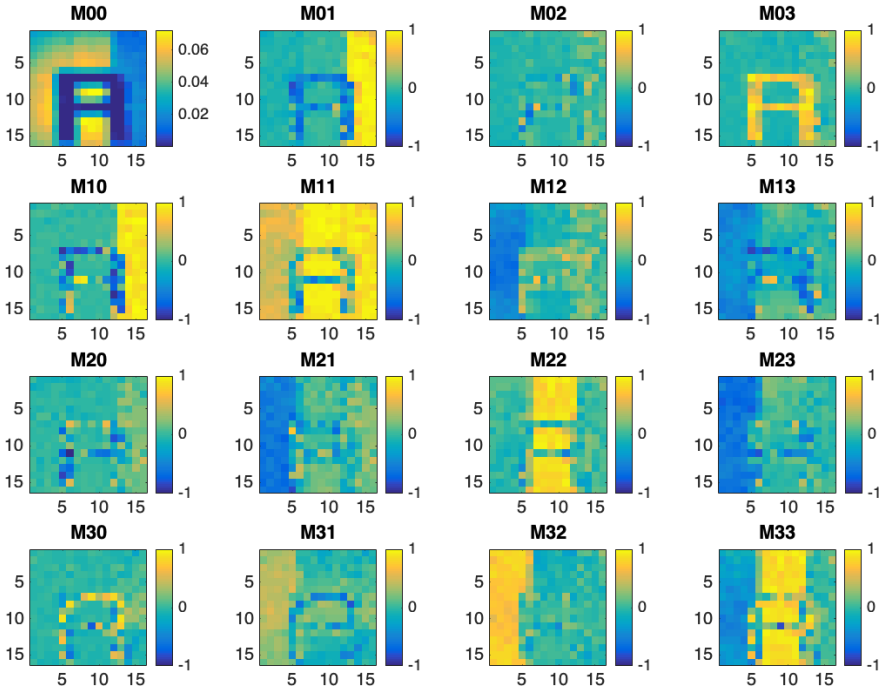

Figure 6.11: Spatially resolved Mueller matrix for the spatially inhomogeneous test object with SM5 present. Matrix elements, other than M_{00}, are normalised to their respective M_{00} values. The x and y axes for each plot correspond to pixel indices.

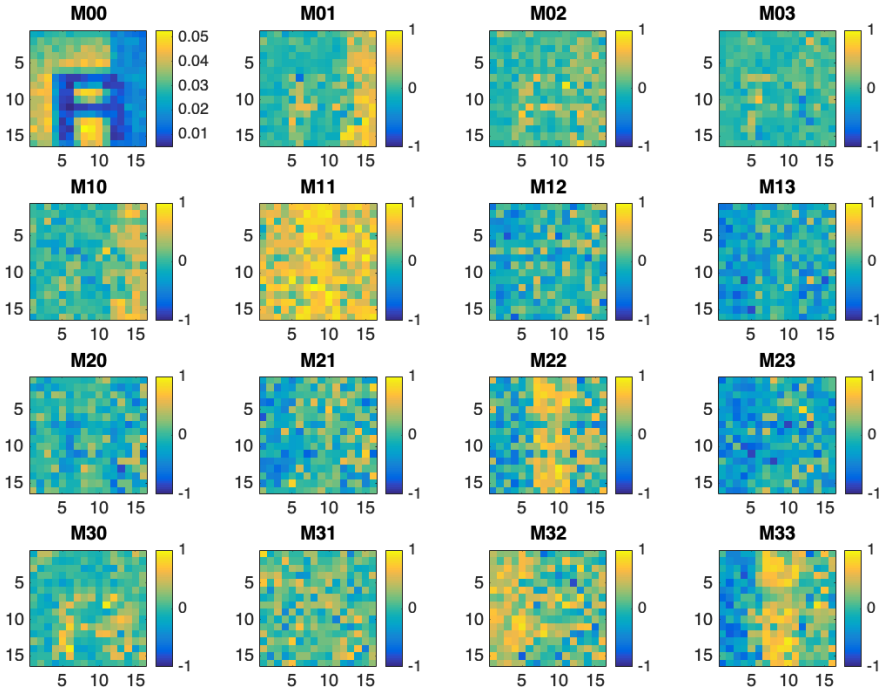

Figure 6.12: Spatially resolved Mueller matrix for the spatially inhomogeneous test object with SM6 present. Matrix elements, other than M_{00}, are normalised to their respective M_{00} values. The x and y axes for each plot correspond to pixel indices.

The letter R is still visible in both Figures 6.11 and 6.12, though the images get visibly noisier with increasing medium thickness. This is to be expected as the intensities detected by the photodiode are inversely related to the medium thickness. As an example, the detected intensities measured by D1 for SM4, SM5 and SM6, using the first input polarisation state, were 5.40, 3.12 and 0.80 respectively. As such, the SNR is expected to degrade with increasing medium thickness, resulting in larger uncertainties in the Mueller matrix. Nevertheless, the three regions corresponding to scotch tape, glass and the linear polariser can still be distinguished in Figures 6.11 and 6.12.

Figure 6.13 shows, as a function of medium thickness, the maximum, minimum and mean element-wise RMSE over all Mueller matrix elements for the test linear polariser, quarter waveplate and inhomogeneous test object. The element-wise RMSE was computed in the manner described previously for the experiments with SM4. It should be noted that for the experiments with SM5 and SM6, the orientation angle of the quarter waveplate was set to 70° instead of 40°. The three plots in Figure 6.13 show a similar increasing trend that is consistent with the degradation of the polarimetric images observed in Figures 6.11 and 6.12. Nevertheless, Figures 6.11 and 6.12 suggest that the method is feasible at larger thicknesses, though ultimately limited by the corresponding decrease in SNR.

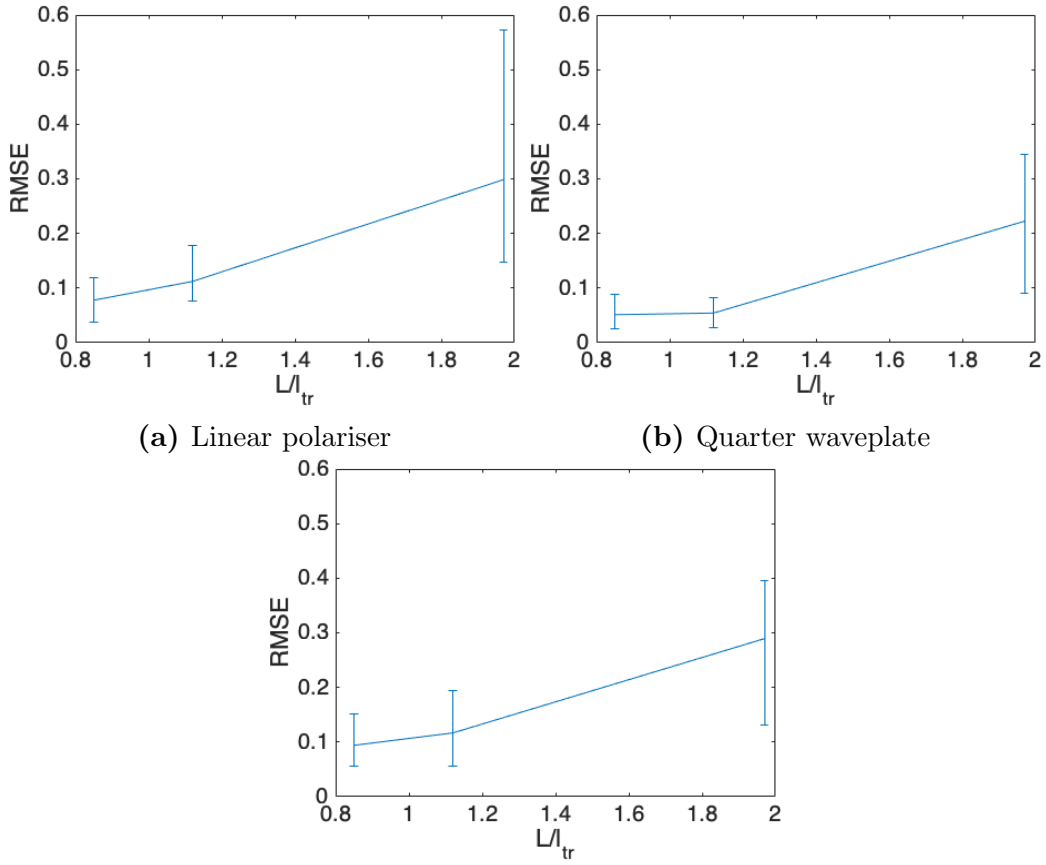

(a) Linear polariser **(b)** Quarter waveplate

(c) Inhomogeneous test object (i.e. letter R)

Figure 6.13: Plots showing the mean, maximum and minimum of the element-wise RMSE computed for all test objects as a function of thickness. The lines in each plot is the mean RMSE computed across all 16 Mueller matrix elements while the error bars denote the maximum and minimum RMSE values.

6.2 Chicken Breast

Encouraged by the results of Section 6.1, the proposed method was tested further with a biological scattering medium - a layer of chicken breast tissue.

6.2.1 Spatially Inhomogeneous Object

Measured Mueller Matrix

The thickness of the chicken slice was measured with a vernier caliper, and was found to be (0.89 ± 0.04)mm, with an increased error margin caused by the compressibility

of the sample, as well as a spatial variation of the sample thickness as it was difficult to cut the sample precisely with the utilised meat slicer. Since chicken breast has a TMFP of 1.25mm and a MFP of 43.7μm (see Section 4.6.2), this thickness corresponds to 0.72 times of the TMFP and 20.37 times of the MFP. Following the same procedure as for the scattering phantoms, the measured Mueller matrix of the chicken breast was

$$\mathbf{M}^{SM} = \begin{bmatrix} 1.00 & -0.07 & 0.00 & 0.00 \\ 0.02 & -0.01 & -0.10 & -0.10 \\ 0.06 & -0.15 & 0.30 & -0.01 \\ 0.01 & 0.06 & 0.04 & -0.03 \end{bmatrix} . \tag{6.12}$$

The corresponding polarimetric properties of this matrix, as computed by a Lu-Chipman decomposition (see Section 2.2.7), were $[\varphi, \mathcal{P}, \mathcal{D}, \Delta] = [0.32, 0.06, 0.07, 0.82]$, where φ has been given in waves. Other than depolarisation, the significant retardance observed is reasonable, since the tissue is composed of aligned fibrous strands, and is also consistent with results found in literature [209, 210].

Spatially Resolved Mueller Matrix

The spatially inhomogeneous test object, depicted in Figure 4.2, was placed in the object plane, hidden behind the chicken breast tissue. The same experimental procedure and data processing methods that were used for the experiments with the scattering phantoms were used here to reconstruct the polarimetric image of the test object. Figure 6.14 shows the resulting spatially resolved Mueller matrix.

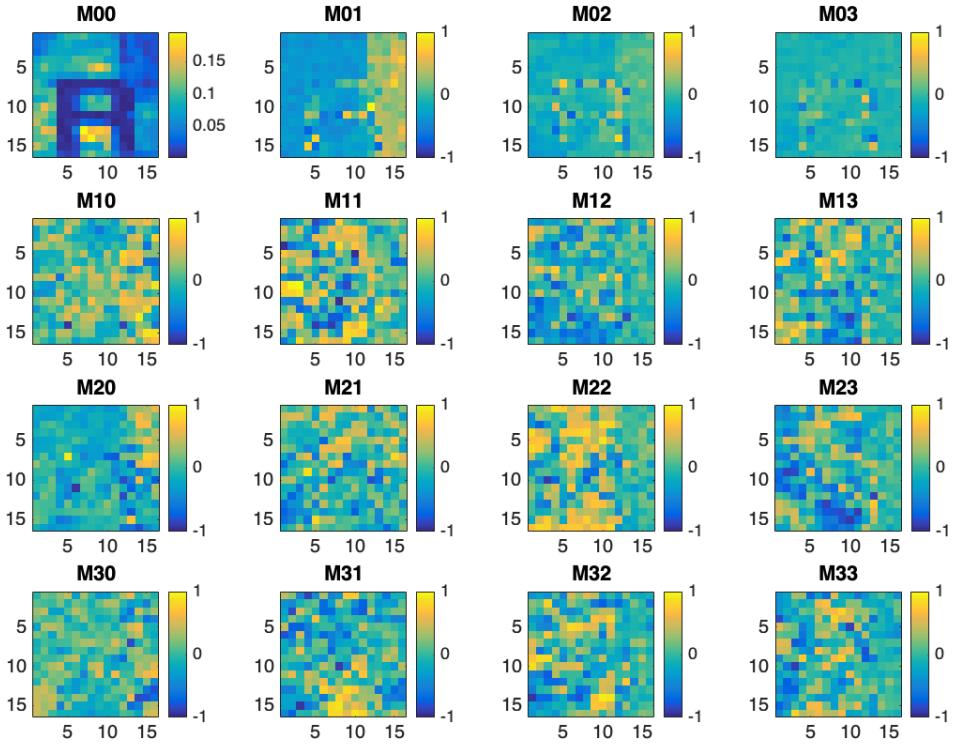

Figure 6.14: Spatially resolved Mueller matrix obtained for the spatially inhomogeneous test object hidden behind a chicken breast layer. Matrix elements, other than M_{00}, are normalised to their respective M_{00} values. The x and y axes for each plot correspond to pixel indices.

Figure 6.14 can be seen to deviate significantly from the reference image in Figure 6.6. The letter R is still visible in the intensity image (i.e. the M_{00} element), but a comparison with Figure 6.6 shows that the polarimetric information about the object was not well recovered. Possible causes of this deviation are discussed later in this section, after a look at the results obtained with the spatially inhomogeneous test objects.

6.2.2 Spatially Homogeneous Objects

The experiment was repeated with the test linear polariser, with its transmission axis oriented at $-30°$, placed in the object plane in the setup (see Figure 4.1). As the sample degrades over time, a fresh slice of chicken breast was cut for this experiment, and a separate set of measurements for the Mueller matrix and thickness of the sample was taken.

Measured Mueller Matrix

The thickness of the chicken breast slice was measured to be (0.74 ± 0.06)mm, which corresponds to 0.59 times of the TMFP and 16.93 times of the MFP. The measured Mueller matrix of the chicken breast was

$$\mathbf{M}^{SM} = \begin{bmatrix} 1.00 & -0.21 & -0.03 & 0.01 \\ -0.16 & 0.60 & -0.01 & -0.02 \\ -0.01 & -0.01 & -0.12 & 0.06 \\ 0.03 & -0.07 & -0.06 & -0.08 \end{bmatrix}. \tag{6.13}$$

The corresponding polarimetric parameters obtained from a Lu-Chipman decomposition were $[\varphi, \mathcal{P}, \mathcal{D}, \Delta] = [0.42, 0.16, 0.21, 0.72]$, where φ has been given in waves. Similar to the chicken breast sample used for the spatially inhomogeneous test object, other than depolarisation, significant retardance can be observed.

Spatially Resolved Mueller Matrix

The test linear polariser, with its transmission axis oriented at $-30°$, was placed in the object plane, and the chicken breast tissue was located between the polariser and the PSA. The reconstructed spatially resolved Mueller matrix of the test linear polariser is shown in Figure 6.15.

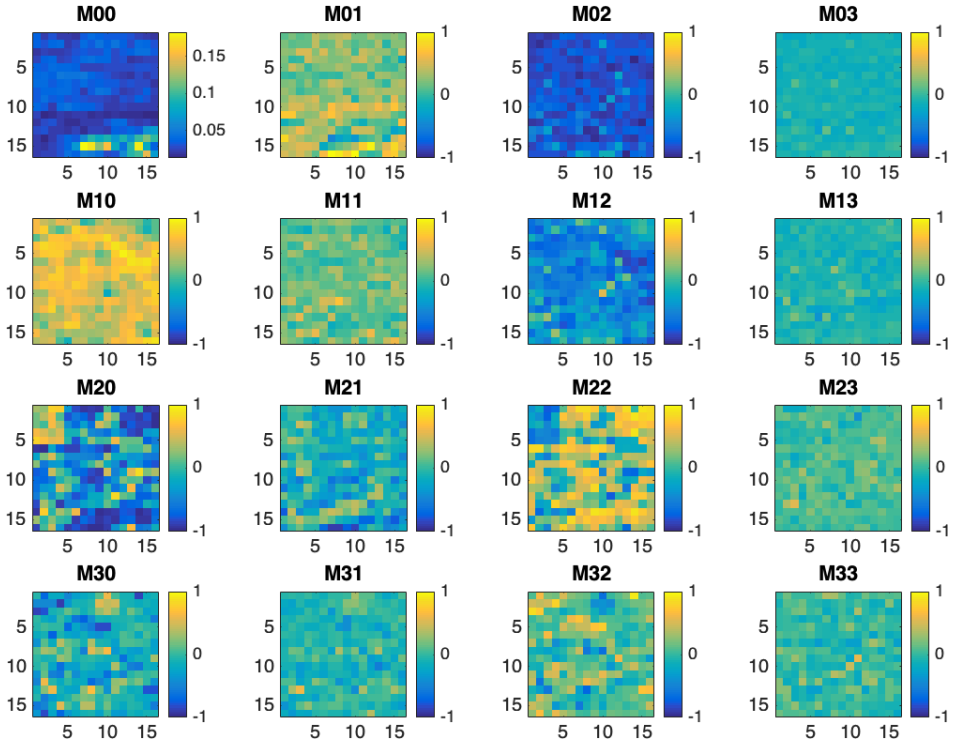

Figure 6.15: Spatially resolved Mueller matrix obtained for a test polariser with its transmission axis at $-30°$ hidden behind a chicken breast layer. Matrix elements, other than M_{00}, are normalised to their respective M_{00} values. The x and y axes for each plot correspond to pixel indices.

Unlike Figure 6.1, the intensity profile of the beam is not visible in the reconstruction shown in Figure 6.15. The element-wise RMSE (see Equation 6.8) that was computed by comparing the normalised spatially resolved Mueller matrix to the same measurements taken of an unobscured linear polariser, was

$$\mathrm{RMSE}^{LP} = \begin{bmatrix} 0.00 & 0.43 & 0.17 & 0.10 \\ 0.20 & 0.35 & 0.27 & 0.12 \\ 0.62 & 0.41 & 0.51 & 0.13 \\ 0.30 & 0.17 & 0.28 & 0.16 \end{bmatrix} . \tag{6.14}$$

It can be seen that the computed RMSE values are much larger than the previous results presented in Equation 6.9, with a maximum value of 0.62. Given that no meaningful results were obtained for the inhomogeneous test object and the linear polariser, the experiment was not repeated for the quarter waveplate. The next part of this section investigates the possible factors that have led to the anomalous

results observed.

6.2.3 Discussion

It has been seen that the polarimetric images obtained of the test objects hidden behind chicken breast samples did not match well to the images taken of the unobscured test objects (i.e. Figures 6.14 and 6.15 compared with Figures 6.6 and 6.1). Comparing the chicken breast samples to the scattering phantoms, it was deduced that there were two possible reasons behind this mismatch - a temporal variation of the sample and a significant variation of the polarimetric properties of the chicken breast samples across pixels. These factors will now be investigated in the rest of this section.

Spatial variation of scattering sample

The spatial variation in the polarimetric properties of the chicken breast samples can be seen from the spatially resolved Mueller matrix of the chicken breast samples without any test objects present, as shown in Figure 6.16. For comparison, the Mueller matrix for SM4 is shown in Figure 6.17.

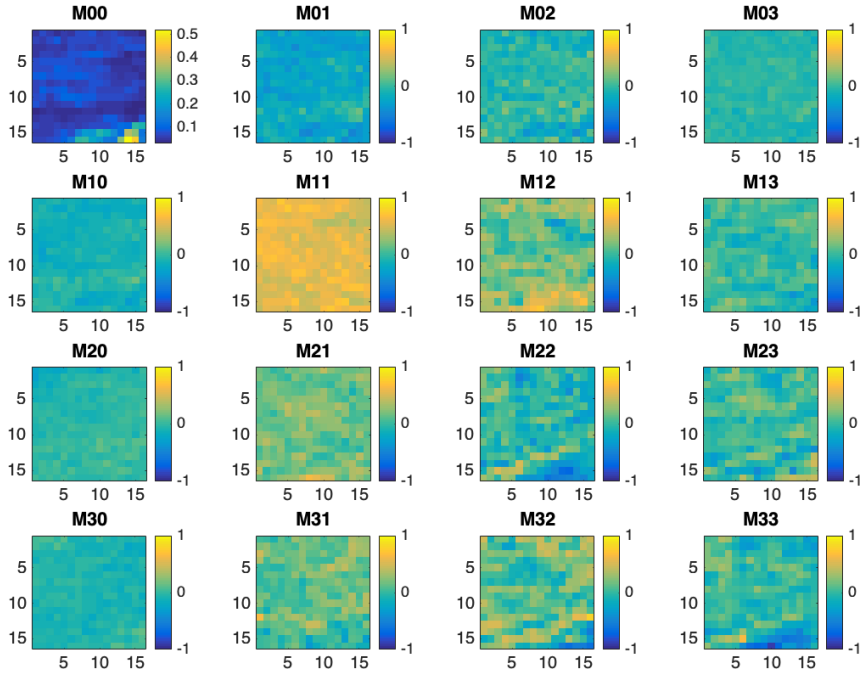

Figure 6.16: Spatially resolved Mueller matrix for the chicken breast layer corresponding to the scattering medium used to obtain the results in Figure 6.15. Matrix elements, other than M_{00}, are normalised to their respective M_{00} values. The x and y axes for each plot correspond to pixel indices.

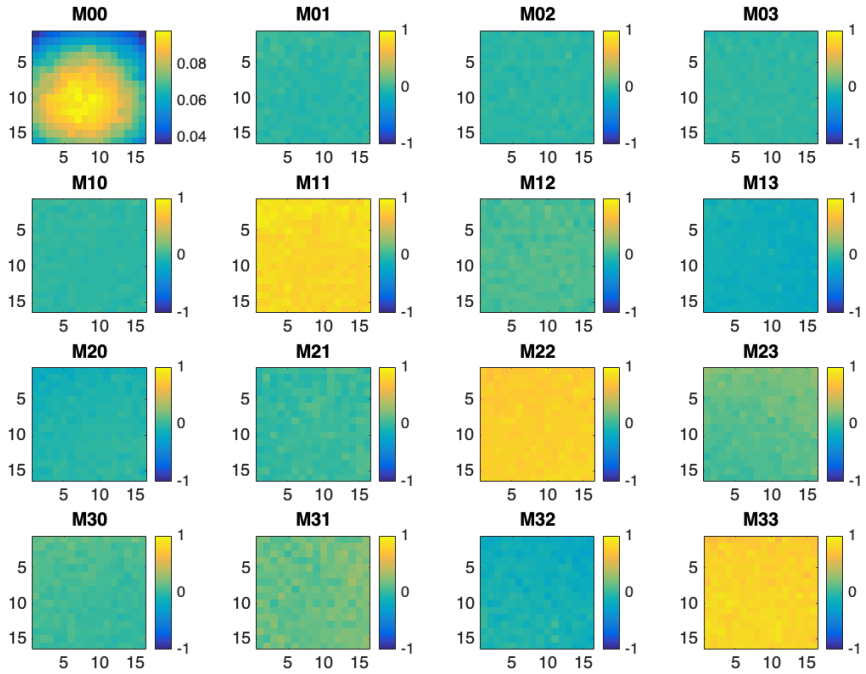

Figure 6.17: Spatially resolved Mueller matrix for the scattering phantom SM4 corresponding to the scattering medium used to obtain the results in Figure 6.2. Matrix elements, other than M_{00}, are normalised to their respective M_{00} values. The x and y axes for each plot correspond to pixel indices.

Though some spatial variation can still seen in the scattering phantoms, the magnitude of the variation is much larger in the chicken breast sample. The spatial variation in the scattering media samples was quantified by computing the standard deviation of the polarimetric parameters φ, $\mathcal{P}$, $\mathcal{D}$ and Δ across all spatial pixels, as obtained from a pixel-wise Lu-Chipman decomposition (see Section 2.2.7) of the spatially resolved Mueller matrices shown in Figures 6.16 and 6.17. The computed standard deviations are shown in Table 6.2, where it can be seen that the values computed for the chicken breast sample are much larger than those for SM4.

	φ	$\mathcal{P}$	$\mathcal{D}$	Δ
Chicken breast	0.839	0.059	0.108	0.125
SM4	0.062	0.053	0.020	0.025

Table 6.2: Standard deviation of the Lu-Chipman parameters across all spatial pixels for the chicken breast sample and SM4.

Using the same dataset that was used to compute Figure 6.14, the spatially resolved Mueller matrix of the chicken breast (i.e. Figure 6.16) was used to recover the polarimetric image of the letter R on a pixel-wise basis via Equation 3.21. If the degradation in the results was due to the spatial variation of the chicken breast sample, it is expected that correcting for the Mueller matrix of the chicken breast on a pixel-wise basis would improve the result. Figure 6.18 shows the reconstructed Mueller matrix.

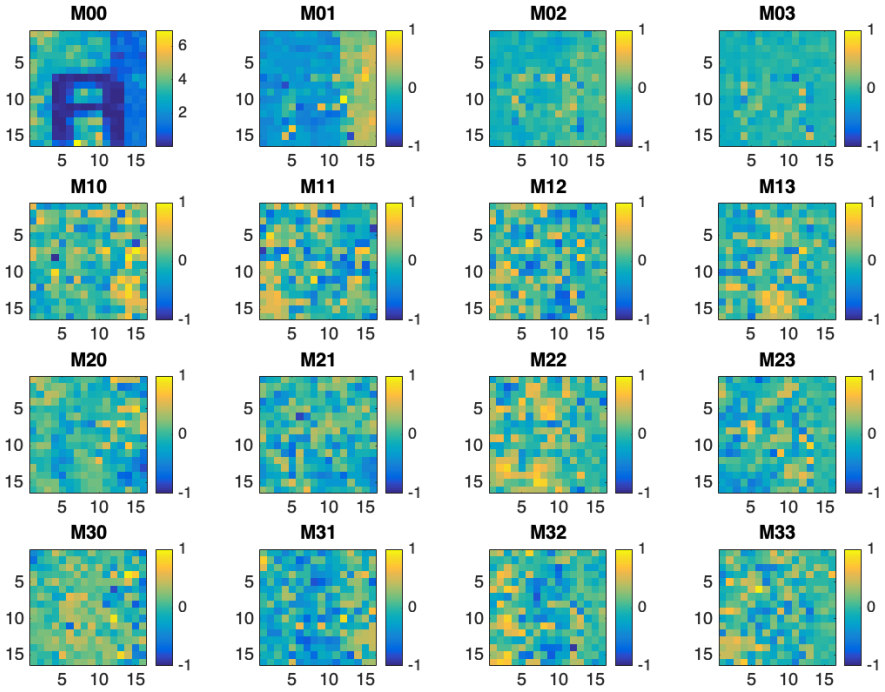

Figure 6.18: Spatially resolved Mueller matrix obtained for the spatially inhomogeneous test object hidden behind a chicken breast layer, corrected using the spatially resolved Mueller matrix of the chicken breast. Matrix elements, other than M_{00}, are normalised to their respective M_{00} values. The x and y axes correspond to pixel indices.

No visible improvement from Figure 6.14 was seen in Figure 6.18. The same procedure was conducted on the dataset that was used to compute the spatially resolved Mueller matrix of the hidden linear polariser in Figure 6.15. Compared to the reconstructed image of the unobstructed linear polariser, the element-wise RMSE obtained was

$$\begin{bmatrix} 0.00 & 0.44 & 0.15 & 0.10 \\ 0.33 & 0.35 & 0.27 & 0.12 \\ 0.76 & 0.39 & 0.61 & 0.13 \\ 0.42 & 0.20 & 0.37 & 0.13 \end{bmatrix}, \tag{6.15}$$

with a maximum value of 0.76. Since no improvement was observed in both datasets, this suggests that spatial variation of the sample was not the main factor affecting the results.

Temporal variation of scattering sample

The temporal variation of a chicken breast sample was investigated by measuring its Mueller matrix over a time span of 150 minutes, with one measurement taken every minute. The acquisition of a 16×16 polarimetric image takes 90 minutes, so this time span is sufficient to investigate the temporal variation during an experiment. These measurements were done without single pixel imaging (i.e. non-imaging polarimetry), with an incident illumination area on the chicken breast sample that is equal to the size of a Hadamard mask. The results are shown in Figure 6.19.

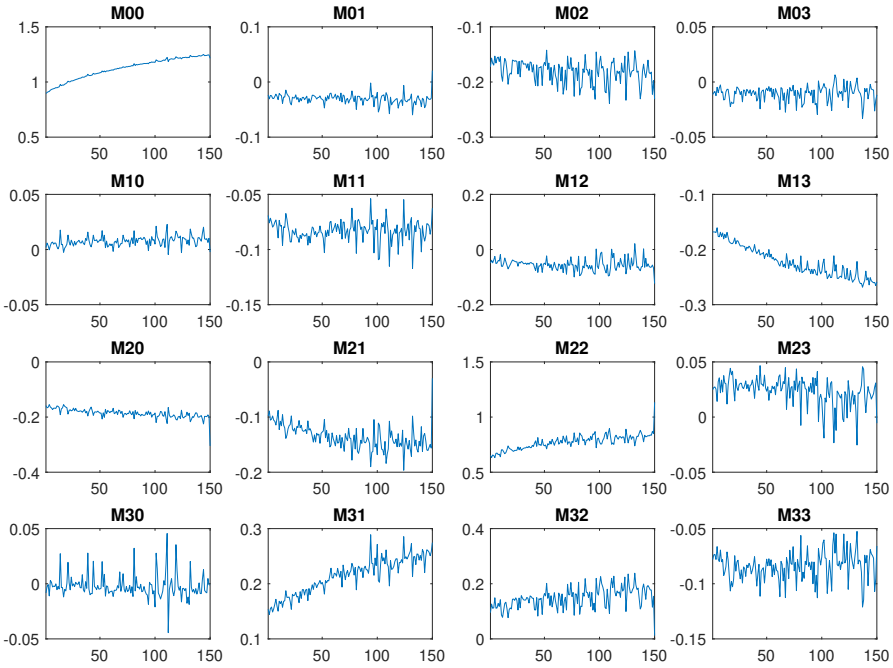

Figure 6.19: Mueller matrix of chicken breast measured over 150 minutes. The x axes describes the time in minutes, while the y axes is the value of the Mueller matrix element.

The matrix element M_{00}, which is directly proportional to the unpolarised transmittance of the sample, increased from an initial value of 0.896 to a final value of 1.245. This implies that there was close to a 40% increase in the sample transmittance. Over a typical image acquisition time of 90 minutes, there was an increase in transmittance of 32%. In contrast, a Lu-Chipman decomposition of the Mueller matrices, which is shown in Figure 6.20, showed no significant change in the polarimetric parameters over time. A further measurement of air with no chicken breast present (see Figure 6.21) showed no such increase in value for the M_{00} element. As such, it

can be concluded that the increase in transmittance was not caused by any instrumental factor, and can be attributed directly to a change in the biological sample. Similar trends were observed, albeit with a smaller magnitude, when the chicken breast sample was sandwiched between two glass slides and scotch tape was used to seal all openings on the mount, which might suggest that sample dehydration was only one of the causes of this observed variation. As the samples were mounted vertically, rather than horizontally as on a microscope stage, another possible reason could be a downward diffusion of water or other constituents in chicken breast due to gravity. Though this was not investigated further, it would be reflected in a spatial inhomogeneity that could, in principle, be tested.

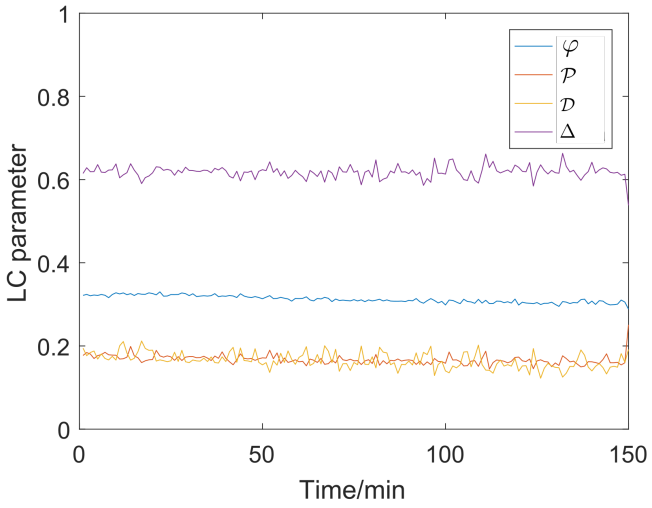

Figure 6.20: Lu-Chipman parameters of diattenuation ($\mathcal{D}$), polarisance ($\mathcal{P}$), depolarisation (Δ) and retardance in waves (φ)) corresponding to the measurements over chicken breast shown in Figure 6.19.

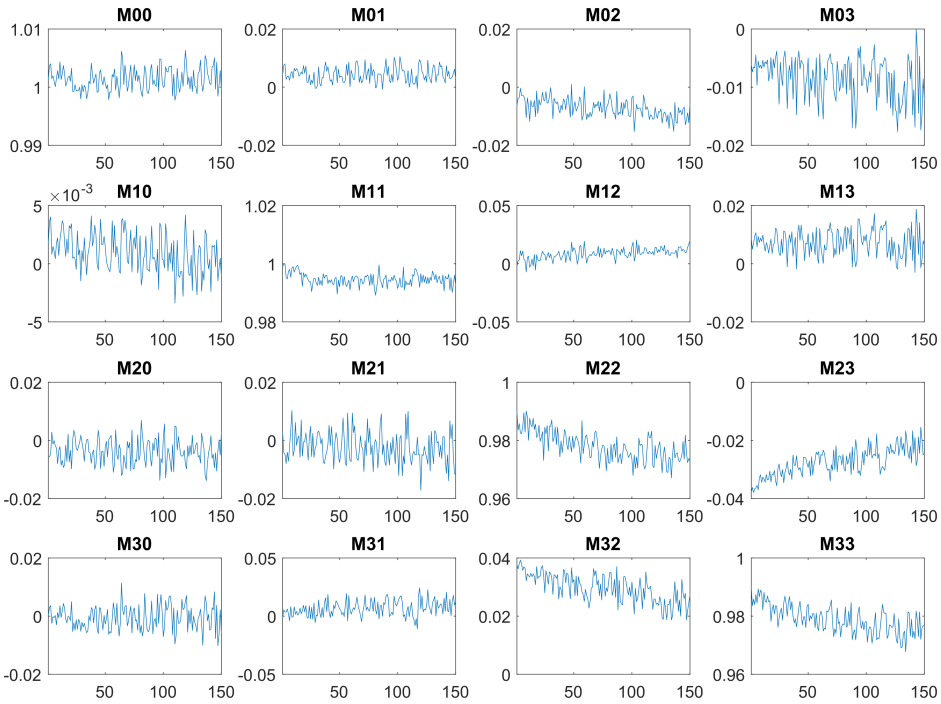

Figure 6.21: Mueller matrix of air measured over 150 minutes. The x axes describes the time in minutes, while the y axes is the value of the Mueller matrix element.

Regardless of the cause, the observed change in transmittance causes a change in the intensity measured by the photodiode over time. This is not ideal for single pixel imaging, whose reconstruction relies on the intensity changes caused by the projection of different spatial masks on the object. As a consequence, it was not possible to normalise the data as measured intensity changes could come either from a change in the sample transmittance or a change in the projected spatial mask. To illustrate this effect, simulations were conducted to investigate the effect of an intensity change during acquisition on the performance of single pixel polarimetric imaging.

The spatially resolved intensities at each detector were simulated using Equation 3.20 for each input polarisation state, with the ideal instrument matrices shown in Equations 4.2 and 4.3. From the computed intensity images, the intensities measured by the photodiodes for each spatial mask were then calculated using Equation 3.19 for each input and analysed polarisation state. A linear increase in intensity of 30% across the experiment was assumed, corresponding to the variation in trans-

mittance of the chicken breast sample observed over the time span of an acquisition. In the laboratory experiment, the detector intensities were taken sequentially, such that for each input polarisation state, all spatial masks were projected, while for each spatial mask, the intensities corresponding to each analysed polarisation state were sequentially measured. With this sequence in mind, the linear intensity increase was simulated as

$$I_p^{tot,\,\prime} = \alpha_p I_p^{tot} \ , \tag{6.16}$$

with I_p^{tot} being the ideal intensity simulated using Equation 3.19 for the input and analysed polarisation states, as well as spatial mask, corresponding to the p^{th} "measured" intensity. The multiplicative factor, α_p, is computed based on the linear equation $\alpha_p = mp + 1$, where $m = \frac{1.3-1}{P}$ is the gradient computed over the total number of "measured" intensities, P.

A theoretical linear polariser with its transmission axis at $-30°$ was used as the test object in these simulations. The linear polariser, in such a configuration, has a Mueller matrix that is given by

$$M^{LP,5°} = \begin{bmatrix} 0.50 & 0.25 & -0.43 & 0.00 \\ 0.25 & 0.13 & -0.22 & 0.00 \\ -0.43 & -0.22 & 0.38 & 0.00 \\ 0.00 & 0.00 & 0.00 & 0.00 \end{bmatrix} . \tag{6.17}$$

On the other hand, the Mueller matrix of the scattering medium was taken to be a depolariser, with its Mueller matrix given by a 4×4 diagonal matrix with M_{11}, M_{22} and M_{33} generated as a random number in the range $[-1, 1]$, resulting in

$$M^{SM} = \begin{bmatrix} 1.00 & 0.00 & 0.00 & 0.00 \\ 0.00 & 0.39 & 0.00 & 0.00 \\ 0.00 & 0.00 & 0.66 & 0.00 \\ 0.00 & 0.00 & 0.00 & 0.17 \end{bmatrix} . \tag{6.18}$$

As mentioned above, the structure of this Mueller matrix is typical of an ensemble of microspheres in the multiple scattering regime [207].

Using these Mueller matrices, two experiments were simulated - the first with the scattering medium located in between the linear polariser and the detector and the second with only the scattering medium present. The spatially resolved Mueller matrix of the scattering medium, obtained from the second experiment, was used to compute the image of the linear polariser in the first experiment.

In the first set of simulations, both the test linear polariser and scattering medium were assumed to be spatially homogeneous. The polarimetric image of the hidden linear polariser obtained from the first experiment with a linear increase in intensity of 30% applied is shown in Figure 6.22. The maximum absolute difference, computed by a pixel-wise comparison with the groundtruth Mueller matrix in Equation 6.17, was 0.0754. In comparison, an experiment without any intensity variation resulted in a maximum absolute difference on the order of 10^{-11}, which can be attributed to numerical error. As expected, an intensity variation during the experiment increased the error in the retrieved Mueller matrix. Since the spatially resolved Mueller matrix of the scattering medium was used for correction, it should be noted that reconstruction errors in the datasets from both experiments have contributed to this result.

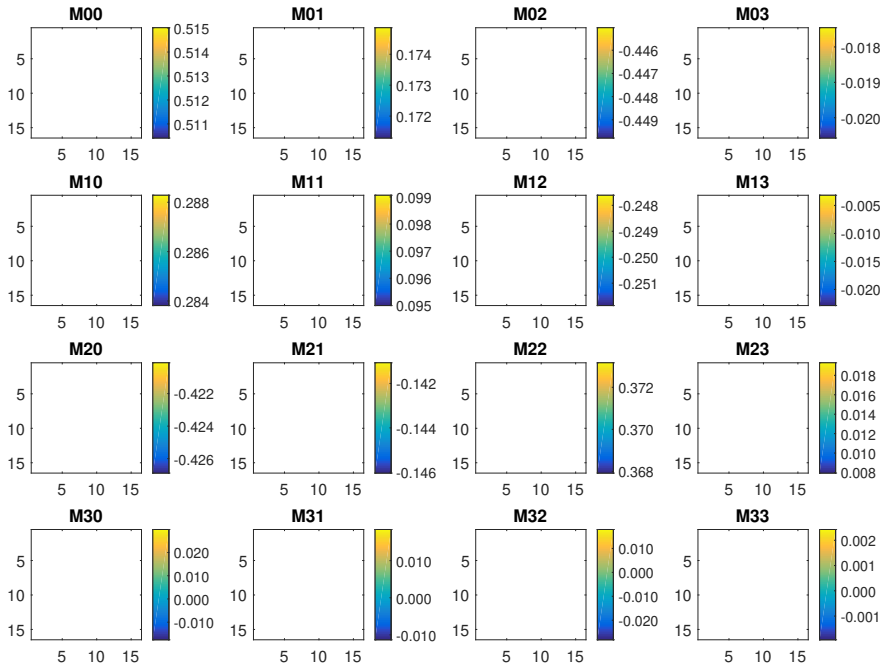

Figure 6.22: Spatially resolved Mueller matrix of the test linear polariser hidden behind a spatially homogeneous scattering medium, obtained using the proposed method from simulated data with an intensity variation of 30%. The x and y axes correspond to pixel indices.

The resulting error caused by the intensity increase also depends on the spatial variation of the scattering medium and/or test object being reconstructed. This can be seen from the computation of the maximum absolute difference for a single image reconstruction via single pixel imaging, corresponding to an intensity image reconstructed for any one input and analysed polarisation state. This can be written, for an ideal noiseless experiment, as

$$\text{Maximum absolute difference} = \max\left|\hat{x} - \vec{x}\right| = \max\left|\left(\mathbf{\Psi}^{-1}\mathbf{T}\mathbf{\Psi} - \mathbb{I}\right)\vec{x}\right| \ . \qquad (6.19)$$

Here, $\vec{x}$ is the ideal groundtruth image that would have been obtained without any temporal intensity variation, $\hat{x} = \mathbf{\Psi}^{-1}\mathbf{T}\mathbf{\Psi}$ is the reconstructed image, and $\mathbf{T}$ is a diagonal matrix with the diagonal elements related to the change in intensity. For the first experiment, $\vec{x}$ would be the combined spatial variation of both the scattering medium and the test object, while in the second experiment, $\vec{x}$ would be the spatial variation of the test object alone. From Equation 6.19, it can be seen that the error in the reconstruction of the intensity images for each input

and analysed polarisation state, and consequently the error in the reconstruction of the spatially resolved Mueller matrix, depends on the variation in $\vec{x}$. This is illustrated in the next two sets of simulations. In the second set of simulations, the test linear polariser was still assumed to be spatially homogeneous, but spatial variation in the scattering medium was simulated by a random spatial modulation of intensity between the values of 0 and 1. The results obtained with a linear variation in intensity of 30% are presented in Figure 6.23. The maximum absolute difference computed was 0.593, which is much larger than the error obtained with a spatially homogeneous scattering medium in Figure 6.22. For comparison, the results obtained without any intensity variation had a maximum absolute difference on the order of 10^{-11}, which, in addition, proves that a spatial variation in the scattering medium can be accounted for by correcting for its Mueller matrix on a pixel-wise basis when no intensity variation is present.

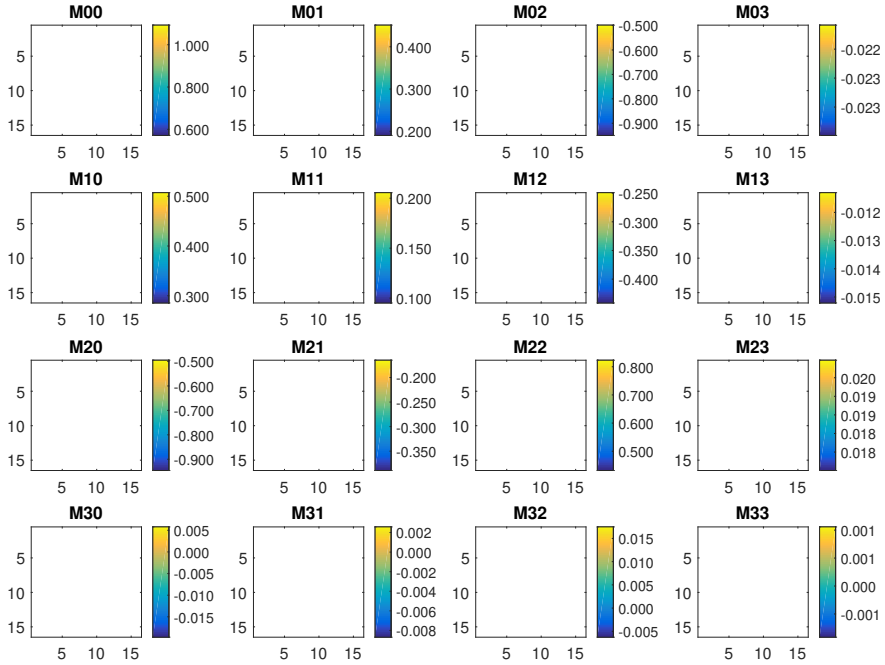

Figure 6.23: Spatially resolved Mueller matrix of the test linear polariser hidden behind a spatially inhomogeneous scattering medium, obtained using the proposed method from simulated data with an intensity variation of 30%. The x and y axes correspond to pixel indices.

As a final demonstration of the effect of an intensity variation during acquisition, a third set of simulations was conducted where both the object and scattering medium

were spatially inhomogeneous. The simulated test object was a linear polariser with its transmission axis at $-30°$, with an 'opaque' letter R that spatially modulated the transmitted intensity. The groundtruth polarimetric image of the test object is shown in Figure 6.24, while the results obtained with the intensity variation applied are shown in Figure 6.25. The maximum absolute difference computed was 0.640, which is larger than that computed from the second set of experiments. This increase in error is to be expected as the combined spatial inhomogeneity of the scattering medium and the test object has increased. In addition, the letter R was still visible in the reconstruction, but the polarimetric information can be seen to be visibly degraded. Qualitatively, this is consistent with the experimental results that were previously shown in Figure 6.14. The deviation of the reconstruction from the groundtruth cannot be compared quantitatively to the experimental results because, as discussed, the error depends on the spatial variation of the test object and the scattering medium. Furthermore, for simplicity, a linear variation in intensity was assumed in the simulation but the actual variation in an experiment does not necessarily follow a linear trend, as evidenced by Figure 6.16. Finally, noise in the experiment has also not been accounted for. All of these factors would affect the magnitude of the observed error. Nevertheless, based on this numerical study, it can be concluded that the intensity variation across the experiment is the most likely cause of the difference between the reconstructed polarimetric images obtained with the chicken breast samples and the images obtained without the samples present. A summary of the simulation results is provided in Table 6.3.

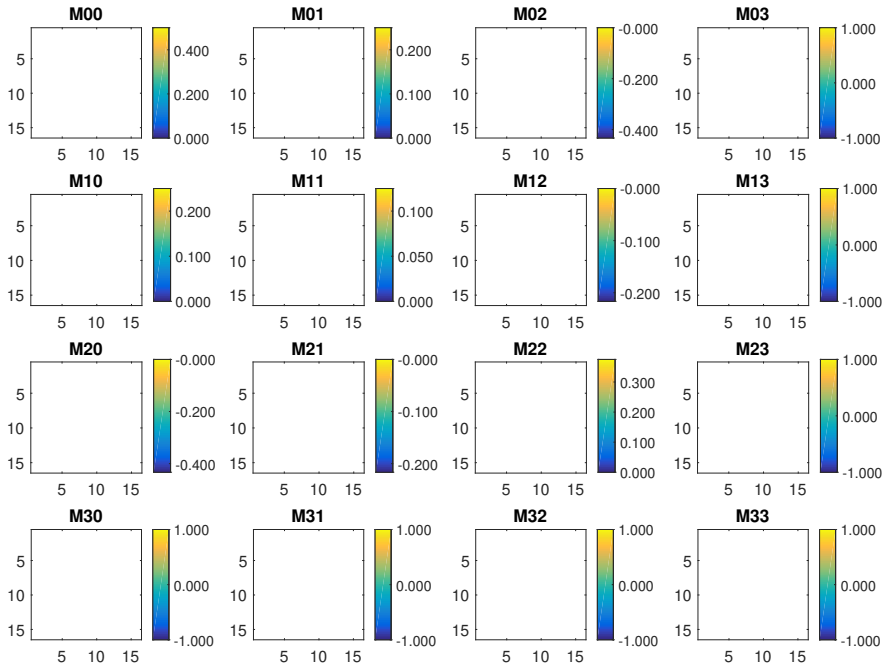

Figure 6.24: Groundtruth spatially resolved Mueller matrix of the test letter R. The x and y axes correspond to pixel indices.

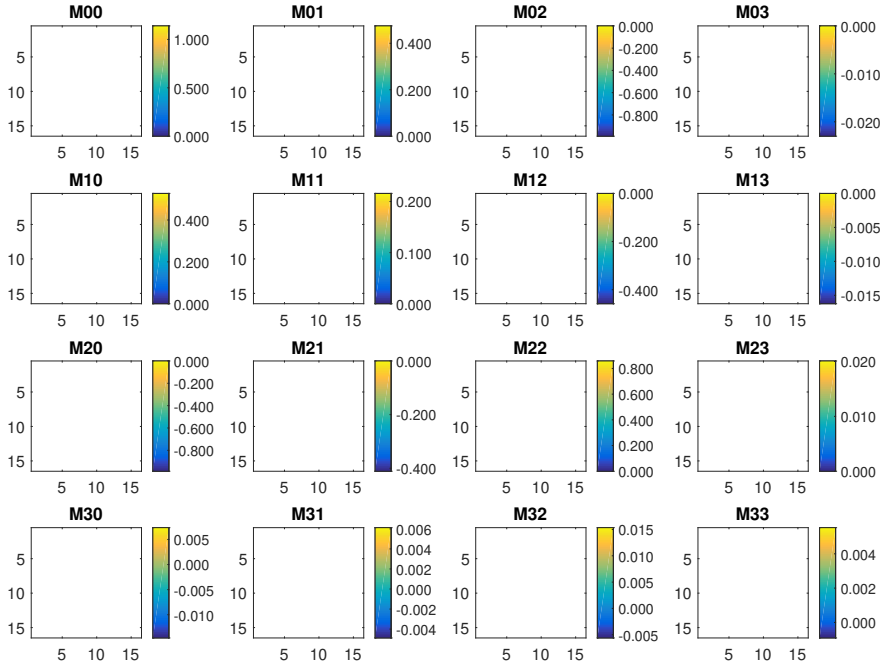

Figure 6.25: Spatially resolved Mueller matrix of the test letter R hidden behind a spatially inhomogeneous scattering medium, obtained using the proposed method from simulated data with an intensity variation of 30%. The x and y axes correspond to pixel indices.

Sets	Experiments	Spatially homogeneous?	Conclusion(s)
Set 1	Scattering medium	✓	• Intensity variation during the experiment increases the error in the reconstructed image.
	Test object	✓	
Set 2	Scattering medium	✗	• Spatial variation in the scattering medium and/or object affects the magnitude of the error in the reconstructed image. • The contribution of a spatially varying scattering medium can be accounted for by correcting for its Mueller matrix on a pixel-wise basis.
	Test object	✓	
Set 3	Scattering medium	✗	• Qualitative illustration of the degradation in the reconstructed polarimetric image.
	Test object	✗	

Table 6.3: Summary of the simulations that have investigated the effect of an increase in sample transmittance during data acquisition in single pixel polarimetric imaging.

6.3 Summary

In summary, the proposed method of single pixel polarimetric imaging has been successfully demonstrated on SM4, a scattering phantom with a thickness that is 18.57 times of the MFP and 0.85 times of the TMFP. The technique was further tested with thicker scattering media, with thicknesses up to a 43.13 times of the MFP or 1.97 of the TMFP. Promising results were achieved, but it was observed that noise in the reconstructed polarimetric images increased with the thickness of the scattering media, which is reasonable since the intensity measured by the photodiodes decreases correspondingly. As mentioned in Section 6.1, the average depolarisation factor for the thickest scattering phantom tested was 0.60. Thus, this suggests that polarisation information will persist for even larger thicknesses and that the proposed method can continue to be applied to even thicker samples, as long as there is sufficient SNR. Unfortunately, the polarimetric images of the same test objects hidden behind a layer of chicken breast did not yield favourable results. Through a numerical study, this was shown to be caused by a temporal variation in the unpolarised transmittance of the object during the experiment. Possible future work to circumvent this issue will be discussed in the next and final chapter of this thesis.

Chapter 7

Conclusion

This work has aimed to find a means of polarimetric imaging through scattering media. After a consideration of the existing literature, single pixel polarimetric imaging was identified as a promising approach, as it is a potentially cost-effective solution that could be adapted to include other imaging functionalities, and does not require any pre-calibration of the scattering medium. As such, the feasibility of single pixel polarimetric imaging was further examined in this project.

A theoretical model for single pixel polarimetric imaging was proposed and studied using 2D coupled line dipole simulations. The imaging configuration considered was a test object that was coherently illuminated by a spatially modulated incident field and hidden behind a statistically homogeneous scattering medium, with the transmitted intensity collected by single pixel detectors in a PSA. With this setup, it was found that single pixel polarimetric imaging is possible under three conditions. The first condition is that the size of each pixel in the utilised spatial mask is larger than the minimum distance between two input points on the scattering medium which produce uncorrelated output speckle. The second condition is that the collection optics has a sufficiently large NA to ensure adequate sampling of the spatial modes in the transmitted speckle. Thirdly, the illumination optics has to be well designed, so that there is minimal spatial overlap between the pixels at the input plane of the scattering medium. These requirements are needed to ensure that the correlation between the output speckle from different pixels is small, so that the photodiode's

measured signal can be considered as an incoherent sum of the contributions from each pixel. When these requirements are satisfied, single pixel polarimetric imaging through a scattering medium is possible, with the presence of the scattering medium corrected for through the use of its Mueller matrix.

A practical consideration for single pixel polarimetric imaging is whether the same correction for the presence of the scattering medium can be applied to all pixels. If the same correction can be applied, only one instance of the scattering medium's Mueller matrix has to be measured, which reduces the amount of pre-calibration that is required. Again using the 2D coupled line dipole simulations, it was shown that for a statistically homogeneous scattering medium and a sufficiently large input pixel size, the Mueller matrix measured for each input pixel is an estimate of an ensemble averaged Mueller matrix. Consequently, the measured Mueller matrix becomes independent of the instance of disorder (i.e. the detailed scattering configuration) and is the same for each input pixel. The minimum pixel size required depends on two length scales. The first length scale is the minimum distance between input points that give rise to uncorrelated output speckle at any given output point, while the second length scale is the size of the diffuse spot which arises from a point source located at the input face of the scattering medium.

Based on the findings from the numerical studies conducted, a single pixel polarimetric system made up of economical off-the-shelf components was designed, built and calibrated. When imaging through scattering media, scattering causes light to be scattered outside of the collection NA, such that the amount of light collected by the detector decreases with the thickness of the scattering medium. As such, in consideration of the system's signal to noise ratio, lock-in detection was implemented in the setup to amplify the weak transmitted signals above the noise floor. Furthermore, a constrained least squares algorithm was utilised to compute the Mueller matrix from the obtained measurements, in order to ensure that the Mueller matrix was physically realisable, even in the presence of noise. In contrast, it was found that a previously proposed algorithm based on the maximum likelihood estimate did not work well for the setup used in this work, possibly because the employed PSA config-

uration conducts a biased sampling of polarisation states across the Poincarè sphere.

The noise characteristics of the constructed system were studied to estimate its polarimetric resolution, which is defined as the smallest change in the Mueller matrix elements which can be reliably detected. Intensity noise was theoretically propagated through the setup, resulting in an estimate of the corresponding standard deviation in the elements of the Mueller matrix. For single pixel polarimetric imaging, the maximum standard deviation predicted was 0.003. When single pixel imaging was not used (i.e. non-imaging polarimetry), the maximum standard deviation was 0.002. These standard deviations are equivalent to the polarimetric resolution expected in each of these imaging modes. Yet, when compared to the variation of the Mueller matrix for air obtained from non-imaging polarimetric experiments, it was found that the experimentally determined standard deviation was much higher than the predicted value, with a maximum value of 0.007. Further investigation suggested the presence of a common mode noise that was unaccounted for, which probably originated from fluctuations in the polarisation states produced by the VWPs. Nonetheless, the measurements of the standard deviation over air provided an estimate of the expected polarimetric resolution of the system.

The experimental system was then used to demonstrate single pixel polarimetric imaging through scattering media, based on the theoretical model proposed. Past 1 TMFP, the direction of the photons exiting the scattering media is fully randomised. Using the proposed method, however, polarimetric imaging of various test objects was demonstrated through scattering phantoms with thicknesses that were 0.85, 1.12 and 1.97 times of the TMFP, thereby establishing the feasibility of the proposed method.

The second set of scattering media tested were slices of chicken breast. Using the proposed method, it was found that reconstructed images of test objects hidden behind the chicken breast samples did not match well to the images obtained when the test objects were unobscured. Two causes of this mismatch were identified. Firstly, unlike the scattering phantoms, the chicken breast samples showed a high degree of

spatial inhomogeneity. As such, the use of the same correction for all pixels would result in an error in the resulting image. Secondly, the intensity transmittance of the chicken breast samples increased over the acquisition time of the experiment. This increase was unaccounted for in the data processing and adversely affected the accuracy of the images produced by the single pixel camera. The origin of this variation remains unclear and needs further investigation, but possible explanations could be dehydration of the sample, or a downward diffusion of water or other constituents in the vertically mounted sample. The spatial inhomogeneity of the sample could be resolved by correcting for the influence of the scattering medium on a pixel-wise basis. To deal with the temporal variation of the sample would require system adjustments to reduce the acquisition time, and potentially to mount the sample horizontally in a sealed container.

Apart from minimising the temporal variation of the sample, a reduction in the acquisition time is also necessary in order for the proposed method to be a practical imaging technique. This is particularly so if one wishes to increase the number of image pixels. The current acquisition time of about 90 minutes per acquisition of a 16×16 polarimetric image is limited mainly by the measures taken to deal with a low detected signal, such as the implementation of lock-in detection. As the lock-in amplifier used only had a single input, sequential readout of the detector signals was required, which increased the acquisition time and also admittedly, nullified one of the main benefits of using a division of amplitude PSA - the ability to take synchronous readings across the analysed polarisation states. Multichannel lock-in amplifiers are one option for speeding up the acquisition. By simply being able to take the measurements at the same time decreases the acquisition time by a factor of four. The acquisition time could also be decreased by improving the signal level or mitigating the noise sources in the measurements, since less temporal averaging would then be required to achieve the same SNR. In this respect, more sensitive detectors could be used, such as avalanche photodiodes, which provide a high gain due to the avalanche effect caused by the operation of the photodiode at a high reverse voltage. In addition, it was observed that the VWPs were a likely source of noise in the measurements. The use of VWPs with higher stability would hence

be beneficial in decreasing the amount of noise in the system. Finally, other than these changes that could be made to the system, compressive sensing could also be employed to decrease the acquisition time, by reducing the number of measurements required for image reconstruction. The reduction in number of measurements can be as much as ten-fold, but depends on the sparsity of the object in the sparsifying basis chosen as well as the incoherence of the measurement and sparsifying bases utilised.

Acquisition time aside, another practical concern that has yet to be addressed in the current work is the prior measurement of the scattering medium's Mueller matrix, which is still currently required for single pixel polarimetric imaging. Such a pre-calibration of the scattering medium without any test object present is not usually possible in practice and is hence an obstacle for the proposed method. A possible means of dealing with this issue could be to measure the Mueller matrix of the scattering medium at different thicknesses, so as to try and identify a trend that could be used to predict the Mueller matrix at any arbitrary thickness. For a sufficiently large pixel size, the measured Mueller matrix is independent of the instance of disorder, and is, therefore, not specific to any particular sample of the same scattering medium. This solution would not be useful, however, for real samples, which tend to demonstrate spatial inhomogeneity, such as the chicken breast tissue tested in this work. A further improvement to this solution could be to develop algorithms that are able to adaptively adjust the Mueller matrix of the scattering medium for each pixel, with the predicted Mueller matrix for a known thickness used as prior information.

An additional consideration that should be looked at in the future is the challenge of delivering the spatially modulated illumination to the object. In this work, access to one end of the object has been assumed, but in practice, it is more likely that the objects of interest are embedded within scattering media such that there is no access to any part of the object. Potential solutions include the adaptation of multi-photon excitation techniques, be it wide field illumination [115] or point sampling [22, 23], which can both deliver light up to a certain depth. Various spatial patterns, such

as the Hadamard patterns used in this work, can be implemented with wide field illumination. With point scanning, images are formed by raster scanning, which can also be thought of as single pixel imaging under a point basis. In both cases, unlike the model considered in this work, the illumination light from the sample plane, emitted by multi-photon fluorescence, is incoherent.

Though the work so far has assumed coherent illumination, there is little restriction to the use of incoherent light for single pixel polarimetric imaging. In fact, the use of spatially incoherent light could relax some of the constraints that have been discussed. For example, in order to consider the signal measured by each photodiode as an incoherent sum of the contributions from each pixel, there were constraints on the minimum pixel size and NA of the system. If, however, spatially incoherent light were used, then the contributions from each input pixel would naturally add incoherently. An additional assumption made in this work was that absorption in the scattering medium is negligible. This is a reasonable assumption for most biological tissue, where scattering tends to dominate over absorption [8]. Nevertheless, in the case of polarisation-insensitive absorption, the primary effect is a decrease in the SNR of the measurements due to the added light attenuation by absorption, such that the maximum thickness, beyond which the measured signal becomes indistinguishable from noise, is also reduced. If the scattering medium exhibits polarisation-sensitive absorption (i.e. diattenuation), this would affect the depolarisation lengths of the various polarisation states differently and could also imply a different SNR for the retrieval of different polarimetric parameters of the object. As such, the presence of absorption does not change the conclusions of this work, and only affects the length scales at which the proposed technique can be applied.

In summary, this work has demonstrated, for the first time, that single pixel polarimetric imaging is possible in the presence of a scattering medium. Polarimetric information of the hidden test object is seen to persist, even at length scales where ballistic light has been effectively extinguished, thereby making it possible to conduct polarimetric imaging through scattering. Experimentally, images of hidden

objects were recovered through scattering phantoms with thicknesses up to 1.97 times of the TMFP. Factors limiting the performance of the proposed method in the presence of scattering media have also been thoroughly studied with theoretical formulations and numerical simulations. Aside from these investigations, a novel constrained least squares algorithm was also proposed for polarimetric setups, enabling the recovery of a physical Mueller matrix even in the presence of noise. The conclusions in this work are not limited to single pixel imaging, but could also be extended to other imaging techniques, such as raster scanning techniques. It is hoped that the outcomes of this work would be instrumental for the future development of practical polarimetric imaging methods through scattering media.

Bibliography

[1] P. G. Ellingsen, M. B. Lilledahl, L. M. S. Aas, C. D. L. Davies, and M. Kildemo, "Quantitative characterization of articular cartilage using Mueller matrix imaging and multiphoton microscopy," *Journal of Biomedical Optics*, vol. 16, no. 11, p. 116002, 2011.

[2] J. Chue-Sang, Y. Bai, S. Stoff, M. Gonzalez, N. Holness, J. Gomes, R. Jung, A. Gandjbakhche, V. V. Chernomordik, and J. C. Ramella-Roman, "Use of Mueller matrix polarimetry and optical coherence tomography in the characterization of cervical collagen anisotropy," *Journal of Biomedical Optics*, 2017.

[3] T. Novikova, A. Pierangelo, A. De Martino, A. Benali, and P. Validire, "Polarimetric imaging for cancer diagnosis and staging," *Optics and Photonics News*, no. October, pp. 26–33, 2012.

[4] M. Sun, H. He, N. Zeng, E. Du, Y. Guo, S. Liu, J. Wu, Y. He, and H. Ma, "Characterizing the microstructures of biological tissues using Mueller matrix and transformed polarization parameters," *Biomedical Optics Express*, vol. 5, no. 12, p. 4223, 2014. [Online]. Available: https://www.osapublishing.org/boe/abstract.cfm?uri=boe-5-12-4223

[5] Y. Wang, M. Kudenov, A. Kashani, J. Schwiegerling, and M. Escuti, "Snapshot retinal imaging Mueller matrix polarimeter," in *Polarization Science and Remote Sensing VII*, 2015.

[6] T. Dada, R. Sharma, D. Angmo, G. Sinha, S. Bhartiya, S. K. Mishra, A. Panda, and R. Sihota, "Scanning laser polarimetry in glaucoma," 2014.

[7] S. Badieyan, A. Dilmaghani-Marand, M. J. Hajipour, A. Ameri, M. R. Razzaghi, H. Rafii-Tabar, M. Mahmoudi, and P. Sasanpour, "Detection and Discrimination of Bacterial Colonies with Mueller Matrix Imaging," *Scientific Reports*, vol. 8, no. 1, pp. 1–10, 2018. [Online]. Available: http://dx.doi.org/10.1038/s41598-018-29059-5

[8] V. Ntziachristos, "Going deeper than microscopy: the optical imaging frontier in biology," *Nature Methods*, vol. 7, no. 8, pp. 603–614, aug 2010. [Online]. Available: http://www.nature.com/articles/nmeth.1483

[9] A. B. E. Attia, S. Y. Chuah, D. Razansky, C. J. H. Ho, P. Malempati, U. S. Dinish, R. Bi, C. Y. Fu, S. J. Ford, J. S. S. Lee, M. W. P. Tan, M. Olivo, and S. T. G. Thng, "Noninvasive real-time characterization of non-melanoma skin cancers with handheld optoacoustic probes," *Photoacoustics*, vol. 7, pp. 20–26, 2017. [Online]. Available: http://dx.doi.org/10.1016/j.pacs.2017.05.003

[10] J. Jonkman and C. M. Brown, "Any way you slice itA comparison of confocal microscopy techniques," *Journal of Biomolecular Techniques*, vol. 26, no. 2, pp. 54–65, 2015.

[11] J. Schmitt, "Optical coherence tomography (OCT): a review," *IEEE Journal of Selected Topics in Quantum Electronics*, vol. 5, no. 4, pp. 1205–1215, 1999. [Online]. Available: http://ieeexplore.ieee.org/document/796348/

[12] L. WANG, P. P. HO, C. LIU, G. ZHANG, and R. R. ALFANO, "Ballistic 2-D Imaging Through Scattering Walls Using an Ultrafast Optical Kerr Gate," *Science*, vol. 253, no. 5021, pp. 769–771, aug 1991. [Online]. Available: http://www.sciencemag.org/cgi/doi/10.1126/science.253.5021.769

[13] M. Paciaroni and M. Linne, "Single-shot, two-dimensional ballistic imaging through scattering media," *Applied Optics*, vol. 43, no. 26, p. 5100, sep 2004. [Online]. Available: https://www.osapublishing.org/abstract.cfm?URI=ao-43-26-5100

[14] S. Sudarsanam, J. Mathew, S. Panigrahi, J. Fade, M. Alouini, and H. Ramachandran, "Real-time imaging through strongly scattering media:

Seeing through turbid media, instantly," *Scientific Reports*, vol. 6, pp. 1–9, 2016. [Online]. Available: http://dx.doi.org/10.1038/srep25033

[15] H. Ramachandran and A. Narayanan, "Two-dimensional imaging through turbid media using a continuous wave light source," *Optics Communications*, vol. 154, no. 5-6, pp. 255–260, 1998.

[16] V. Sankaran, K. Schönenberger, J. T. Walsh, and D. J. Maitland, "Polarization discrimination of coherently propagating light in turbid media," *Applied Optics*, vol. 38, no. 19, p. 4252, jul 1999. [Online]. Available: https://www.osapublishing.org/abstract.cfm?URI=ao-38-19-4252

[17] W.-F. CHEONG, S. A. PRAHL, and A. J. WELCH, "A Review of the Optical Properties of Biological Tissues," *IEEE Journal of Quantum Electronics*, vol. 26, no. 12, 1990.

[18] S. L. Jacques, "Optical properties of biological tissues: a review." *Physics in medicine and biology*, vol. 58, no. 11, pp. R37–61, 2013. [Online]. Available: http://iopscience.iop.org/article/10.1088/0031-9155/58/11/R37

[19] J. Sharpe, U. Ahlgren, P. Perry, B. Hill, A. Ross, J. Hecksher-Sørensen, R. Baldock, and D. Davidson, "Optical projection tomography as a tool for 3D microscopy and gene expression studies," *Science*, 2002.

[20] M. Xu and L. V. Wang, "Photoacoustic imaging in biomedicine," *Review of Scientific Instruments*, vol. 77, no. 4, p. 041101, apr 2006. [Online]. Available: http://aip.scitation.org/doi/10.1063/1.2195024

[21] J. Xia, J. Yao, and L. V. Wang, "Photoacoustic tomography: Principles and advances," *Progress in Electromagnetics Research*, vol. 147, pp. 1–22, 2014.

[22] F. Helmchen and W. Denk, "Deep tissue two-photon microscopy," *Nature Methods*, vol. 2, no. 12, pp. 932–940, 2005.

[23] C. Lefort, "A review of biomedical multiphoton microscopy and its laser sources," *Journal of Physics D: Applied Physics*, vol. 50, no. 42, 2017.

[24] N. Ji, "Adaptive optical fluorescence microscopy," *Nature Methods*, vol. 14, no. 4, pp. 374–380, 2017.

[25] R. Davies and M. Kasper, "Adaptive Optics for Astronomy," *Annual Review of Astronomy and Astrophysics*, vol. 50, no. 1, pp. 305–351, 2012.

[26] M. Pircher and R. J. Zawadzki, "Review of adaptive optics OCT (AO-OCT): principles and applications for retinal imaging [Invited]," *Biomedical Optics Express*, vol. 8, no. 5, p. 2536, 2017.

[27] X. Tao, B. Fernandez, O. Azucena, M. Fu, D. Garcia, Y. Zuo, D. C. Chen, and J. Kubby, "Adaptive optics confocal microscopy using direct wavefront sensing," *Optics Letters*, vol. 36, no. 7, p. 1062, 2011.

[28] K. Wang, D. E. Milkie, A. Saxena, P. Engerer, T. Misgeld, M. E. Bronner, J. Mumm, and E. Betzig, "Rapid adaptive optical recovery of optimal resolution over large volumes," *Nature Methods*, vol. 11, no. 6, pp. 625–628, 2014.

[29] M. J. Booth, "Adaptive optical microscopy: The ongoing quest for a perfect image," *Light: Science and Applications*, vol. 3, no. January, pp. 1–7, 2014.

[30] I. M. Vellekoop and a. P. Mosk, "Focusing coherent light through opaque strongly scattering media." *Optics letters*, vol. 32, no. 16, pp. 2309–2311, 2007.

[31] I. M. Vellekoop, E. G. van Putten, A. Lagendijk, and A. P. Mosk, "Demixing light paths inside disordered metamaterials," *Optics Express*, vol. 16, no. 1, p. 67, 2008. [Online]. Available: https://www.osapublishing.org/oe/abstract.cfm?uri=oe-16-1-67

[32] I. M. Vellekoop and A. P. Mosk, "Phase control algorithms for focusing light through turbid media," *Optics Communications*, vol. 281, no. 11, pp. 3071–3080, 2008.

[33] D. Akbulut, T. J. Huisman, E. G. Van Putten, W. L. Vos, and A. P. Mosk, "Focusing light through turbid media by binary amplitude modulation," *2011 Conference on Lasers and Electro-Optics Europe and 12th European Quantum Electronics Conference, CLEO EUROPE/EQEC 2011*, vol. 19, no. 5, pp. 4017–4029, 2011.

[34] I. M. Vellekoop, "Feedback-based wavefront shaping," *Optics Express*, vol. 23, no. 9, p. 12189, may 2015. [Online]. Available: https://www.osapublishing.org/abstract.cfm?URI=oe-23-9-12189

[35] D. Dudley, W. M. Duncan, and J. Slaughter, "Emerging digital micromirror device (DMD) applications," *MOEMS Display and Imaging Systems*, vol. 4985, no. January 2003, p. 14, 2003.

[36] O. Katz, E. Small, Y. Guan, and Y. Silberberg, "Noninvasive nonlinear focusing and imaging through strongly scattering turbid layers," *Optica*, vol. 1, no. 3, pp. 170–174, 2014. [Online]. Available: http://arxiv.org/abs/1405.4826

[37] P. Lai, L. Wang, J. W. Tay, and L. V. Wang, "Photoacoustically guided wavefront shaping for enhanced optical focusing in scattering media," *Nature Photonics*, vol. 9, no. 2, pp. 126–132, feb 2015. [Online]. Available: http://www.nature.com/articles/nphoton.2014.322

[38] J. W. Tay, P. Lai, Y. Suzuki, and L. V. Wang, "Ultrasonically encoded wavefront shaping for focusing into random media," *Scientific Reports*, vol. 4, no. 1, p. 3918, 2015. [Online]. Available: http://www.nature.com/articles/srep03918

[39] J.-H. Park, C. Park, H. Yu, Y.-H. Cho, and Y. Park, "Dynamic active wave plate using random nanoparticles," *Optics Express*, vol. 20, no. 15, p. 17010, jul 2012. [Online]. Available: https://www.osapublishing.org/oe/abstract.cfm?uri=oe-20-15-17010

[40] Y. Guan, O. Katz, E. Small, J. Zhou, and Y. Silberberg, "Polarization control of multiply scattered light through random media by wavefront shaping," *Optics Letters*, vol. 37, no. 22, p. 4663, nov 2012. [Online]. Available: https://www.osapublishing.org/abstract.cfm?URI=ol-37-22-4663

[41] J.-H. Park, C. Park, H. Yu, Y.-H. Cho, and Y. Park, "Active spectral filtering through turbid media," *Optics Letters*, vol. 37, no. 15, p. 3261, aug 2012. [Online]. Available: https://www.osapublishing.org/abstract.cfm?URI=ol-37-15-3261

[42] E. Small, O. Katz, Y. Guan, and Y. Silberberg, "Spectral control of broadband light through random media by wavefront shaping," *Optics Letters*, 2012.

[43] J. Aulbach, B. Gjonaj, P. M. Johnson, A. P. Mosk, and A. Lagendijk, "Control of light transmission through opaque scattering media in space and time," *Physical Review Letters*, vol. 106, no. 10, pp. 5–8, 2011.

[44] D. J. McCabe, A. Tajalli, D. R. Austin, P. Bondareff, I. a. Walmsley, S. Gigan, and B. Chatel, "Spatio-temporal focusing of an ultrafast pulse through a multiply scattering medium." *Nature communications*, vol. 2, no. May, p. 447, 2011.

[45] I. M. Vellekoop and C. M. Aegerter, "Scattered light fluorescence microscopy: imaging through turbid layers," *Optics Letters*, vol. 35, no. 8, p. 1245, 2010.

[46] S. Feng, C. Kane, P. A. Lee, and A. D. Stone, "Correlations and fluctuations of coherent wave transmission through disordered media," *Physical Review Letters*, vol. 61, no. 7, pp. 834–837, 1988.

[47] T. Cizmar, M. Mazilu, and K. Dholakia, "In situ wavefront correction and its application to micromanipulation," *Nature Photonics*, vol. 4, no. 6, pp. 388–394, 2010.

[48] A. Derode, A. Tourin, J. de Rosny, M. Tanter, S. Yon, and M. Fink, "Taking Advantage of Multiple Scattering to Communicate with Time-Reversal Antennas," *Physical Review Letters*, vol. 90, no. 1, p. 014301, jan 2003. [Online]. Available: https://link.aps.org/doi/10.1103/PhysRevLett.90.014301

[49] C. Draeger and M. Fink, "One-Channel Time Reversal of Elastic Waves in a Chaotic 2D-Silicon Cavity," *Physical Review Letters*, vol. 79, pp. 407–410, 1997.

[50] J. Feinberg and R. W. Hellwarth, "Phase-conjugating mirror with continuous-wave gain," *Optics Letters*, vol. 5, no. 12, p. 519, dec 1980. [Online]. Available: https://www.osapublishing.org/abstract.cfm?URI=ol-5-12-519

[51] Z. Yaqoob, D. Psaltis, M. S. Feld, and C. Yang, "Optical phase conjugation for turbidity suppression in biological samples," *Nature Photonics*, vol. 2, no. 2, pp. 110–115, feb 2008. [Online]. Available: http://www.nature.com/articles/nphoton.2007.297

[52] Y. M. Wang, B. Judkewitz, C. A. Dimarzio, and C. Yang, "Deep-tissue focal fluorescence imaging with digitally time-reversed ultrasound-encoded light," *Nature Communications*, vol. 3, no. May, 2012.

[53] C.-L. Hsieh, Y. Pu, R. Grange, and D. Psaltis, "Digital phase conjugation of second harmonic radiation emitted by nanoparticles in turbid media," *Optics Express*, vol. 18, no. 12, p. 12283, jun 2010. [Online]. Available: https://www.osapublishing.org/oe/abstract.cfm?uri=oe-18-12-12283

[54] I. M. Vellekoop, M. Cui, and C. Yang, "Digital optical phase conjugation of fluorescence in turbid tissue," *Applied Physics Letters*, vol. 101, no. 8, pp. 1–5, 2012.

[55] E. J. McDowell, M. Cui, I. M. Vellekoop, V. Senekerimyan, Z. Yaqoob, and C. Yang, "Turbidity suppression from the ballistic to the diffusive regime in biological tissues using optical phase conjugation." *Journal of biomedical optics*, vol. 15, no. 2, p. 025004, 2010. [Online]. Available: http://www.pubmedcentral.nih.gov/articlerender.fcgi?artid=2874046{&}tool=pmcentrez{&}rendertype=abstract

[56] M. Cui, E. J. McDowell, and C. Yang, "An in vivo study of turbidity suppression by optical phase conjugation (TSOPC) on rabbit ear." *Optics express*, vol. 18, no. 1, pp. 25–30, 2010. [Online]. Available: http://www.ncbi.nlm.nih.gov/pubmed/20173817

[57] Y. Liu, P. Lai, C. Ma, X. Xu, A. A. Grabar, and L. V. Wang, "Optical focusing deep inside dynamic scattering media with near-infrared time-reversed ultrasonically encoded (TRUE) light," *Nature Communications*, vol. 6, no. May 2014, p. 5904, 2015. [Online]. Available: http://www.nature.com/ncomms/2015/150105/ncomms6904/full/ncomms6904.html

[58] B. Judkewitz, Y. M. Wang, R. Horstmeyer, A. Mathy, and C. Yang, "Speckle-scale focusing in the diffusive regime with time-reversal of variance-encoded light (TROVE)." *Nature photonics*, vol. 7, no. 4, pp. 300–305, 2013. [Online]. Available: http://www.nature.com/nphoton/journal/v7/n4/full/nphoton.2013.31.html

[59] C. Gu and P. Yeh, "Partial phase conjugation, fidelity, and reciprocity," *Optics Communications*, vol. 107, no. 5-6, pp. 353–357, 1994.

[60] I. Freund, "Looking through walls and around corners," *Physica A: Statistical Mechanics and its Applications*, vol. 168, no. 1, pp. 49–65, 1990.

[61] I. Freund, M. Rosenbluh, and S. Feng, "Memory Effects in Propagation of Optical Waves through Disordered Media," *Physical Review Letters*, vol. 61, no. 20, pp. 2328–2331, nov 1988. [Online]. Available: https://link.aps.org/doi/10.1103/PhysRevLett.61.2328

[62] J. Bertolotti, E. G. Van Putten, C. Blum, A. Lagendijk, W. L. Vos, and A. P. Mosk, "Non-invasive imaging through opaque scattering layers," *Nature*, vol. 491, no. 7423, pp. 232–4, 2012. [Online]. Available: http://www.ncbi.nlm.nih.gov/pubmed/23135468

[63] J. W. Goodman, *Speckle phenomena in optics: theory and applications*. Roberts and Company Publishers, 2007.

[64] O. Katz, P. Heidmann, M. Fink, and S. Gigan, "Non-invasive single-shot imaging through scattering layers and around corners via speckle correlations," *Nature Photonics*, vol. 8, no. 10, pp. 784–790, oct 2014. [Online]. Available: http://www.nature.com/articles/nphoton.2014.189

[65] J. R. Fienup, "Phase retrieval algorithms: a comparison," *Applied Optics*, vol. 21, no. 15, p. 2758, aug 1982. [Online]. Available: https://www.osapublishing.org/abstract.cfm?URI=ao-21-15-2758

[66] X. Yang, Y. Pu, and D. Psaltis, "Imaging blood cells through scattering biological tissue using speckle scanning microscopy," *Optics Express*, vol. 22, no. 3, p. 3405, 2014.

[67] M. Cua, E. H. Zhou, and C. Yang, "Imaging moving targets through scattering media," *Optics Express*, vol. 25, no. 4, p. 3935, feb 2017. [Online]. Available: https://www.osapublishing.org/abstract.cfm?URI=oe-25-4-3935

[68] M. Hofer, C. Soeller, S. Brasselet, and J. Bertolotti, "Wide field fluorescence epi-microscopy behind a scattering medium enabled by speckle correlations," *Optics Express*, vol. 26, no. 8, p. 9866, apr 2018. [Online]. Available: https://www.osapublishing.org/abstract.cfm?URI=oe-26-8-9866

[69] E. Edrei and G. Scarcelli, "Memory-effect based deconvolution microscopy for super-resolution imaging through scattering media," *Scientific Reports*, vol. 6, no. September, pp. 1–8, 2016. [Online]. Available: http://dx.doi.org/10.1038/srep33558

[70] Y. Okamoto, R. Horisaki, and J. Tanida, "Noninvasive three-dimensional imaging through scattering media by three-dimensional speckle correlation," *Optics Letters*, vol. 44, no. 10, p. 2526, 2019.

[71] K. T. Takasaki and J. W. Fleischer, "Phase-space measurement for depth-resolved memory-effect imaging," *Optics Express*, vol. 22, no. 25, p. 31426, 2014.

[72] A. K. Singh, D. N. Naik, G. Pedrini, M. Takeda, and W. Osten, "Exploiting scattering media for exploring 3D objects," *Light: Science and Applications*, vol. 6, no. 2, pp. e16 219–7, 2017. [Online]. Available: http://dx.doi.org/10.1038/lsa.2016.219

[73] Y. Shi, Y. Liu, J. Wang, and T. Wu, "Non-invasive depth-resolved imaging through scattering layers via speckle correlations and parallax," *Applied Physics Letters*, vol. 110, no. 23, 2017. [Online]. Available: http://dx.doi.org/10.1063/1.4985010

[74] B. Judkewitz, R. Horstmeyer, I. M. Vellekoop, I. N. Papadopoulos, and C. Yang, "Translation correlations in anisotropically scattering media," *Nature Physics*, vol. 11, no. 8, pp. 684–689, aug 2015. [On-

line]. Available: http://www.nature.com/doifinder/10.1038/nphys3373http://www.nature.com/articles/nphys3373

[75] G. Osnabrugge, R. Horstmeyer, N. Ioannis, B. Judkewitz, and I. M. Vellekoop, "The generalized optical memory effect," *Optica*, vol. 4, no. 8, pp. 886–892, 2017.

[76] P. A. Mello, P. Pereyra, and N. Kumar, "Macroscopic approach to multichannel disordered conductors," *Annals of Physics*, vol. 181, no. 2, pp. 290–317, 1988.

[77] O. Dorokhov, "On the coexistence of localized and extended electronic states in the metallic phase," *Solid State Communications*, vol. 51, no. 6, pp. 381–384, aug 1984. [Online]. Available: https://linkinghub.elsevier.com/retrieve/pii/0038109884901170

[78] C. W. J. Beenakker, "Random-matrix theory of quantum transport," *Reviews of Modern Physics*, vol. 69, no. 3, pp. 731–808, jul 1997. [Online]. Available: https://link.aps.org/doi/10.1103/RevModPhys.69.731

[79] B. Gérardin, J. Laurent, A. Derode, C. Prada, and A. Aubry, "Full Transmission and Reflection of Waves Propagating through a Maze of Disorder," *Physical Review Letters*, vol. 113, no. 17, p. 173901, oct 2014. [Online]. Available: https://link.aps.org/doi/10.1103/PhysRevLett.113.173901

[80] M. Kim, Y. Choi, C. Yoon, W. Choi, J. Kim, Q.-H. Park, and W. Choi, "Maximal energy transport through disordered media with the implementation of transmission eigenchannels," *Nature Photonics*, vol. 6, no. 9, pp. 583–587, 2012. [Online]. Available: http://dx.doi.org/10.1038/nphoton.2012.159

[81] S. M. Popoff, G. Lerosey, R. Carminati, M. Fink, A. C. Boccara, and S. Gigan, "Measuring the transmission matrix in optics: An approach to the study and control of light propagation in disordered media," *Physical Review Letters*, vol. 104, no. 10, pp. 1–4, 2010.

[82] H. Yu, T. R. Hillman, W. Choi, J. O. Lee, M. S. Feld, R. R. Dasari, and Y. Park, "Measuring Large Optical Transmission Matrices of Disordered Media," *Physical Review Letters*, vol. 111, no. 15, p. 153902, oct 2013. [Online]. Available: https://link.aps.org/doi/10.1103/PhysRevLett.111.153902

[83] H. Yu, J. H. Park, and Y. Park, "Measuring large optical reflection matrices of turbid media," *Optics Communications*, vol. 352, pp. 33–38, 2015. [Online]. Available: http://dx.doi.org/10.1016/j.optcom.2015.04.073

[84] A. Goetschy and A. D. Stone, "Filtering random matrices: The effect of incomplete channel control in multiple scattering," *Physical Review Letters*, vol. 111, no. 6, pp. 1–5, 2013.

[85] V. A. Marčenko and L. A. Pastur, "DISTRIBUTION OF EIGENVALUES FOR SOME SETS OF RANDOM MATRICES," *Mathematics of the USSR-Sbornik*, 1967.

[86] E. van Putten and A. Mosk, "The information age in optics: Measuring the transmission matrix," *Physics*, vol. 3, p. 22, mar 2010. [Online]. Available: https://link.aps.org/doi/10.1103/Physics.3.22

[87] S. Popoff, G. Lerosey, M. Fink, A. C. Boccara, and S. Gigan, "Image transmission through an opaque material," *Nature Communications*, vol. 1, no. 6, pp. 1–5, sep 2010. [Online]. Available: http://www.nature.com/doifinder/10.1038/ncomms1078

[88] I. Yamaguchi and T. Zhang, "Phase-shifting digital holography," *Optics Letters*, vol. 22, no. 16, pp. 1268–1270, 1997.

[89] A. Drémeau, A. Liutkus, D. Martina, O. Katz, C. Schülke, F. Krzakala, S. Gigan, and L. Daudet, "Reference-less measurement of the transmission matrix of a highly scattering material using a DMD and phase retrieval techniques," *Optics Express*, vol. 23, no. 9, p. 11898, 2015.

[90] D. Akbulut, T. Strudley, J. Bertolotti, E. P. A. M. Bakkers, A. Lagendijk, O. L. Muskens, W. L. Vos, and A. P. Mosk, "Optical transmission matrix as a probe of the photonic strength," *Physical Review A*,

vol. 94, no. 4, p. 043817, oct 2016. [Online]. Available: https://link.aps.org/doi/10.1103/PhysRevA.94.043817

[91] S. Tripathi, R. Paxman, T. Bifano, and K. C. Toussaint, "Vector transmission matrix for the polarization behavior of light propagation in highly scattering media," *Optics Express*, vol. 20, no. 14, p. 16067, jul 2012. [Online]. Available: https://www.osapublishing.org/oe/abstract.cfm?uri=oe-20-14-16067

[92] O. Katz, F. Ramaz, S. Gigan, and M. Fink, "Controlling light in complex media beyond the acoustic diffraction-limit using the acousto-optic transmission matrix," *Nature Communications*, vol. 10, no. 1, pp. 1–10, 2019. [Online]. Available: http://dx.doi.org/10.1038/s41467-019-08583-6

[93] T. Chaigne, O. Katz, A. C. Boccara, M. Fink, E. Bossy, and S. Gigan, "Controlling light in scattering media non-invasively using the photoacoustic transmission matrix," *Nature Photonics*, vol. 8, no. 1, pp. 58–64, jan 2014. [Online]. Available: http://www.nature.com/articles/nphoton.2013.307

[94] D. Andreoli, G. Volpe, S. Popoff, O. Katz, S. Grésillon, and S. Gigan, "Deterministic control of broadband light through a multiply scattering medium via the multispectral transmission matrix," *Scientific Reports*, vol. 5, no. 1, p. 10347, sep 2015. [Online]. Available: http://www.nature.com/articles/srep10347

[95] M. Mounaix, D. Andreoli, H. Defienne, G. Volpe, O. Katz, S. Grésillon, and S. Gigan, "Spatiotemporal Coherent Control of Light through a Multiple Scattering Medium with the Multispectral Transmission Matrix," *Physical Review Letters*, vol. 116, no. 25, p. 253901, jun 2016. [Online]. Available: https://link.aps.org/doi/10.1103/PhysRevLett.116.253901

[96] S. Kang, S. Jeong, W. Choi, H. Ko, T. D. Yang, J. H. Joo, J.-s. Lee, Y.-s. Lim, Q.-h. Park, and W. Choi, "Imaging deep within a scattering medium using collective accumulation of single-scattered waves," *Nature Photonics*, vol. 9, no. 4, pp. 253–258, apr 2015. [Online]. Available: http://www.nature.com/articles/nphoton.2015.24

[97] Y. Choi, T. R. Hillman, W. W. Choi, N. Lue, R. R. Dasari, P. T. C. So, W. W. Choi, and Z. Yaqoob, "Measurement of the Time-Resolved Reflection Matrix for Enhancing Light Energy Delivery into a Scattering Medium," *Physical Review Letters*, vol. 111, no. 24, p. 243901, dec 2013. [Online]. Available: https://link.aps.org/doi/10.1103/PhysRevLett.111.243901

[98] A. Liutkus, D. Martina, S. Popoff, G. Chardon, O. Katz, G. Lerosey, S. Gigan, L. Daudet, and I. Carron, "Imaging With Nature: Compressive Imaging Using a Multiply Scattering Medium," *Scientific Reports*, vol. 4, no. 1, p. 5552, may 2015. [Online]. Available: http://www.nature.com/articles/srep05552

[99] C. Park, J. H. Park, C. Rodriguez, H. Yu, M. Kim, K. Jin, S. Han, J. Shin, S. H. Ko, K. T. Nam, Y. H. Lee, Y. H. Cho, and Y. Park, "Full-field subwavelength imaging using a scattering superlens," *Physical Review Letters*, vol. 113, no. 11, pp. 1–5, 2014.

[100] Youngwoon Choi, Changhyeong Yoon, Moonseok Kim, Wonjun Choi, and Wonshik Choi, "Optical Imaging With the Use of a Scattering Lens," *IEEE Journal of Selected Topics in Quantum Electronics*, vol. 20, no. 2, pp. 61–73, mar 2014. [Online]. Available: http://ieeexplore.ieee.org/document/6582553/

[101] J. W. Goodman, *Introduction to Fourier Optics*, 3rd ed. Roberts & Company Publishers, 2005.

[102] Y. Choi, C. Yoon, M. Kim, T. D. Yang, C. Fang-Yen, R. R. Dasari, K. J. Lee, and W. Choi, "Scanner-Free and Wide-Field Endoscopic Imaging by Using a Single Multimode Optical Fiber," *Physical Review Letters*, vol. 109, no. 20, p. 203901, nov 2012. [Online]. Available: https://link.aps.org/doi/10.1103/PhysRevLett.109.203901

[103] D. Loterie, S. Farahi, I. Papadopoulos, A. Goy, D. Psaltis, and C. Moser, "Digital confocal microscopy through a multimode fiber," *Optics Express*, vol. 23, no. 18, p. 23845, 2015.

[104] M. M. Qureshi, J. Brake, H.-J. Jeon, H. Ruan, Y. Liu, A. M. Safi, T. J. Eom, C. Yang, and E. Chung, "In vivo study of optical

speckle decorrelation time across depths in the mouse brain," *Biomedical Optics Express*, vol. 8, no. 11, p. 4855, nov 2017. [Online]. Available: https://www.osapublishing.org/abstract.cfm?URI=boe-8-11-4855

[105] M. Jang, H. Ruan, I. M. Vellekoop, B. Judkewitz, E. Chung, and C. Yang, "Relation between speckle decorrelation and optical phase conjugation (OPC)-based turbidity suppression through dynamic scattering media: a study on in vivo mouse skin," *Biomedical Optics Express*, vol. 6, no. 1, p. 72, 2015.

[106] N. Fayard, A. Cazé, R. Pierrat, and R. Carminati, "Intensity correlations between reflected and transmitted speckle patterns," *Physical Review A - Atomic, Molecular, and Optical Physics*, vol. 92, no. 3, pp. 1–9, 2015.

[107] T. Ando, R. Horisaki, and J. Tanida, "Speckle-learning-based object recognition through scattering media," *Optics Express*, vol. 23, no. 26, p. 33902, 2015. [Online]. Available: https://www.osapublishing.org/abstract.cfm?URI=oe-23-26-33902

[108] Y. Li, Y. Xue, and L. Tian, "Deep speckle correlation: a deep learning approach toward scalable imaging through scattering media," *Optica*, vol. 5, no. 10, p. 1181, 2018.

[109] M. Lyu, H. Wang, G. Li, S. Zheng, and G. Situ, "Learning-based lensless imaging through optically thick scattering media," *Advanced Photonics*, vol. 1, no. 03, p. 1, 2019.

[110] E. Tajahuerce, V. Durán, P. Clemente, E. Irles, F. Soldevila, P. Andrés, and J. Lancis, "Image transmission through dynamic scattering media by single-pixel photodetection," *Optics Express*, vol. 22, no. 14, p. 16945, jul 2014. [Online]. Available: https://www.osapublishing.org/oe/abstract.cfm?uri=oe-22-14-16945

[111] H. B. de Aguiar, S. Gigan, and S. Brasselet, "Polarization recovery through scattering media," *Science Advances*, vol. 3, no. 9, p. e1600743, sep 2017. [Online]. Available: http://advances.sciencemag.org/lookup/doi/10.1126/sciadv.1600743

[112] A. Beling and J. C. Campbell, "High-Speed Photodiodes," *IEEE Journal on Selected Topics in Quantum Electronics*, vol. 20, no. 6, pp. 57–63, 2014.

[113] E. Candes and M. Wakin, "An Introduction To Compressive Sampling," *IEEE Signal Processing Magazine*, vol. 25, no. 2, pp. 21–30, 2008.

[114] R. M. Willett, R. F. Marcia, and J. M. Nichols, "Compressed sensing for practical optical imaging systems: a tutorial," *Optical Engineering*, vol. 50, no. 7, p. 72601, 2011. [Online]. Available: http://dx.doi.org/10.1117/1.3596602

[115] A. Escobet-Montalbán, R. Spesyvtsev, M. Chen, W. A. Saber, M. Andrews, C. Simon Herrington, M. Mazilu, and K. Dholakia, "Wide-field multiphoton imaging through scattering media without correction," *Science Advances*, vol. 4, no. 10, 2018.

[116] F. Soldevila, E. Irles, V. Duran, P. Clemente, M. Fernandez-Alonso, E. Tajahuerce, and J. Lancis, "Single-pixel polarimetric imaging spectrometer by compressive sensing," *Applied Physics B: Lasers and Optics*, vol. 113, no. 4, pp. 551–558, 2013.

[117] F. C. MacKintosh, J. X. Zhu, D. J. Pine, and D. A. Weitz, "Polarization memory of multiply scattered light," *Physical Review B*, vol. 40, no. 13, pp. 9342–9345, nov 1989. [Online]. Available: https://link.aps.org/doi/10.1103/PhysRevB.40.9342

[118] D. J. Griffiths, *Introduction to Electrodynamics*, 4th ed. Cambridge University Press, 2017.

[119] J. D. Jackson, *Classical Electrodynamics*, 3rd ed. John Wiley & Sons, 1998.

[120] M. Kahnert, "Numerical solutions of the macroscopic Maxwell equations for scattering by non-spherical particles: A tutorial review," *Journal of Quantitative Spectroscopy and Radiative Transfer*, vol. 178, pp. 22–37, 2016. [Online]. Available: http://dx.doi.org/10.1016/j.jqsrt.2015.10.029

[121] R. F. Harrington, *Field Computation by Moment Methods*. IEEE, 1993. [Online]. Available: http://ieeexplore.ieee.org/xpl/bkabstractplus.jsp?bkn=5264934

[122] A. S. van de Nes, "Rigorous electromagnetic field calculations for advanced optical systems," Ph.D. dissertation, 2005.

[123] J. W. W. and M. R. Spiegel, "Mathematical Handbook of Formulas and Tables," *Mathematics of Computation*, vol. 23, no. 108, p. 886, oct 1969.

[124] C. F. Bohren and D. R. Huffman, *Absorption and scattering of light by small particles*. John Wiley & Sons, 2008.

[125] Y. Q. Zhang, G. C. Wan, K. Yang, and M. S. Tong, "On the point-matching method for solving electromagnetic radiation problems," in *2013 IEEE Antennas and Propagation Society International Symposium (APSURSI)*. IEEE, jul 2013, pp. 1526–1527. [Online]. Available: http://ieeexplore.ieee.org/document/6711422/

[126] T. A. Nieminen, H. Rubinsztein-Dunlop, and N. R. Heckenberg, "Calculation of the T-matrix: General considerations and application of the point-matching method," *Journal of Quantitative Spectroscopy and Radiative Transfer*, vol. 79-80, pp. 1019–1029, 2003.

[127] R. Azzam and N. M. Bashara, *Ellipsometry and polarized light*. North-Holland, 1977.

[128] J. J. Gil Pérez and R. Ossikovski, *Polarized Light and the Mueller Matrix Approach*. Boca Raton, FL : CRC Press, Taylor & Francis Group, [2016] — 2016 — Series: Series in optics and optoelectronics ; 21: CRC Press, jul 2017. [Online]. Available: https://www.taylorfrancis.com/books/9781482251562

[129] M. R. Foreman, "Informational limits in optical polarimetry and vectorial imaging," Ph.D. dissertation, Imperial College London, 2012.

[130] R. Penrose, "A generalized inverse for matrices," *Mathematical Proceedings of the Cambridge Philosophical Society*, 1955.

[131] A. De Martino, Y.-K. Kim, E. Garcia-Caurel, B. Laude, and B. Drévillon, "Optimized Mueller polarimeter with liquid crystals." *Optics letters*, vol. 28, no. 8, pp. 616–618, 2003.

[132] A. Ambirajan, "Optimum angles for a polarimeter," *Optical Engineering*, 1995.

[133] M. R. Foreman, A. Favaro, and A. Aiello, "Optimal Frames for Polarization State Reconstruction," *Physical Review Letters*, vol. 115, no. 26, pp. 1–6, 2015.

[134] M. R. Foreman and F. Goudail, "On the equivalence of optimization metrics in Stokes polarimetry," *Optical Engineering*, vol. 58, no. 08, p. 1, 2019.

[135] D. G. M. Anderson and R. Barakat, "Necessary and sufficient conditions for a Mueller matrix to be derivable from a Jones matrix," *Journal of the Optical Society of America A*, vol. 11, no. 8, p. 2305, 1994.

[136] R. Barakat, "Conditions for the physical realizability of polarization matrices characterizing passive systems," *Journal of Modern Optics*, vol. 34, no. 12, pp. 1535–1544, 1987.

[137] J. J. Gil, "Characteristic properties of Mueller matrices." *Journal of the Optical Society of America. A, Optics, image science, and vision*, vol. 17, no. 2, pp. 328–34, 2000. [Online]. Available: http://www.ncbi.nlm.nih.gov/pubmed/10680635

[138] R. A. Chipman, *Handbook of optics, Volume II: Devices, Measurements, & Properties*, 2nd ed., M. Bass, E. W. Van Stryland, D. R. Williams, and W. L. Wolfe, Eds. McGraw-Hill, Inc., 1995.

[139] S.-Y. Lu and R. A. Chipman, "Interpretation of Mueller matrices based on polar decomposition," *Journal of the Optical Society of America A*, vol. 13, no. 5, p. 1106, 1996. [Online]. Available: https://www.osapublishing.org/abstract.cfm?URI=josaa-13-5-1106

[140] R. Ossikovski, "Differential matrix formalism for depolarizing anisotropic media," *Optics Letters*, vol. 36, no. 12, p. 2330, 2011.

[141] R. Ossikovski, "Analysis of depolarizing Mueller matrices through a symmetric decomposition," *Journal of the Optical Society of America A*, vol. 26, no. 5, p. 1109, 2009. [Online]. Available: https://www.osapublishing.org/abstract.cfm?URI=josaa-26-5-1109

[142] H. C. van de Hulst, *Light scattering by small particles*. Courier Corporation, 1981.

[143] M. I. Mishchenko, L. D. Travis, and A. A. Lacis, *Multiple scattering of light by particles: radiative transfer and coherent backscattering*. Cambridge University Press, 2006.

[144] D. Bicout, C. Brosseau, A. S. Martinez, and J. M. Schmitt, "Depolarization of multiply scattered waves by spherical diffusers: Influence of the size parameter," *Physical Review E*, vol. 49, no. 2, pp. 1767–1770, 1994.

[145] V. Sankaran, M. J. Everett, D. J. Maitland, and J. T. Walsh, "Comparison of polarized-light propagation in biological tissue and phantoms," *Optics letters*, vol. 24, no. 15, pp. 1044–1046, 1999.

[146] M. P. Edgar, G. M. Gibson, and M. J. Padgett, "Principles and prospects for single-pixel imaging," *Nature Photonics*, vol. 13, no. 1, pp. 13–20, 2019. [Online]. Available: http://dx.doi.org/10.1038/s41566-018-0300-7

[147] M. F. Duarte, M. A. Davenport, D. Takhar, J. N. Laska, T. Sun, K. F. Kelly, and R. G. Baraniuk, "Single-pixel imaging via compressive sampling," *IEEE Signal Processing Magazine*, vol. 25, no. 2, pp. 83–91, mar 2008. [Online]. Available: http://ieeexplore.ieee.org/document/4472247/

[148] G. Strang, *Linear Algebra and its Applications*, 4th ed. Thomson Brookes/Cole, 2006.

[149] J. J. Gil, "Intrinsic stokes parameters for 3D and 2D polarization states," *Journal of the European Optical Society*, vol. 10, pp. 1–5, 2015.

[150] R. M. A. Azzam, "Mueller-matrix measurement using the four-detector photopolarimeter," *Optics Letters*, vol. 11, no. 5, p. 270, may 1986. [Online]. Available: https://www.osapublishing.org/abstract.cfm?URI=ol-11-5-270

[151] D. H. Goldstein, "Mueller matrix dual-rotating retarder polarimeter," *Applied Optics*, vol. 31, no. 31, p. 6676, 1992.

[152] P. R. T. Munro and P. Török, "Properties of high-numerical-aperture Mueller-matrix polarimeters," *Optics Letters*, vol. 33, no. 21, p. 2428, nov 2008. [Online]. Available: https://www.osapublishing.org/abstract.cfm?URI=ol-33-21-2428

[153] F. Kahnert, "Numerical methods in electromagnetic scattering theory," *Journal of Quantitative Spectroscopy and Radiative Transfer*, vol. 79-80, pp. 775–824, jun 2003. [Online]. Available: https://linkinghub.elsevier.com/retrieve/pii/S0022407302003217

[154] M. I. Mishchenko, H. J. W, Travis LD, and Editors, "Light Scattering by Nonspherical Particles: Theory, Measurements, and Applications," *Measurement Science and Technology*, 2000.

[155] K. S. Yee, "Numerical Solution of Initial Boundary Value Problems Involving Maxwell's Equations in Isotropic Media," 1966.

[156] J. L. Volakis, A. Chatterjee, and L. C. Kempel, "Review of the finite-element method for three-dimensional electromagnetic scattering," *Journal of the Optical Society of America A*, vol. 11, no. 4, p. 1422, 1994.

[157] M. Xu, "Electric field Monte Carlo simulation of polarized light propagation in turbid media," *Optics Express*, vol. 12, no. 26, p. 6530, 2004. [Online]. Available: https://www.osapublishing.org/oe/abstract.cfm?uri=oe-12-26-6530

[158] J. C. Ramella-Roman, S. A. Prahl, and S. L. Jacques, "Three Monte Carlo programs of polarized light transport into scattering media: part I," *Optics Express*, vol. 13, no. 12, p. 4420, 2005. [Online]. Available: https://www.osapublishing.org/oe/abstract.cfm?uri=oe-13-12-4420

[159] L. Novotny, B. Hecht, and D. W. Pohl, "Interference of locally excited surface plasmons," *Journal of Applied Physics*, vol. 81, no. 4, pp. 1798–1806, 1997. [Online]. Available: http://aip.scitation.org/doi/10.1063/1.364036

[160] M. Abramowitz and I. A. Stegun, *Handbook of mathematical functions: with formulas, graphs, and mathematical tables*. Courier Corporation, 1965, vol. 55.

[161] O. Svelto, *Principles of Lasers*. Boston, MA: Springer US, 2010. [Online]. Available: http://link.springer.com/10.1007/978-1-4419-1302-9

[162] R. M. A. Azzam, "Photopolarimetric measurement of the Mueller matrix by Fourier analysis of a single detected signal," *Optics Letters*, vol. 2, no. 6, p. 148, 1978.

[163] J. Lee, J. Koh, and R. W. Collins, "Dual rotating-compensator multichannel ellipsometer: Instrument development for high-speed Mueller matrix spectroscopy of surfaces and thin films," *Review of Scientific Instruments*, vol. 72, no. 3, pp. 1742–1754, 2001.

[164] S. N. Jasperson and S. E. Schnatterly, "An improved method for high reflectivity ellipsometry based on a new polarization modulation technique," *Review of Scientific Instruments*, vol. 40, no. 6, pp. 761–767, 1969.

[165] D. Lara and C. Dainty, "Double-pass axially resolved confocal Mueller matrix imaging polarimetry," *Optics Letters*, vol. 30, no. 21, p. 2879, 2005.

[166] F. H. Delplancke, "Investigation of rough surfaces and transparent birefringent samples with Mueller-matrix scatterometry," *Applied Optics*, vol. 36, no. 30, p. 7621, 1997.

[167] J. S. Tyo and T. S. Turner, Jr., "Imaging spectropolarimeters for use in visible and infrared remote sensing," in *Imaging Spectrometry V*, M. R. Descour and S. S. Shen, Eds., vol. 3753, no. October 1999, oct 1999, pp. 214–224. [Online]. Available: http://proceedings.spiedigitallibrary.org/proceeding.aspx?articleid=994800

[168] E. Garcia-Caurel, A. De Martino, and B. Drévillon, "Spectroscopic Mueller polarimeter based on liquid crystal devices," *Thin Solid Films*, vol. 455-456, pp. 120–123, 2004.

[169] J. M. Bueno, "Polarimetry using liquid-crystal variable retarders: Theory and calibration," *Journal of Optics A: Pure and Applied Optics*, vol. 2, no. 3, pp. 216–222, 2000.

[170] ARCOptix, *Variable Phase Retarder User Manual*. [Online]. Available: http://www.arcoptix.com/variable{_}phase{_}retarder.htm

[171] B. Lee, "Introduction to 12 Degree Orthogonal Digital Micromirror Devices (DMDs)," *Texas Instrument*, 2008.

[172] S. Turtaev, I. T. Leite, K. J. Mitchell, M. J. Padgett, D. B. Phillips, and T. Čižmár, "Comparison of nematic liquid-crystal and DMD based spatial light modulation in complex photonics," *Optics Express*, vol. 25, no. 24, p. 29874, 2017.

[173] S. N. Chandrasekaran, H. Ligtenberg, W. Steenbergen, and I. M. Vellekoop, "Using digital micromirror devices for focusing light through turbid media," *Emerging Digital Micromirror Device Based Systems and Applications VI*, vol. 8979, no. March 2014, p. 897905, 2014.

[174] E. G. Loewen, M. Nevière, and D. Maystre, "Grating efficiency theory as it applies to blazed and holographic gratings," *Applied Optics*, 1977.

[175] J. S. Tyo, D. L. Goldstein, D. B. Chenault, and J. A. Shaw, "Review of passive imaging polarimetry for remote sensing applications," *Applied Optics*, vol. 45, no. 22, p. 5453, aug 2006. [Online]. Available: https://www.osapublishing.org/abstract.cfm?URI=ao-45-22-5453

[176] J. S. Tyo, "Hybrid division of aperture/division of a focal-plane polarimeter for real-time polarization imagery without an instantaneous field-of-view error," *Optics Letters*, vol. 31, no. 20, p. 2984, 2006.

[177] T. Mu, C. Zhang, and R. Liang, "Demonstration of a snapshot full-Stokes division-of-aperture imaging polarimeter using Wollaston prism array," *Journal of Optics (United Kingdom)*, vol. 17, no. 12, 2015.

[178] J. L. Pezzaniti and D. B. Chenault, "A division of aperture MWIR imaging polarimeter," *Polarization Science and Remote Sensing II*, vol. 5888, no. August 2005, p. 58880V, 2005.

[179] R. M. A. Azzam, "Rotating-detector ellipsometer for measurement of the state of polarization of light," *Optics Letters*, vol. 10, no. 9, p. 427, 1985.

[180] B. Kaplan, G. Ledanois, and B. Drévillon, "Mueller matrix of dense polystyrene latex sphere suspensions: measurements and Monte Carlo simulation." *Applied Optics*, vol. 40, no. 16, pp. 2769–77, 2001. [Online]. Available: http://www.ncbi.nlm.nih.gov/pubmed/18357294

[181] J. D. Barter, P. H. Lee, H. R. Thompson, Jr., and T. G. Schneider, "Stokes parameter imaging of scattering surfaces," *Polarization: Measurement, Analysis, and Remote Sensing*, vol. 3121, no. October 1997, p. 314, 1997.

[182] A. van der Sluis, "Condition numbers and equilibration of matrices," *Numerische Mathematik*, vol. 14, no. 1, pp. 14–23, 1969.

[183] J. S. Tyo, "Design of optimal polarimeters: maximization of signal-to-noise ratio and minimization of systematic error," *Applied Optics*, vol. 41, no. 4, p. 619, feb 2002. [Online]. Available: https://www.osapublishing.org/abstract.cfm?URI=ao-41-4-619

[184] A. Semrock, T. Internal, and R. Fluorescence, "Flatness of Dichroic Beamsplitters Affects Focus and Image Quality," *Most*, pp. 2–3.

[185] D. Malacara, *Optical Shop Testing*, D. Malacara, Ed. Hoboken, NJ, USA: John Wiley & Sons, Inc., jun 2007. [Online]. Available: http://doi.wiley.com/10.1002/9780470135976

[186] P. S. Hauge, "Mueller Matrix Ellipsometry With Imperfect Compensators." *J Opt Soc Am*, vol. 68, no. 11, pp. 1519–1528, 1978.

[187] R. M. A. Azzam and A. G. Lopez, "Accurate calibration of the four-detector photopolarimeter with imperfect polarizing optical elements," *Journal of the Optical Society of America A*, 1989.

[188] R. W. Collins, "Automatic rotating element ellipsometers: Calibration, operation, and real-time applications," *Review of Scientific Instruments*, vol. 61, no. 8, pp. 2029–2062, 1990.

[189] O. Arteaga, J. Freudenthal, B. Wang, and B. Kahr, "Mueller matrix polarimetry with four photoelastic modulators: Theory and calibration," *Applied Optics*, vol. 51, no. 28, pp. 6805–6817, 2012.

[190] R. M. A. Azzam, E. Masetti, I. M. Elminyawi, and F. G. Grosz, "Construction, calibration, and testing of a fourdetector photopolarimeter," *Review of Scientific Instruments*, vol. 59, no. 1, pp. 84–88, jan 1988. [Online]. Available: http://aip.scitation.org/doi/10.1063/1.1139971

[191] E. Compain, S. Poirier, and B. Drevillon, "General and self-consistent method for the calibration of polarization modulators, polarimeters, and Mueller-matrix ellipsometers," *Applied Optics*, vol. 38, no. 16, p. 3490, 1999.

[192] C. Macías-Romero and P. Török, "Eigenvalue calibration methods for polarimetry," 2012.

[193] Thorlabs, "Thorlabs LPVISE100-A 1" Linear Polariser with N-BK7 Windows (400-700nm)." [Online]. Available: https://www.thorlabs.com/newgrouppage9.cfm?objectgroup{_}id=4984{&}pn=LPVISE100-A

[194] Thorlabs, "Thorlabs Zero Order Quarter waveplates." [Online]. Available: https://www.thorlabs.com/newgrouppage9.cfm?objectgroup{_}id=7234

[195] T. T. Do, L. Gan, N. H. Nguyen, and T. D. Tran, "Fast and efficient compressive sensing using structurally random matrices," *IEEE Transactions on Signal Processing*, vol. 60, no. 1, pp. 139–154, 2012.

[196] D. H. Brainard, "The Psychophysics Toolbox," *Spatial Vision*, vol. 10, no. 4, pp. 433–436, 1997. [Online]. Available: https://brill.com/view/journals/sv/10/4/article-p433{_}15.xml

[197] D. G. Pelli, "The VideoToolbox software for visual psychophysics: Transforming numbers into movies," *Spatial Vision*, 1997.

[198] M. Kleiner, D. H. Brainard, D. G. Pelli, C. Broussard, T. Wolf, and D. Niehorster, "What's new in Psychtoolbox-3?" *Perception*, 2007.

[199] R. Burdett, "Amplitude Modulated Signals: The Lock-in Amplifier," in *Handbook of Measuring System Design*, 2005.

[200] S. R. Cloude, "Conditions For The Physical Realisability Of Matrix Operators In Polarimetry," *Polarization Considerations for Optical Systems II*, vol. 1166, no. January 1990, p. 177, 1990.

[201] A. Aiello, G. Puentes, D. Voigt, and J. P. Woerdman, "Maximum-likelihood estimation of Mueller matrices," *Optics Letters*, vol. 31, no. 6, p. 817, mar 2006. [Online]. Available: https://www.osapublishing.org/abstract.cfm?URI=ol-31-6-817

[202] I. H. Malitson, "Interspecimen Comparison of the Refractive Index of Fused Silica," *Journal of the Optical Society of America*, 1965.

[203] W. F. Su, Y. C. Fu, and W. P. Pan, "Thermal properties of high refractive index epoxy resin system," *Thermochimica Acta*, 2002.

[204] K. Tahir and C. Dainty, "Experimental measurements of light scattering from samples with specified optical properties," *Journal of Optics A: Pure and Applied Optics*, vol. 7, no. 5, pp. 207–214, 2005.

[205] S. Schott, J. Bertolotti, J.-F. Léger, L. Bourdieu, and S. Gigan, "Characterization of the angular memory effect of scattered light in biological tissues," *Optics Express*, vol. 23, no. 10, p. 13505, 2015.

[206] J. Vargas, N. Uribe-Patarroyo, J. A. Quiroga, A. Alvarez-Herrero, and T. Belenguer, "Optical inspection of liquid crystal variable retarder inhomogeneities," *Applied Optics*, vol. 49, no. 4, pp. 568–574, 2010.

[207] B. Kaplan, E. Compain, and B. Drevillon, "Phase-modulated Mueller ellipsometry characterization of scattering by latex sphere suspensions," *Applied Optics*, vol. 39, no. 4, p. 629, feb 2000. [Online]. Available: https://www.osapublishing.org/abstract.cfm?URI=ao-39-4-629

[208] A. Patel, O. Kravchenko, and I. Manas-Zloczower, "Effect of curing rate on the microstructure and macroscopic properties of epoxy fiberglass composites," *Polymers*, vol. 10, no. 2, 2018.

[209] J. C. Ramella-Roman and S. L. Jacques, "Mueller-matrix description of collimated light transmission through liver, muscle, and skin," *Laser-Tissue Interaction XII: Photochemical, Photothermal, and Photomechanical*, vol. 4257, no. July 2001, p. 110, 2001.

[210] J. C. Ramella-Roman, A. Nayak, and S. A. Prahl, "Spectroscopic sensitive polarimeter for biomedical applications," *Journal of Biomedical Optics*, vol. 16, no. 4, p. 047001, 2011.